Author:
Fang, Xue

Title:
Investigation of Perylene Diimide Functional Supramolecular Polymers

Investigation of Perylene Diimide Functional Supramolecular Polymers

Xue Fang

School of Chemistry

UNIVERSITY OF BRISTOL

A dissertation submitted to the University of Bristol in accordance with the requirements for award of the degree of MASTER BY RESEARCH in the Faculty of Science

December 2020

Word count: Thirty-eight thousand and eight

Abstract

In this project, 4-bromobenzamide di-substituted perylene diimide (**PDI-BA-1**) was synthesized and investigated by solvent-, concentration- and temperature-dependent studies. Controllable self-assembly behaviour and morphologies were observed by ultraviolet-visible-near infrared absorbance spectrometry (UV-Vis) and transmission electron microscopy (TEM), providing a ground for further investigation of formation of supramolecular polymers. Solubilities of **PDI-BA-1** in fourteen solvents were evaluated by Hansen solubility parameters (HSP). A relationship between solvent HSP and self-assembly behaviour of **PDI-BA-1** was proposed. By tuning the hydrogen-bonding component and dipolar cohesive component of HSP (δ_H, δ_P), controllable self-assembly behaviour was observed in the ethyl acetate/n-hexane dual-solvent system. A set of computational methods were studied for monomeric **PDI-BA-1** geometry optimization and excitation behaviour. Two critical conformers of **PDI-BA-1** (reactive-open and trapped-closed) regarding controllable inter-/intra-molecular hydrogen bonds were found and optimized. To further explore functional supramolecular perylene diimide derivatives, a preliminary synthesis and modelling work of tetra(aniline)-substituted perylene diimide (**TANI-PDI**) was started, which lays the groundwork for further studies in the future.

Acknowledgements

I would first like to express my sincere appreciation for all the efforts and help from my supervisor Prof. Charl FJ Faul. I would like to thank Charl for offering me a place to join the Faul Research group. Charl's professional knowledge, dedicated instruction, insightful advice and encouragement during the past year were very helpful to improve my work.

As a beginner in the field of modelling, I would also thank Dr. Natalie Fey for her patient guidance and help in computational chemistry during the lockdown of the wet labs.

I would thank everyone in the Faul research group for their warm welcome during my first year in the UK, and all their cooperation during the COVID-19 pandemic period. I would especially thank my lab colleagues Henry Symons, Maximilian Hagemann, and Robert Wilson-Kovacs for helping with the perylene diimide studies; Esther Townsend for helping with tetra(aniline) work; Basiram Brahma Narzary and previous lab member Jie Chen for Hansen Solubility Parameters investigations; Pongsathon Boonrod for computational studies. I also want to thank my friend/roommate Bo Gao from School of Physics for helping with programming study during the lockdown. I would also thank my APM assessor Dr. Avinash Patil for offering advice in the development of this project.

I would thank all the staff and teams helping with the instrumental and theoretical work. Thanks go to Jean-Charles Eloi, Robert Harniman and Sean Davis from School of Chemistry's Imaging Facility; Germinal Magro for temperature-dependent ultraviolet-visible-near infrared spectrometer training; NMR team; Mass spectrometry team; and Advanced Computing Research Centre (ACRC).

Most importantly, I would like to sincerely thank my parents for their fully support and encouragement to my life and study.

2020 is a very special year due to the influence of COVID-19 pandemic. I would particularly express my appreciation to all the medical workers in the world, and I hope those who had lost their lives during the pandemic could rest in peace. I would also like to thank the Chinese Embassy in the UK for offering PPE support. Although part of the lab work in this project was influenced by the pandemic, I still want to say a big thank to all the staff of University of Bristol for their efforts to run the school smoothly.

Authors Declaration

I declare that the work in this dissertation was carried out in accordance with the requirements of the University's Regulations and Code of Practice for Research Degree Programmes and that it has not been submitted for any other academic award. Except where indicated by specific reference in the text, the work is the candidate's own work. Work done in collaboration with, or with the assistance of, others, is indicated as such. Any views expressed in the dissertation are those of the author.

SIGNED: ..... DATE:.....

Table of Contents

List of Figures

List of Schemes

List of Tables

List of Abbreviations

Table 0-1 List of abbreviations

Abbreviation	Full name
°C	Degree Celsius
A	Acceptor
a.u.	Atomic unit energy (Hartree Energy, 1 a.u. = 4.359744×10^{-18}J) Arbitrary unit (for absorbance/emission intensity)
B3LYP	Becke, 3-parameter, Lee–Yang–Parr (functional) [1–3]
BA-1	N-2(aminoethyl)-4-bromobenzamide
B-H Coupling	Buchwald-Hartwig coupling
Boc	*tert*-Butyloxycarbonyl protecting group
Boc-	*tert*-Butyloxycarbonyl (protecting group)
Bz-	Benzophenonyl (functional group)
c	Speed of light (2.99792458×10^{8} m / s) [4]
CAM-B3LYP	Coulomb-attenuating method based on B3LYP (functional) [5]
CT	Charge transfer (transition)
D	Donor
D_2O	Deuterium oxide
DCM	Dichloromethane
DFT	Density functional theory (method)
DMF	N,N-dimethylformamide
DMSO	Dimethyl sulfoxide
DMSO-d6	Dimethyl sulfoxide-d6
EA	Ethyl acetate
EB	Emeraldine base
EDA	Ethylene diamine
ES	Emeraldine salt

Abbreviation	Full name
ESI	Electrospray ionization
eV	Electron volt (1 eV = $1.602176634 \times 10^{-19}$ J) [6]
h	Planck constant ($6.62607015 \times 10^{-34}$ m^2 kg / s) [7]
Hex	n-Hexane
HF	Hartree Fock Theory
HOMO	Highest occupied molecular orbitals
i-PrOH	Isopropanol
IR	Infrared spectra
LEB	Leucoemeraldine base
LUMO	Lowest unoccupied molecular orbitals
MALDI	Matrix-assisted laser desorption/ionization
MB	Methyl 4-bromobenzoate
MS	Mass spectrometry
nm	Nanometre
NMI	1-Methylimidazole
NMR	Nuclear magnetic resonance spectroscopy
PB	Pernigraniline base
PCM	Polarizable continuum model
$Pd(dba)_2$	Bis (dibenzylideneacetone) palladium(0)
Pd/C	Palladium on activated carbon
PDI	Perylene Diimide
PDI-BA-1	N,N'-((1,3,8,10-tetraoxo-1,3,8,10-tetrahydroanthra[2,1,9-def:6,5,10-d'e'f']diisoquinoline-2,9-diyl)bis(ethane-2,1-diyl))bis(4-bromobenzamide)
PE	Petroleum ether/ Petroleum spirit 40-60 °C
Ph-	Phenyl (functional group)
Ph/NH_2-Boc-TANI-PDI	di-tert-butyl ((((((((((1,3,8,10-tetraoxo-1,3,8,10-tetrahydroanthra[2,1,9-def:6,5,10-d'e'f']diisoquinoline-2,9-diyl)bis(ethane-2,1-diyl))bis(azanediyl))bis(carbonyl))bis(4,1-phenylene))bis((tert-butoxycarbonyl)azanediyl))bis(4,1-

Abbreviation	Full name
	phenylene))bis((tert-butoxycarbonyl)azanediyl))bis(4,1-phenylene))bis((tert-butoxycarbonyl)azanediyl))bis(4,1-phenylene))bis(phenylcarbamate)
PTCDA	Perylene-3,4,9,10-tetracarboxylic dianhydride
S_0	Spin-singlet ground state
S_1	Spin-singlet 1st excited state
SCIPCM	Self-consistent isodensity Polarizable continuum model
SME	Semi-empirical (method)
TANI	Tetra(aniline)
TANI-PDI	N,N'-((1,3,8,10-tetraoxo-1,3,8,10-tetrahydroanthra[2,1,9-def:6,5,10-d'e'f']diisoquinoline-2,9-diyl)bis(ethane-2,1-diyl))bis(4-((4-((4-((4-(phenylamino)phenyl)amino)phenyl)amino)phenyl)amino)benzamide)
t-BuOH	tert-Butanol
THF	Tetrahydrofuran
UV-Vis	Ultraviolet–visible absorbance spectroscopy
v_n	The nth vibrational state
XPhos	2-Dicyclohexylphosphino-2′,4′,6′-triisopropylbiphenyl
λ	Wavelength

1. Introduction

1.1. Supramolecular polymers

Owing to the reversible intermolecular interactions and guest selectivity, the supramolecular polymers are controllable and expandable, while their mechanical properties are comparable with covalent polymers.[8–10] Supramolecular polymers thus show wide applications in functional materials, e. g., bio-compatible materials,[11,12] drug-delivery intermediates,[13] chemical sensors,[14] optoelectronic device,[15] etc. through the introduction of appropriate moieties.

In the following section, the general definition, interactions and linear polymerization theories of supramolecular polymers will be introduced.

1.1.1. Definition of supramolecular polymers

Compared with traditional covalent polymers, supramolecular polymers are defined as polymers whose monomeric units are connected through highly directional non-covalent interactions (Figure 1-1).[8] The key features of such non-covalent interactions should be 1) reversibility, which leads to a controllable self-assembly system, 2) directionality, which ensures the strength for holding monomeric units together as polymers.[8] The Van der Waals forces, also a non-covalent force found in supramolecular polymers systems, is not directional. Instead, the strength of Van der Waals force is reversibly affected by the increase of distance and occurs when two moieties are close enough.[16,17]

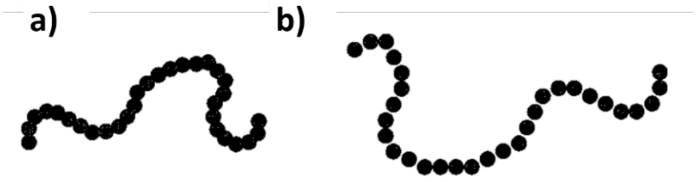

Figure 1-1 a) Covalent polymers and b) supramolecular polymers.[8]

1.1.2. Non-covalent interactions in supramolecular polymers

Common directional non-covalent interactions are hydrogen bonding, π-π interaction, host–guest interaction and metal coordination.[8,9,18] For studies of perylene diimide supramolecular

systems in this research, the hydrogen bonding and π interactions are the key non-covalent interactions to take into consideration. Different non-covalent interactions can work cooperatively or orthogonally to influence the character of materials.[19,20] The combined force can be either strengthened or attenuated compared with each of the original individual force component and will eventually reach a balance at a given condition, resulting in wide range of tunability of corresponding materials. Unlike the covalent bond, which is mainly determined by the intrinsic properties of atoms, non-covalent interactions are much more sensitive to external environmental factors, including the temperature, pH, concentration and polarity of solvents. Thus, by carefully tuning such conditions, the non-covalent interactions can be optimized to fit different application purposes. Owing to its controllable features, the non-covalent interactions play an important role in supramolecular polymers design.

In the following paragraphs, hydrogen bonding, π-π interaction and host–guest interaction will be briefly introduced.

1.1.2.1. Hydrogen bonding

Hydrogen-bonding interaction is an important secondary interaction in polymer science. It restricts the conformations and structures as well as the freedom of motion in molecules, e.g., α helices (Figure 1-2a) and β sheets (Figure 1-2b) with different folding parameters being determined by hydrogen bonding.[21,22]

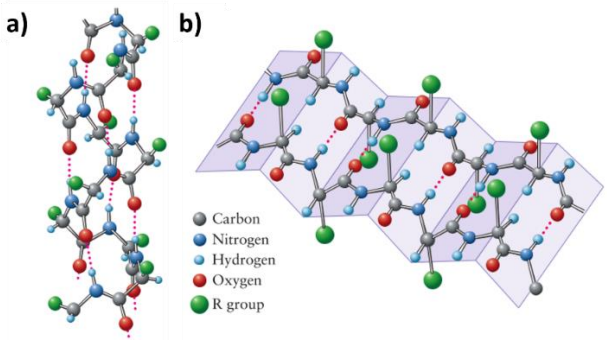

Figure 1-2 Hydrogen bonds in a) α helix and b) β sheets (the red dash lines denote the hydrogen-bonding interactions).[18]

Hydrogen-bonding interactions usually exist between hydrogen atoms and highly electronegative atoms with a free electron pair or lone pair, e.g., nitrogen atoms, oxygen atoms and fluorine atoms, etc., or groups with large polarity. The difference between electronegativity will introduce a dipole moment inside the molecule, causing the partial charge (δ) distributed on each atom. Thus, the negatively charged atom will form an interaction with the positively charged hydrogen atom from the neighbouring molecule as the hydrogen bond. Scheme 1-1

shows an example of partial charge distribution and hydrogen-bond formation between two neighbouring water molecules, in which the **d** is the distance between hydrogen atom and oxygen atom of the neighbouring water molecule, while **D** is the distance between two oxygen atoms in this system. The proton acceptor should be sterically accessible to the proton donor of the hydrogen bond.[23]

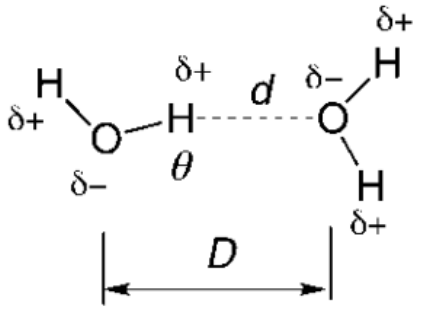

*Scheme 1-1 Partial charge distribution and hydrogen bond (dash line) in water molecules (**d** is the distance between hydrogen atom and oxygen atom of the neighbouring water molecule. **D** is the distance between two oxygen atoms in this system.)*[23]

The dissociation energy of hydrogen bond ranges from 0.2 to 40 kcal mol^{-1}, depending on the interaction type.[23] For symmetric hydrogen bonds, in which the hydrogen donor and acceptor are from the same group, the non-covalent hydrogen bond will be indistinguishable from a covalent bond, becoming a quasi-covalent bond (i.e., a strong hydrogen bond), with energy from 15 to 40 kcal mol^{-1}.[24,25] For groups with non-zero net charge, e.g., hydroxyl groups, carboxylate groups, ammonium ions, etc., the hydrogen bond behaves similar to an ionic interaction, with energies ranging from 4 to 15 kcal mol^{-1}.[21] When a hydrogen-donating group is interacting with a π-system, e.g., tryptophan, phenylalanine, a dipole-quadrupole interaction (similar to a cation-π interaction) will be formed as a weaker hydrogen bond (Figure 1-3), whose energy is less than 4 kcal mol^{-1}.[26–29]

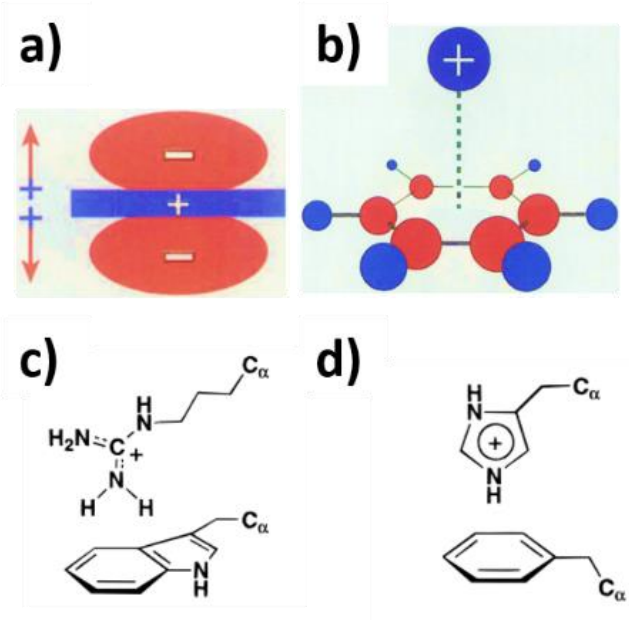

Figure 1-3 Cation-π-type hydrogen-bonding interaction. a) Schematic of benzene quadrupole. b) Schematic of cation-π interaction. Hydrogen bonding between perpendicularly placed c) arginine and tryptophan, d) histidine and phenylalanine.[26,27,29]

Hydrogen bonds can be formed either within a molecule or between the neighbouring molecules, corresponding to intramolecular and intermolecular hydrogen bonds, respectively. In 2015, Soichiro Ogi et al. found the reversibly convertible conformers of trialkoxybenzamide-substituted perylene diimide when studying its self-assembly mechanism (Scheme 1-2).[30]

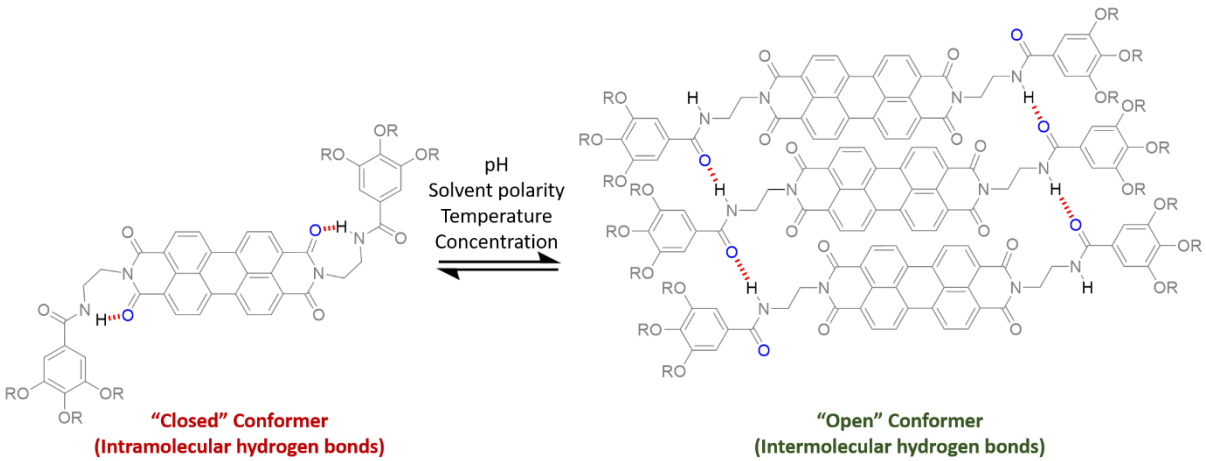

Scheme 1-2 Reversible conversion between 'closed' and 'open' conformers controlled by inter- and intra-molecular hydrogen bond of perylene diimide containing amide groups. Intramolecular hydrogen bonds between H atom on the amide group and O atom on the carbonyl group are formed in closed conformer. Intermolecular hydrogen bonds between H atom on the amide group and O atom on the amide group of adjacent monomer in open conformer.[30]

The "closed" conformer is restricted to its monomeric state at higher temperatures in toluene, a low polarity solvent, where intramolecular hydrogen bonds are formed between hydrogen atoms on the benzamide moiety and one of the oxygen atoms on the perylene diimide. In this case, the monomer will not be connected to the neighbouring molecules through hydrogen-bonding interactions. When the temperature decreases, the "open" form dominates and the assembly process can occur as amide groups can now interact with its neighbour molecules, introducing intermolecular hydrogen bonds. In those bonds, the oxygen of the amide group of the benzamide structure can interact with the hydrogen atoms of the amide group from the neighbouring molecules. The temperature range of such conversion is also dependent on the hydrogen-bond donor ability from the environment (solvent), which poses competition with the studied material itself. Other studies have also showed that factors like solvent polarity, concentration and pH can all control the hydrogen-bonding interactions.[30–32]

1.1.2.2. π-π interaction

π-π interaction (stacking) is a common interaction among molecules with π-conjugated surfaces and plays an important role in supramolecular polymerization.[33] Figure 1-4 shows the calculated surface potential of benzene and its simple derivatives.[34] The electronegativity difference between carbon atoms and substituted atoms on the aromatic ring will cause uneven distribution of surface charge, which further introduces a quadrupole moment in the π ring.[35,36] For example, the negative charges of benzene (Figure 1-4a) tend to locate on the more electronegative carbon ring instead of the peripheral hydrogen atoms. As a result, the benzene ring itself is partially negatively charged, while the surrounding space close to the ring is positive. For strongly electronegative atoms or strong electron withdrawing groups substituted aromatic molecules, e.g., hexafluorobenzene (Figure 1-4b), the quadrupole moment will be the opposite, with the aromatic ring positively charged and the surrounding space negative.

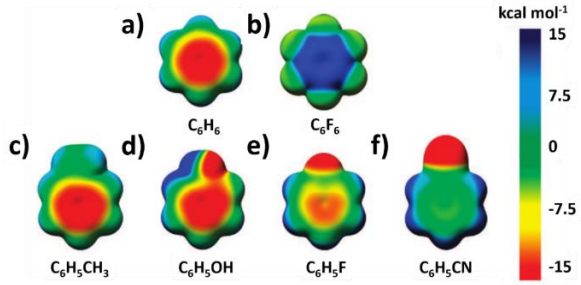

Figure 1-4 Calculated surface potential of aromatic rings with different substituents: a) benzene, b) hexafluorobenzene, c) toluene, d) phenol, e) 1-fluorobenzene, f) benzonitrile, with B3LYP/6-31g(d).[34]

The quadrupole moment will interact with the moment formed through other aromatic molecules or functional groups.[36,37] Based on the calculation results, for benzene dimers, whose quadrupole moments are same, the sandwiched structure (Figure 1-5a) is less favoured than the perpendicular (Figure 1-5b) and parallelly displaced (Figure 1-5c) structures in gas phase due to the repulsion of same charges.[38] Experimental results suggest that in the gas phase, the perpendicular structure is most favoured between dimers with the same quadrupole moments, while parallel planes are preferred for those with opposite quadrupole moments.[39] However, in the liquid phase, the dimer of hexafluorobenzene (with same quadruple moments) tends to be parallel, suggesting the π-π interaction is also influenced by the polarity of solvents.[39–41]

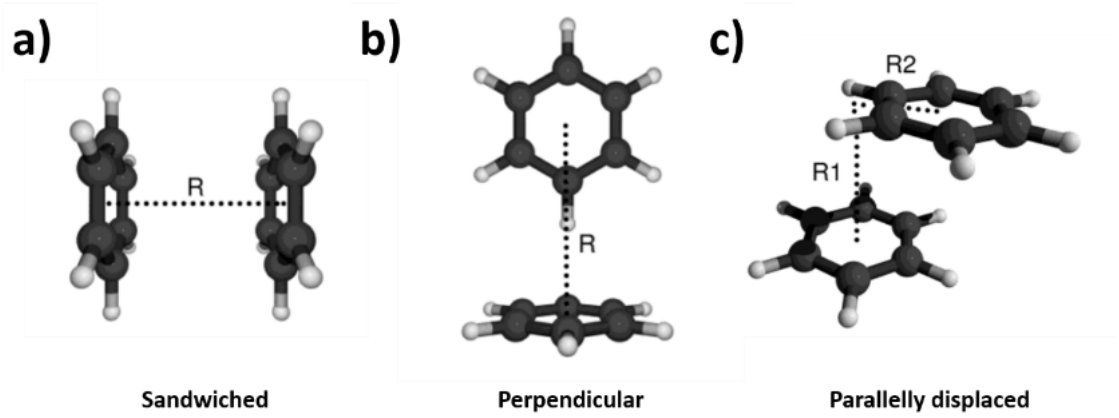

Figure 1-5 Structures of benzene dimers: a) sandwiched, b) perpendicular, c) parallelly displaced array.[38]

Both intra- and intermolecular π-π interaction are important in molecular functionalities. For intramolecular π-π interaction, the stacking of two aromatic functional groups can restrict the configuration and expose or protect the reaction site, which will functionalize the compounds with controllable photoelectronic response, chemical reactivity and binding selectivity.[42,43] Scheme 1-3 shows an X-ray structure of a supramolecular cage, an iridium complex cation named $[Ir(dmppz)_2(pbpy)]^+$, which is a solution-processable light-emitting ionic transition-metal complex, with much higher stability compared with traditional organic light-emitting diodes.[43] The key improvement of stability comes from its intramolecular π-π stacking of C_{33} and C_1 ring (highlighted in the structure), which effectively protects the complex from being attacked by nucleophilic reagents and opening of the complex.[43]

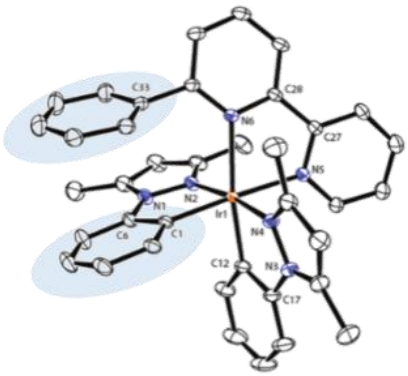

Scheme 1-3 Chemical structure and intramolecular π-π interaction in $[Ir(dmppz)_2(pbpy)]^{+}$[43]

Intermolecular π interactions can lead to 1D long-range organized supramolecular chains. One example is perylene-based supramolecular polymers (Figure 1-6), whose diimide derivatives will be further discussed in Section 1.2.[44] Perylene is a polycyclic aromatic hydrocarbon, which can form strong π-π stacking. Owing to the resonance property of electrons in large conjugated systems, the energy required for excitement in a perylene molecule corresponds to the visible light region, making perylene appears red. The strong stacking also limits its solubility. Thus, perylene is widely applied as a red pigment.[45]

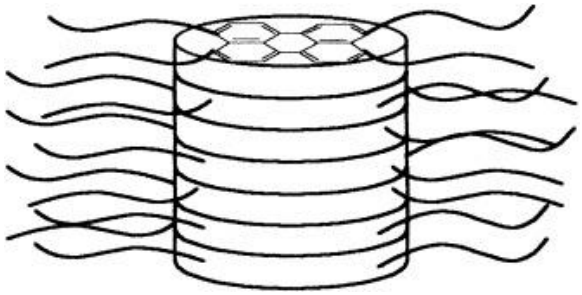

Figure 1-6 Stacking of perylene derivatives.[44]

π interactions are an important factor that will influence structures and geometries, which will further influence the chemical reactivity and assembly behaviour. Previous studies in π-conjugated supramolecular polymerization also suggest that the solvophobic effects overwhelm the electrostatic effects in π-π interaction, which provides theoretical guidance to design controllable self-assembly processes.[33,46]

1.1.2.3. Host–guest interaction

Host–guest interactions is a steric-sensitive and conformation-sensitive interaction, which specifically results in a unique dual-molecule system bound through non-covalent interaction.[47,48] With stimulation by pH, light, enzyme, etc., the releasing/binding behaviour of

host–guest system can be reversibly controlled.[49–51] Based on this property, host–guest interactions are widely applied in controllable molecular device engineering.[49,52] For example, a light-switchable molecule carrier based on cinnamamide-functionalized mesoporous silica nanoparticles/cucurbit[7]uril host–guest system was studied by Yang et.al (Figure 1-7). The cucurbit[7]uril can be bound by the end group of *trans*-cinnamamide via host–guest interaction. When stimulated by 300 nm UV light, the *trans*-cinnamamide is converted to its *cis*-conformer, whose steric effect is too large to fit the cavity of cucurbit[7]uril. As a result, the cargo molecule (rhodamine B) can be released.[53]

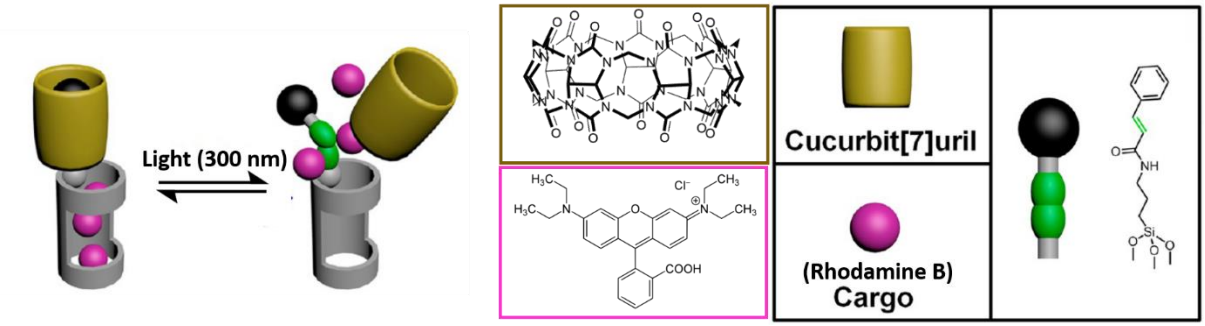

Figure 1-7 Reversible host–guest interaction between cucurbit[7]uril and cinnamamide-functionalized mesoporous silica nanoparticles controlled by light stimuli. Where the yellow column stands for cucurbit[7]uril. The green structure stands for the double bond, whose conformers are reversibly controlled by 300 nm light. Once stimulated into cis-conformer, the host-guest interaction will break, leading to the cargo molecules Rhodamine B (pink sphere in the figure) to be released.[49]

1.1.3. Principles of supramolecular polymerization

Supramolecular polymerization can be described by several criteria, including driving forces, monomer's functional binding moieties and free energy changes during the polymerization process. Thermodynamic factors from the environment and stoichiometric equivalence of monomers influence the extent of supramolecular polymerization together.[33] Depending on concentrations and functional moieties of the monomers, supramolecular polymerization can reach different morphologies and dimensions, including 1D linear fibres, 2D layers, 3D cross-linked networks and supramolecular gels.[54–57] In this research, linear polymerization in dilute solutions will be the main focus. Isodesmic polymerization, ring-chain polymerization and cooperative polymerization mechanism will be briefly introduced in the following sections.[33]

General parameters of polymerization include weight-average/number-average molar mass, polydispersity index (*Đ*), and weight-average/number-average degree of polymerization. *Đ* is defined by Eq. 1-1, where M_W and M_N are weight-average molar mass (Eq. 1-2) and number-average molar mass (Eq. 1-3), respectively. By dividing M_W and M_N with molar mass of

monomeric unit (m), weight-average degree of polymerization (DP_W) and number-average degree of polymerization (DP_N) can be calculated by Eq. 1-4 and Eq. 1-5, respectively.[58]

$$Đ = \frac{M_W}{M_N} \quad \text{Eq. 1-1}$$

$$M_W = \frac{\sum_{i=1}^{N} N_i M_i^2}{\sum_{i=1}^{N} N_i M_i} \quad \text{Eq. 1-2}$$

$$M_N = \frac{\sum_{i=1}^{N} N_i M_i}{\sum_{i=1}^{N} N_i} \quad \text{Eq. 1-3}$$

$$DP_W = \frac{M_W}{m} \quad \text{Eq. 1-4}$$

$$DP_N = \frac{M_N}{m} \quad \text{Eq. 1-5}$$

1.1.3.1. Isodesmic polymerization

The equilibrium of isodesmic polymerization is described with Eq. 1-6, Eq. 1-7, where concentration of M_i is described by Eq. 1-8.[33]

$$M_1 + M_1 \overset{K}{\rightleftharpoons} M_2 \quad \text{Eq. 1-6}$$

$$M_{i-1} + M_1 \overset{K}{\rightleftharpoons} M_i \quad \text{Eq. 1-7}$$

$$[M_i] = K^{-1}(K[M_1])^i \ (i = 1, 2, 3, \ldots, \infty) \quad \text{Eq. 1-8}$$

Isodesmic polymerization is characterized by a constant molar equilibrium constant, K. As a result, differences of Gibbs free energy between each polymerization step are identical (Figure 1-8). The energy of an isodesmic polymerization system is independent of polymer's chain length, with no cyclization occurring.[33]

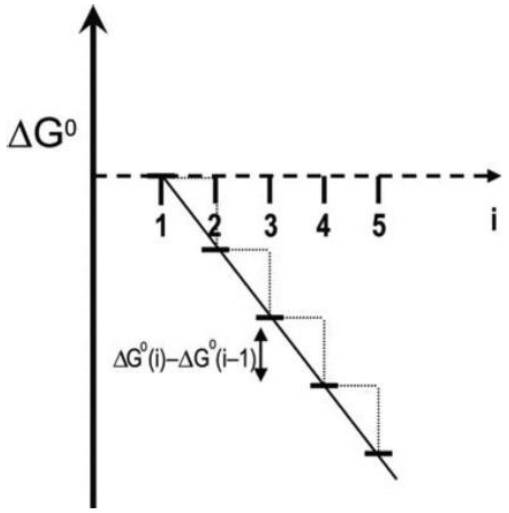

Figure 1-8 Change of Gibbs free energy during isodesmic supramolecular polymerization.[33]

Hereby K can be calculated by measuring concentration-dependent absorbance, fluorescence or calorimetry, provided that the results are proportional to their concentrations.[33,59–61] However, since only the nearest neighbouring molecules in these methods are considered, further confirmation to distinguish the isodesmic mechanism from dimerization, which includes determining concentration-dependent degree of polymerization (DP) and temperature-dependent properties should be tested.[33,59]

With the isodesmic mechanism, discotic monomers can grow in a face-to-face order (Figure 1-9a), while the bifunctional monomers will grow through connecting its functional ending with the neighbour's functional groups (Figure 1-9b).[33]

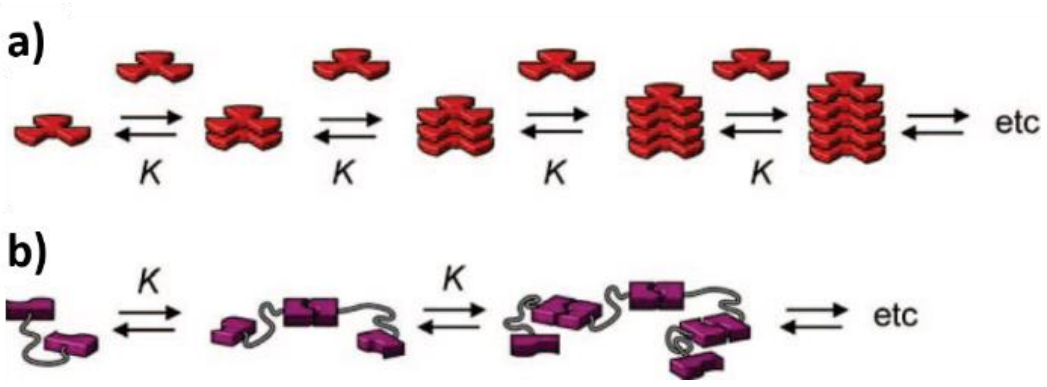

Figure 1-9 Schematic of isodesmic polymerization of a) face-to-face polymerization, b) bifunctional polymerization, where K is the equilibrium constant for each step.[33]

The concentration-dependent degree of polymerization and dispersity are plotted in Figure 1-10.[58,62]

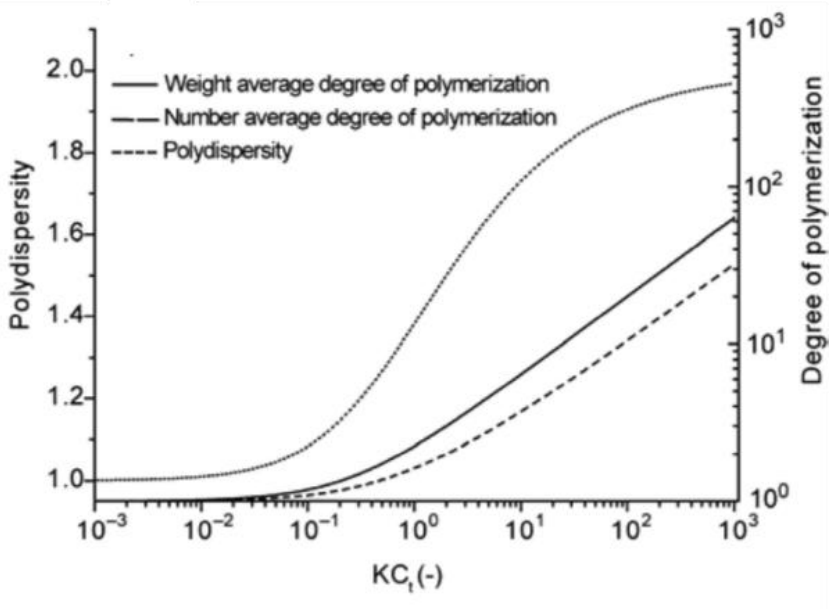

Figure 1-10 Concentration-dependent dispersity and degree of polymerization of isodesmic growth. (K denotes association constant. C_t denotes total concentration of monomers. KC_t denotes the dimensionless concentration.)[33]

It is found that a high M_W material can only be achieved at high concentration, with the polydispersity index limited to 2.[58] However, the amount of monomer in the system grows with the number of polymers and is always the most abundant component in the system, which suggests that their size distribution is wide.[33] When DP_N is significantly larger than 1, its size distribution follows a broad exponential distribution.[62] Since there is no clear threshold between monomers and polymers, no critical concentration or temperature is observed in an isodesmic polymerization processes.[49,48,50]

1.1.3.2. Ring–chain polymerization

The equilibrium of ring–chain polymerization is described in Scheme 1-4, where C denotes cyclized conformers and M denotes linear monomeric structures. K is the equilibrium constant, where the subscript "inter" denotes an intermolecular equilibrium constant, and "intra" denotes an intramolecular equilibrium constant.[33]

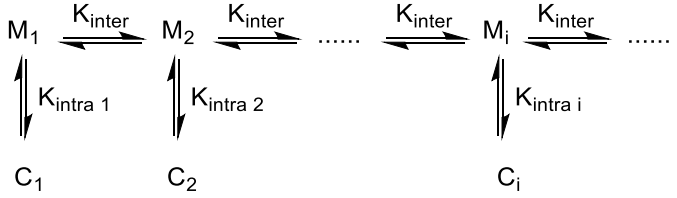

Scheme 1-4 Equilibrium of ring–chain polymerization, where K_{inter} is intermolecular equilibrium constant, and K_{intra} is intramolecular equilibrium constant.[33]

Ring-chain polymerization usually occurs in molecules with two open ends that can either form intra- or intermolecular connections. Its mechanism can be regarded as a competitive polymerization process within and between molecules, controlled both by the inter- and intramolecular equilibrium (Figure 1-11). The intramolecular equilibrium enables the formation of rings, while the intermolecular equilibrium elongates the chain. The ratio of K_{intra} and K_{inter} is defined as effective molarity (EM), which helps to quantitively describe the relative preference of these two equilibriums (Eq. 1-9).[33,63] According to Ercolani's theory,[64] the EM of degree of polymerization (i) can be expressed by Eq. 1-10, where λ equals to -5/2 when all the rings are provided to be strainless.[33,65,66]

$$EM_i = \frac{K_{intra(i)}}{K_{inter}} \quad \text{Eq. 1-9}$$

$$EM_i = EM_1 i^{\lambda} \quad \text{Eq. 1-10}$$

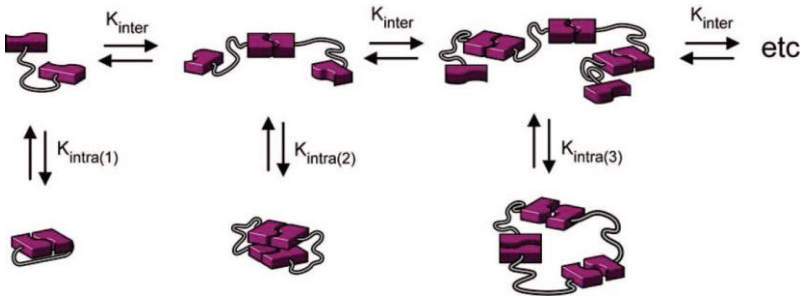

Figure 1-11 Schematic of ring-chain polymerization, where K_{inter} is intermolecular equilibrium constant and K_{intra} is intramolecular equilibrium constant.[33]

Different from isodesmic polymerization, the ring-chain polymerization has a clear critical concentration below which the chain growth is dominated by ring formation (Figure 1-12), and a critical temperature (depending on EM and polymerization driving force).[67,68] Hereby C_T denotes the total concentration of monomers, which is largely determined by spacer rigidity and shows a descending trend with increasing chain flexibility.[69]

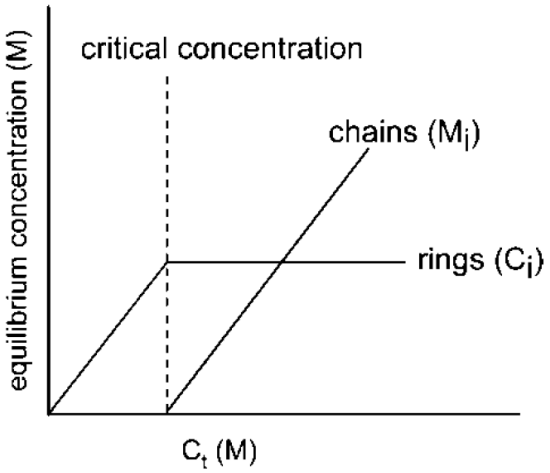

Figure 1-12 Equilibrium concentration of ring-chain polymerization, where C_t is the total concentration, M_i is the chain with i units, C_i is the ring with i unit.[33]

1.1.3.3. Cooperative polymerization

Cooperative polymerization is characterized by nucleation, followed by further elongation (Figure 1-13). The corresponding assembly constants are K_n and K_e. This type of polymerization can be divided into cooperative nucleated and cooperative downhill supramolecular polymerization, which can be distinguished through concentration-dependent kinetic tests. At high concentrations, cooperative nucleated polymerization can be converted to cooperative downhill polymerization.[33,70,71]

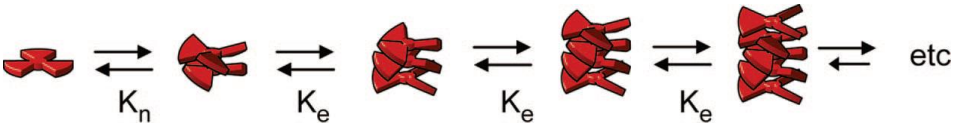

Figure 1-13 Schematic of cooperative polymerization, where K_n is assembly equilibrium constant for nucleation, and K_e is assembly equilibrium constant for elongation.[33]

Cooperative nucleated supramolecular polymerization is characterized by an increase of free energy change followed by a decrease (Figure 1-14a).[33] At the initial stage, an energetically-unfavoured nucleus formation process occurs. This process introduces a time lag that can be tuned with external nucleus/seed addition. As a result, a critical concentration or temperature can be observed in cooperative nucleated supramolecular polymerization.[72]

Cooperative downhill supramolecular polymerization however shows a globally decreasing Gibbs free energy (Figure 1-13b),[33] with its nucleation energetically less favoured than the later elongation phase.[70,73]

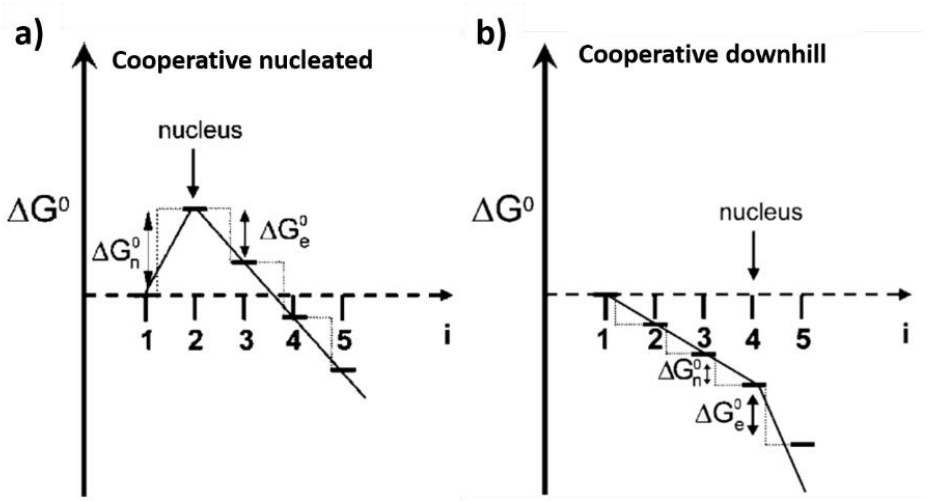

Figure 1-14 Change of Gibbs free energy in a) cooperative nucleated and b) cooperative downhill supramolecular polymerization.[33]

There is an opposite polymerization mechanism called anti-cooperative polymerization, in which the elongation is less favoured than the initial nucleation, resulting in the formation of oligomers with low dispersity.[33,74] The polarity and steric effect of head groups of amphiphilic monomers, which lead to different extents of electrostatic interaction, potentially influence their polymerization mechanism.[33,74–76]

1.2. PDI-based supramolecular polymers

1.2.1. Structures of PDI monomer

The key structure of PDI monomers is shown in Scheme 1-5. There are two diimide structures at the termini of the perylene core.[77] The N-substituted R groups could be alkyl chains, aryl groups, etc.[78,79] The substituted moieties tune the functions and assembly behaviour of the PDIs.[77,80–82]

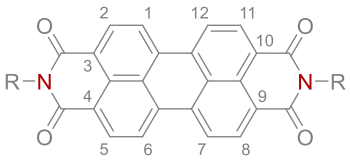

Scheme 1-5 Key structure of PDI monomer.

In this research, the symmetric PDIs (i.e., with the R groups are identical, e.g., PDIs shown in Scheme 1-6a) will be the focus. Asymmetric PDIs (Scheme 1-6b), with the two R groups different from each other, will not be discussed here.[78,80–84]

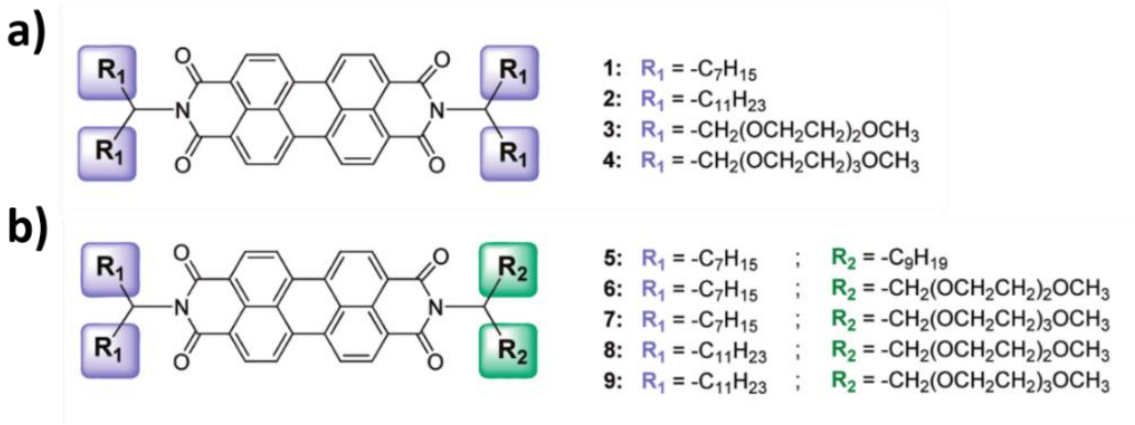

Scheme 1-6 Examples of a) Symmetric PDIs, and b) Asymmetric PDIs, with different R groups (Wicklein et al.)[78]

The PDIs can be modified at three different positions, which are imide- (the imide nitrogen atoms, Scheme 1-7a), *ortho*- (2, 5, 8, 11 sites on the perylene ring, Scheme 1-7b) and bay-position (positions 1, 6, 7, 12 on the perylene core, Scheme 1-7c).[77] Due to the steric and electronic effects, the locations and properties of substituents will influence the molecular geometries and electron density distributions, which will further affect the properties of PDI compounds. [85–87]

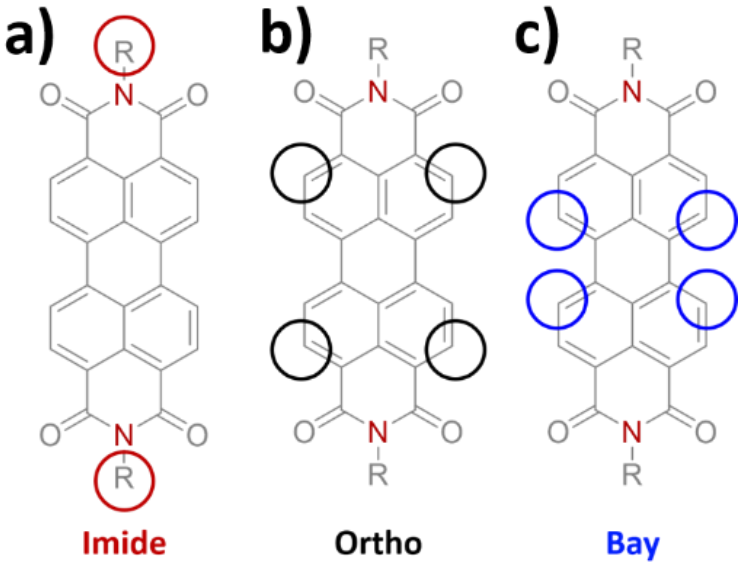

Scheme 1-7 a) Imide-substituted, b) ortho-substituted, c) bay-substituted positions of PDI compounds.

1.2.2. Common synthesis routes of PDIs

Perylene-3,4,9,10-tetracarboxylic dianhydride (**PTCDA**, Scheme 1-8), a commercially available red pigment (Red 224) is the usual starting point for the synthesis of PDIs.[88,89]

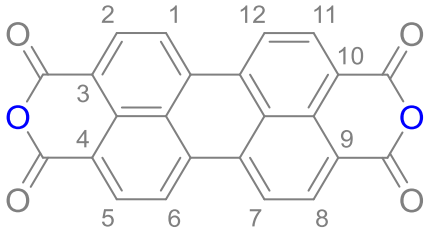

*Scheme 1-8 Perylene-3,4,9,10-tetracarboxylic dianhydride (**PTCDA**).*

The formation of bay-, imide- and *ortho*- substituted PDIs are illustrated in Scheme 1-9. To modify the bay positions (Scheme 1-9a), the **PTCDA** is first reacted with chlorine or bromine, with the aid of sulfuric acid, resulting in fully substituted (tetrachloro) or half substituted (dibromo, mainly in the 1, 7 positions) intermediates, respectively. The second step is to attack the dianhydride structures with primary amine derivatives. Moieties can further be attached to the activated bay area through nucleophilic substitution reactions.[16]

Directly reacting **PTCDA** with primary amine compounds will break the anhydride structures and yield imide-substituted products (Scheme 1-9b).[89] There is limiting reports about directly obtaining *ortho*-substituted products from **PTCDA** without any modification at the imide positions. However, further reaction with imide-substituted PDIs using a ruthenium catalyst

will selectively add groups like alkenes[90] or arylboronates[91] to the *ortho* positions (Scheme 1-9c).[77]

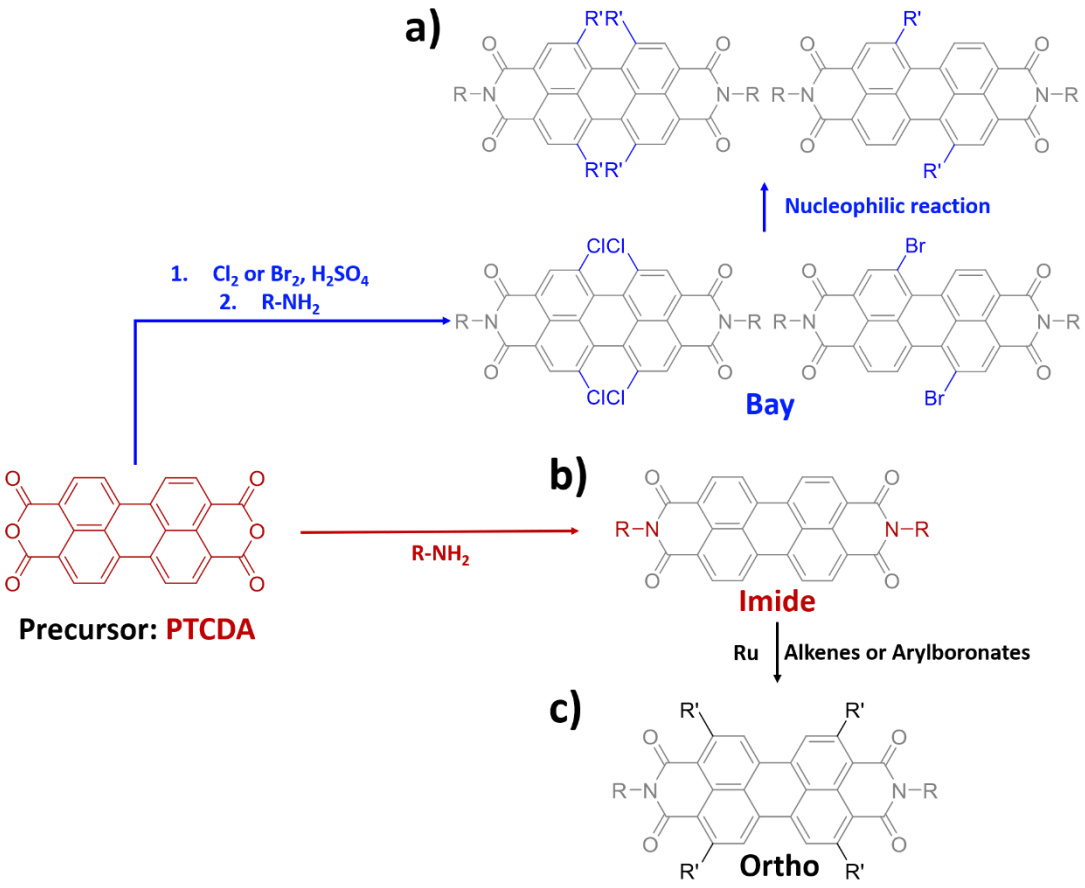

Scheme 1-9 Common synthesis routes to achieve a) bay-substituted, b) imide-substituted and c) ortho-substituted PDIs.

1.2.3. Effects of substituted positions

The perylene core has a rigid planar π-conjugated system. For **PTCDA**, this π–π stacking limits the distance between two neighbour molecular planes to 3.21 Å (Figure 1-15).[92,93]

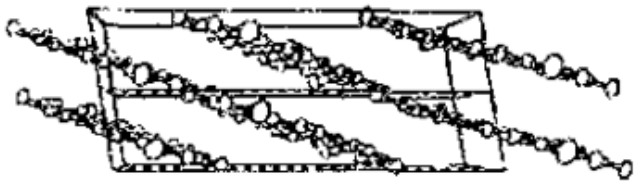

*Figure 1-15 **PTCDA** stacking structure.*[92]

The short distance between rigid π-conjugated planes endows **PTCDA** with significant absorbance in the visible light region[93,94] and anisotropic electronic transport properties, i.e.

only electrons transport along the molecular plane, while holes transport perpendicularly to the plane, making **PTCDA** an n-type organic semiconductor (electrons as major carriers).[93,95,96] Since most organic semiconductors are p-type (holes as major carriers),[78,97] the study of n-type organic semiconductors could provide a pathway to process organic photovoltaics device and field effect transistors.[95,98]

The UV-Vis absorbance and emission spectra of **PTCDA** a) dispersed in DMSO and b) in solid-state film are shown in Figure 1-16.[93] In the solution state, the major absorbance is at 555 nm, and an excitation around 590 nm (CT [0-F]) is explained as Frankel-like state, whose weak intensity is due to the tail of S_1[0-0] excitation at 555 nm.[99] The direct transition configurations of **PTCDA** are illustrated in Figure 1-16c and d.[100]

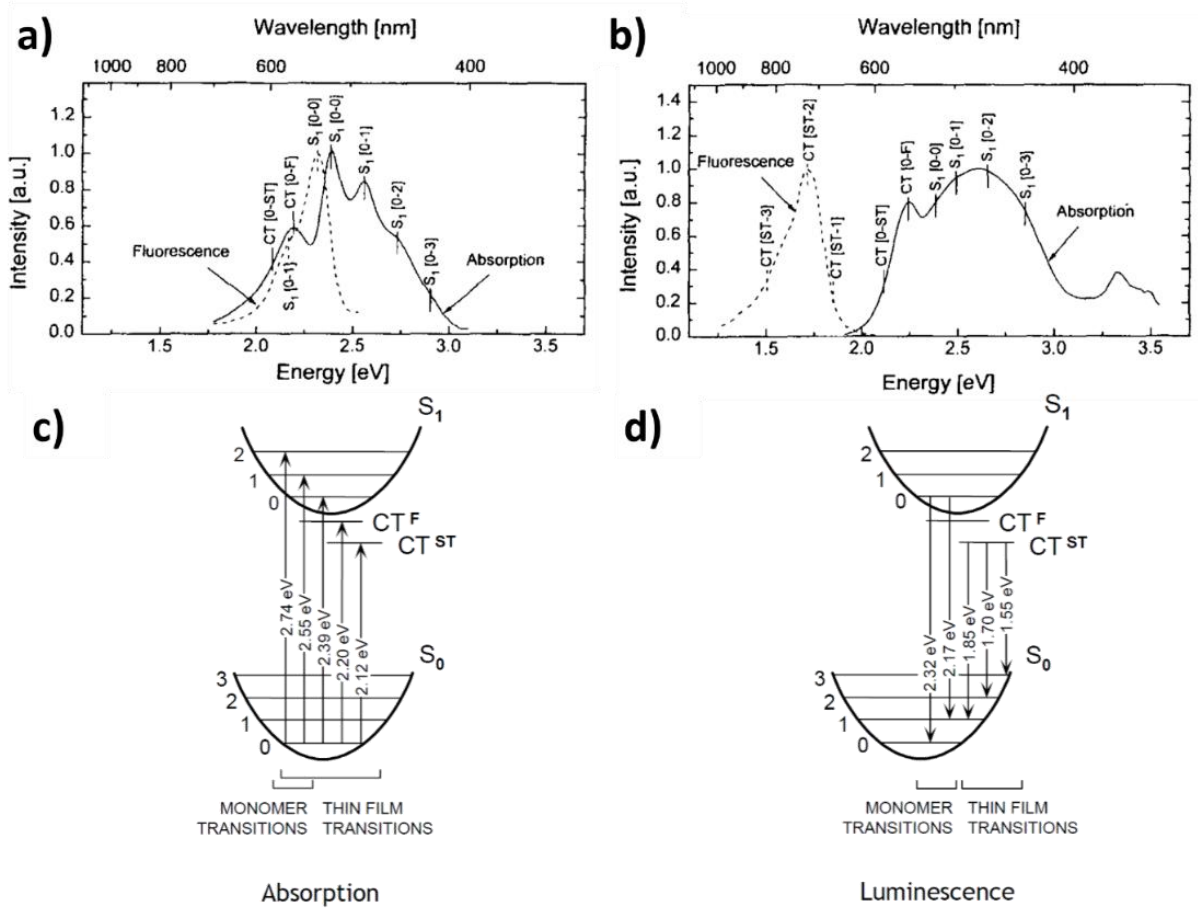

*Figure 1-16 Absorbance and fluorescence spectra of **PTCDA** in a) DMSO (0.2 μM), b) solid state film (100 nm thick), with solid line as absorbance, dash line as fluorescence. CT denotes charge transfer exciton states.[93] c) Absorbance and d) fluorescence of monomer and thin film transition configurations of **PTCDA** .[100]*

The introduction of imide substituents can improve the polarity of the material and attenuate the stacking tendency of the planar π-conjugated perylene core, which will thus depress the extent of assembly by limiting its association constant.[33,101]

Based on the frontier orbitals calculations, the electron density distribution of the highest occupied molecular orbitals (HOMO) and the lowest unoccupied molecular orbitals (LUMO) of non-substituted PDI are shown in Figure 1-17.

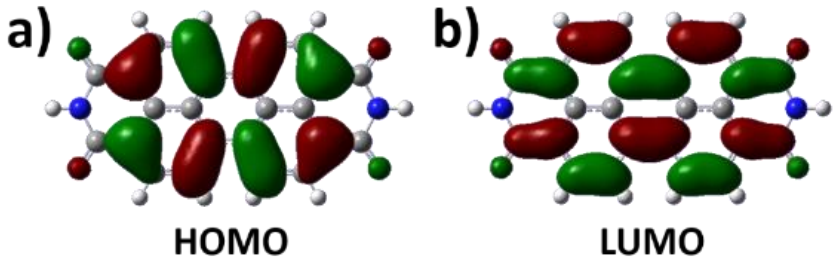

Figure 1-17 Frontier orbitals of non-substituted PDI (with each substituted position hydrogen atom). a) HOMO, b) LUMO.

The imide position acts as a node for the frontier orbitals, which suggests that it does not contribute to the electronic density distribution of the perylene core. However, the bay and *ortho* positions directly influence the perylene electronic structure as well as its geometry. Based on their molecular orbital differences, the imide-, *ortho*-, and bay-substituted PDIs can therefore be applied in various fields.

To illustrate the effects of substituted positions, computational optimized geometries of fluoride PDIs are shown in Figure 1-18. The fluorine atom here acts as a simplification of large electronegative atoms or electron-withdrawing groups. The details for each substituted mode will be explained in the following sections.

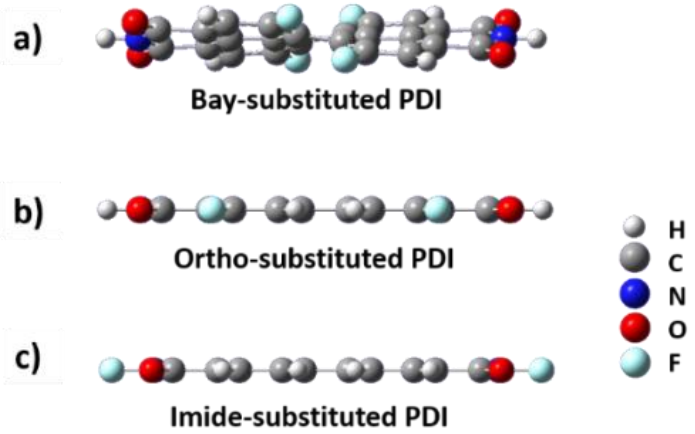

Figure 1-18 Computational geometries of a) bay-, b) ortho-, c) imide-substituted fluoride PDIs (optimized with PM6 in vacuum).

1.2.3.1. Bay-substituted PDIs

Since the bay positions of PDIs are close to each other, their electronic and steric repulsion effects are significant. As shown in Figure 1-18a, the large repulsion between the substituents forces the perylene plane to be twisted, which decreases the intensity of π-π stacking between the molecules. Previous research about core-twisted PDI studies led by Würthner et al. (Figure 1-19),[102] proved that in such situations the long-ranged supramolecular structures cannot be formed. Instead, only dimers or short-ranged stacking are available.[33,102]

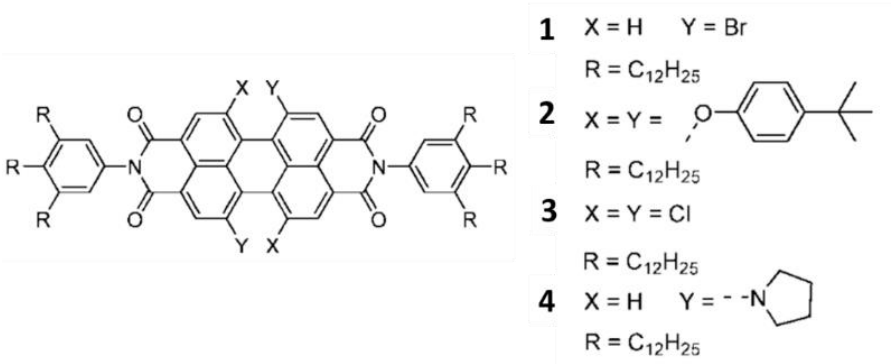

Figure 1-19 Chemical structures of bay-substituted PDIs studied by Würthner et al.[102]

In addition, by studying the crystalline structure of a bay-substituted PDI (N,N′-dicyclohexyl-1,7-dibromo-PDI) dimer (Figure 1-20), Würthner's team have observed a 35° rotational replacement in the aggregate and a 24° dihedral angle within the twisted perylene plane.[102,103] In further research of bay-substituted PDIs, this research group also found that the dihedral angle within the perylene plane can vary from 15° to 40°, which is proportional to both the Gibbs energy of dimerization and the aggregation emission band shift.[102]

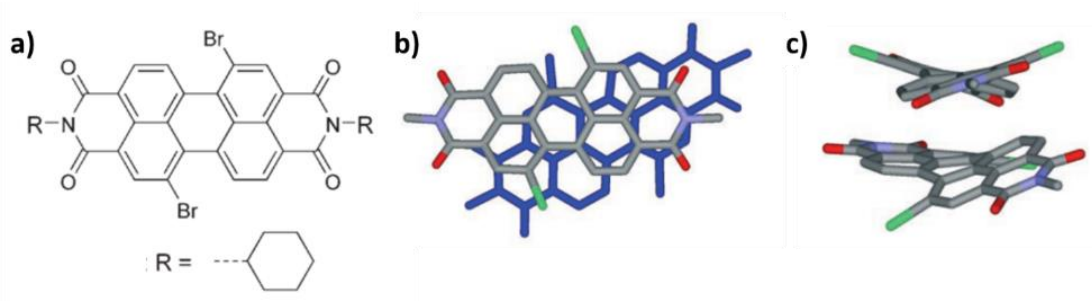

Figure 1-20 a) Chemical scheme, b) top view and c) side view of N,N'-Dicyclohexyl-1,7-dibromo-PDI crystalline dimer studied by Würthner et al.[102,103]

Furthermore, the optoelectronic properties of bay-substituted PDIs are more flexible to control. By characterizing a group of bay-substituted PDIs shown in Figure 1-21a, Würthner's team have found a broad shift of absorbance (from 524 nm to 705 nm) in the visible light region

when changing the substituents (Figure 1-21b), with their corresponding steady-state photoluminescence emission spectra shown in Figure 1-21c.[102]

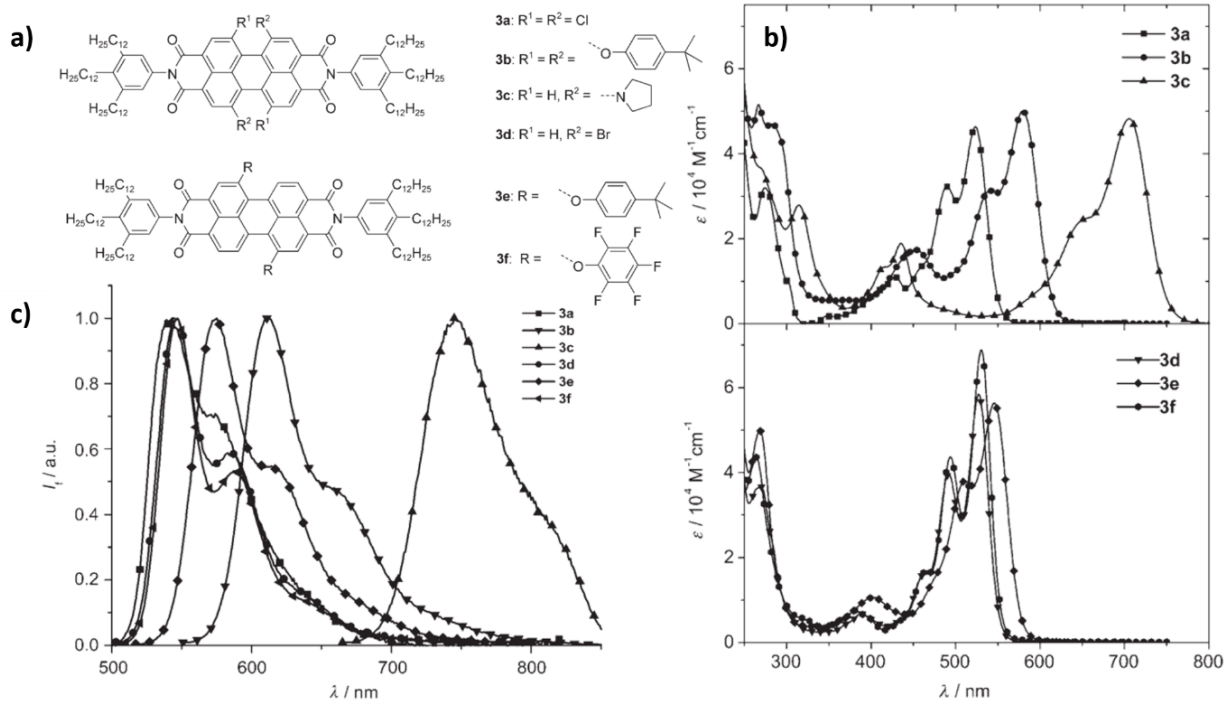

Figure 1-21 a) Chemical schemes of bay-substituted PDIs studied by Würthner et al., and their b) UV-Vis absorbance spectra, and c) normalized photoluminescence spectra.[102]

Various investigations have shown that the bay-substituted PDIs with electro-donating groups display a larger shift than those with electro-withdrawing groups do. For example, the PDI substituted with pyrrolidine (3c in Figure 1-21a), showed an 181 nm absorbance displacement, while those substituted by halogens did not change much in their absorbance and emission spectra.[102] Optimized with the PM6 method in vacuum, the geometry and frontier orbitals of 3c are visualized in Figure 1-22, from which it can be observed that the HOMO (Figure 1-22b, e) and LUMO (Figure 1-22c, f) are significantly different from which has been shown in Figure 1-17, i.e., the planar structures of perylene orbitals are twisted and a part of orbitals from bay-substituents is contributing to the frontier orbitals of the corresponding PDI.

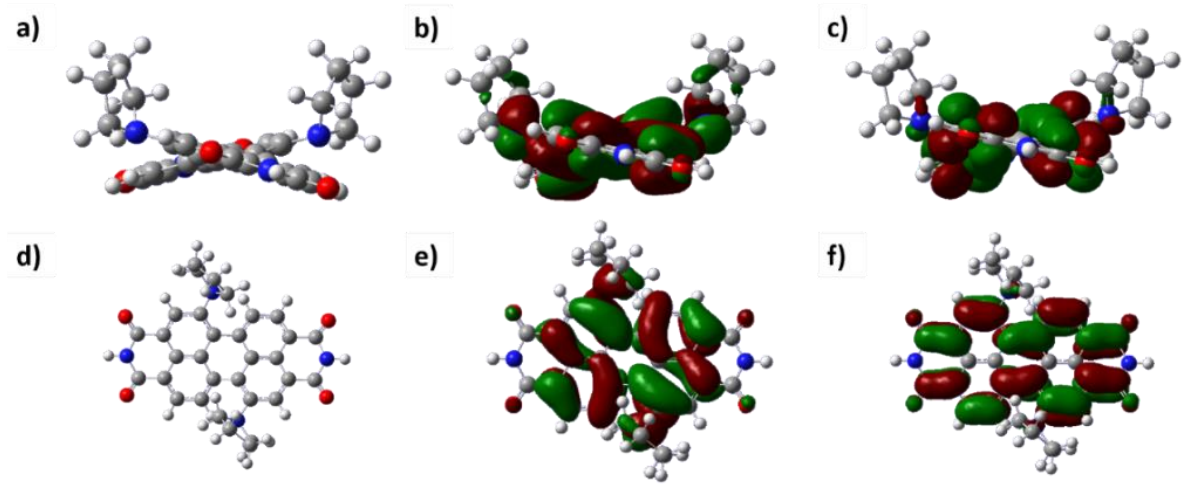

Figure 1-22 Calculated geometry of PDI substituted with pyrrolidine at the 1, 7 bay position. a) side view of calculated geometry. b) side view of HOMO. c) Side view of LUMO. d) top view of geometry. e) top view of HOMO. f) top view of LUMO. (Optimized with PM6 in vacuum).

The symmetry-breaking effect in bay-substituted PDIs also induces increasing intensities of transitions that are previously forbidden, e.g., S_0-S_2 transition.[102,104] Based on their easily tuned excitation behaviour and high quantum yields, the bay-substituted PDIs are particular suitable for organic photovoltaic devices.[102] However, the twisted perylene plane in bay-PDIs simultaneously holdback their applications in which strong intermolecular interactions are required, e.g., organic field effect transistors.[77,105] In the next section, an alternative, *ortho*-substituted PDIs, will be introduced.

1.2.3.2. *Ortho*-substituted PDIs

Different from bay-substituted PDIs, *ortho*-substituted PDIs hold the planar structure in the perylene region (Figure 1-18b), which can be explained by the relative large distance between four *ortho* positions and thus their low steric repulsion between each other. However, the *ortho* positions still contribute to the frontier orbitals of the corresponding PDI. As a result, the transition energy gap as well as the photo response of *ortho*-substituted PDIs are also influenced by modifying its substituent structures.[77,90]

The regioselective synthesis of *ortho*-substituted PDIs was previously a big challenge, until Shinokubo et al. discovered the Ru-catalysed synthesis pathway and successfully obtained a set of alkyl- and alkoxylsilyl-based *ortho*-substituted PDIs (Figure 1-23a). They studied the emission (Figure 1-23b) and absorbance behaviour of solution-based (Figure 1-23c) and solid-state (Figure 1-23d) *ortho*-substituted PDIs. They found the alkyl substituents greatly

influenced the quantum yields of solid-state PDIs and showed a slight enhancing effect on molar absorbance coefficients of solution-based PDIs.[90]

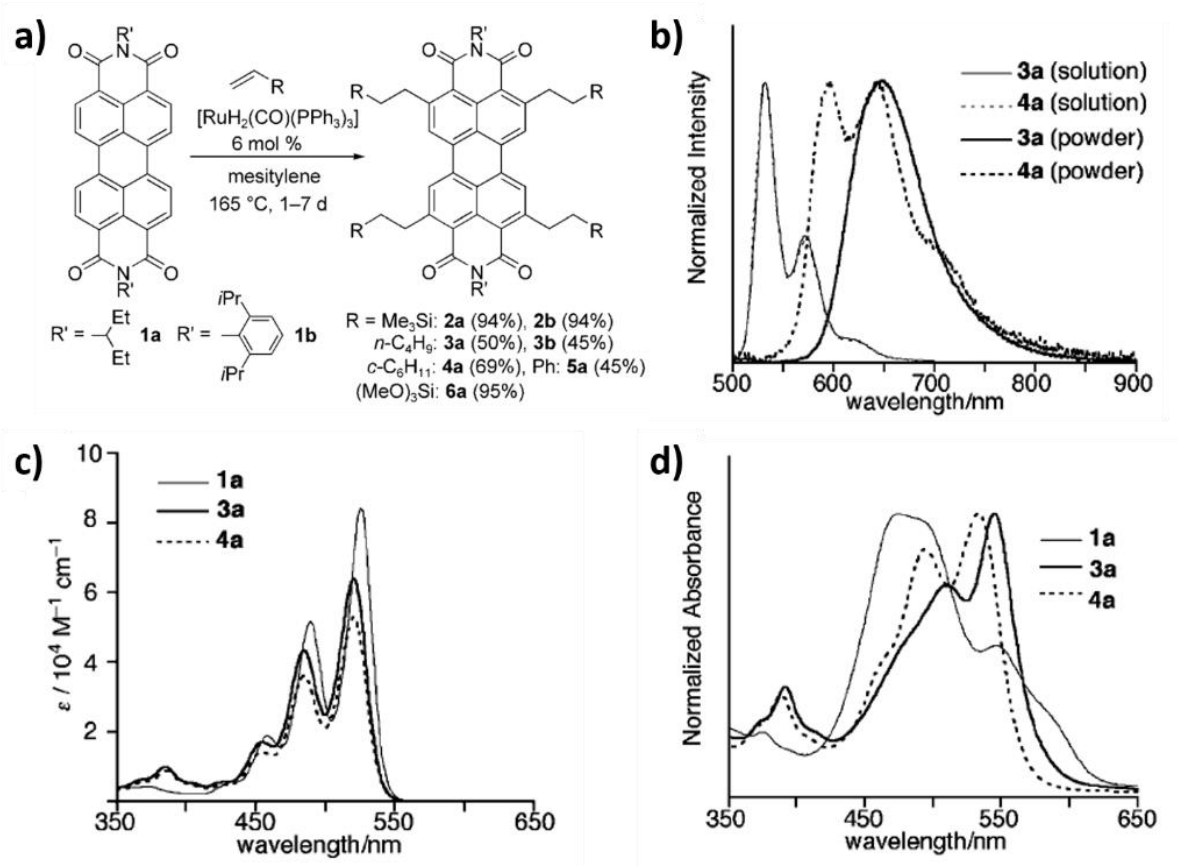

Figure 1-23 Synthesis and optical properties of ortho-substituted PDIs. a) Chemical structures and synthesis conditions. b) Emission spectra of solid-state ortho-substituted PDIs and that in toluene. c) Molar absorbance coefficient of ortho-substituted PDIs in toluene. d) Absorbance of solid-state ortho-substituted PDIs.[90]

The morphology and aggregation behaviour of *ortho*-substituted PDIs are also controlled by their side-chain structures. When its imide positions were fixed with 3-pentyl groups, trimethylsilyl-substituted *ortho*-PDI (2a in Figure 1-23a) showed a herringbone stacking structure, as revealed by X-ray studies. The cyclohexyl-substituted *ortho*-PDI (4a in Figure 1-23a) however formed a parallel alignment, which was mainly due to its alkyl groups steric interaction.[90]

Another study done by Hartnett et al. showed the morphology and optoelectronic performance of *ortho*-substituted PDIs was influenced by 1) the substituents on the *ortho* positions, 2) the alkyl chains on the imide positions and 3) solvent composition (Figure 1-24).[106]

In their work, they fixed the *ortho* positions of PDI with phenyl groups and modified the imide substituents with a set of alkyl chains (Figure 1-24a). PDIs with sterically hindered solubilizing head groups, e.g., 3-pentyl, 3,7-dimethyloctyl, tended to form a herringbone alignment in

concentrated toluene (Figure 1-24b). However, for those with less hindered structures, e.g., n-octyl group, the slip-stacked geometry was preferred in concentrated toluene. When toluene was diluted by methanol, slip-stacking structures were also observed in 3,7-dimethyloctyl system (Figure 1-24c).[106] The details of morphologies will be introduced in Section 1.2.4.

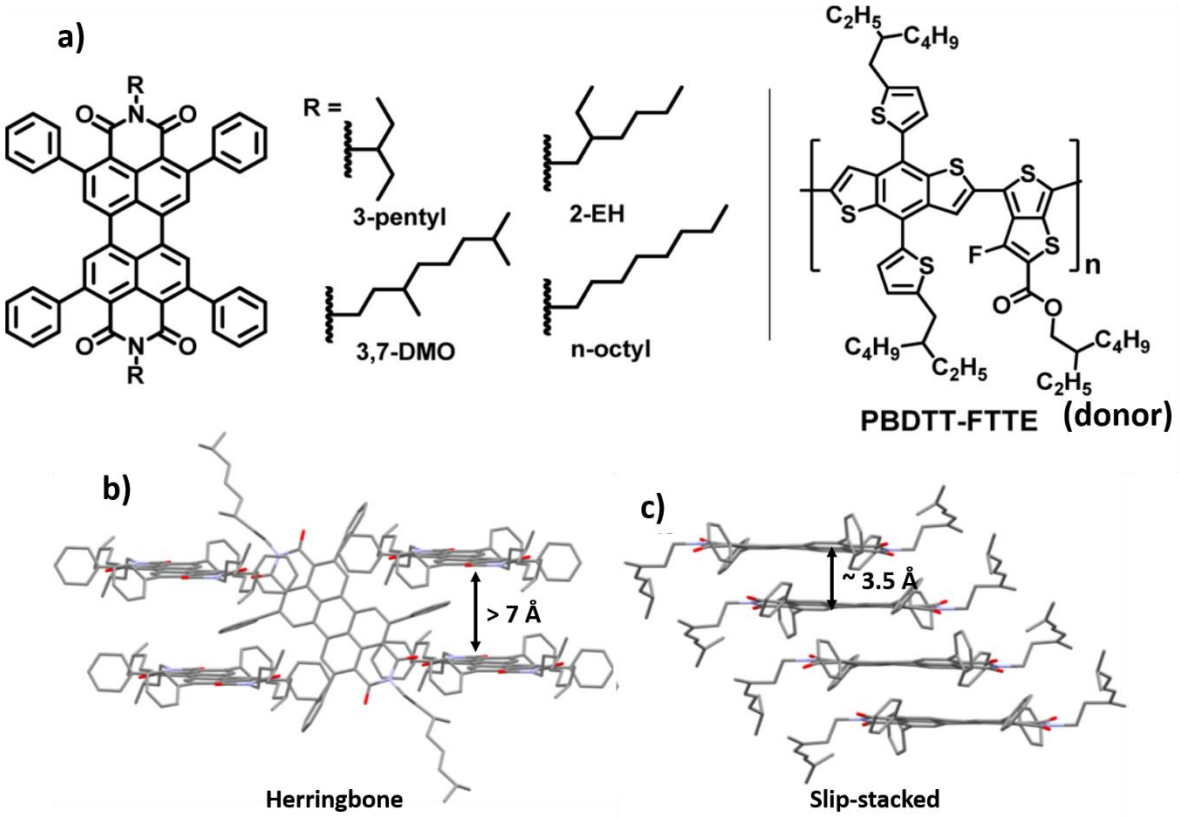

Figure 1-24 a) Chemical structures of tetraphenyl-substituted ortho PDIs with 3-pentyl, 3,7-dimethyloctyl (DMO), 2-ethylhexyl (EH) and n-octyl substituted on diimide positions and the donor material PBDTT-FTTE. b) Herringbone packing (leading to rhombus crystalline structure) of 3, 7-dimethyloctyl disubstituted ortho-PDIs, c) Slip-stacking (leading to needle-like crystalline structure) of 3, 7-dimethyloctyl disubstituted ortho-PDIs.[106]

Hartnel's team had also revealed the assembly mechanism of herringbone and slipped-stack *ortho*-substituted PDIs. In herringbone structures, the phenyl groups substituted on the *ortho* positions participated in the stacking of perylene. Thus, there were two assembly directions in this system that formed rhombic crystals (Figure 1-24b). However, in slipped-stack structures, PDIs were only assembled perpendicular to the perylene plane, which resulted in the needle-like crystals (Figure 1-24c). Herringbone structures restricted the distance between molecules to be larger than 7 Å, whilst this distance in slipped-stack structures was only around 3.5 Å. As a result, herringbone structures limited electronic coupling compared with slipped-stack structures.

When blended with a donor material, *ortho*-substituted PDI can serve as an acceptor material. The donor-acceptor pair can then be utilized in optoelectronic devices. Hartnel's team suggested that the device performance can be controllable by crystalline structures (herringbone or slipped-stack) of PDI. They observed that in **PBDTT-FTTE** blended systems (Figure 1-24a), it was much easier for (N,N-bis(3,7-dimethyloctyl)-2,5,8,11-tetraphenyl-PDI with herringbone structures to undergo charge separation. However, it is also easier for the carriers (electrons and holes) to undergo charge recombination for herringbone structures, which caused a loss in the power conversion efficiency by 0.6 %.[106,107]

Like bay-substituted PDI, *ortho*-PDI is also a suitable material for photoelectronic device especially in its solid state. Moreover, using the conjugated planar core of *ortho*-substituted PDIs makes it easier to control its morphologies and thus photoelectronic performance.[106]

1.2.3.3. Imide-substituted PDIs

Imide-substituted PDIs, as mentioned before, retain both the planar structure and frontier orbitals electronic distribution in their perylene region, which particularly provide opportunities for self-assembly studies.

The dominant driving force in this system is π interaction, which can be mediated with side-chain properties and external solvation effects.[57] Substituents with large steric effects and hydrophobic association, e.g., bulk groups and long alkyl chains, can improve the solubilities of resulting imide-substituted PDIs.[57,86,108] In addition, as mentioned in Section 1.1.2.1, moieties containing both hydrogen bond donors and acceptors, e.g., amide groups, can introduce controllable inter/intra-molecular hydrogen-bonding interactions to cooperate with or mediate π interactions. The combined non-covalent interaction leads to controllable self-assembly behaviour of corresponding PDIs.[30]

By introducing moieties with amphiphilic properties and solvents with various polarities, the morphologies of corresponding PDIs are controllable.[109] For example, in 2007, Zhang et al. synthesized four amphiphilic imide-substituted PDIs, with two of them wedge- and the rest dumbbell-shaped (Figure 1-25). The wedge-shaped PDIs formed spherical micelles in 2% THF in water, while the symmetric dumbbell-shaped PDIs formed nanorods. Hereby water was a poor solvent while THF was a good one. The co-polymers formed from PDIs with different shape and side chain hydrophobicities assembled as vesicles, where sizes and curvatures were tuneable with variations of the stoichiometry ratio of the individual PDI components.[109]

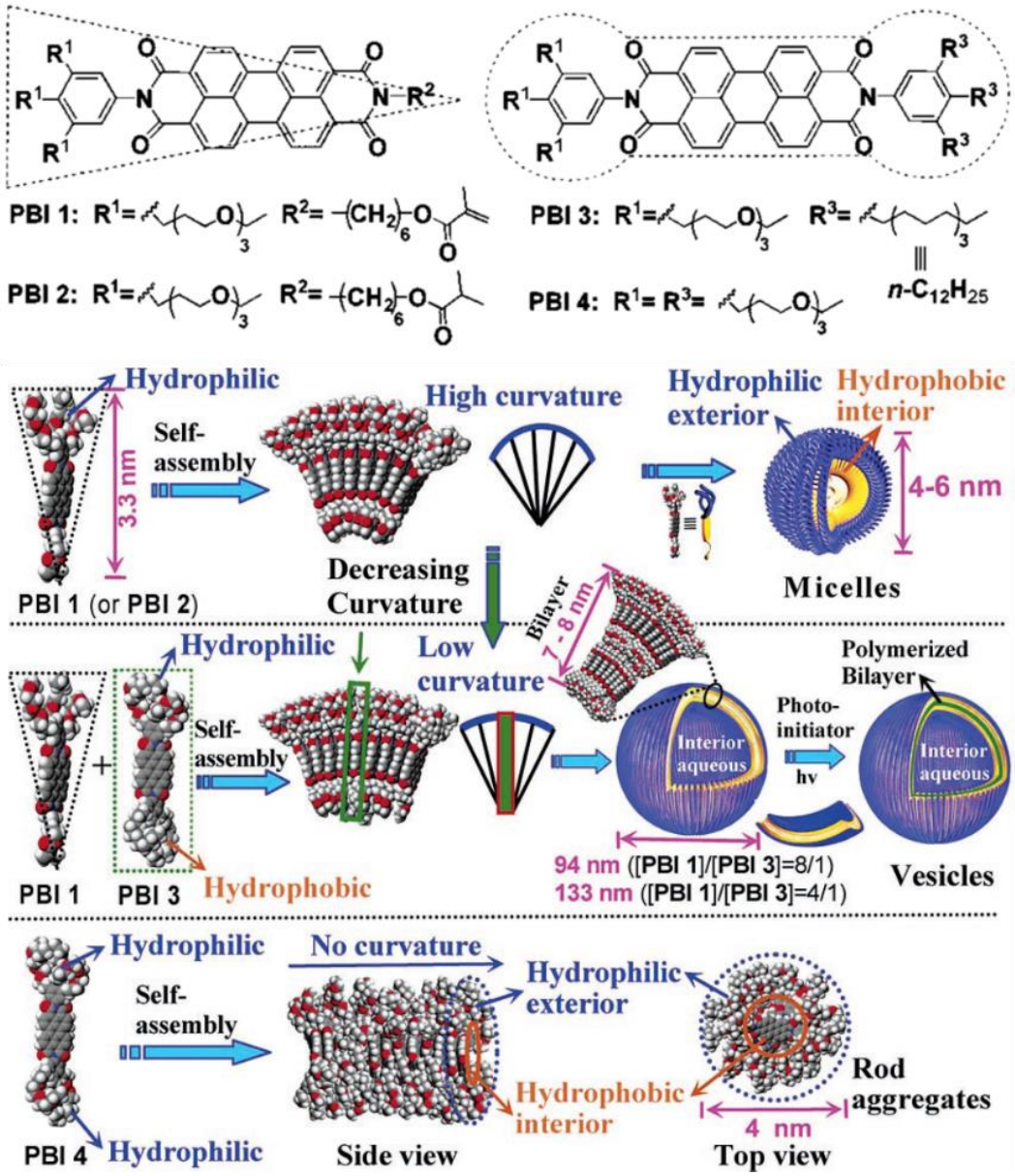

Figure 1-25 Morphology-controllable (including curvature and shape, i.e., micelles, vesicles and rod aggregates) imide-substituted PDIs with amphiphilic side chains. Self-assembly behaviour of wedge- and dumbbell-shaped PDIs.[109]

For seeded-growth supramolecular polymerization, the resulting morphologies can also be controlled with the ratio between monomers and seeds. Hereby monomer is the naturally dissolved form of molecules, while seeds are pre-treated by sonication of long fibres, which helps inducing nucleation and crystal growth.[30,108] Two PDIs substituted with oligo(ethylene glycol) at their imide positions were studied by Jarrett-Wilkins et al. (Figure 1-26a). The difference between fibres and seeds was clearly shown in their UV-Vis absorbance spectra (Figure 1-26b), where an aggregation peak around 560 nm disappeared in the seeds solution. Their characterization results suggested a linear relationship between fibre length and

monomer/seeds mass ratio, which was not only effective in homo supramolecular elongation (Figure 1-26c, e), but also performed well in bi-molecular systems (Figure 1-26d, f).[108]

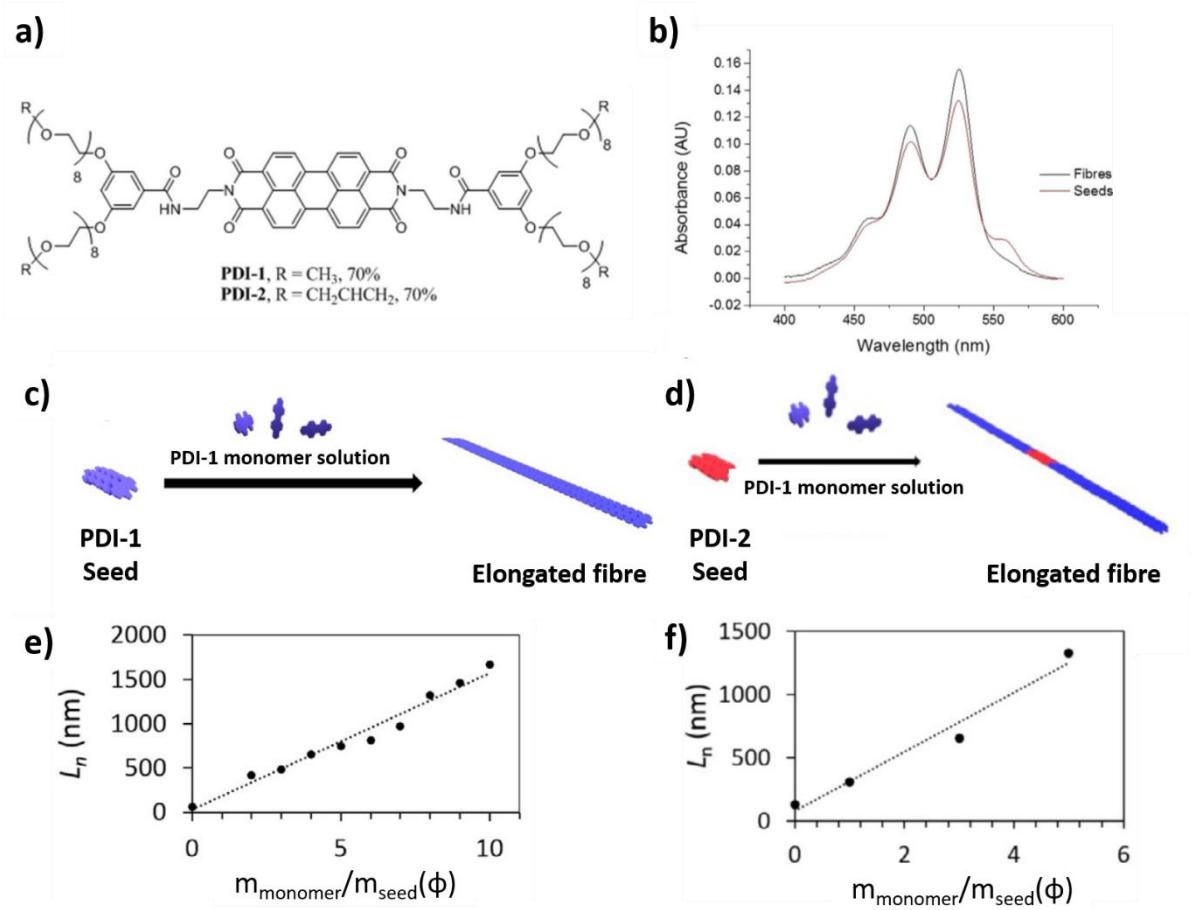

Figure 1-26 Seeded-growth supramolecular polymerization of oligo(ethylene glycol) derivatives PDIs. a) Chemical structures. b) UV-Vis absorbance spectra of fibres and seeds. c) Schematic of elongation process of adding PDI-1 seed to PDI-1 monomer solution and e) its resulting fibre length versus mass ratio between monomer and seeds. d) Schematic of elongation process of adding PDI-2 seed to PDI-1 monomer solution and f) its resulting fibre length versus mass ratio between monomer and seeds.[108]

To further develop supramolecular polymerization rules for PDIs, the imide-substituted PDIs will be the focus of this project.

PDI oligomers with aromatic substituents on their imide positions linked by a bridge molecule (linker) are regarded as electron donor-acceptor (D-A) dyads (Figure 1-27).[86,110–112] The linker molecules are able to control the assembly behaviour and thus the morphology.[86,113] The π-conjugated donor units are able to transfer electrons to the perylene core.[112,114]

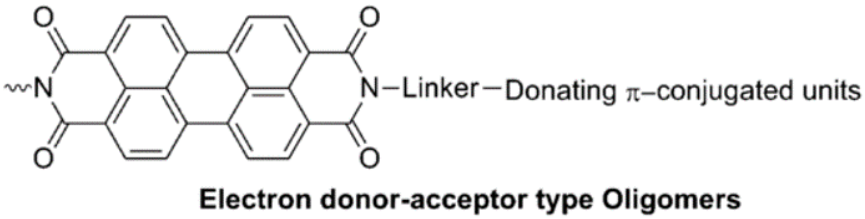

Figure 1-27 Electron donor-acceptor type PDI compound.[86]

1.2.4. Aggregation behaviour and characterization of imide-substituted PDIs

Based on their rigid planar structures and conjugated properties, imide-substituted PDIs have attracted great interest in self-assembly studies in solution.[33,115] The self-assembly behaviour of PDIs is controlled by concentration, temperature and solvent. By launching concentration-, temperature- and solvent-dependent characterization, its aggregation behaviour can be indirectly observed by UV-Vis absorbance ratio of vibrational transition peaks and NMR signals displacement of perylene hydrogen atoms.[81,116] The aggregation mechanism, i.e., H- or J- aggregation, which will be introduced at the end of this section, can be distinguished by the displacement of UV-Vis absorbance energies.[117]

According to concentration-dependent NMR studies, Wang's team found that the assembly of PDIs generally occurs when their concentration is higher than 1×10^{-3} M, below which the monomer state will dominate.[116] Self-assembly of PDIs is an enthalpy dominated process, proved by Wang et al.[116] Aggregation can be induced by relatively poor solvents, with the extent of assembly being increased at lower temperatures and higher concentrations.

In experimental UV-Vis absorbance spectra, the aggregation mechanism can be distinguished by comparing the displacement of 0-0 and 0-1 vibrational transition peaks. For those with neither bathochromic nor hypsochromic shift while losing fine vibronic structure during the aggregation process, the parallel center-to-center H-aggregation structure is formed.[118] Observation of bathochromic shift suggests the respective solvent can stabilize the excited states.[119] Hereby all the peak displacement occurs with an increase of the extent of aggregation, which is usually measured by the aggregation signal around 560 nm.

A general method to quantitively describe the extent of aggregation is shown in Eq. 1-11, where A_{agg_i} is the aggregation signal of the investigated system, A_{agg_lowest} is that of the lowest aggregation state, i.e., system with the highest temperature or the lowest concentration, $A_{agg\_highest}$ is that of the highest aggregation situation, i.e., system with the lowest temperature

or the highest concentration. The denominator can be replaced by the difference between $A_{agg\_highest}$ and A_{agg_lowest} to get the result normalized (Eq. 1-12).

$$Aggregation\ extent = \frac{A_{agg\_i} - A_{agg\_lowest}}{A_{agg\_highest}} \quad \text{Eq. 1-11}$$

$$Normalized\ aggregation\ extent = \frac{A_{agg\_i} - A_{agg\_lowest}}{A_{agg\_highest} - A_{agg\_lowest}} \quad \text{Eq. 1-12}$$

In a system dominated by monomers, the intensities of vibrational transition absorbance are dominated by the 0-0 transition, followed by the 0-1 and 0-2 transition (Figure 1-28a). Hereby all the vibrational transitions mentioned are coupled by the π to π* transition.[116] By increasing the extent of aggregation, the absorbance intensities of 0-1 and 0-2 will increase and surpass the 0-0 transition due to the growing preference and overlap of the Franck-Condon factor $\langle \chi_{\text{excited state}} | \chi_{\text{ground state}} \rangle$. On the contrary, for those with larger extent of aggregation, the emission from the 0^{th} vibrational energy level of the excited state prefers radiative transitions to higher vibrational energy levels of the ground state (i.e., the preference of 0'-3, 0'-2, 0'-1 will increase as the extent of aggregation is increased), which consequently leads to the bathochromic shift of the emission spectra (Figure 1-28b).[116,120] The schematics of transition processes in absorbance and emission are shown in Figure 1-28c.

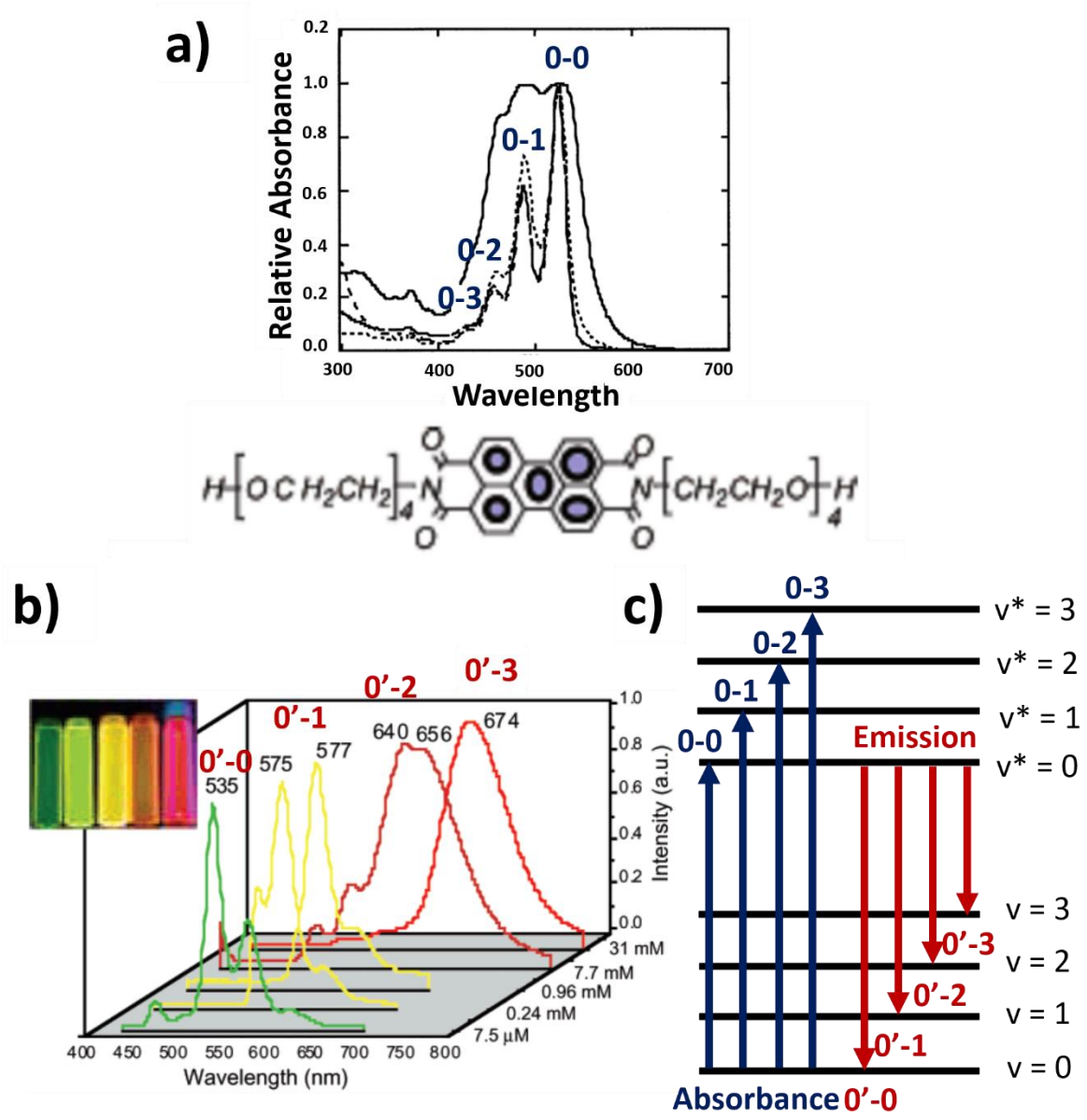

Figure 1-28 a) Chemical structure and 0-0, 0-1, 0-2, 0-3 vibrational transition peaks coupled with π to π transition of perylene derivative (bis-N,N-(2-(2-(2-(2-hydroxyethoxy)ethoxy)ethoxy)ethyl) perylene tetracarboxylic diimide), b) 0'-0, 0'-1, 0'-2, 0'-3 radiative transition peaks of photoluminescence, c) schematics of absorbance and emission processes.*[116]

During the stacking process, the centre of the poly aromatic planes can be either displaced (head-to-tail) or non-displaced (parallel), corresponding to the J- and H-aggregates, respectively. The extent of displacement is defined as the slippage angle (θ), which for values less than 54.7 ° is formally defined as a J-aggregate, while for α larger than 54.7 °, the aggregate is classified as an H-aggregate (Figure 1-29). The extent of twisting is defined as the twisting angle (α), whose values are between 0° and 90°.[121]

The aggregation mode can be characterized through UV-Vis absorbance investigations based on the energy split of the excitonic state during the aggregation process (Figure 1-29). For H-aggregates, the transition moment is parallel, reaching the upper excitonic state (S_2) with a higher energy gap compared to the monomer's, thus corresponding to a hypsochromic shift (blue shift). For J-aggregation, the transition moment is perpendicular, reaching the lower excitonic state (S_1) with a smaller energy gap, resulting in a bathochromic shift (red shift) in the absorbance spectra.[122,123]

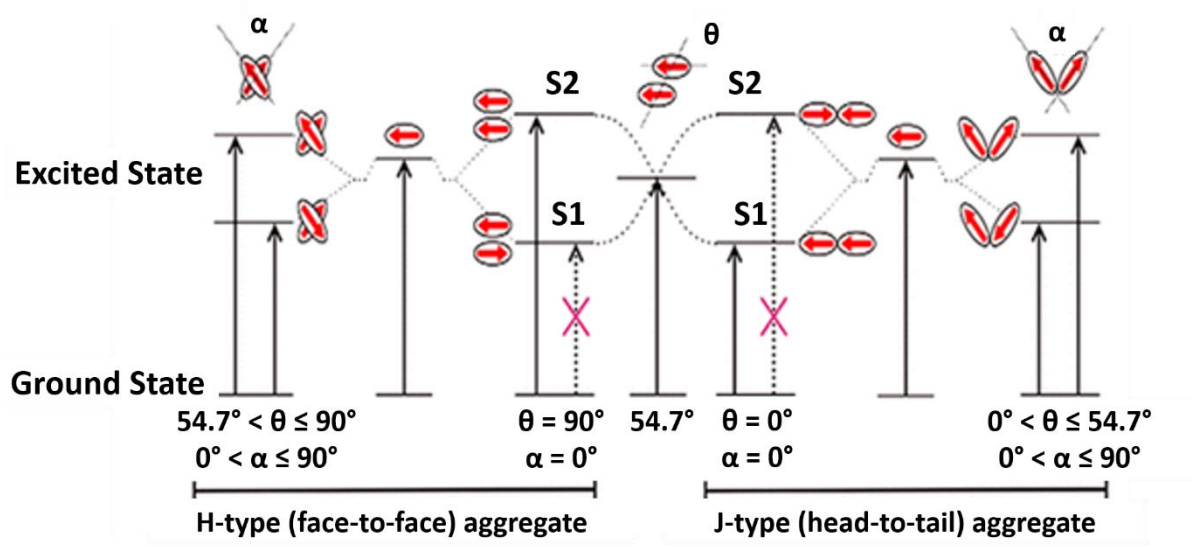

Figure 1-29 The energy split and absorbance shift between monomer and H-/J- aggregate (θ denotes the slippage angle. α denotes twisting angle. S1, S2 denotes lower and higher energy state. Red arrows denote dipole moments).[121]

The mechanism of aggregation is not completely dependent on the π-π stacking itself, but also influenced by factors such as the side chain hydrophobicity, steric effects, hydrogen bonding, solvation effects, etc.[101,117,123,124] For example, Figure 1-30 shows the combined effect of hydrogen bonding and steric effects from branched groups on the side chains that influenced aggregation mode (H and J) of perylene diimide, studied by Würthner's team.[117] They found that H-aggregate usually formed with side chains causing less steric hindrance, while J-aggregates were obtained when space-filling branched structures were introduced.

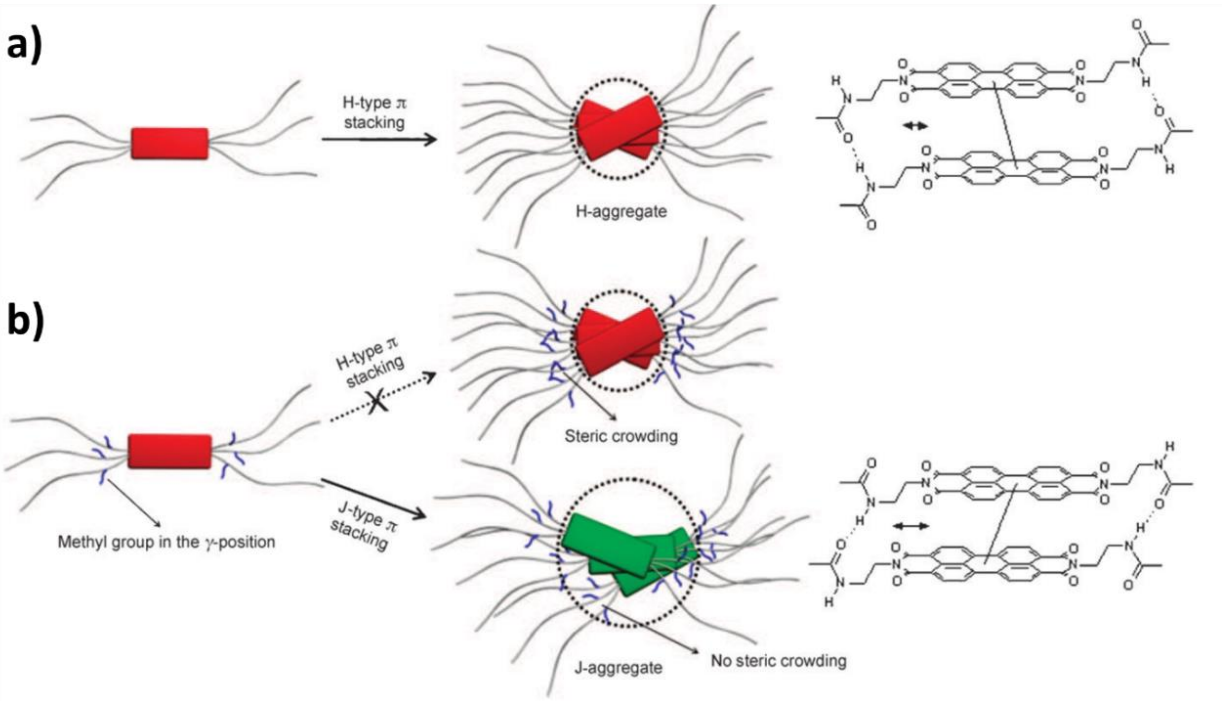

Figure 1-30 Stacking behaviour of perylene diimide supramolecular polymers: a) H-aggregate (non-displaced centre), b) J-aggregate (displaced centre, preferred when γ position of amide is substituted with large steric group, e.g., methyl group).[117]

1.3. Poly(aniline) and tetra(aniline)

Phenyl/amine end-capped tetra(aniline) (Ph/NH_2-TANI) is a π-conjugated electron donor. In a previous research led by Chiang et al, a dyad formed with Ph/NH_2-TANI (donor) and C60 (acceptor) was studied.[125] As mentioned in Section 1.2.3.3, the donor property of Ph/NH_2-TANI suggests that it is a potential substituent for the formation of functional PDIs.

The properties of poly(aniline) and Ph/NH_2-TANI will be introduced in this section.

1.3.1. Structures of poly(aniline) and tetra(aniline)

Poly(aniline) (PANI) is a polymer with controllable conductivities with three typical oxidation states, i.e., the fully reduced leucoemeraldine base (LEB), the partially oxidized emeraldine base (EB) and the fully-oxidized pernigraniline base (PB) (Scheme 1-10).[126] The oxidized parts share quinoid structures, while the reduced parts are benzenoid structures connected by amine nitrogen atoms.[127]

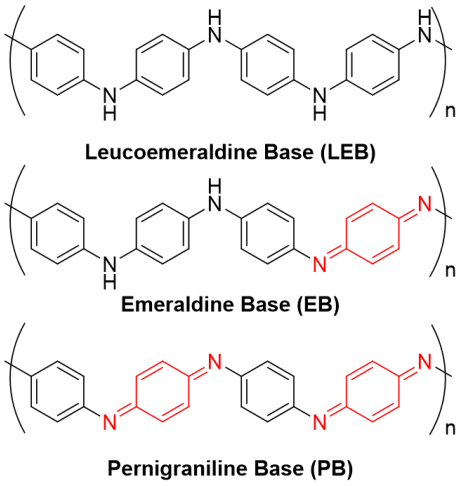

Scheme 1-10 Three oxidation states of poly(aniline)

Ph/NH_2 TANI is the simplest unit of PANI that contains all the three oxidation states, with one end terminated with a phenyl group and the other with amine group (Scheme 1-11).[128]

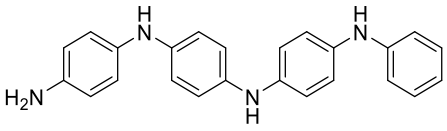

Scheme 1-11 Chemical structure of Ph/NH_2 TANI

1.3.2. Converting methods and mechanisms

The all three introduced states can be converted to the conducting emeraldine salt (ES) state. The ES state can be either reversibly oxidized from the LEB state or acid doped from the EB

state followed by charge redistribution (Scheme 1-12).[128,129] The doping process introduces radical cation structures, where the positive charges are mainly located on the nitrogen atoms. This conversion causes an increasing contribution of the polaronic conduction band, which further improves the conductivities of poly(aniline).[128] The doping from EB to ES state can be achieved by common acids like hydrochloric acid (HCl),[128,130] camphorsulfonic acid (CSA),[131] dodecyl-benzene-sulfonic acid (DBSA),[132] and reversibly de-doped with a base, for exampleammonium vapor.[130]

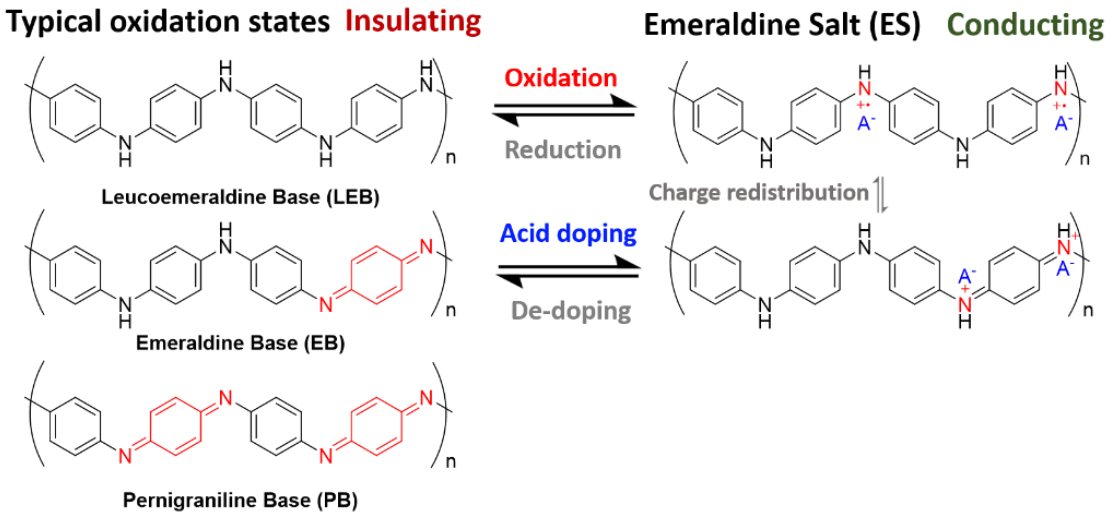

Scheme 1-12 Chemical structures and conversion processes of poly(aniline) ('A' denotes a counterion), from oxidation states to emeraldine salts state.

1.3.3. Properties and applications

The fully reduced non-conjugated LEB state is studied to be insulating, with a 3.6 eV band gap in solution (N-methyl-pyrrolidinone, NMP) and 3.8 eV in the solid state (films).[133,134] The partially oxidized EB state shows an additional band gap of 2.0 eV that corresponds to an excitonic behaviour caused by the charge transfer between quinoid structure and the neighbouring benzene groups.[127,135,136] The fully oxidized PB state however, has a linear conjugated structure, which results in a 2.3 eV Peierls gap and 3.8, 4.3 eV optical band gaps in solution (NMP), with its ground state two-fold degenerated.[127,137–139] The doped-ES state shows a 1.5 eV band gap for an excitation to the polaron band,[133,140] with its conductivity bumping from 10^{-10} S·cm^{-1} (PB state) to a metallic level as 10^{2} to 10^{3} S·cm^{-1} while its total electron number remains unchanged.[128,141,142] Simultaneously, its solubility is improved to be able to dissolve in less polar solvents.[143]

The conductivities of doped-ES state are controllable by tuning temperatures and acids.[132] The CSA-doped product shows a nearly constant resistivity of 4.2×10^{3} Ω·cm at 300 K, studied by

M. Reghu et al., while a four times increase in its resistivity was observed when the temperature decreased from 300 K to 1.2 K and 10% decreases between 300 K and 190 K.[132,144] The HCl-doped product, however, shows a 10^3 times changes in resistivity from 300 K to 30 K.[132,145]

Taking advantage of its reversely convertible states with different conjugated extent, PANI has controllable conductivities that introduce potential applications in conductive organic materials, light-emitting diodes, etc.[141,146,147] The morphology, including chirality, dimension and free volume in the film, of ES state PANI can be controlled by changing the doping ratio, enantiomer structures or the acidity of the doping acid, which leads to its application in selective sensors and separators.[148,149] LEB, EB and ES PANI are also proved to be biocompatible, with no sensitization or irritation to skin.[150] After proper reprecipitation purification cycles from NMP, its cytotoxicity can be reduced or even removed, which further increases its potentials for application in biomedical fields.[151]

1.4. Hansen solubility parameters (HSP)

Hansen solubility parameter is an indicator that aimed at quantitatively comparing the compatibility of the solute and solvent, which is one of the suitable guidelines for solvent choosing when designing the synthesis routes and self-assembly tests.[152]

The key thought to compare the extent of compatibility between two materials, A and B, is to compare the change of energy during the mixing process, which is quantified with the cohesive energy (E_{coh}) as a function of enthalpy of vaporization (H_{vap}) and absolute temperature (T) (Eq. 1-13, where R is the ideal gas constant).[153–155] E_{coh} can be further separated into three components: 1) the atomic dispersion interaction (E_D), 2) the permanent dipole-dipole interaction (E_P) and 3) the hydrogen-bonding interaction (E_H) (Eq. 1-14). The more compatible the two systems are, the less the difference is between their cohesive energies.

$$E_{coh} = H_{vap} - RT \quad \text{Eq. 1-13}$$

$$E_{coh} = E_D + E_P + E_H \quad \text{Eq. 1-14}$$

Since E_{coh} is a volume-dependent value, it is transferred to an energy density form for easier comparison. The HSP (δ_i) are defined in Eq. 1-15, where V is the volume of the system, and the subscripts, D, P, H and T mean dispersion, permanent dipole-dipole, hydrogen bonding and total interactions, respectively. The total HSP (δ_T) also equals to the norm of three individual HSP (Eq. 1-16).[152]

$$\delta_i^2 = \frac{E_i}{V}, i = D, P, H, T \quad \text{Eq. 1-15}$$

$$\delta_T^2 = \delta_D^2 + \delta_P^2 + \delta_H^2 \quad \text{Eq. 1-16}$$

To measure the similarity of A and B, the HSP are compared through an error function $\Delta\delta_T$ (Eq. 1-17). If $\Delta\delta_T$, is larger than 3, A and B are almost incompatible. If $\Delta\delta_T$ is less than 1, A and B are well-compatible. If $\Delta\delta_T$ is between 1 and 3, A and B are intermediately-compatible.[156]

$$\Delta\delta_T = \left|\delta_{T_A} - \delta_{T_B}\right| \quad \text{Eq. 1-17}$$

1.5. Aim and Objectives

The semiconducting properties of PDI and controllable conductivities of Ph/NH_2-TANI have led to great interest and research activity in functional polymers, especially in photoelectronic devices. As mentioned in the previous sections, PDI is a suitable core to introduce π-π stacking interactions for the formation of supramolecular polymers, while the challenge for application is its poor solubility that limits the solution-based process pathway and product morphology. The morphology of material is crucial to its application. Thus, it is meaningful to optimize the conditions for controllable morphology, which can be done through modifying the non-covalent interaction in supramolecular polymers. Based on this approach, additional moieties with properties that mediate the stacking, e.g., hydrogen bonding, steric effects, solvation effects, can be attached to the PDI scaffold.

From 2018 to 2019, Faul research group member Robert Wilson-Kovacs initiated studies in this topic area for his MSc by Research project, and successfully reached a well-controlled supramolecular nanowire structure of **Boc-protected-TANI-PDI** in ethyl acetate. Analysis of these supramolecular wire structures yielded a dispersity of 1.09 at a concentration of 6×10^{-4} M in ethyl acetate (Figure 1-31).

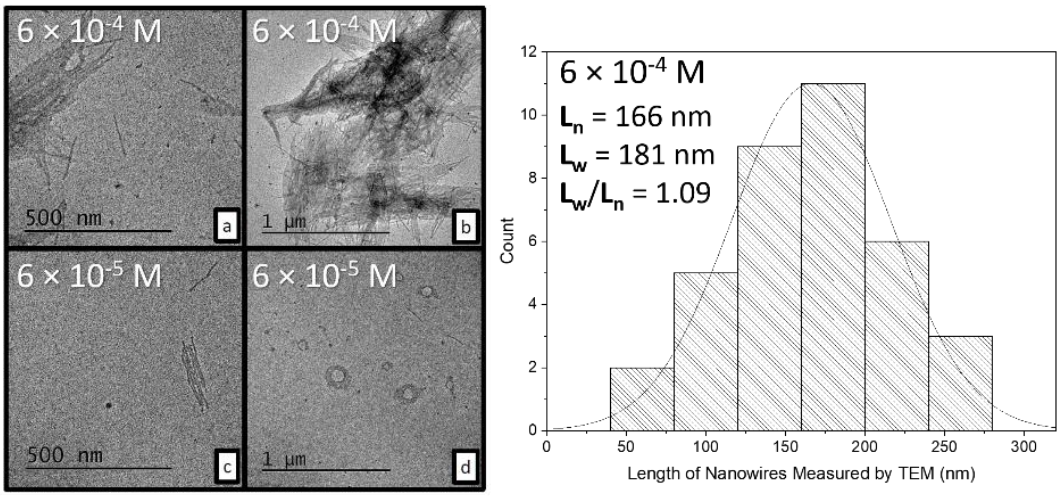

*Figure 1-31 TEM images and dispersity analysis of **Boc-TANI-PDI** in ethyl acetate (6×10^{-4} M and 6×10^{-5} M) (from Wilson-Kovacs). The dispersity analysis plots the count of nanowires with different length measured by TEM, where L_N demotes number-averaged length and L_W denotes weight-averaged length.*

The synthesis pathway Wilson-Kovacs applied is shown in Scheme 1-13 (pathway A), where **PTCDA** (**A**) was first imidized by ethylene diamine (**B**), and **boc-protected TANI** (**D**) was

coupled with 4-bromobenzoic acid (**C**). The resulting products were further coupled to obtain the **TANI-PDI** monomer in very low yield (20%).

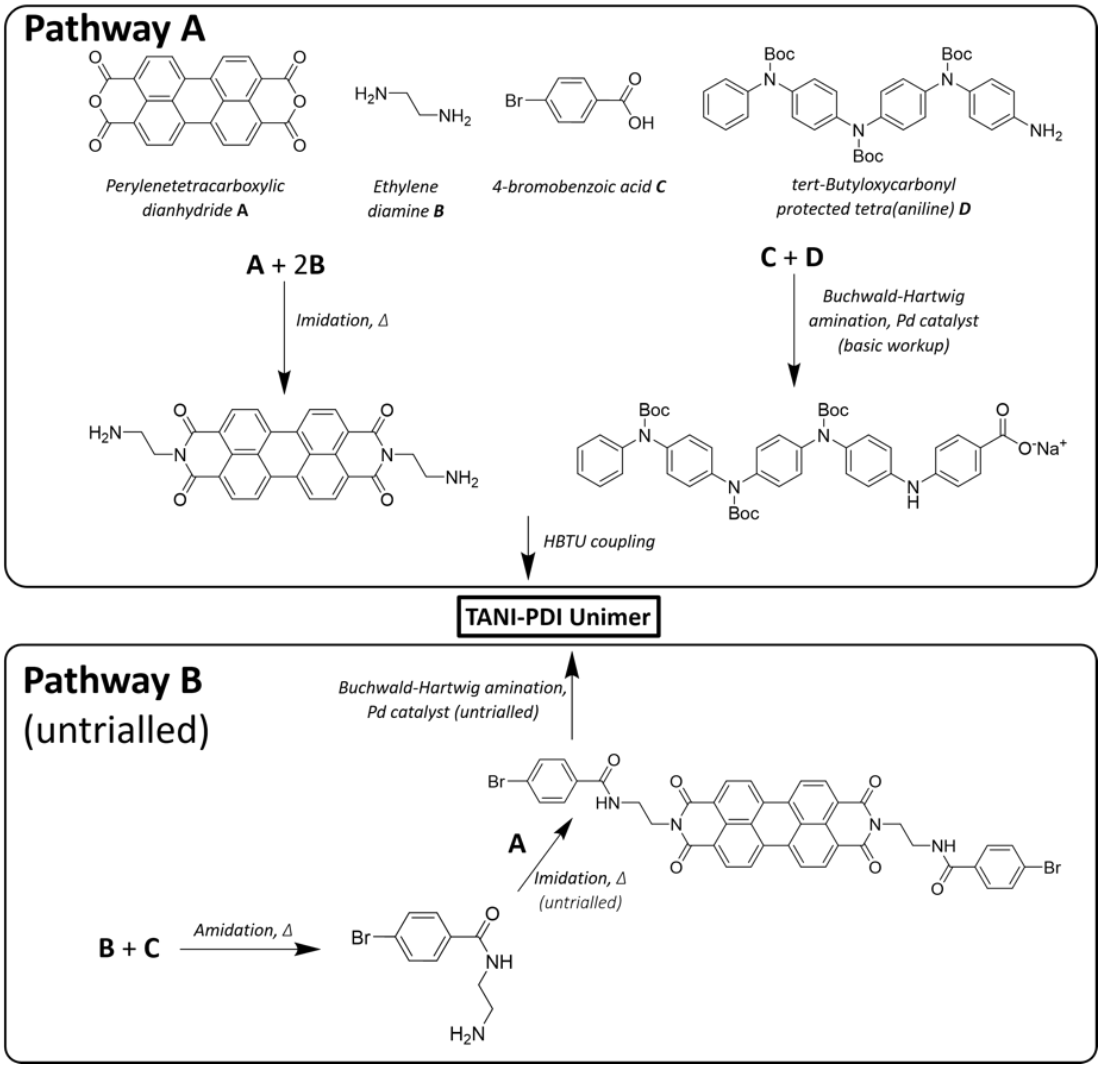

*Scheme 1-13 Synthesis pathway of **TANI-PDI** monomer (work of Robert), where Pathway A has been tried and Pathway B is untrialled.*

As a key challenge of PDI processing, the poor solubility of perylene-contained core not only limits the reaction scale and yield, but also limits the solvent choice as well as the reaction diversity. Thus, it is a promising approach to improve the solubility of PDI core before attaching to the rest of substituted moieties, which should enable reactions possible in a wider range of solvents. Based on this, the untrialled pathway B in Scheme 1-13 is considered in this project. The intermediate, N-2-(aminoethyl)-4-bromobenzamide-susbstituted PDI (**PDI-BA-1**) will also be characterized and studied in order to provide further insights into this approach.

*The aim for this project is to develop controllable functional supramolecular polymers based on tetra(aniline)-substituted perylene diimide (**TANI-PDI**). In order to reach this aim, the following three objectives have been identified.*

The first objective is to prepare N-2-(aminoethyl)-4-bromobenzamide (**BA-1**)-disubstituted PDI (**PDI-BA-1**) and **TANI-PDI** In this stage, synthesis will be operated several times to reach the optimized reaction conditions with higher yields.

The second step is to explore the conditions for controllable self-assembly behaviour of **PDI-BA-1** and **TANI-PDI**. In this stage, variables that may influence the self-assembly behaviour, including solvent, concentration and temperature, will be studied. The morphology and mechanisms will be characterized by UV-Vis, TEM and AFM. The expected and desired morphology of supramolecular polymers in this work will be well-organized fibres.

The third objective is to explore the conditions for the formation of controlled **PDI-BA-1** and **TANI-PDI** supramolecular polymers. In this stage, different nucleation and crystal growing methods will be tested and compared. It can also be aided with computational modelling and develop further guides for related PDI supramolecular polymerization in the future.

2. Results and Discussions

2.1. Synthesis

2.1.1. Overall synthesis route

As shown in Scheme 2-1, **TANI-PDI** consists of three moieties, the phenyl-/amine-capped tetra(aniline) (**Ph/NH$_2$-TANI**), the PDI core, and the linker molecule N-2(aminoethyl)-4-bromobenzamide (**BA-1**). Hereby the **TANI** is in its LEB state if not specified otherwise.

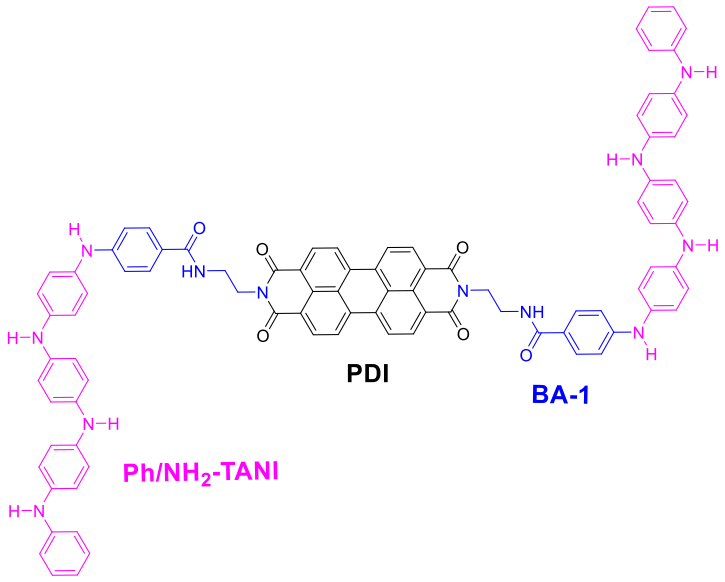

*Scheme 2-1 Chemical structure of **TANI-PDI***

As mentioned in Section 1.3.2, LEB state **TANI** can be oxidized to its EB or PB state. To avoid any purification issues caused by its oxidation, it is desirable for the aniline nitrogen atoms of **TANI** are desired to be protected by tert-butyloxycarbonyl (**boc**) groups during the reactions. The boc-protected state of **TANI-PDI** (**Ph/NH$_2$-Boc-TANI-PDI**) can be synthesized through three pathways (Scheme 2-2).

Pathway (A) has been mentioned in Section 1.5. In pathway A, **PTCDA** is first disubstituted by ethylene diamine (**EDA**) to obtain the **PDI-EDA**, followed by reacting with Ph/NH$_2$-Boc-TANI-benzoate sodium salt (**Ph/NH$_2$-Boc-TANI-BS**) to form the amide bonds.

Pathway (B) is to first connect **BA-1** and **Ph/NH$_2$-Boc-TANI-PDI** by Buchwald-Hartwig (B-H) coupling,[157] obtaining the side chain with an amine as its end group (**Ph/NH$_2$-Boc-TANI-BA-1**). The whole side chain is then attached to **PTCDA** by imidation.

Pathway (C) is to first imidize the **PTCDA** with **BA-1** to obtain the **PDI-BA-1**. Then the **Ph/NH₂-Boc-TANI** is attached to **PDI-BA-1** by B-H coupling.

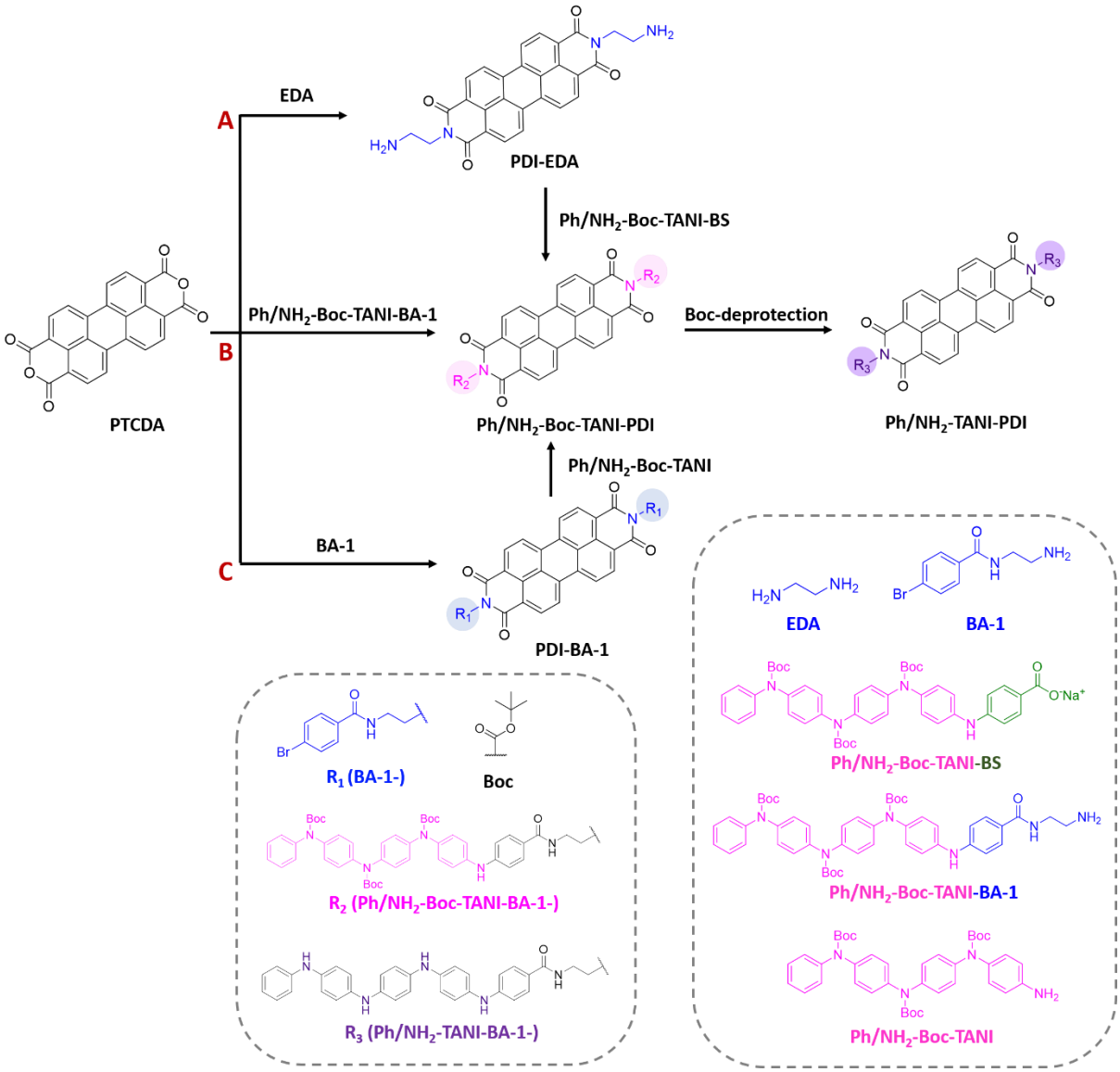

*Scheme 2-2 Three pathways to approach the synthesis of **TANI-PDI**. Pathway A is to first attach **EDA** with **PTCDA** followed by further attaching the rest of side chain. Pathway B is to attach the entire side chain to **PTCDA**. Pathway C is to first attach **BA-1** with **PTCDA** followed by further attaching **Ph/NH₂-Boc-TANI**.*

Both pathway A and B are challenged by the solubility of **PDI-EDA** and **PTCDA**, which limits the choices of reaction solvent. However, in pathway C, the intermediate, **PDI-BA-1**, is expected to be soluble in a wider range of solvents, which will improve the efficiency of reactions. As a result, pathway C was mainly applied in this research. **Ph/NH₂-Boc-TANI-BA-1** in pathway B was also synthesized to test the reaction conditions, including the temperature and the catalyst loading.

2.1.2. Synthesis of BA-1

BA-1 was synthesized according to Scheme 2-3. 1:4 Methyl 4-bromobenzoate (**MB**) and ethylenediamine (**EDA**) were reacted at 132 °C for 1 hour (76% yield). This reaction was with neat **EDA**, i.e., as both the reactant and the solvent.[158] The excess of **EDA** also decreased the possibility to form the di-substituted by-product.

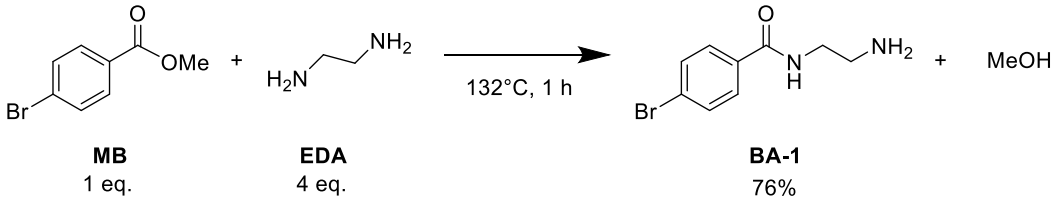

*Scheme 2-3 Synthesis of **BA-1**.*

After completion, the reaction mixture was washed with toluene to remove **EDA**, followed by washing with 5 M sodium hydroxide to ionize the unreacted **MB**. **BA-1** was then extracted by chloroform before separation. The presence of **BA-1** was confirmed by NMR (Figure 7-1) and ESI (m/z: 243.0).

2.1.3. Synthesis of PDI-BA-1

As shown in Scheme 2-4, **PDI-BA-1** was synthesized through the imidization of 1 eq. **PTCDA** with 8 eq. **BA-1** in 1-methylimidazole (NMI) at 160 °C for 88 hours (85% yield). The diimide structures were formed through nucleophilic attack of the amine group of **BA-1** towards the dianhydride structure of **PTCDA**.

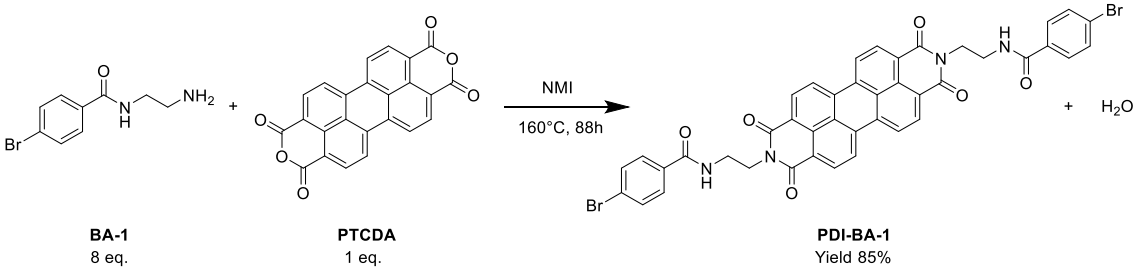

*Scheme 2-4 Synthesis of **PDI-BA-1**.*

After the reaction had completed, the NMI was protonated by 1 M hydrochronic acid, followed by separation in chloroform. The crude product was purified by column chromatography (95 : 4.5 : 0.5 chloroform : methanol : triethylamine). The successful synthesis of **PDI-BA-1** was confirmed by MALDI (m/z: 841.523).

Hereby ^{1}H NMR was also carried out for component characterization, whilst the quality of the spectra was challenging for analysis. The progress will be discussed here.

To prepare the NMR sample, the purified product was dissolved in deuterium substituted solvents according to solubilities and stabilities towards each solvent and whether peak residues of solvents may overlap with critical samples signals. DMSO-d_6, with solvent residues at 2.50 ppm and 3.33 ppm, affected the signals of protons in aliphatic environment. Whilst $CDCl_3$, whose residue is at 7.26 ppm, also overlapped with the signals of protons on the aromatic moieties. In addition, at room temperature, the product formed aggregates at high concentration. Thus, to maintain a well-dissolved solution during the NMR investigation, the concentration of PDIs sample needs to be very low, which is too weak to obtain enough signal/noise ratio for NMR spectra. The quality of signals is determined both by the sample concentration and solubility, whose balance, especially for perylene-containing materials, is hard to find. In the future characterization of PDIs, improvement can be applied by adding scanning times or by increasing temperature if the equipment allows.

2.1.4. Synthesis of Ph/NH_2-Boc-TANI

As shown in Scheme 2-5, **Ph/NH_2-Boc-TANI** was obtained from the deprotection of 1 eq. benzophenyl/phenyl-Boc-TANI (**Bz/Ph-Boc-TANI**), with 10 eq. ammonium formate. The ammonium formate was from commercial source while the **Bz/Ph-Boc-TANI** was synthesized by previous Faul research group members.[159] The reaction was catalysed by 5.5 mol% of palladium on carbon (Pd/C) in anhydrous methanol and THF (1 : 2.5 v/v). The reaction temperature was kept at 67 °C to prevent the Boc groups from degrading, leading to premature deprotection of the TANI.[157,160]

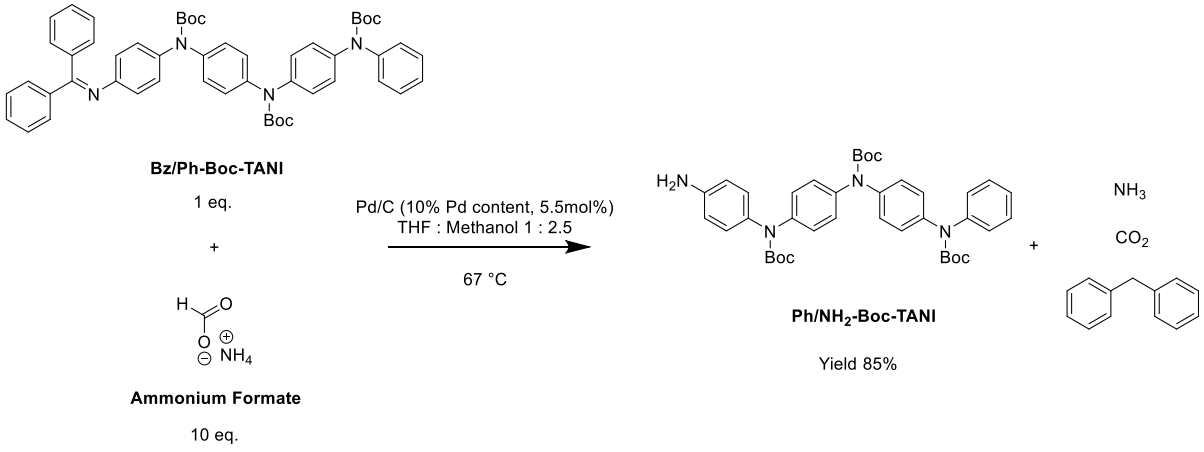

*Scheme 2-5 Synthesis of **Ph/NH_2-Boc-TANI**.*

The reaction was followed by thin-layer chromatography (TLC), with a mobile phase of 1:1 (v/v) ethyl acetate : hexane. After the reaction was completed, the solvent was removed. The residue was taken up in dichloromethane (DCM) followed by the filtration to remove the catalyst. After removing DCM from the filtrate, the crude product was purified by hexane washing. The presence of **Ph/NH$_2$-Boc-TANI** was confirmed by NMR (Figure 7-2).

2.1.5. Synthesis of Ph/NH$_2$-Boc-TANI-PDI

Ph/NH$_2$-Boc-TANI was attached to the **PDI-BA-1** through B-H coupling reaction (mechanism shown in Scheme 2-6).[157] XPhos and Pd (dba)$_2$ are commonly applied as ligand and palladium source. K_2CO_3 was selected as the base for its weaker basicity, which could prevent potential side reactions, e.g., the degradation of amide or aromatic bromide.[161]

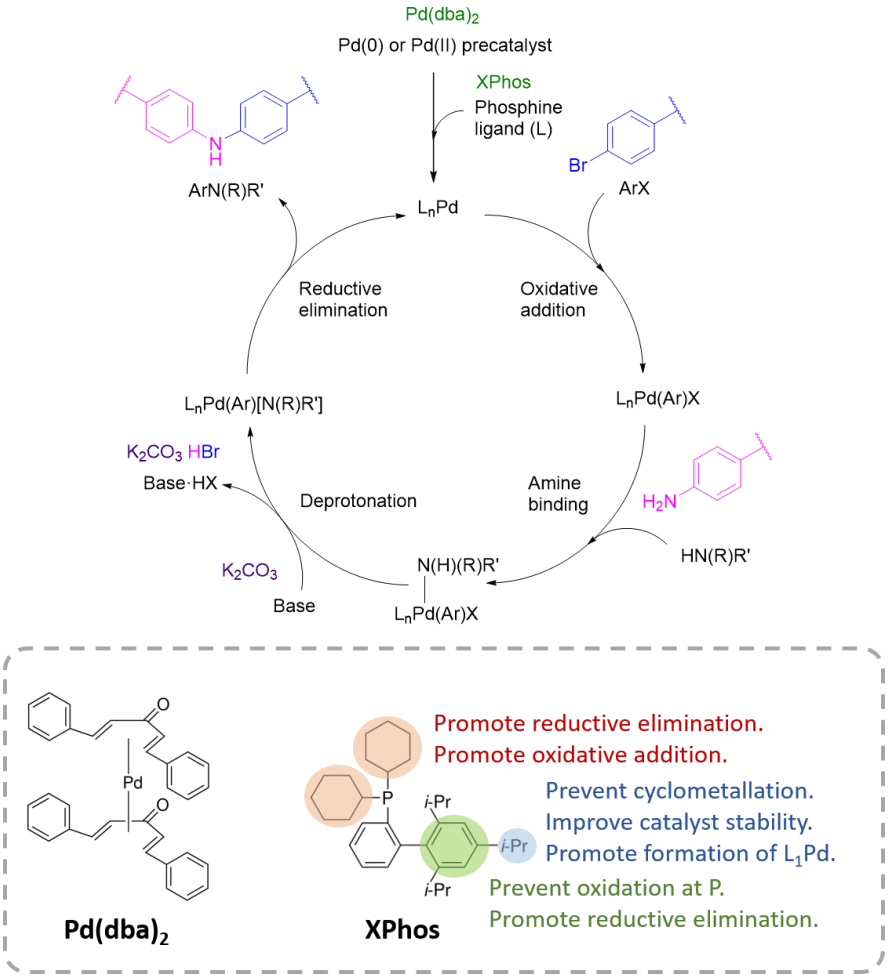

Scheme 2-6 Mechanism of B-H coupling applied in this research.[157]

The synthesis of **Ph/NH$_2$-Boc-TANI-PDI** was tested in two different solvents (*t*-BuOH and toluene) and two different temperatures (67 °C and 110 °C). The reaction scale was kept small, with 50 mg **PDI-BA-1** applied in each reaction if not specified. Unfortunately, due to the

restricted laboratory access during the COVID-19 period, the aspect of the work had not been fully completed. Progress will be discussed in the following paragraphs.

As shown in Scheme 2-7, 2.4 eq. **Ph/NH$_2$-Boc-TANI** was reacted with **PDI-BA-1**. The 0.4 eq. excess of **Ph/NH$_2$-Boc-TANI** was aimed at promoting the formation of di-substituted product. 2 mol% Pd(dba)$_2$, Xphos and 2 eq. K_2CO_3 were added. The reaction temperature was initially set as 67 °C to prevent the boc groups from degradation, though the literature had recommended a higher temperature (110 °C) for B-H coupling with a weak base.[157,160] *t*-BuOH was selected as the solvent for two reasons: 1) the solubilities of compounds in the reaction mixture were acceptable in *t*-BuOH, 2) the boiling point of *t*-BuOH (83 °C) was high enough for this reaction temperature (67 °C).[157,161,162]

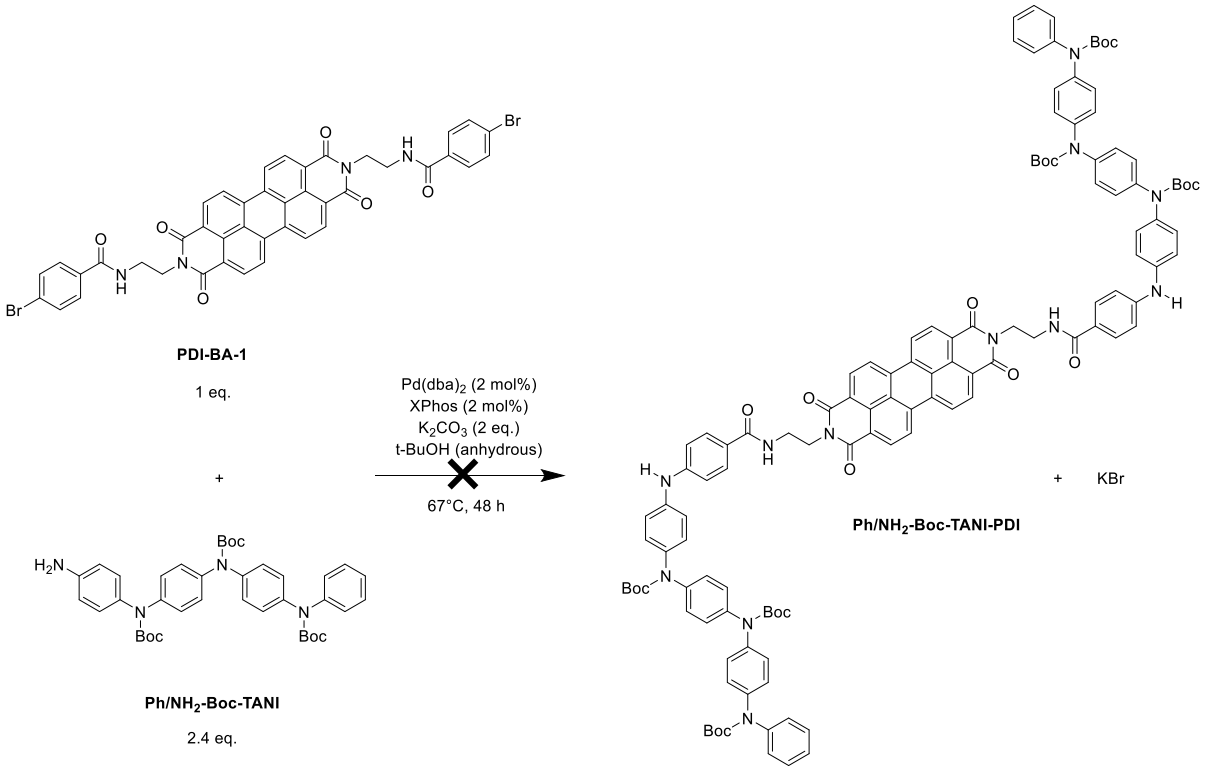

*Scheme 2-7 Synthesis of **Ph/NH$_2$-Boc-TANI-PDI** with t-BuOH as the solvent.*

After reacting for 48 hours, the reaction mixture was characterized by MALDI. However, there were no signals matching either the full boc-protected product (exact mass: 2012.85) or any partially boc-protected products (exact mass: 1912.80, 1812.75, 1712.70, 1612.65, 1512.60, 1412.55) according to the MALDI results.

The reasons for not obtaining products were possibly 1) the catalyst loading was too low, and 2) the temperature was too low to trigger the B-H coupling reaction.

It was found that Boc-deprotection was accelerated both by longer reaction time and higher temperature, whilst B-H coupling would be restricted by low temperature. Thus, the reaction conditions needed to be carefully controlled to meet both ends.

To explore the optimized conditions, B-H coupling reactions between **BA-1** and **Ph/NH$_2$-Boc-TANI** were tested. The solvent was changed into anhydrous toluene (boiling point: 110 °C), which enabled the reaction to run at a higher temperature (110 °C). These results are summarized below.

2.1.5.1. Synthesis of Ph/NH$_2$-Boc-TANI-BA-1

The reactions performed in toluene were tested at a ratio of 1:1.2 **BA-1** to **Ph/NH$_2$-Boc-TANI** (Scheme 2-8), which provided a guide for **Ph/NH$_2$-Boc-TANI-PDI** synthesis design. K_2CO_3 was increased to 10 eq. due to its limited solubility in toluene. Both $Pd(dba)_2$ and XPhos were increased to 10 mol% to study the influence of catalyst load. The reaction was started at 67 °C. However, no product was observed by TLC after three hours, suggesting that the catalyst loading was not the dominant factor to hinder the reaction at 67 °C.

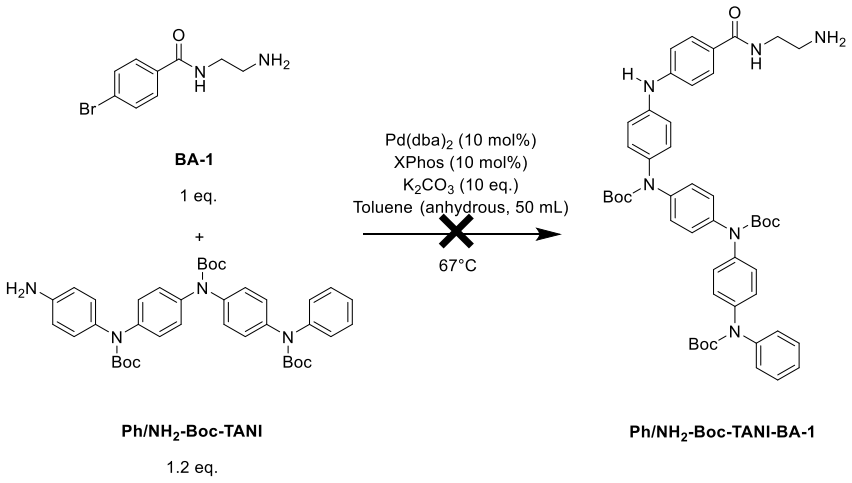

*Scheme 2-8 B-H coupling between **BA-1** and **Ph/NH$_2$-Boc-TANI** (67 °C in toluene).*

The reaction in Scheme 2-8 was further heated to 110 °C for 48 hours (Scheme 2-9). After the reaction was completed, the reaction mixture was filtered followed by the removal of solvent. The residue was washed by diethyl ether and centrifuged three times. Both the residue and supernatant were characterized by ESI-MS.

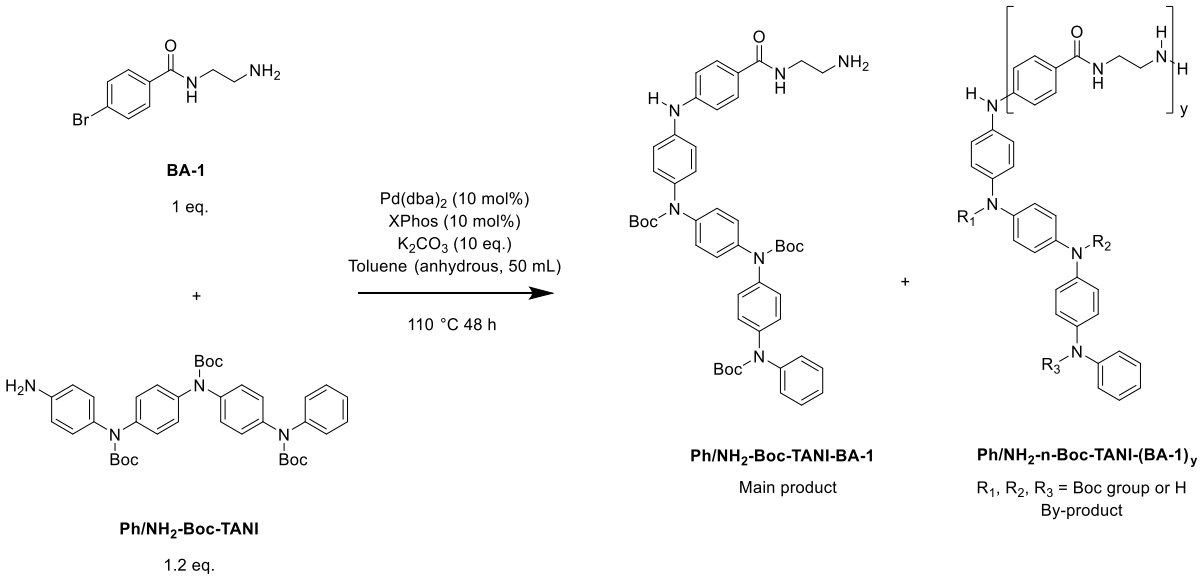

*Scheme 2-9 B-H coupling between **BA-1** and **Ph/NH₂-Boc-TANI** (110 °C in toluene).*

As shown in Table 2-1, ESI-MS results suggested that fully boc-protected state of **Ph/NH₂-Boc-TANI-BA-1** was the main product found in the centrifuge residue. However, because of 1) the bi-functionality of **BA-1** and 2) the high reaction temperature, side reactions regarding 1) **BA-1** oligomerization and 2) boc-deprotection were potentially introduced. Thus, by-products (**Ph/NH₂-n-Boc-TANI-(BA-1)$_y$**) were also expected to be formed, where n is the number of remaining boc groups on the **TANI** chain, and y is the number of **BA-1** units. ESI-MS results suggested the formation of **Ph/NH₂-Boc-TANI-(BA-1)₂**. The fully boc-deprotected **Ph/NH₂-TANI-(BA-1)₂** was also found in the supernatant. Other expected by-products, e.g., oligomers of **BA-1**, fully or partially boc-deprotected **Ph/NH₂-Boc-TANI-BA-1**, etc., were not detected in either supernatant or residue.

*Table 2-1 ESI-MS-detected compounds formed by B-H coupling between **BA-1** and **Ph/NH₂-Boc-TANI**. (y is the number of **BA-1** units. n is the number of boc groups.)*

Compound Name	y (BA-1)	n (Boc)	Exact mass	Location
Ph/NH₂-Boc-TANI-BA-1	1	3	828.42	Residue
Ph/NH₂-Boc-TANI-(BA-1)₂	2	3	990.50	Residue
Ph/NH₂-TANI-(BA-1)₂	2	0	690.34	Supernatant

The reaction between **BA-1** and **Ph/NH₂-Boc-TANI** indicated that B-H coupling reaction with K_2CO_3 as the base should occur at 110 °C instead of 67 °C. The fully boc-protected and de-protected products can be separated by centrifuging with diethyl ether. In addition, to avoid oligomerization in similar reactions in the future, the amount of bi-functional reactant should

be specifically limited, which can be realized by slowly adding the bi-functional reactant into an excess of mono-functional reactant.

In the future, **Ph/NH$_2$-Boc-TANI-PDI** will be synthesized based on the experience of synthesizing **Ph/NH$_2$-Boc-TANI-BA-1**. The proposed synthesis route is shown in Scheme 2-10. An increase amount of catalysts (20 mol%) will be applied. The reaction temperature will be increased to 110 °C.

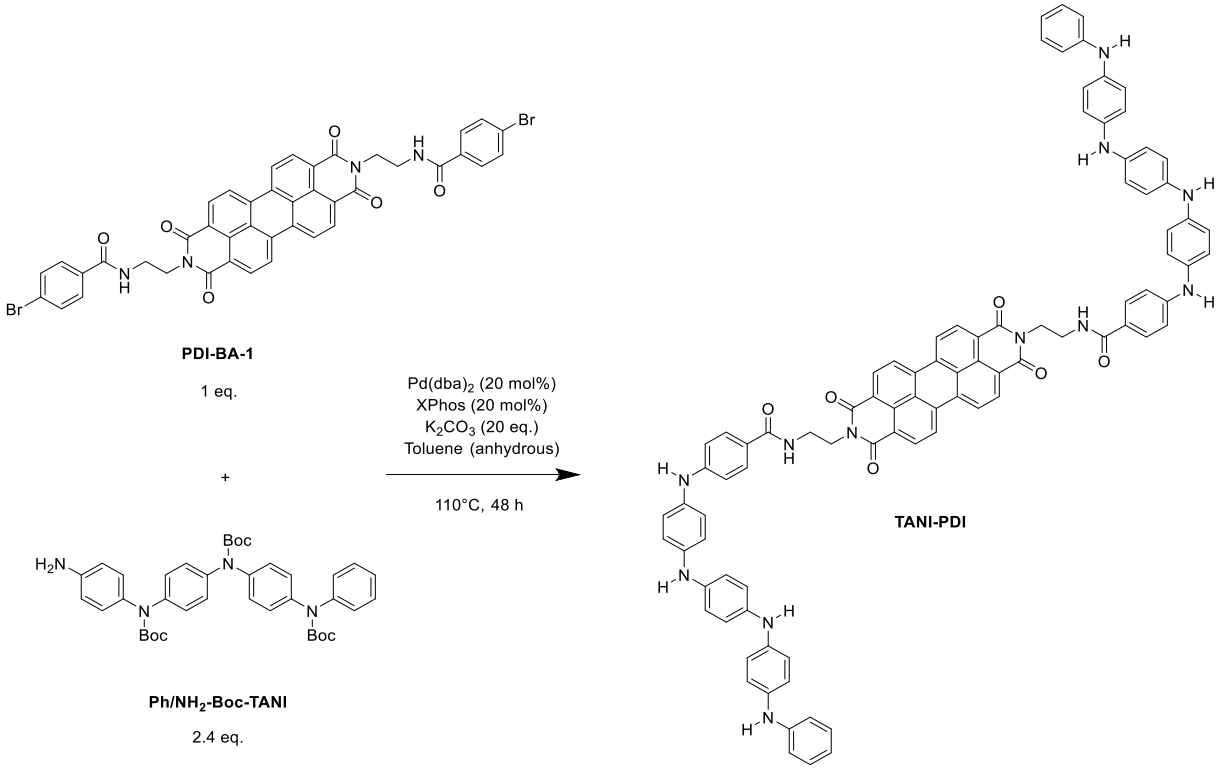

*Scheme 2-10 Proposed synthesis route for **TANI-PDI**.*

The reaction time will first be set as 48 hours. However, since the boc groups will be partially lost at 110 °C, the reaction time for the future synthesis are expected to be longer to deprotect all the boc groups. The resulting **TANI-PDI** (LEB state) will be protected in nitrogen atmosphere before further characterization.

2.2. Self-assembly studies

2.2.1. Solubility studies

2.2.1.1. Solubility tests for PTCDA

To choose a suitable solvent for **PTCDA**-based reaction, the solubility of **PTCDA** was both qualitatively and quantitively tested.

The extent of **PTCDA** solubility was first qualitatively tested by dispersing equal amounts of **PTCDA** (0.01 g) to four common solvents with increasing polarities, including toluene, chloroform, methanol and dimethyl sulfoxide (DMSO) (5 mL each). The suspensions were sonicated well and left overnight (Figure 2-1a), with the DMSO system showing the best dispersion, followed by methanol and chloroform system, while the solute and solvent phase in the toluene system were almost completely separated and the supernatant was nearly colourless. The suspensions were observed again after five days without any disturbance (Figure 2-1b). All the four systems showed a separated bi-phase system, with the supernatant varying in colour. The supernatant was still colourless in toluene, whilst it was light pink in chloroform, and was light pink to deeper pink in DMSO. The methanol system was different from others, showing a yellow colour.

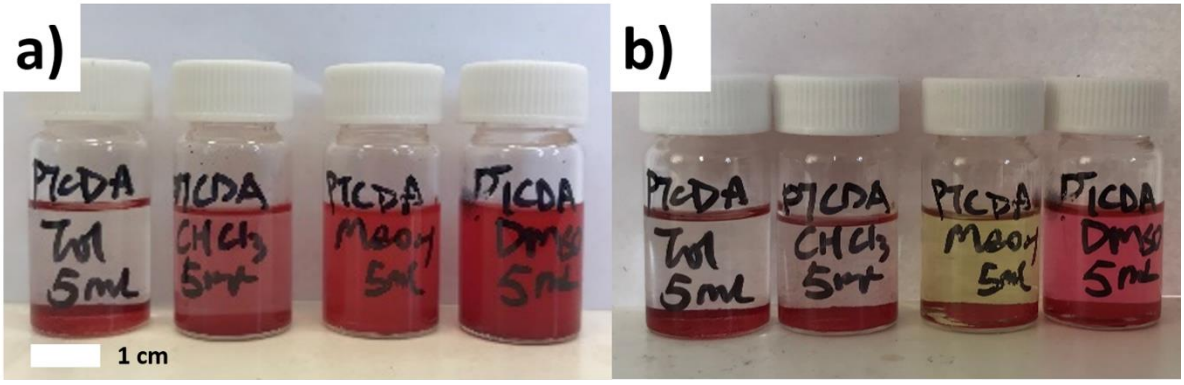

*Figure 2-1 From left to right: dispersion of 0.01 g **PTCDA** in 5 mL toluene, chloroform, methanol, DMSO a) overnight b) 5 days after sonication.*

The qualitative results suggest that DMSO was the best solvent among the four tested solvents. The yellow solution of **PTCDA** in methanol indicates that the absorbance feature of the suspensions was influenced by the solvent.

To quantitively explain the observed dispersion phenomenon, UV-Vis absorbance spectroscopy was performed at the concentration of 5×10^{-6} M and 5×10^{-5} M in twelve

different solvents, including 1-methylimidazole (NMI), acetonitrile (ACN), N, N'-dimethylformamide (DMF), methanol, DMSO, tetrahydrofuran (THF), *tert*-butanol, 1,4-dioxane, ethyl acetate, chloroform, toluene and xylenes, as shown in Figure 2-2. The absorbance spectra were recorded at room temperature, if not specified.

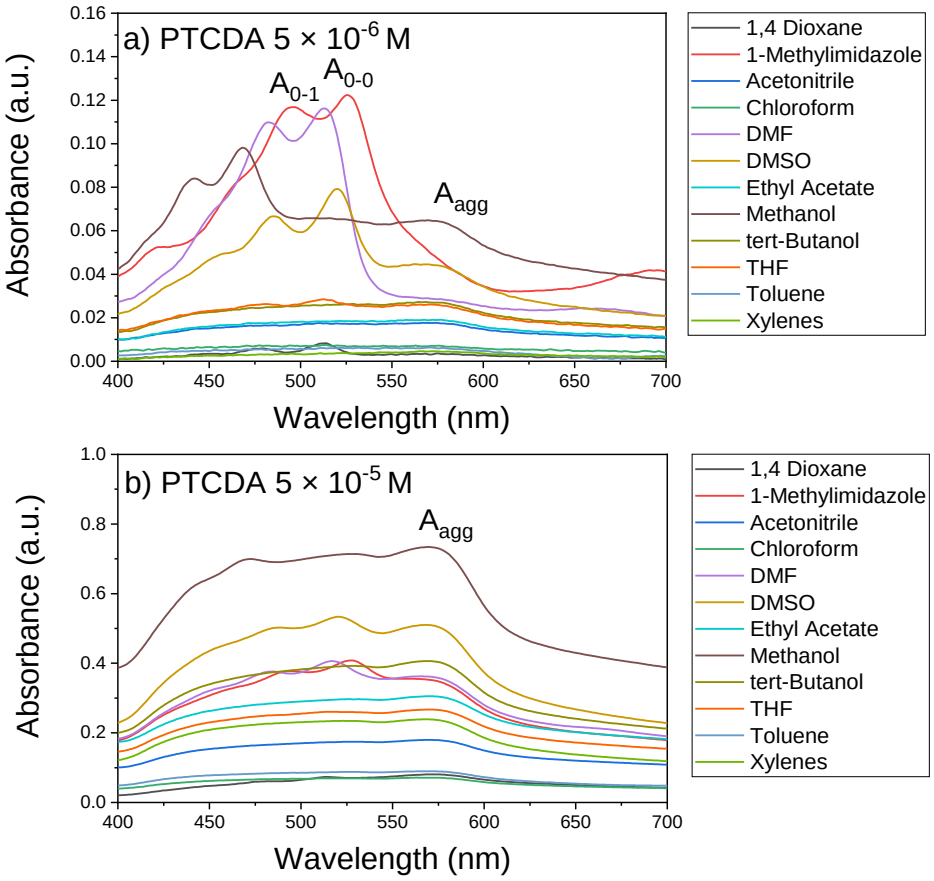

*Figure 2-2 Solvent-dependant UV-Vis spectra of a) 5 × 10^{-6} M, b) 5 × 10^{-5} M **PTCDA** in different solvents.*

At 5 × 10^{-6} M, the A_{0-0} and A_{0-1} transitions of **PTCDA** in 1-methylimidazole, DMF, DMSO, methanol and THF were mostly distinguishable. In the visible light region, the S_0-S_1 excitation with its coupled vibrational transitions (0-0, 0-1) could be recognized. Broad aggregation peaks (A_{agg}) were found around 572 nm. The methanol system, however, showed a significant blue shift of absorbance, which is approximately 30 nm from that of 1-methylimidazole. This result emphasized the effect of solution towards materials optical response.

When the concentration increased from 5 × 10^{-6} M to 5 × 10^{-5} M, the absorbance peaks become significantly broader and less structured because of the stacking effect. The strong stacking effect negatively affected the solubility of **PTCDA** and led the system to be a suspension

instead of a well-dissolved solution, which explains the high baseline in corresponding absorbance spectra. The aggregation peaks around 570 nm also grew fast and even exceeded S_0-S_1 intensities. Thus, to get a high-quality spectra with distinguishable absorbance properties, the concentrations of PDI derivatives were maintained at low levels (less than 10^{-4} M order).

It needs to be clarified that **PTCDA** has a wide absorbance that not only limited to the visible light region, i.e., in UV region, transition from ground state (S_0) to higher excitation states also exists, as appended in Figure 7-3 and Figure 7-4. Whilst signals that could reflect the self-assembly behaviour of PDI derivatives are located in the visible light region. As previously mentioned in Section 1.2.4, the relative intensity between $A_{0\text{-}0}$ and $A_{0\text{-}1}$ as well as the aggregation shoulder band together reflect the extent of aggregation. The displacement of the vibrational transition wavelength also suggests the aggregation mechanism (H- or J-aggregation). Thus, in this work, absorbance in the visible light region is mainly focused.

Based on the intensities of UV-Vis spectra, the Hansen Solubility Parameters (HSP, as introduced in Section 1.4) of **PTCDA** was then calculated through plotting $A_{0\text{-}0}$ of 0.005 mM **PTCDA** in different solvents to the corresponding HSP of the solvents, followed by fitting with a B-Spline method.[156] The maximum points found by the B-spline fitting plot corresponded to HSP of **PTCDA** (Figure 2-3), with δ_D = 19.2, δ_H = 11.6, δ_P = 14.8. The δ_T obtained directly through the fitting plot is 26.3, while that calculated through the individual fitting HSP components is 26.9, suggesting the fitting plot had a -2.2% error.

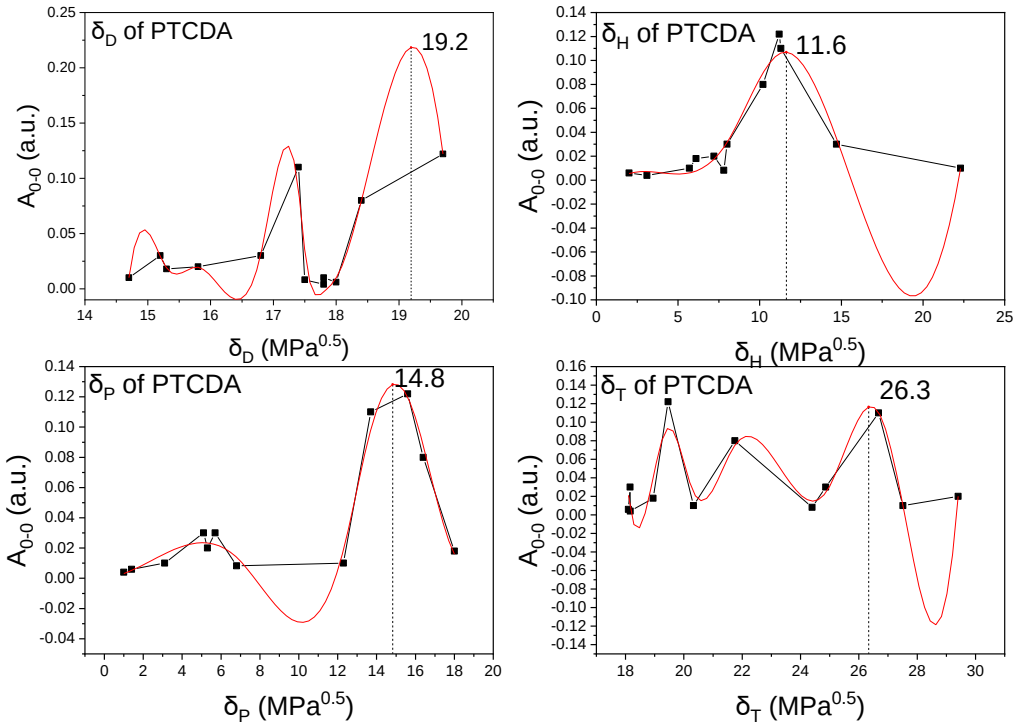

*Figure 2-3 a) Dispersion b) Hydrogen bond c) Polar cohesive d) Total Hansen Solubility Parameters of **PTCDA**, measured with UV-Vis absorbance intensity in a series of solvents.*

By comparing the relative δ_T of the solvent and the studied material, the solvent can be divided into 1) suitable solvent, with the absolute difference $|\Delta\delta_T|$ less than 1; 2) intermediary solvent, with $|\Delta\delta_T|$ between 1 and 3; and 3) poor solvent, with $|\Delta\delta_T|$ greater than 3.[163] The individual HSP of the solvents in this research were from literatures.[65] The results are listed in Table 2-2, in which DMSO is proven to be the best solvent, followed by NMI ($|\Delta\delta_T| = 1.2$), DMF ($|\Delta\delta_T| = 1.4$) and acetonitrile ($|\Delta\delta_T| = 1.9$). Methanol ($|\Delta\delta_T| = 3.1$) is close to the threshold 3. The rest of the solvents are all with their $|\Delta\delta_T|$ significantly larger than 3, which are not preferred for synthesis. Based on this, DMF and NMI were chosen for synthesis involving **PTCDA**. DMSO was not applied because it was not easy to remove from the reaction system.

*Table 2-2 Hansen Solubility Parameters and relative δ_T between studied solvents and **PTCDA** (5×10^{-6} M).*

Solvent/Compound	δ_D	δ_P	δ_H	δ_T	$\lvert\Delta\delta_T\rvert$
Xylenes	17.8	1	3.1	18.1	8.2
EA	15.8	5.3	7.2	18.2	8.1
Toluene	18	1.4	2	18.2	8.1
Chloroform	17.8	3.1	5.7	18.9	7.4
THF	16.8	5.7	8	19.5	6.8
1, 4-Dioxane	17.5	6.8	7.8	20.3	6.0
t-BuOH	15.2	5.1	14.7	21.8	4.5
Acetonitrile	15.3	18	6.1	24.4	**1.9**
DMF	17.4	13.7	11.3	24.9	**1.4**
DMSO	18.4	16.4	10.2	26.7	**0.4**
NMI	19.7	15.6	11.2	27.5	**1.2**
MeOH	14.7	12.3	22.3	29.4	**3.1**
PTCDA	**19.2**	**14.8**	**11.6**	**26.3**	-

2.2.1.2. Solubility tests for PDI-BA-1

The UV-Vis spectrum for 1.0×10^{-4} M **PDI-BA-1** in fourteen different solvents was also studied (Figure 2-4). Compared to **PTCDA**, $A_{0\text{-}0}$ and $A_{0\text{-}1}$ of **PDI-BA-1** were distinguishable in a wider range of solvents except n-hexane, which confirmed the improvement of its solubility.

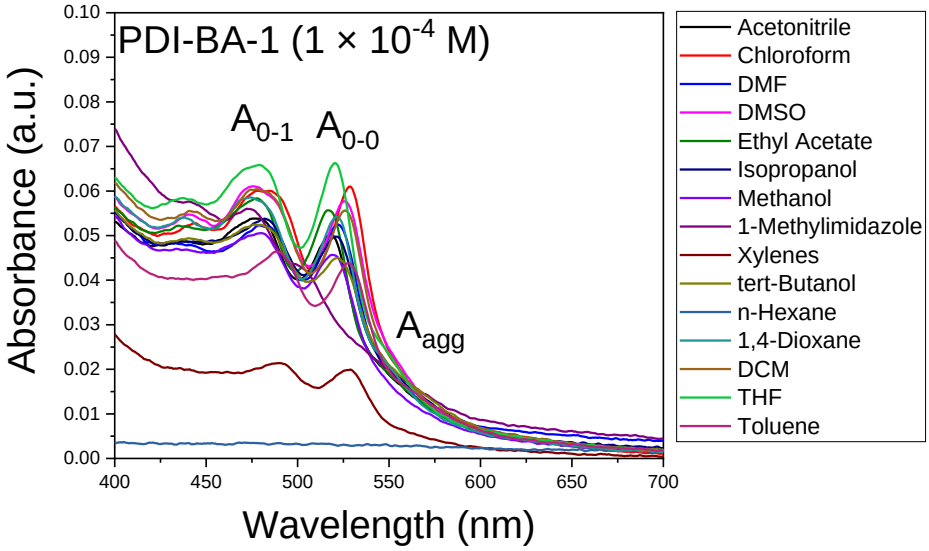

*Figure 2-4 Solvent-dependant UV-Vis absorbance spectra of 1.0 × 10^{-4} M **PDI-BA-1** in different solvents.*

The HSP of **PDI-BA-1** were calculated with the same method as for **PTCDA**, as shown in Table 2-3 and Figure 2-5. The fitting results showed two sets of possible HSP for **PDI-BA-1**. The first set (HSP1) is δ_D = 19.0, δ_P = 17.3, δ_H = 9.0, $\delta_{T\_calculated}$ = 27.2, $\delta_{T\_fitting}$ = 26.1 (error = -4.0%), which is close to the HSP of **PTCDA**. According to HSP1, DMSO is the best solvent, followed by DMF, NMI, acetonitrile, isopropanol and methanol as intermediate solvents. The second set (HSP2) is δ_D = 16.5, δ_P = 2.4, δ_H = 9.0, $\delta_{T\_calculated}$ = 18.9, $\delta_{T\_fitting}$ = 18.8 (error = -0.5%). According to HSP2, chloroform, toluene, ethyl acetate, xylenes, THF and DCM are good solvents, whilst 1, 4-dioxane, and *tert*-butanol are intermediary solvents.

*Table 2-3 HSPs and relative δ_T between studied solvents and **PDI- BA-1** (1.0×10^{-4} M), where $|\Delta\delta_{T1}|$, $|\Delta\delta_{T2}|$ are the difference between δ_T of solvents and HSP1, and HSP2, respectively.*

Solvent/Compound	δ_D	δ_P	δ_H	δ_T	$\|\Delta\delta_{T1}\|$	$\|\Delta\delta_{T2}\|$
n-Hexane	14.9	0.0	0.0	14.9	11.2	3.9
Xylenes	17.8	1.0	3.1	18.1	8.0	**0.7**
Ethyl acetate	15.8	5.3	7.2	18.2	7.9	**0.6**
Toluene	18.0	1.4	2.0	18.2	7.9	**0.6**
Chloroform	17.8	3.1	5.7	18.9	7.2	**0.1**
THF	16.8	5.7	8.0	19.5	6.6	**0.7**
DCM	17.0	7.3	7.1	19.8	6.3	**1.0**
1,4-Dioxane	17.5	6.8	7.8	20.3	5.8	**1.5**
t-BuOH	15.2	5.1	14.7	21.8	4.3	**3.0**
Isopropanol	15.8	6.1	16.4	23.6	**2.5**	4.8
Acetonitrile	15.3	18.0	6.1	24.4	**1.7**	5.6
DMF	17.4	13.7	11.3	24.9	**1.2**	6.1
DMSO	18.4	16.4	10.2	26.7	**0.6**	7.9
NMI	19.7	15.6	11.2	27.5	**1.4**	8.7
MeOH	14.7	12.3	22.3	29.4	**3.3**	10.6
PDI-BA-1(HSP1)	**19.0**	**17.3**	**9.0**	**26.1**	**-**	**-**
PDI-BA-1(HSP2)	**16.5**	**2.4**	**9.0**	**18.8**	**-**	**-**

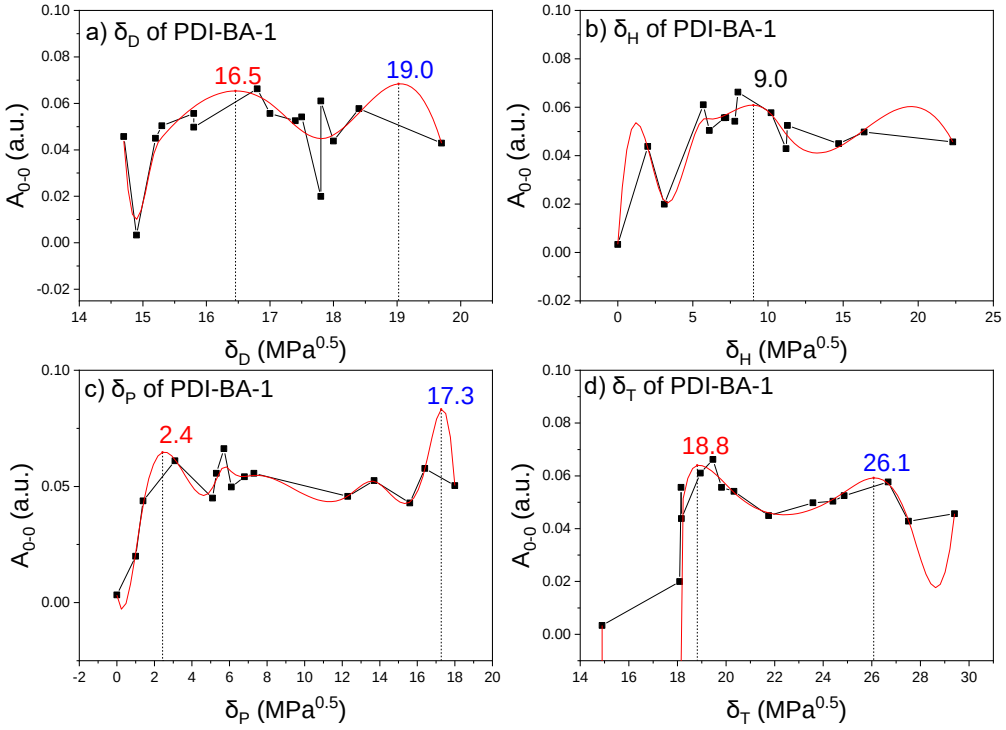

*Figure 2-5 a) Dispersion b) Hydrogen bond c) Polar cohesive d) Total Hansen Solubility Parameters of **PDI-BA-1** (1.0 × 10^4 M), measured with UV-Vis absorbance intensity in a series of solvents.*

The two sets of HSP can be explained by both the properties of the perylene and substituents, corresponding to HSP1 and HSP2, respectively. Compared to the unsubstituted **PTCDA**, **PDI-BA-1** was substituted with **BA-1** that contained large electronegative atoms (bromine) as well as hydrogen bond donors and acceptors (amide hydrogen and oxygen atoms). As a result, the interaction between solvent and **PDI-BA-1** was strengthened, which further improved the solubility of **PDI-BA-1**. It is therefore worthwhile to further develop how HSP can theoretically guide the self-assembly study of PDIs and supramolecular polymers.

In multi-solvent systems, the HSP of each solvent component can be linearly combined.[163] This approach provides a theoretical guide to precisely tune the dipole and hydrogen-bonding interactions contributed by the solvent. In the solvent-dependent self-assembly study of **PDI-BA-1** (discussed in the end of Section 2.2.2), the dual solvent system (ethyl acetate/hexane) was studied because of the unique HSP of n-hexane ($\delta_H = \delta_P = 0$), which specifically evaluated how δ_H and δ_P of solvent would affect the self-assembly behaviour.

2.2.2. Solvent-, concentration- and temperature-dependent self-assembly studies

Concentrations, temperatures and solvent properties are important factors that influence the non-covalent interactions during supramolecular polymers formation, which is the main focus of this self-assembly study.

PDI-BA-1 ranging in concentration from 2.5×10^{-6} M to 1.0×10^{-4} M was studied in a series of solvents (toluene, isopropanol, acetonitrile, chloroform, DMF, DMSO, methanol and THF). The displacement of the 0-0, 0-1 vibrational transition wavelength ($\lambda_{0\text{-}0}$, $\lambda_{0\text{-}1}$), the relative intensity ratio of the 0-0, 0-1 absorbance ($A_{0\text{-}0}/A_{0\text{-}1}$) and the extent of aggregation calculated by A_{agg} were compared among different systems.

The concentration-dependent UV-Vis absorbance spectra of **PDI-BA-1** in toluene are shown in Figure 2-6a. The spectra of low concentrations (from 2.5×10^{-6} M to 1.0×10^{-5} M) are expanded in Figure 2-6c, where a poor signal/noise ratio was observed, which potentially influenced the quality and effectiveness of data regarding $\lambda_{0\text{-}1}$, $A_{0\text{-}1}$ and A_{agg}. As a result, the analysis regarding $\lambda_{0\text{-}1}$, A_{agg} and $A_{0\text{-}0}/A_{0\text{-}1}$ were only valid in concentrations ranging from 1.0×10^{-5} M to 1.0×10^{-4} M.

$\lambda_{0\text{-}0}$ was found with a slight hypsochromic shift between 529 nm and 527 nm as concentration increased, whilst the absorption maximum for $\lambda_{0\text{-}1}$ stayed constant at 489 nm when the concentration was larger than 1.0×10^{-5} M (Figure 2-6b). The shift in the wavelength suggested the formation of H-aggregates. However, the 2 nm shifting extent was too small to determine the aggregation type, which required further confirmation by TEM. The aggregation peak (A_{agg}) of toluene system was found around 560 nm. A_{agg} at 560 nm showed a clear increasing trend after being normalized by concentration (Figure 2-6d), which suggested a higher extent of aggregation at higher concentration. A decreasing trend was observed in $A_{0\text{-}0}/A_{0\text{-}1}$, which implicated the preference for the 0-0 transition was decreasing as concentration increased.[116,164]

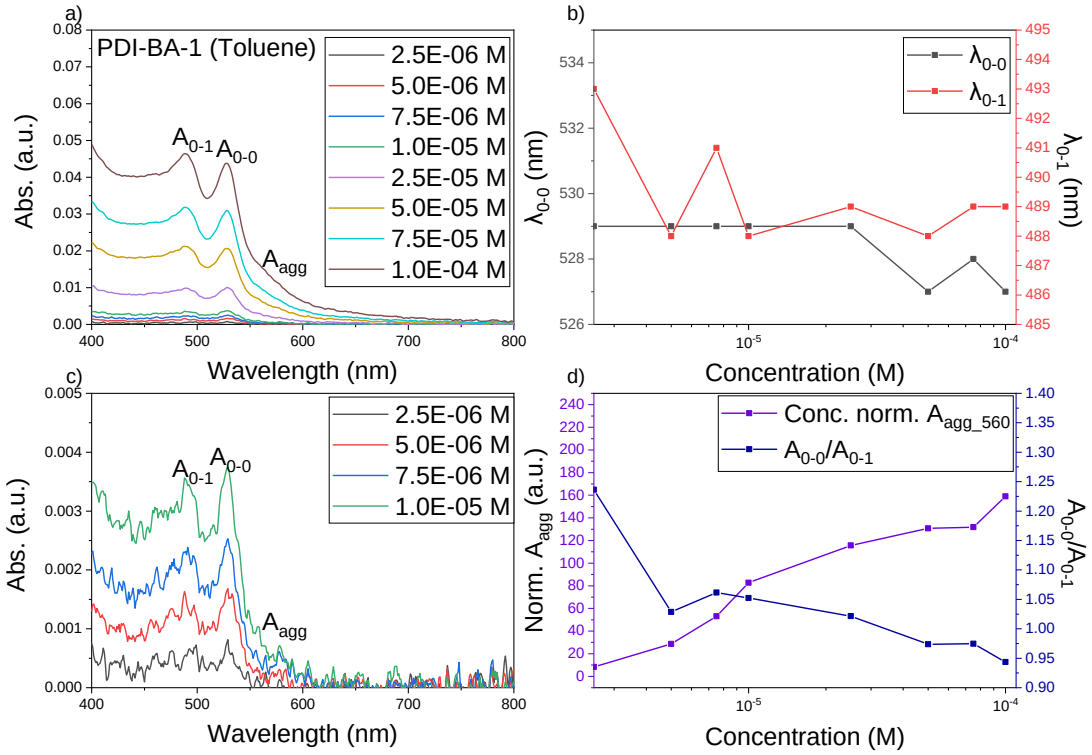

*Figure 2-6 a) Concentration-dependent UV-Vis absorbance spectra of **PDI-BA-1** in toluene, with concentrations ranging from 2.5 × 10^{-6} M to 1.0 × 10^{-4} M. b) The 0-0 and 0-1 vibrational transition wavelengths of **PDI-BA-1** in toluene, with concentrations ranging from 2.5 × 10^{-6} M to 1.0 × 10^{-4} M. c) Concentration-dependent UV-Vis absorbance spectra of **PDI-BA-1** in toluene (zoom in for concentrations from 2.5 × 10^{-6} M to 1.0 × 10^{-5} M). d) Normalized absorbance intensities of aggregation peaks (A_{agg} at 560 nm, normalized by concentration) and relative intensities of the 0-0, 0-1 absorbance (A_{0-0}/A_{0-1}), **PDI-BA-1** in toluene, with concentrations ranging from 2.5 × 10^{-6} M to 1.0 × 10^{-4} M.*

It was found that in acetonitrile and chloroform, the trends of extent of aggregation (Figure 2-7a) and normalized A_{0-0}/A_{0-1} absorbance ratios (Figure 2-7b) were similar to that of toluene. Hereby the extent of concentration-dependent aggregation for each solvent system was calculated by Eq. 2-1, where the lowest concentration (c_{min} = 1.0 × 10^{-5} M) was expected with the lowest extent of aggregation. All the intensities of the aggregation peaks were normalized by their concentrations, ensuring that results were thus comparable.

$$\alpha(c)\% = \frac{\frac{A_{agg}(c)}{c} - \frac{A_{agg}(c_{min})}{c_{min}}}{\frac{A_{agg}(c_{max})}{c_{max}}} \times 100\% \quad \text{..... Eq. 2-1}$$

PDI-BA-1 in toluene exhibited the most significant change in the extent of aggregation (48% increased) when its concentration was increased from 1.0 × 10^{-5} M to 1.0 × 10^{-4} M. The normalized absorbance ratio of A_{0-0} and A_{0-1} of the toluene system decreased by 0.1. **PDI-BA-**

1 in chloroform and acetonitrile showed a weaker tendency for aggregation in the same concentration range, with the extent of aggregation increased by 20% and 3%, respectively. Their normalized absorbance ratio both dropped by 0.04. Although this change was very small, it could suggest a slight influence of concentration on the transition behaviour of **PDI-BA-1**. In addition, it implied that aggregates formed in chloroform and acetonitrile were less structured than those formed in toluene. UV-Vis absorbance spectra of **PDI-BA-1** in acetonitrile and chloroform are appended in Figure 7-5 and Figure 7-6.

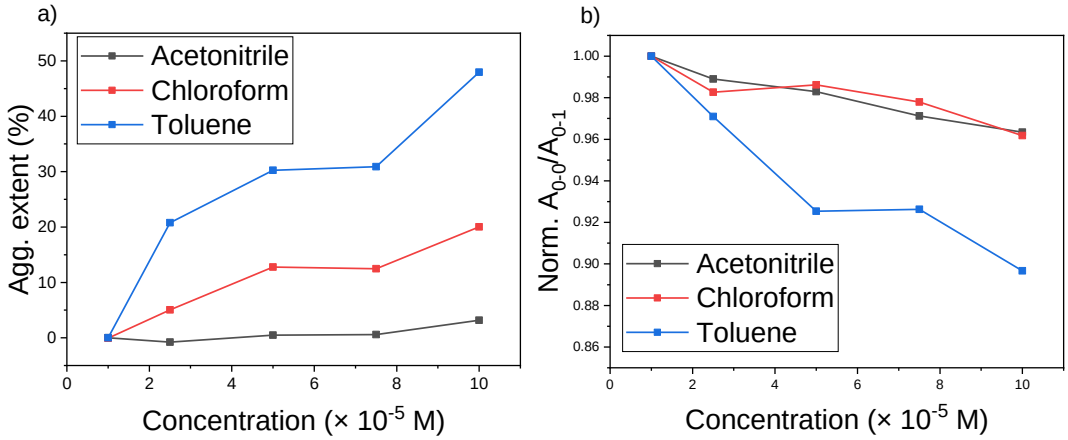

*Figure 2-7 a) Concentration-dependent extent of aggregation and b) normalized $A_{0\text{-}0}/A_{0\text{-}1}$ of **PDI-BA-1** in acetonitrile, chloroform and toluene, where concentration is ranging from 1 × 10^{-5} M to 1 × 10^{-4} M.*

The morphologies of 1 × 10^{-4} M **PDI-BA-1** in toluene, chloroform and acetonitrile were characterized by TEM (Figure 2-8). The detected structures fit the results in Figure 2-7 well. Crystalline structures were detected in toluene (Figure 2-8a, Figure 7-18). Amorphous aggregates coexisting with films were found in chloroform (Figure 2-8b, Figure 7-27). The size of aggregates was measured by ImageJ. Among 70 measurements, the average length is 0.45 μm (sample standard deviation = 0.44 μm). The less structured morphology in chloroform explained the tiny decrease in absorbance ratio. Small aggregates with a maximum of 80 nm length were found in acetonitrile (Figure 2-8c, Figure 7-20), with average length as 28 nm (sample standard deviation = 15 nm, 29 measurements), corresponding to its calculated low extent of aggregation.

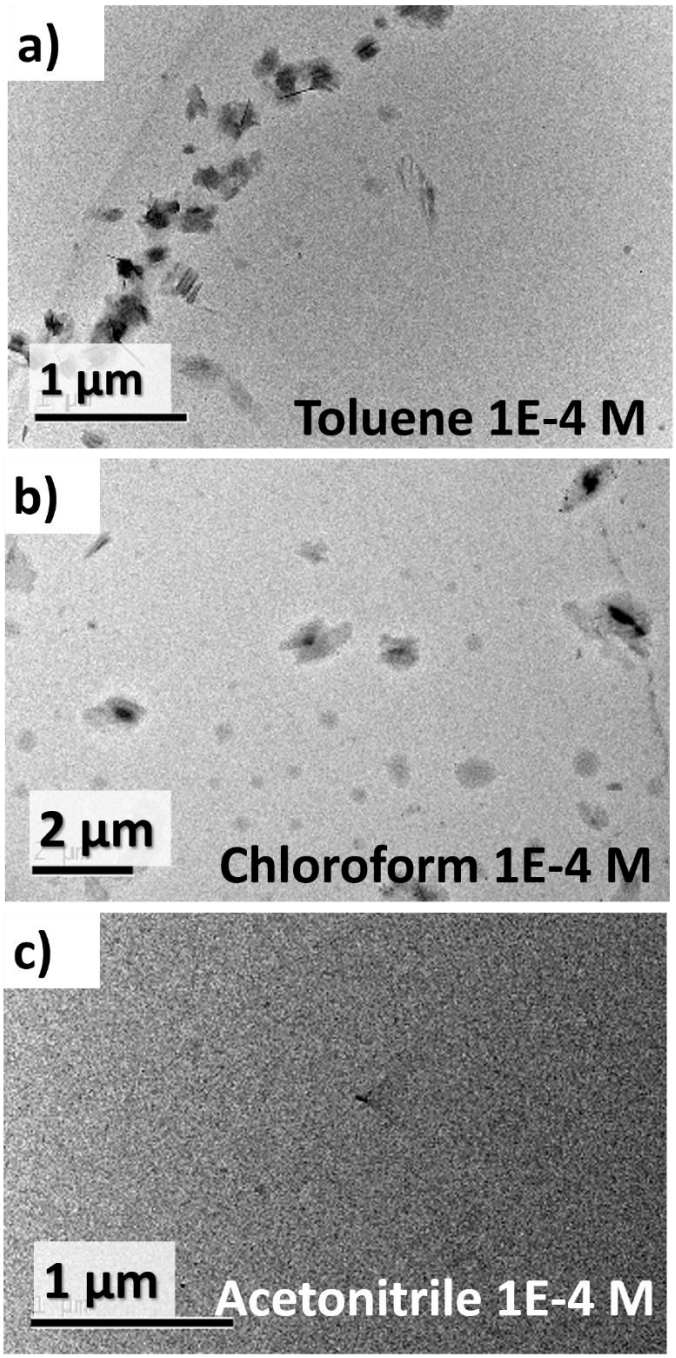

Figure 2-8 TEM images of 1 × 10^{-4} M ***PDI-BA-1*** *drop cast from a) toluene, b) chloroform, c) acetonitrile at 1 × 10^{-4}M.*

There was no clear concentration-dependent trend observed in the rest of solvents (isopropanol, methanol, EA, THF, DMSO and DMF) from 1.0 × 10^{-5} M to 1.0 × 10^{-4} M (Figure 2-9). Compared to toluene, these solvents all showed a fluctuation in their extent of aggregation (Figure 2-9a) and normalized absorbance ratio (Figure 2-9b), suggesting there was no significant aggregates formed in this concentration window. It needs to be mentioned that the negative calculated extent of aggregations is due to the normalization at 1.0 × 10^{-5} M, which

was expected with the lowest extent of aggregation (0%). However, for systems with no obvious aggregation tendency in this concentration range, the fluctuation would result in negative aggregation values. Extra concentration-dependent UV-Vis absorbance spectra of corresponding solvent systems recorded at room temperature are also appended in Section 7.3.2 (Figure 7-7 for DMF, Figure 7-8 for DMSO, Figure 7-9 for ethyl acetate, Figure 7-10 for methanol, Figure 7-11 for THF, Figure 7-12 for isopropanol).

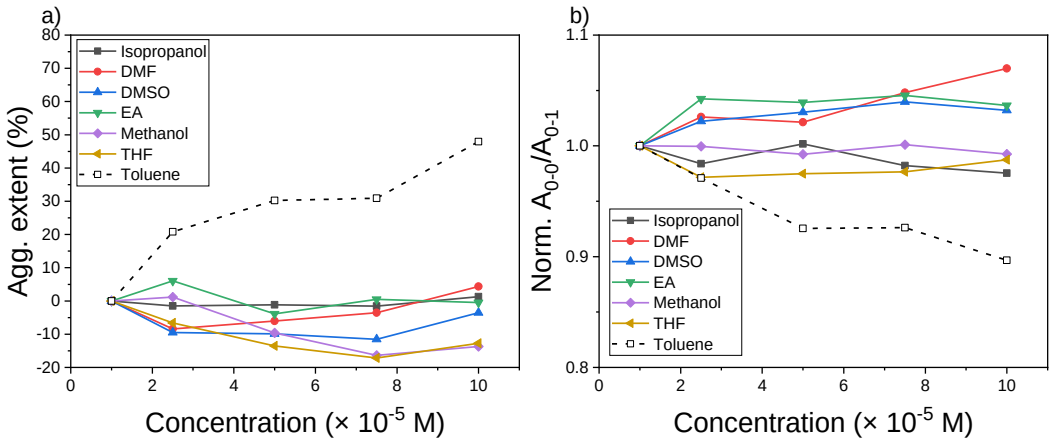

*Figure 2-9 a) Extent of aggregation and b) normalized absorbance ratio of **PDI-BA-1** in isopropanol, DMF, DMSO, EA, methanol, THF and toluene (dash line) (from 1.0 × 10^{-5} M to 1.0 × 10^{-4} M).*

The morphologies of 1 × 10^{-4} M **PDI-BA-1** in isopropanol, methanol, EA, THF, DMSO and DMF were also characterized by TEM, with results confirming that no well-defined aggregates were formed (Figure 2-10). Small aggregates with their lengths ranging from 12 to 25 nm was observed in isopropanol (Figure 2-10a, Figure 7-25), methanol (Figure 2-10b, Figure 7-23) and ethyl acetate (Figure 2-10c, Figure 7-21). Large amorphous films were found in DMF (Figure 2-10d, Figure 7-26) and DMSO (Figure 2-10e, Figure 7-24), which could possibly be due to the overcast (means the sample on the TEM sample grid is too thick) of sample caused by the high boiling points of DMF (b.p. 153 °C) and DMSO (b.p. 189 °C). The quality of TEM image is determined by the thickness of sample, which requires the sample to be as thin as possible. All the TEM samples were prepared by dropping 10 μL solution to the sample grid, followed by the evaporation of excess solvent, which leaves a thin film of sample. As a result, solvents with higher boiling points (e.g., DMF, DMSO, etc.) are less easy to evaporate, leaving relatively thicker and less-structured sample films, which is not preferred in TEM characterization. In the THF system, spherical-like films were observed (Figure 2-10f, Figure 7-22). Because the solvent itself contained 240 ppm butylated hydroxytoluene (BHT) to

prevent the formation of peroxides, the residue after THF was removed might contain a small amount of BHT in addition to **PDI-BA-1**.

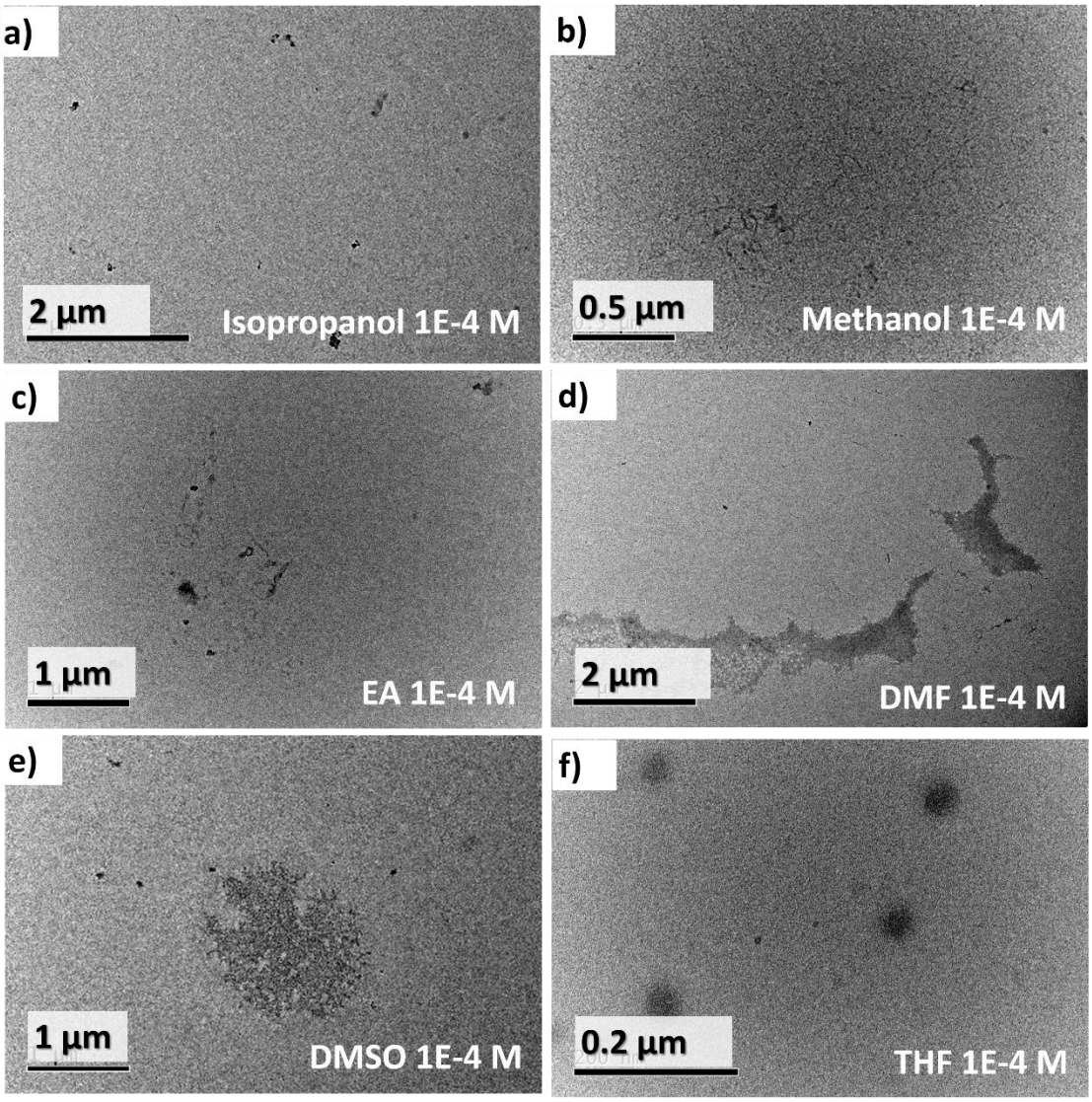

*Figure 2-10 TEM images of **PDI-BA-1** drop cast from 1 × 10^{-4} M a) isopropanol, b) methanol, c) ethyl acetate, d) DMF, e) DMSO, f) THF.*

The concentration window was further expanded to 1.0 × 10^{-3} M for the isopropanol system to ascertain if any aggregates would form at a higher concentration. The UV-Vis spectra of **PDI-BA-1** in isopropanol at 1.0 × 10^{-4} M and 1.0 × 10^{-3} M were compared in Figure 2-11a. As the concentration increased, the intensity of $A_{0\text{-}1}$ surpassed $A_{0\text{-}0}$. $\lambda_{0\text{-}0}$ experienced a 5 nm hypsochromic shift (from 521 nm to 516 nm), whilst $\lambda_{0\text{-}1}$ remained constant. The extent of aggregation and relative intensity of $A_{0\text{-}0}$ and $A_{0\text{-}1}$ were compared in Figure 2-11b, where a 21% increase of aggregation and a 0.11 decrease of $A_{0\text{-}0}/A_{0\text{-}1}$ were observed. The hypsochromic shift of $\lambda_{0\text{-}0}$ implicated the formation of H-aggregates. The main change occurred between 1.0 × 10^{-4} M and 1.0 × 10^{-3} M, which should be a suitable concentration window for controllable self-

assembly behaviour of **PDI-BA-1** in isopropanol. However, the spectrum was also found to be less-structured due to the enhanced stacking at higher concentration. Thus, concentrations higher than 1.0×10^{-3} M were not studied.

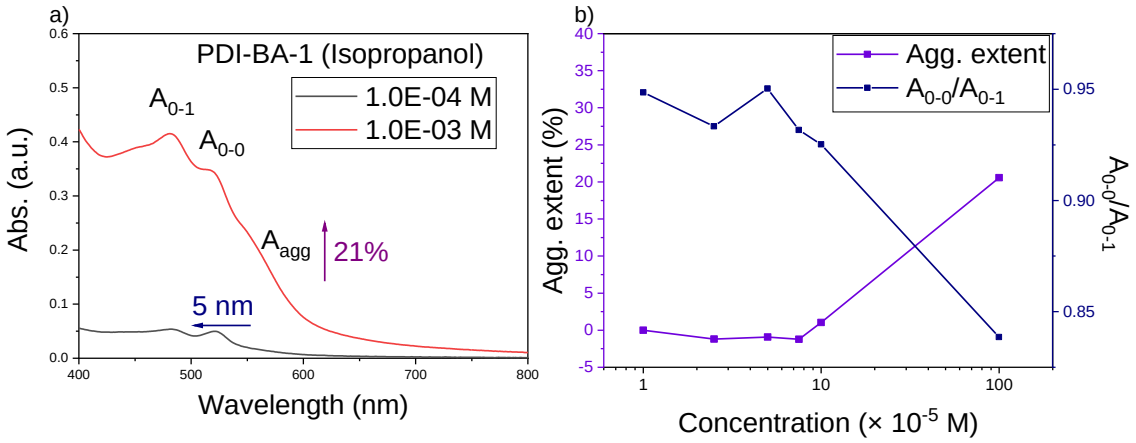

*Figure 2-11 a) Concentration-dependent UV-Vis spectra of **PDI-BA-1** in isopropanol at 1.0 × 10^{-4} M and 1.0 × 10^{-3} M. (The arrows indicate the trend with increasing concentration.) b) Extent of aggregation and relative intensities of 0-0, 0-1 absorbance ($A_{0\text{-}0}/A_{0\text{-}1}$) (from 1.0 × 10^{-5} M to 1.0 × 10^{-3} M).*

Crystalline structures originated from 1.0×10^{-3} M isopropanol were observed by TEM characterization (Figure 2-12a, Figure 7-17). However, the crystalline structures did not form exclusively on the grid, with amorphous thin film was also observed in the background. Compared with the morphology of 1.0×10^{-4} M **PDI-BA-1** in isopropanol (Figure 2-10a), where no significant well-defined aggregates were detected, the existence of crystalline structures in 1.0×10^{-3} M isopropanol also suggested that the increase of concentration could promote the aggregation of **PDI-BA-1**.

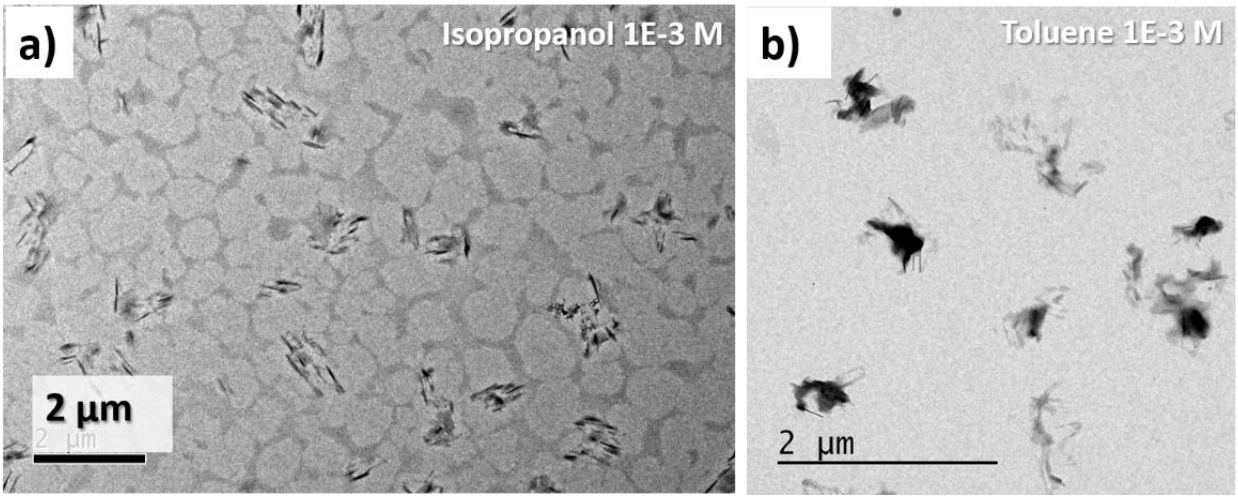

*Figure 2-12 TEM images of 1.0 × 10^{-3} M **PDI-BA-1** drop cast from a) isopropanol and b) from toluene, at room temperature.*

The morphologies of **PDI-BA-1** originated from toluene and isopropanol were further compared at 1.0 × 10^{-3} M to evaluate the morphology-controllable concentration window in two different solvent systems. However, in the toluene system, the increase of concentration from 1.0 × 10^{-4} M (Figure 2-8a) to 1.0 × 10^{-3} M (Figure 2-12b, Figure 7-19) negatively affected the well-defined crystalline structures, resulting in less structured aggregates, which suggested that the controllable self-assembly behaviour had been lost at high concentration.

The temperature-dependent assembly properties of **PDI-BA-1** in 1 × 10^{-4} M and 1 × 10^{-3} M isopropanol and 1 × 10^{-4} M in toluene were further investigated from 293 K to 323 K. A tendency of aggregates to disassociate was observed in all the three systems when the temperature was increased, suggesting the aggregation process was controllable by tuning the temperatures.

The temperature-dependent analysis of **PDI-BA-1** in isopropanol (1.0 × 10^{-3} M) is shown in Figure 2-13. As the temperature increases, the aggregation peak around 565 nm (A_{agg}) decreased, suggesting the dissociation of aggregates, which was confirmed by the isosbestic point (i.e., at which the UV-Vis absorbance remain constant) at 537 nm. The presence of isosbestic point means there are two species in the system, corresponding to the monomer and aggregate of **PDI-BA-1**, respectively. The absorbance wavelength of the 0-0 transition ($\lambda_{0\text{-}0}$) experienced a 3 nm bathochromic shift (from 517 nm to 520 nm) as the temperature increased, whilst $\lambda_{0\text{-}1}$ remained constant. The shift of $\lambda_{0\text{-}0}$ suggested the aggregates at low temperature to be H-type, which fit well with the concentration-dependent UV-Vis result. The ratio of $A_{0\text{-}0}$

and $A_{0\text{-}1}$ also experienced an ascending trend as expected (Figure 2-13b), suggesting the relative preference of the 0-1 transition decreased as the aggregates disassembled.

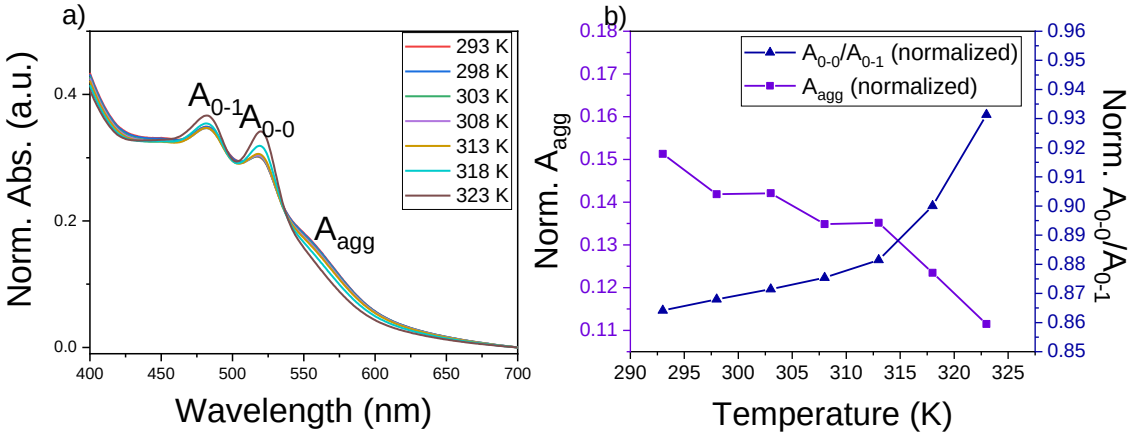

*Figure 2-13 Temperature-dependent analysis of **PDI-BA-1** in isopropanol (1.0×10^{-3} M) from 293 K to 323 K. a) Normalized UV-Vis absorbance spectra (normalized at 700 nm). b) Absorbance intensities of normalized aggregation peak (A_{agg}) and ratio of 0-0, 0-1 absorbance intensities ($A_{0\text{-}0}/A_{0\text{-}1}$).*

Compared with 1.0×10^{-3} M, 1.0×10^{-4} M **PDI-BA-1** in isopropanol did not show a clear crystalline structure in TEM characterization. According to its temperature-dependent UV-Vis study, no significant displacement of $\lambda_{0\text{-}0}$ and $\lambda_{0\text{-}1}$ was observed (Figure 2-14a). A_{agg} at 570 nm exhibits a slight descending trend, whilst the ratio of $A_{0\text{-}0}$ to $A_{0\text{-}1}$ shows an ascending trend, with increasing temperature (Figure 2-14b). However, the extent of change in both A_{agg} and absorbance ratio of 1.0×10^{-4} M isopropanol group are smaller than which in 1.0×10^{-3} M, which corresponds to their relative size of aggregates detected by TEM.

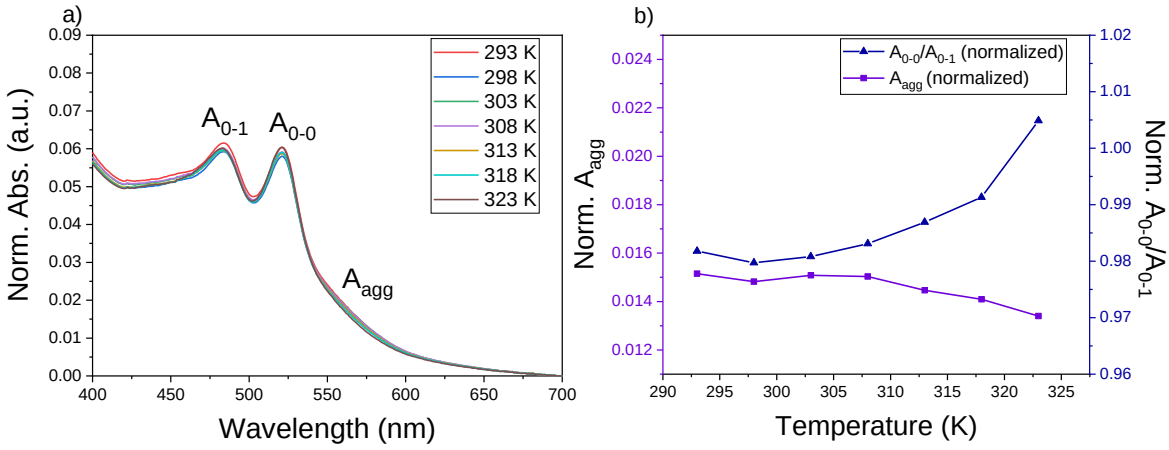

*Figure 2-14 Temperature-dependent analysis of **PDI-BA-1** in isopropanol (1.0 × 10^{-4} M) from 293 K to 323 K. a) Normalized UV-Vis absorbance spectra (normalized at 700 nm). b) Absorbance intensities of normalized aggregation peak (A_{agg}) and ratio of 0-0, 0-1 absorbance intensities ($A_{0\text{-}0}/A_{0\text{-}1}$).*

The toluene system at 1.0 × 10^{-4} M is shown in Figure 2-15. A_{agg} at 569 nm showed a descending trend as temperature increased (Figure 2-15b), where the main change occurred in the range from 298 K to 313 K. The increasing trend of $A_{0\text{-}0}/A_{0\text{-}1}$ between 298 K and 313 K was clearer than found for higher temperatures. The results implied that the critical temperature-controllable window for 1.0 × 10^{-4} M **PDI-BA-1** in toluene was between 298 K and 313 K, after which the monomeric structure dominates. $\lambda_{0\text{-}0}$ and $\lambda_{0\text{-}1}$ both showed a very small hypsochromic shift from 298 K to 313 K; this small shift was however not sufficient enough to determine the aggregation mechanism.

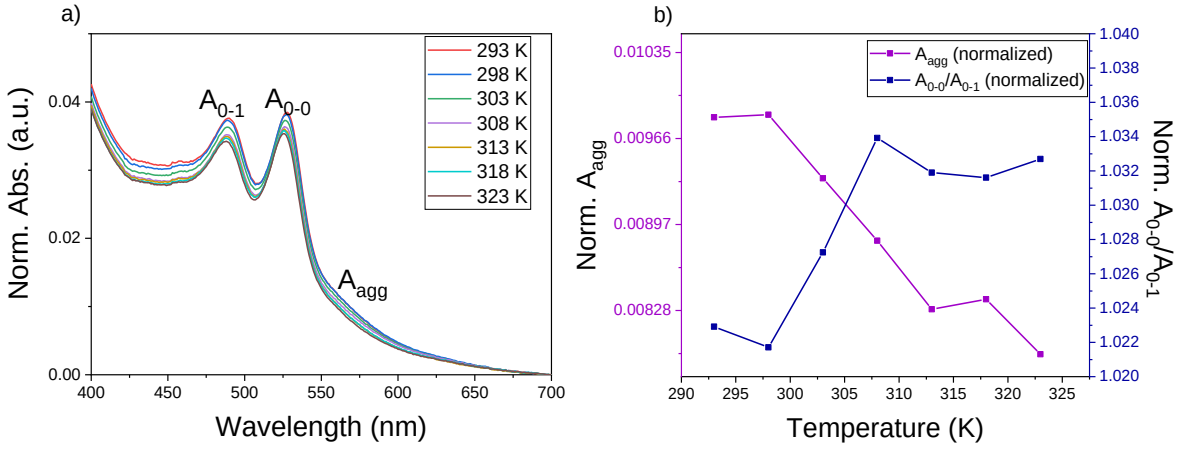

*Figure 2-15 Temperature-dependent analysis of **PDI-BA-1** in toluene (1.0 × 10^{-4} M) from 293 K to 323 K. a) Normalized UV-Vis absorbance spectra (normalized at 700 nm). b) Absorbance intensities of normalized aggregation peak (A_{agg}) and ratio of 0-0, 0-1 absorbance intensities ($A_{0\text{-}0}/A_{0\text{-}1}$).*

The temperature-dependent extent of aggregation (α, Eq. 2-2) was also analysed to compare degrees of aggregation between different solvents and at different concentrations.

$$\alpha(T) = \frac{A_{agg}(T) - A_{agg}(T_{max})}{A_{agg}(T_{min})} \quad \text{Eq. 2-2}$$

As shown in Figure 2-16, from 293 K to 323 K, the change of extent of aggregation of **PDI-BA-1** in 1.0 × 10^{-3} M isopropanol was 15% higher than which in 1.0 × 10^{-4} M isopropanol. The change of extent of aggregation in 1.0 × 10^{-4} M toluene was 9% higher than which in 1.0 × 10^{-4} M isopropanol, which also proved the extent of aggregation was solvent-specific, as discussed in the following paragraphs.

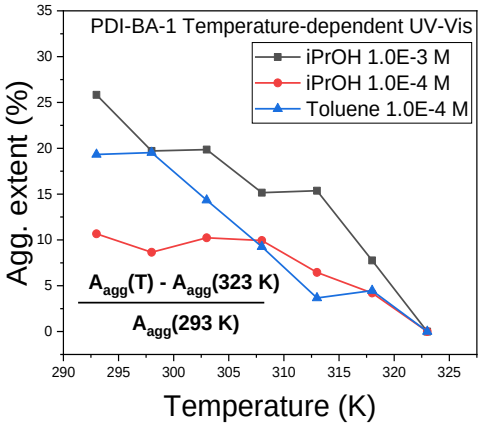

*Figure 2-16 Temperature-dependent extent of aggregation of **PDI-BA-1** in isopropanol (1.0 × 10^{-3} M, 1.0 × 10^{-4} M) and toluene (1.0 × 10^{-4} M), ranging from 293 K to 323 K.*

To understand the mechanism behind solvent-dependent self-assembly behaviour, the HSP of the above solvents were analysed (Figure 2-17). A decreasing trend of aggregation was found both in δ_P (Figure 2-17b) and δ_H (Figure 2-17c), which suggested that when the concentration was below 1.0 × 10^{-4} M, aggregation was preferred in solvents with smaller δ_P and δ_H values. This discovery implicated that the hydrogen-bonding interactions and permanent dipole-dipole interactions contributed by the solvent influenced the extent of aggregation in the studied concentration range. For solvents with larger δ_P and δ_H values, their dipole-dipole interactions and hydrogen-bonding interactions with **PDI-BA-1** overwhelm the hydrogen-bonding interactions and π-stacking interactions between **PDI-BA-1** molecules, which thus limits the formation of aggregates. On the contrary, for solvents with smaller δ_P and δ_H values, the interactions between solvents and **PDI-BA-1** are less competitive than the intermolecular interactions between **PDI-BA-1** molecules, which promotes the aggregation process.

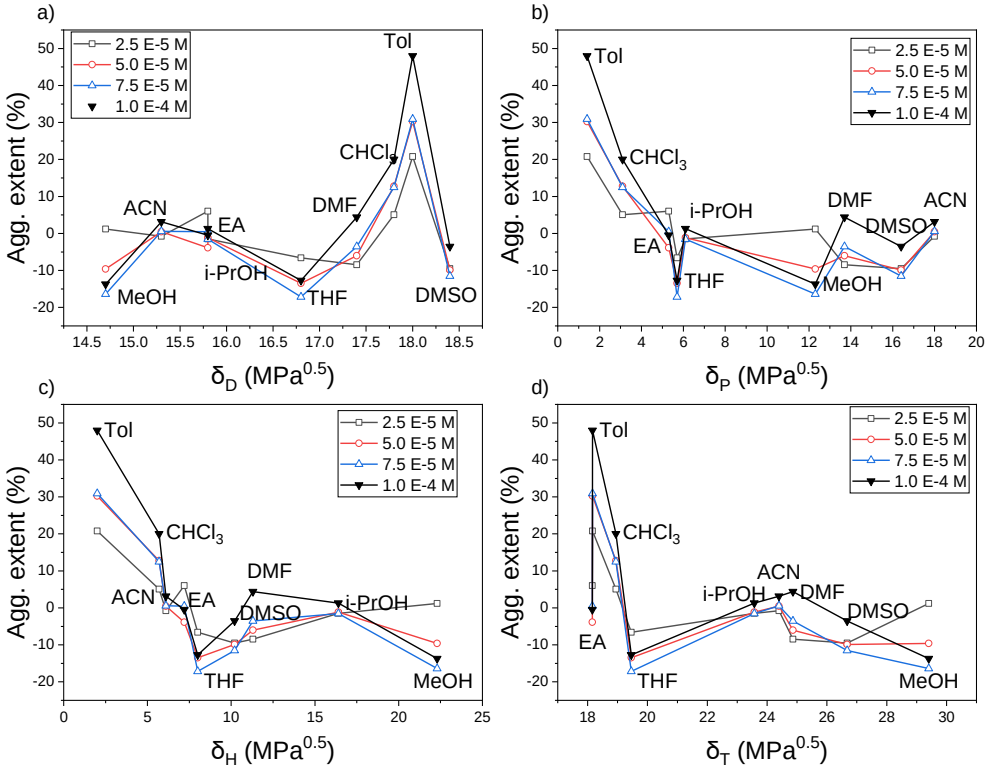

*Figure 2-17 Extent of aggregation of **PDI-BA-1** in different solvents at different concentrations (from 2.5 × 10^{-5} M to 1.0 × 10^{-4} M) versus corresponding a) dispersion HSP, b) dipolar cohesive HSP, c) hydrogen bonding HSP, d) total HSP of solvents. All the data are obtained at room temperature.*

As mentioned in Section 2.2.1.2, it was noticed that both δ_P and δ_H of n-hexane were 0, which provided an opportunity to control the self-assembly behaviour by tuning the δ_P and δ_H components of HSP. To evaluate this hypothesis, a dual-solvent system with ethyl acetate and n-hexane was further studied. By tuning the percentage of hexane from 0% to 75%, controllable self-assembly behaviour was observed.

The HSP of multi-solvent systems were calculated by linearly combining each HSP with the volume percentage of solvents. HSP of 1:3, 1:1, 3:1 ethyl acetate : n-hexane (EA/Hex) were calculated in Table 2-4. A set of δ_P and δ_H values with equal intervals were obtained.

Table 2-4 HSP for 100% ethyl acetate (EA), 100% n-hexane (Hex), and EA/Hex dual-solvent system, where EA and Hex are mixed at 3:1, 1:1, 1:3 (v/v)

Solvent/Compound	δ_D	δ_P	δ_H	δ_T
100% n-Hexane	14.9	0.0	0.0	14.9
75% Hex + 25% EA	15.1	1.3	1.8	15.3
50% Hex + 50% EA	15.4	2.7	3.6	16.0
25% Hex + 75% EA	15.6	4.0	5.4	17.0
100% EA	15.8	5.3	7.2	18.2

The UV-Vis absorbance spectra of EA/Hex system from 2.5×10^{-6} M to 1.0×10^{-4} M were recorded at room temperature (as appended in Figure 7-13, Figure 7-14 and Figure 7-15), among which the UV-Vis absorbance spectra at 1.0×10^{-4} M was analysed. As shown in Figure 2-18a, the aggregation peak (A_{agg}) at 579 nm was more significant in 75% hexane, followed by 50% hexane, whereas 25% hexane and pure ethyl acetate system did not show clear aggregation signals. As the percentage of hexane was increased, the extent of aggregation increased by 30%, whilst the relative absorbance ratio ($A_{0\text{-}0}/A_{0\text{-}1}$) showed a decreasing trend from 25% hexane to 75% hexane (Figure 2-18b). $\lambda_{0\text{-}0}$ showed a 7 nm hypsochromic shift from 517 nm to 510 nm when hexane was increased from 0% to 75%, suggesting the formation of H-aggregates.

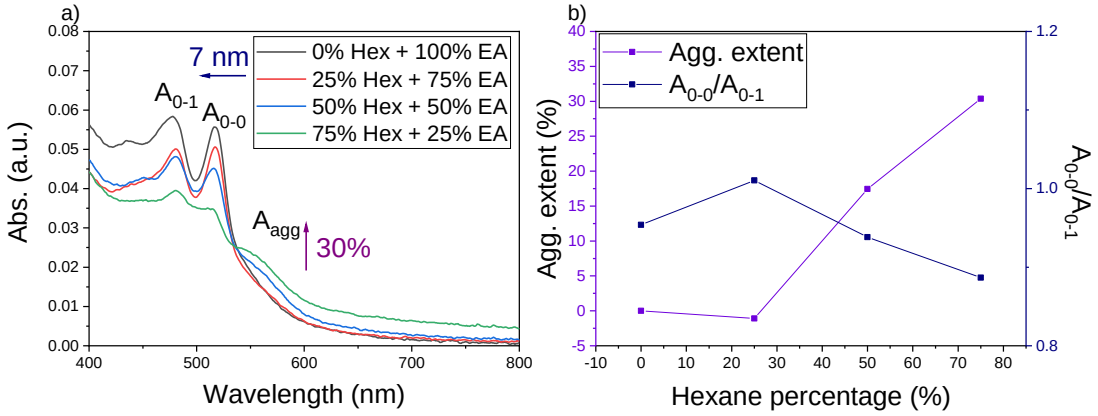

Figure 2-18 a) UV-Vis absorbance spectra of EA/Hex dual-solvent system (1.0×10^{-4} M, at room temperature). b) Extent of aggregation and relative intensities of 0-0, 0-1 absorbance ($A_{0\text{-}0}/A_{0\text{-}1}$) versus percentage of hexane.

It was also noticed that the absolute intensities of $A_{0\text{-}0}$ and $A_{0\text{-}1}$ and spectral resolution were decreasing as the percentage of hexane was increased, which was due to the decrease of solvent

δ_T. The difference between δ_T of the mixed solvent system and the calculated δ_T of **PDI-BA-1** (18.8) became larger when the hexane content was increased, which resulted in a decrease of solubility and thus the absorbance intensities.

The morphology of **PDI-BA-1** in EA/Hex dual-solvent system was characterized by TEM (Figure 2-19). In pure EA, no significant aggregates were formed (Figure 2-19a). In 3:1 EA/Hex system, large amorphous film of 1 μm scale began to appear (Figure 2-19b, Figure 7-28). When the percentage of hexane was increased to 50%, the large film was broken into stripe-like structures (Figure 2-19c, Figure 7-29). Further increasing the percentage of hexane to 75%, crystalline structures were observed (Figure 2-19d, Figure 7-30). However, there are still amorphous films appeared in the background. Based on the morphologies at different hexane content, it worth to further restrict the ratio of EA/Hex between 1:3 and 1:1, e.g., 40% EA + 60% Hexane, to further study the controllable self-assembly behaviour.

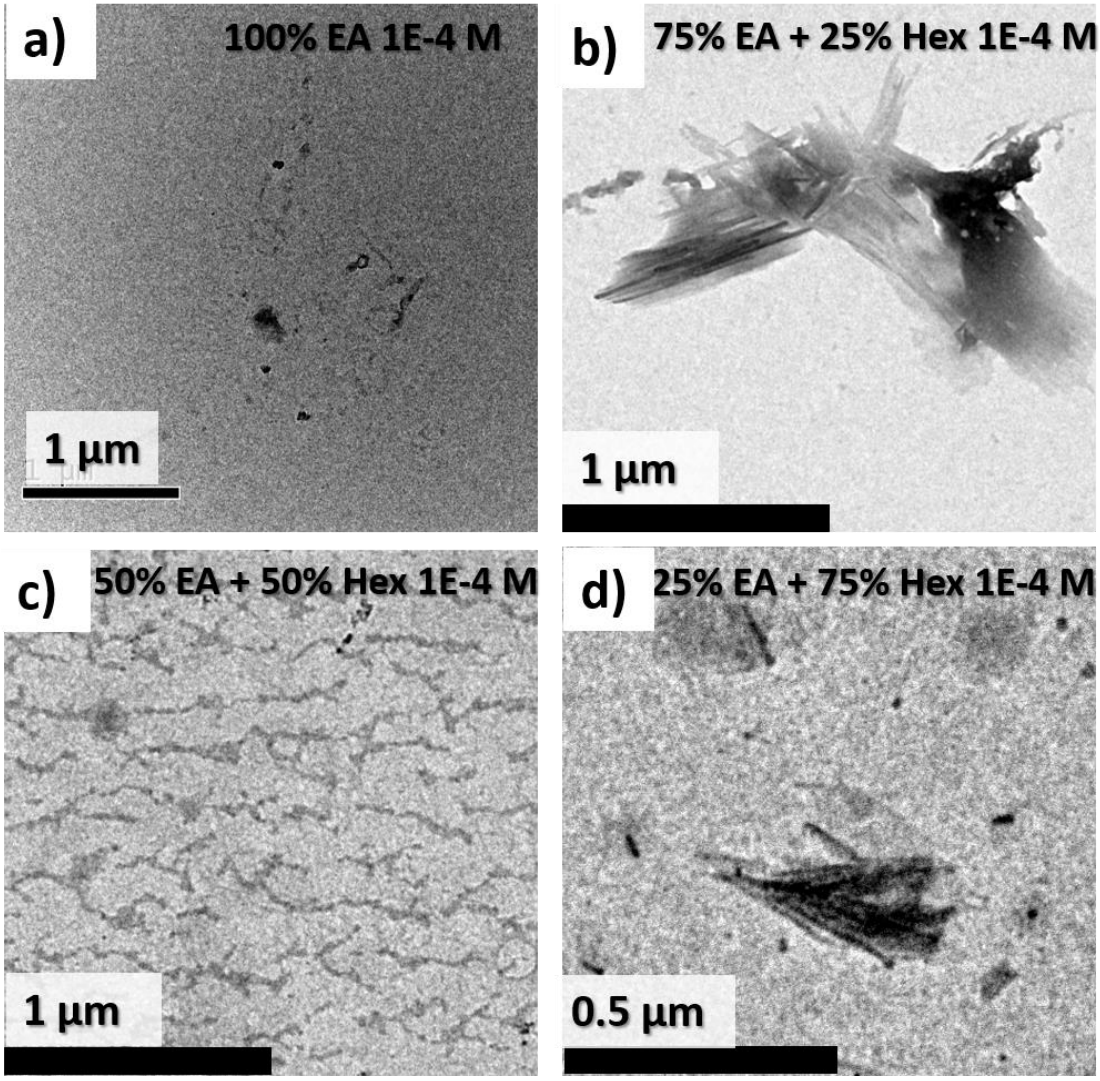

*Figure 2-19 TEM images of **PDI-BA-1** drop cast from a) 100% EA, b) 75% EA and 25% hexane, c) 50% EA and 50% hexane, d) 25% EA and 75% hexane at 1.0 × 10^{-4} M, at room temperature.*

The difference between crystalline structure, amorphous aggregates and amorphous film in this work is based on the shape and darkness in colour observed in the TEM images. The shape of structures reflects whether controlled self-assembly has occurred. The darkness of colour reflects whether electrons has scattered when passing through certain area of the sample grid. For objects with no regular shape and light in colour, it is regarded as amorphous film, whilst for objects dark in colour but with random shape, it is regarded as amorphous aggregate. Structures with regular shape that dark in colour are expected to be crystalline structures. The formation of crystalline structures can also be identified when electron diffraction pattern is observed, as appended in Figure 7-16. However, due to the limit of time, the details of crystals

have not been fully characterized yet. In the future, techniques including X-ray diffraction will be applied for further investigation of crystalline structures.

TEM characterization is a common technique to investigate the morphology of sample in the dried state. According to Jarrett-Wilkins et al., by comparing the UV-Vis absorbance spectra with the TEM images, the morphology characterized at dried state can represent the situation in solution state.[108] The morphologies observed by TEM in this work also correlate well with the UV-Vis absorbance spectra. However, it worth to further analyse how the drying process during TEM sample preparation will affect the morphology of supramolecular polymers. The evaporation of solvent from a droplet will lead to an increase of concentration in a short period of time, depending on the volatility of solvent. For volatile solvent, the evaporation process will complete rapidly, leaving a limited time for monomers and polymers in the droplet to respond towards the change of concentration. Whilst for non-volatile solvent, concentration-dependent morphology change might be allowed during the evaporation process. The morphology of materials may also be affected by the surface tension of solvent, which, in this work, has been taken into consideration that the sample grids were coated with a layer of carbon.

In the next phase, morphology characterization will also be applied in the liquid state, which will provide more *in-situ* details of the studied material in its solution state.

Based on the preliminary results of HSP-tuneable assembly behaviour, it is worthwhile to further discuss the application of HSP in general supramolecular polymerization studies. The influence of solvent δ_H and δ_P towards intermolecular interactions involved in supramolecular systems with hydrogen-bonding interactions as the key polymerization driving force are analysed in Figure 2-20. As illustrated in Figure 2-20a, if the monomer of studied material contains large dipoles, solvents with either large δ_H or δ_P will be competitive to other monomers in the solution, which restricted the supramolecular polymerization. Thus, solvents with small δ_H and δ_P are expected to promote supramolecular polymerization. On the contrary, if the monomer of studied material does not contain large dipoles, only solvents with large δ_H will be expected to compete with other monomers and hinder the supramolecular polymerization (Figure 2-20b).

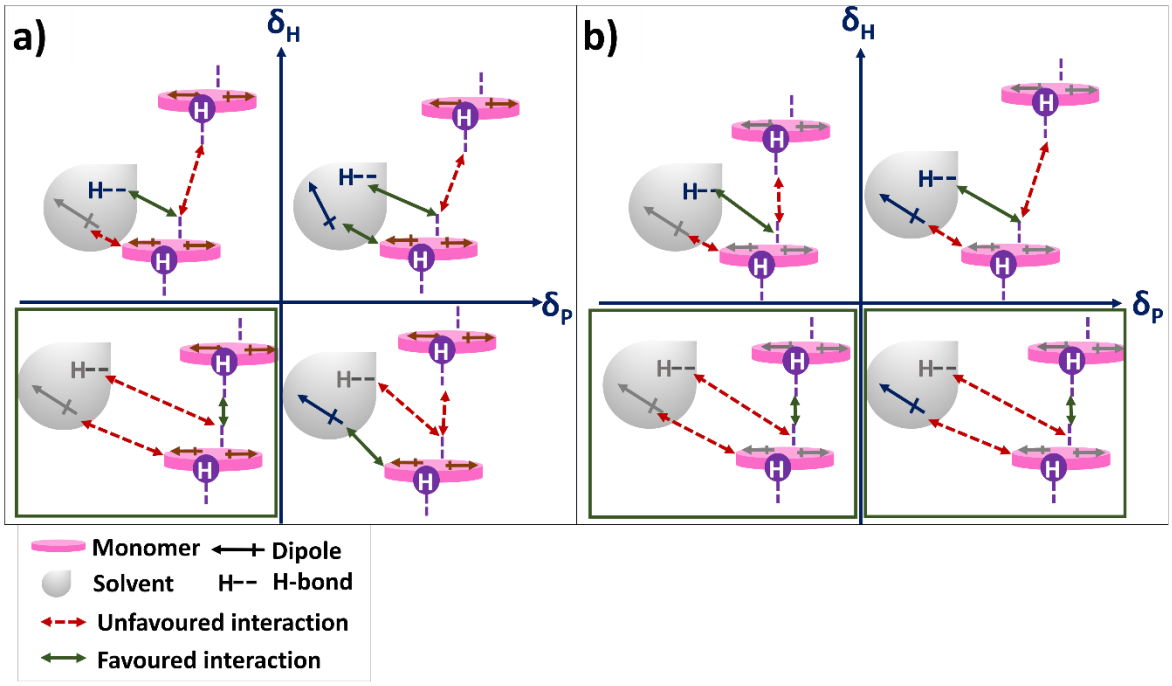

Figure 2-20 Schematics of intermolecular interactions influenced by solvent δ_H and δ_P in supramolecular solution. a) Monomers contain large dipoles, where solvents containing large dipoles will be competitive. b) Monomers do not contain large dipoles, where solvents containing large dipoles will be less competitive. (Supramolecular polymerizations are expected to be preferred in the highlighted groups. Green arrows stand for favoured interaction. Red dash arrows stand for less favoured interaction.)

It is also possible to apply HSPs for control over supramolecular co-polymerizations. The HSP of two supramolecular polymers with different components, e.g., perylene diimides with different side chains, can first be individually calculated with a series of solvents, followed by comparing their similarities of their respective HSPs. As described in Figure 2-21, if δ_H of two compounds are similar in value, the hydrogen-bonding interactions between them are expected to be enhanced (Figure 2-21a). If δ_H between two compounds are significantly different from each other, the hydrogen-bonding interaction between them is expected to be weaker (Figure 2-21b). Since the strength of non-covalent interaction between each supramolecular unit is important to determine the self-assembly behaviour and overall morphologies, studying HSPs provides a potential route to indirectly guiding the design of supramolecular co-polymers, which is worthwhile to be investigated in the future.

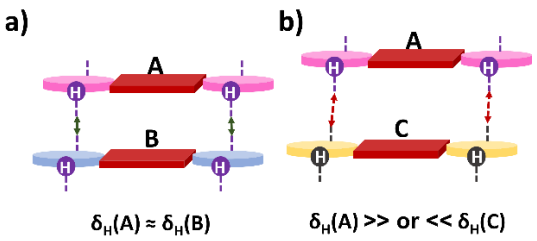

Figure 2-21 Schematics of intermolecular hydrogen bonds between monomers with different components. a) δ_H of two compounds are close to each other. b) δ_H of two compounds are significantly different from each other, where green arrow denotes favoured interaction and red dash arrow denotes unfavoured interaction.

2.3. Modelling

2.3.1. Geometry optimizations of PDI-BA-1

The geometry optimization in this work included conformer searching with the Merck molecular force field (MMFF) followed by semi-empirical method optimization (PM6) in Spartan 14.[165,166] The final optimization was done by density functional theory (DFT) in Gaussian.

2.3.1.1. Conformer searching

The conformer searching tests were aimed at obtaining a set of low-energy conformers of **PDI-BA-1** monomers in vacuum at 298.15K.

After the initial searching turn by MMFF, 30 conformers with the lowest MMFF energies were optimized by Spartan using PM6. The resulting geometries (from lowest energy to highest) are shown in Figure 2-22, with their PM6 energies appended in Figure 7-31.

Among 30 conformers, **M0002**, **M0001**, **M0004**, **M0003**, **M0005**, **M0010** and **M0009** were successfully converged, whose energies were plot in Figure 2-23. The geometries of **M0002, M0001, M0004** and **M0003** were very similar in: 1) their side chains were on different sides of the perylene plane, 2) their perylene cores remain untwisted and 3) their linker structure (N-C-C-N part) were not folded over. These properties ensured that little repulsion potential was built up between moieties, which enabled them to converge to relative low energies. The later three conformers (**M0005**, **M0010** and **M0009**), however, appeared to have a twisted perylene plane, with their side chains folded towards the same face of perylene core. As mentioned in Section 1.2.3.3, the twisted perylene plane was not expected in imide-substituted PDIs based on its electron density distribution. However, MMFF is a classical mechanics method, where electron density distribution is not fully considered. As a result, some geometries with twisted perylene plane could still exist, but their energies would not be favourable.

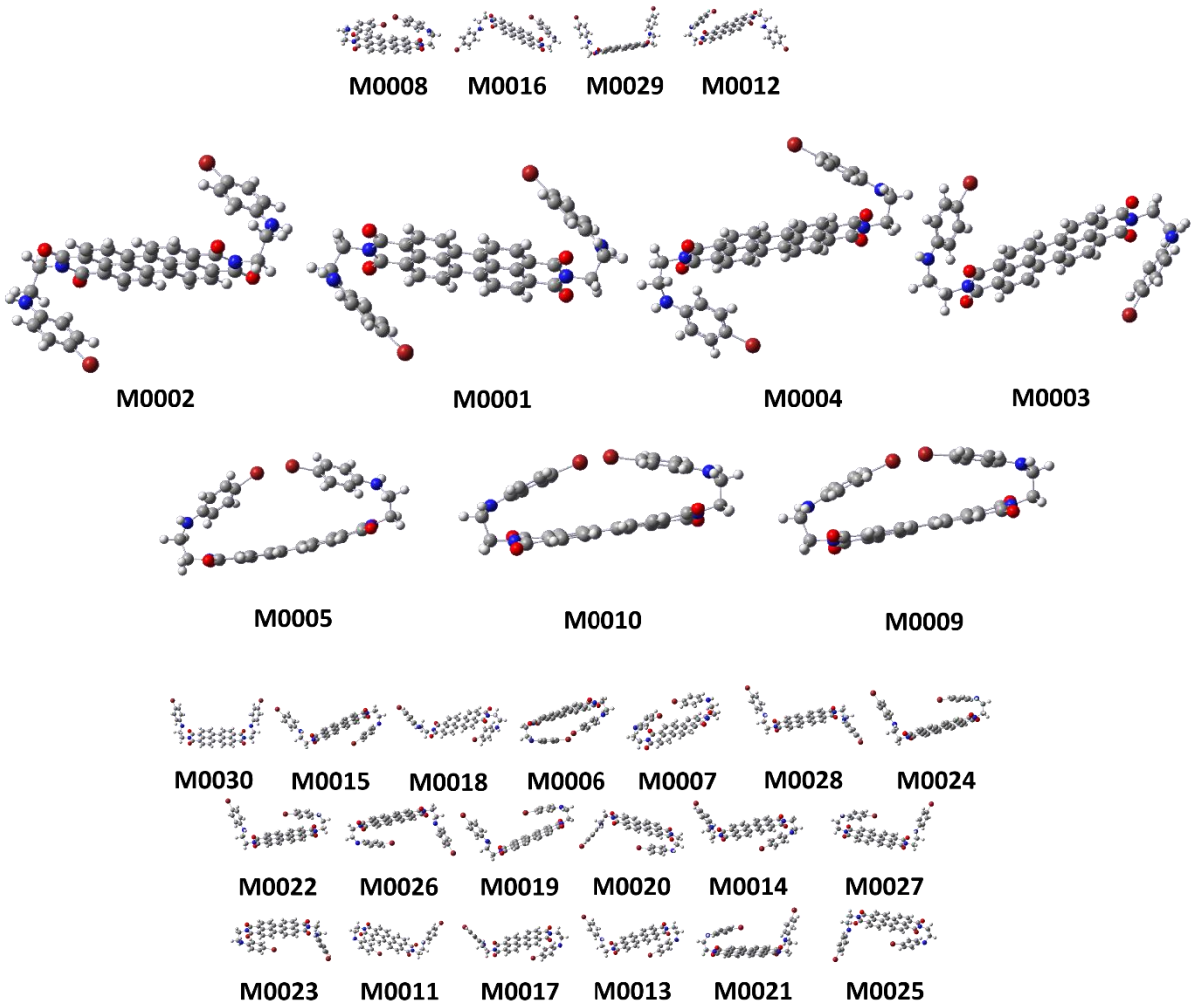

*Figure 2-22 30 Conformers of **PDI-BA-1** searched by MMFF-PM6 (Spartan).*

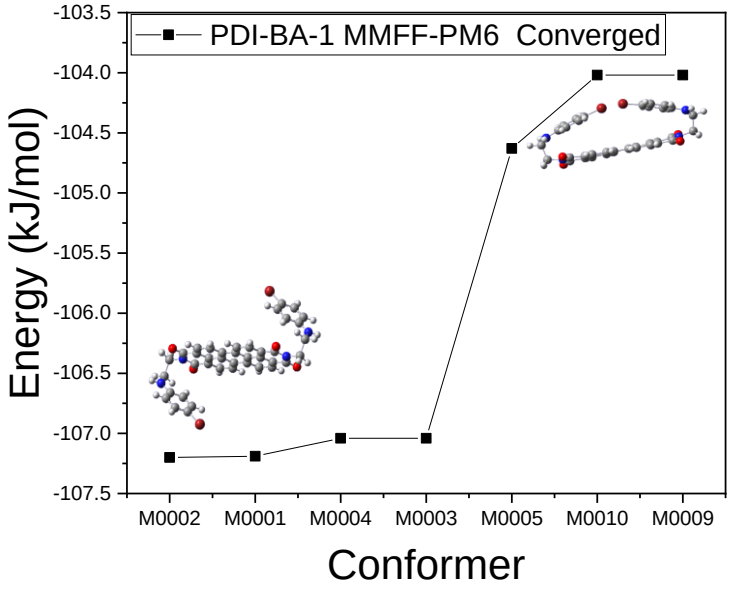

*Figure 2-23 Energies of PM6-converged **PDI-BA-1** conformers (within 30 conformers).*

It was noticed that some conformers shown in Figure 2-22 had several 'degenerated' structures that shared symmetric geometries, which suggested that the conformers variety was limited by only selecting 30 of them. Thus, a larger scale search was conducted for 100 conformers of **PDI-BA-1**, with their PM6 energies were appended in Figure 7-32. Typical geometries among 100 conformers were shown in Figure 2-24, with the degenerate structures ignored.

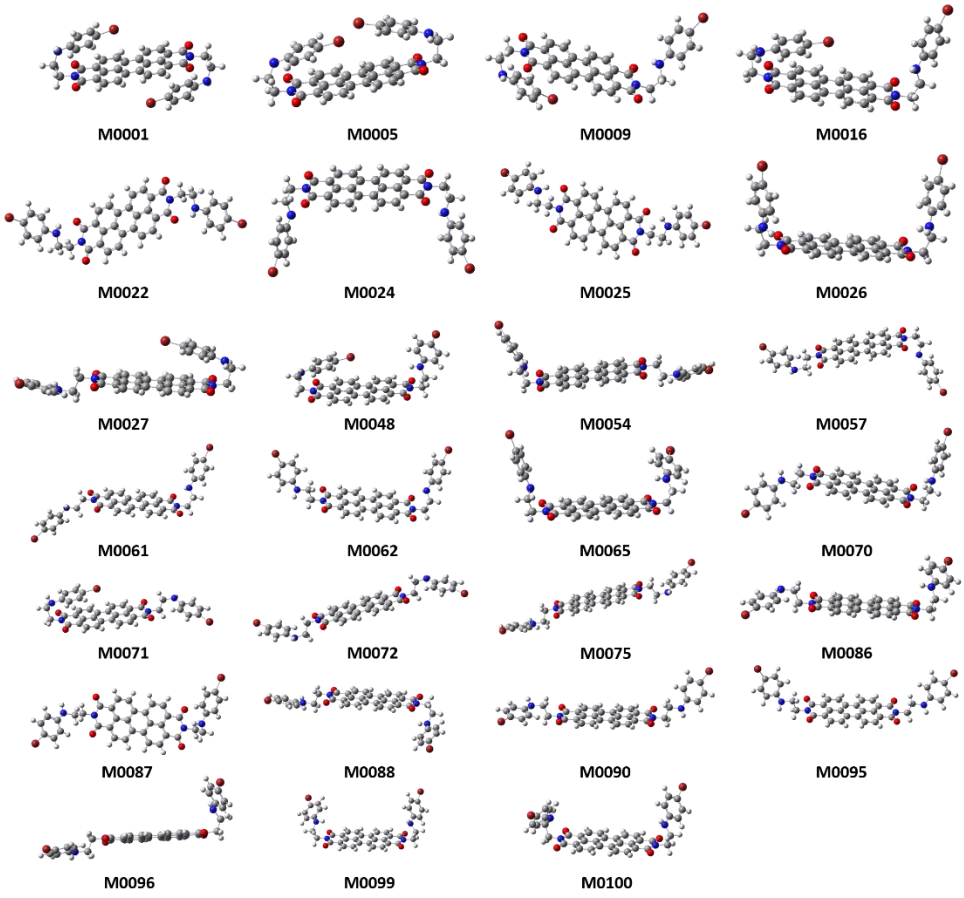

Figure 2-24 Typical conformers from 100 ***PDI-BA-1*** *conformers searched by MMFF-PM6 (Spartan).*

The converged conformers were shown in Figure 2-25. The low energy conformers (**M0001, M0002, M0003**) still had their side chains folded on the opposite sides towards the perylene plane. The higher energy structures (**M0038, M0031**) showed one side chain folded towards the perylene with the other one not. Structures with even higher energies all had their side chains folded or stretched on the same side of perylene, among which **M0005** had a slightly twisted perylene core due to the defects of utilising a non-electron-based method. The increasing energies implicated the unignorable effect of repulsion between side chains.

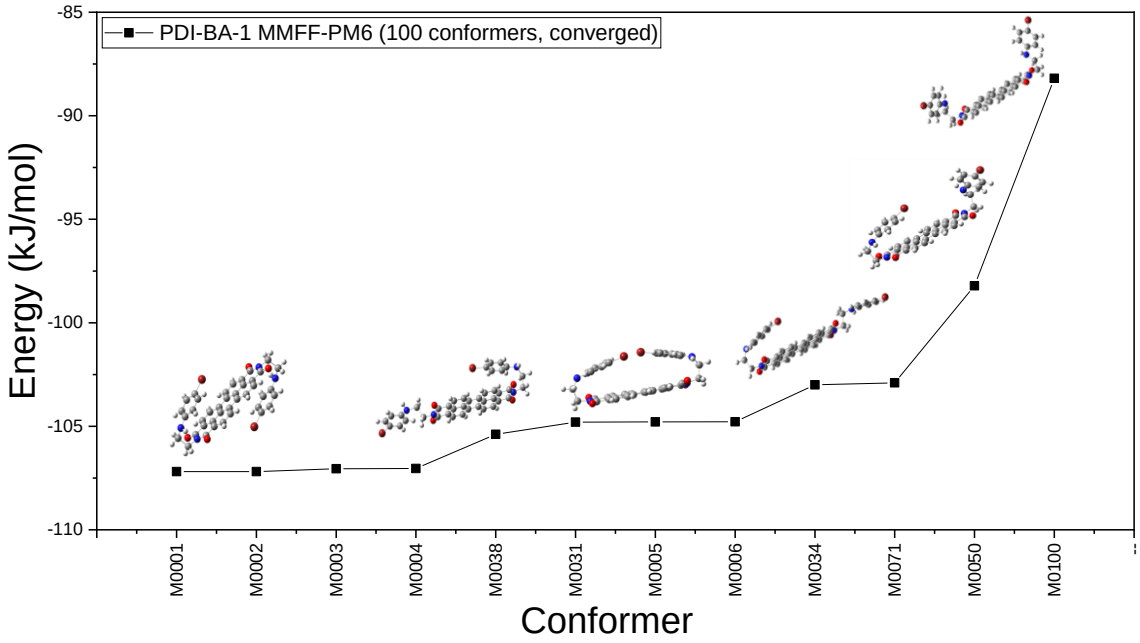

*Figure 2-25 Energies of PM6-converged **PDI-BA-1** conformers (within 100 conformers).*

The results from this conformer search provided a rough guide for higher-level optimization. In particular, the side chains should be spread in opposite sides of perylene plane. To obtain more accurate geometries of **PDI-BA-1**, solvation effects and electron densities were taken into consideration in the next level of optimization performed in Gaussian.

2.3.1.2. Optimization methods comparison

To determine a suitable combination of calculation method/functional/basis set for **PDI-BA-1**, the HOMO-LUMO energy gap calculated by different methods were compared to the $\lambda_{0\text{-}0}$ observed in the UV-Vis absorbance spectra (530 nm). Hereby $\lambda_{0\text{-}0}$ corresponds to the dominant contribution of the π (HOMO) to π* (LUMO) transition, which is comparable to the calculated HOMO-LUMO gap.

A pre-optimization step (Opt 1-1) was applied by the inbuilt Gaussian PM6 method. As shown in Figure 2-26, the default geometry (**PDI-BA-1-def**) built in GaussView was first optimized by inbuilt Gaussian PM6[166–169] in vacuum (**PDI-BA-1-PM6-G-VAC**), whose atom coordinates are appended in Table 7-4 and Table 7-5. The aim of this pre-optimization step was to ensure that the input geometry for further electron-based calculations would not deviate significantly from their converged results.

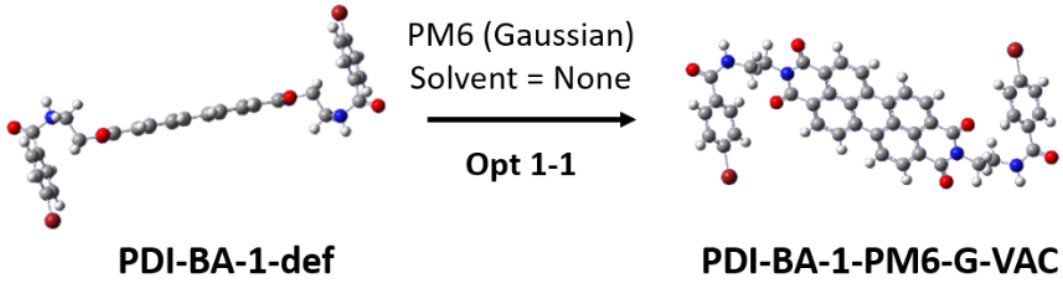

*Figure 2-26 Pre-optimization process of **PDI-BA-1-PM6-G-VAC** (PM6) from **PDI-BA-1-def** (Opt 1-1).*

As listed in Table 2-5, common functionals (B3LYP[170], PBEPBE[171], CAM-B3LYP[5]) and basis sets (6-31g(d), 6-31g+(d), 6-31+g(d,p))[172–176] were applied with DFT[177,178] and Hartree-Fock (HF)[179] methods. Chloroform was applied as solvent through polarizable continuum model (PCM).[179] The resulting energy gaps between HOMO and LUMO (ΔE) were converted to wavelength (λ) by $\Delta E = \frac{hc}{\lambda}$, where h is Planck's constant and c is the speed of light. All the calculated λ values were rounded up to the nearest integer to be comparable with experimental data.

*Table 2-5 Optimization methods of **PDI-BA-1** (all the solvents were chloroform).*

No.	Method	Functionals	Basis Sets	Solvation	Δ E (eV)	λ (nm)
Opt 1-2	DFT	B3LYP	6-31g(d)	PCM	2.50	495
Opt 1-3	DFT	PBEPBE	6-31g(d)	PCM	1.46	849
Opt 1-4	HF	-	6-31g(d)	PCM	7.40	168
Opt 1-5	DFT	CAM-B3LYP	6-31g(d)	PCM	4.66	266
Opt 1-6	DFT	B3LYP	6-31+g(d)	PCM	2.45	506
Opt 1-7	DFT	CAM-B3LYP	6-31+g(d)	PCM	4.58	271
Opt 1-8	DFT	PBEPBE	6-31+g(d)	PCM	1.42	871
Opt 1-9	DFT	B3LYP	6-31+g(d, p)	PCM	2.59	478

The resulting λ were compared to 530 nm. According to the results, Opt 1-2 (DFT/B3LYP/6-31g(d), λ = 495 nm) and Opt 1-6 (DFT/B3LYP/6-31+g(d), λ = 506 nm) were closest to 530 nm, whilst λ of HF, CAM-B3LYP and PBEPBE methods deviated significantly from 530 nm by 362 nm (HF, Opt 1-4), 264 nm (CAM-B3LYP/6-31g(d), Opt 1-5), 259 nm (CAM-B3LYP/6-

31+g(d), Opt 1-7), 319 nm (PBEPBE/6-31g(d), Opt 1-3), and 341 nm (PBEPBE/6-31+g(d), Opt 1-8), respectively. After balancing the calculation cost, DFT/B3LYP/6-31g(d) was regarded most suitable for **PDI-BA-1** calculation.

The effect of the pre-optimization step with PM6 was re-evaluated after obtaining the suitable parameters for DFT. The results however, showed less than 0.5 nm difference of the calculated λ (0.06 nm by B3LYP/6-31g(d) and 0.4 nm by B3LYP/6-31+g(d)), which suggested a limiting effect of the PM6 pre-optimization. As a result, the geometry directly optimized from **PDI-BA-1-def** by B3LYP/6-31g(d) with PCM (**PDI-BA-1-DFT**) was regarded to be acceptable for further geometry analysis. The optimization process of **PDI-BA-1-DFT** (Opt 2-1) and optimized geometry are shown in Figure 2-27, with the atomic coordinates appended in Table 7-6.

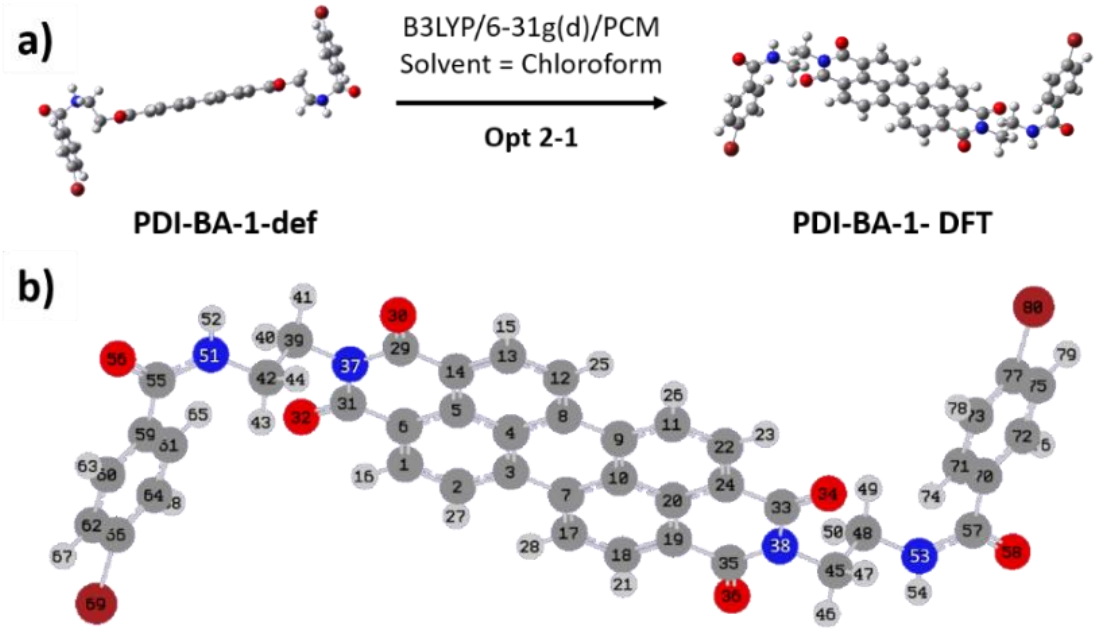

*Figure 2-27 a) Optimization process of **PDI-BA-1- DFT** (B3LYP/6-31g(d)/PCM) from **PDI-BA-1-def** (Opt 2-1). b) Geometry of **PDI-BA-1-DFT**.*

The key variance during the optimization process was observed in the amide-ethylene diamine (EDA) linker, which contained C59, C55, N51, C42 (Figure 2-28a). The distance between the amide hydrogen (H52) and imide oxygens (O32, O30) (Figure 2-28b, c) were also compared to evaluate the potential intramolecular hydrogen-bonding interactions, i.e., if the distance between H52 and O32 or O30 is between 1.5 to 2.5 Å, the hydrogen bond will form. Geometry parameters processed by Opt 1-1, Opt 1-2 and Opt 2-1 are compared in Table 2-6, with **PDI-BA-1-def** as the input reference.

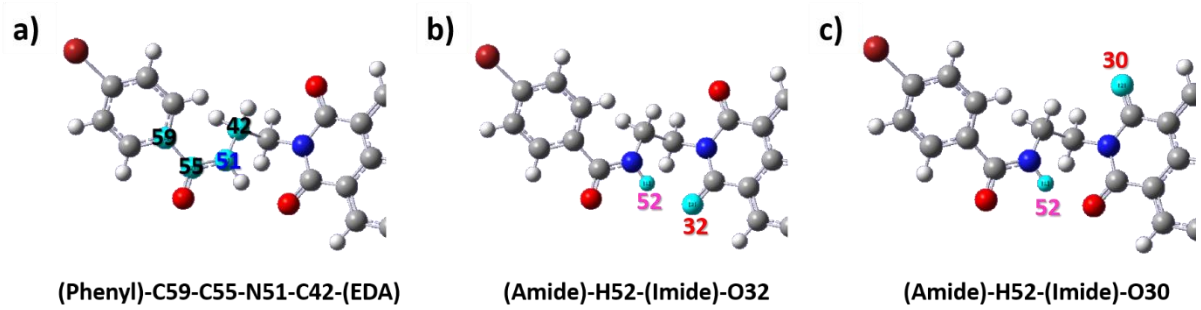

*Figure 2-28 key variance structures during the optimization process of **PDI-BA-1**.a) C59-C55-N51-C42 structure connecting 4-bromophenyl group and ethylene diamine. b) H atom (H52) on the amide group and O atom (O32) on one side of the carbonyl group on the perylene core. c) H atom (H52) on the amide group and O atom (O30) on the other side of the carbonyl group on the perylene core.*

*Table 2-6 Geometry parameters processed by Opt 1-1, Opt 1-2 and Opt 2-1. The reference geometry is **PDI-BA-1-def** (Input)*

Fragment	Explanation	Input	Opt 1-1	Opt 1-2	Opt 2-1
C55-N51-C42	Amide-EDA (Bond angle, °)	109.471	125.857	130.427	130.246
C55-N51	Amide-EDA (Bond length, Å)	1.47000	1.39916	1.36981	1.36998
C55-N51	Amide-EDA (Bond order, a.u.)	1	1	1.5	1.5
C59-C55-N51	Phenyl-Amide (Bond angle, °)	115.550	118.594	120.125	120.025
C59-C55-N51-C42	Phenyl-Amide (Dihedral angle, °)	-37.429	6.078	-17.584	-18.256
H52-O32	Amide H -Imide O (H-O distance, Å)	5.33522	5.13503	5.15198	5.15083
H52-O30	Amide H - Imide O (H-O distance, Å)	4.04613	4.53719	4.38074	4.38549

According to Table 2-6, Opt 1-1 (PM6) mainly led to an improvement in the amide-EDA fragment. However, its effect on the phenyl-amide dihedral angle was over-processed. The bond orders of amide-EDA were both changed from 1 to 1.5 in Opt 1-2 and Opt 2-1 due to the delocalization effect when the solvation was included. Opt 1-2 and Opt 2-1 (B3LYP/6-31g(d)/PCM) were observed with all the geometry parameters identical when rounded up to

the nearest integral, which suggested that the default input geometry (**PDI-BA-1-def**) can be directly optimized by DFT method instead of being pre-optimized by PM6.

2.3.1.3. Reactive-open (RO) and trapped-closed (TC) conformers

As mentioned in Section 1.1.2.1, one of the key structures expected to control the self-assembly behaviour of **PDI-BA-1** is hydrogen atoms on the amide groups. The reactive-open (**RO**) and trapped-closed (**TC**) conformers were thus studied. The results from the optimization process are shown in Figure 2-29, with their atomic coordinates appended in Table 7-7, Table 7-8, Table 7-9 and Table 7-10. Hereby pathway **a** was already discussed in Section 2.3.1.2, whose energy and geometry served as references for the other two conformers (**RO** and **TC**).

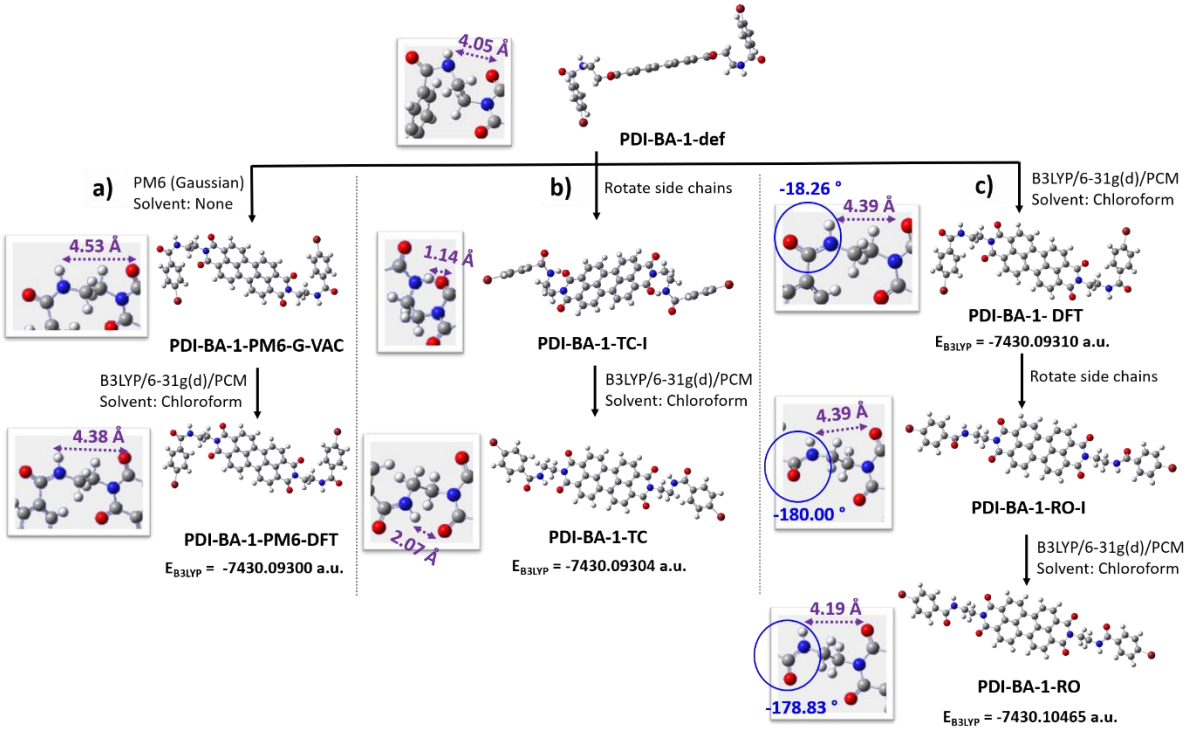

*Figure 2-29 Optimization process of reactive-open (**PDI-BA-1-RO**) and trapped-closed (**PDI-BA-1-TC**) conformers. a) Optimized by PM6 followed by B3LYP/6-31g(d)/PCM. b) Optimized by B3LYP/6-31g(d)/PCM after rotating the side chains, getting trapped-closed conformer. c) Optimized by B3LYP/6-31-g(d)/PCM followed by rotating side chains to a trans- amide structure and optimized by B3LYP/6-31g(d)/PCM again, getting reactive-open conformer.*

Structure parameters of **PDI-BA-1-TC** and **PDI-BA-1-RO** before and after optimization are listed in Table 2-7 (molecules with their names ending with **-I** were input geometries of corresponding conformers).

*Table 2-7 Geometry parameters (bond angle, bond length, dihedral angle and H-O distance) of **PDI-BA-1-TC-I, PDI-BA-1-TC, PDI-BA-1-RO-I, PDI-BA-1-RO**.*

Structure fragment	Explanation	**-TC-I**	**-TC**	**-RO-I**	**-RO**
C55-N51-C42	Amide-EDA (Bond angle, °)	109.471	128.272	130.246	122.159
C55-N51	Amide-EDA (Bond length, Å)	1.47000	1.36522	1.36998	1.36533
C59-C55-N51	Phenyl-Amide (Bond angle, °)	115.55	119.083	120.025	116.305
C59-C55-N51-C42	Phenyl-Amide (Dihedral angle, °)	-37.429	-19.842	-180	-178.833
H52-O32	Amide H -Imide O (H-O distance, Å)	5.14565	4.72513	5.15083	5.33744
H52-O30	Amide H - Imide O (H-O distance, Å)	1.13613	2.06508	4.38549	4.19098

Pathway **b** processed the **TC** conformer (**PDI-BA-1-TC**), whose amide H-imide O (H52-O30) distance resulted as 2.07 Å, which suggested the existence of intramolecular hydrogen bond. The hydrogen bond formed in this way restricted the intermolecular hydrogen-bonding interactions with the amide group of its neighbouring molecule. When the molecule is exposed to an environment that π-π interaction is not favoured, it will predominantly be trapped in its monomer form (Figure 2-30a).

Pathway **c** proposed two geometries. The first (**PDI-BA-1-DFT**) was directly optimized from **PDI-BA-1-def**, whose amide H-imide O (H52-O30) distance was 4.39 Å, suggesting that no intramolecular hydrogen bond was formed. However, the H and O atoms on its amide group were on the same side (cis-), which was expected to pose a hindrance for intermolecular interaction between its neighbouring molecule (Figure 2-30b). By tuning the dihedral angle between phenyl and EDA groups to -180 °, the amide part was placed as a trans- form, which was further set as the input geometry for **RO** conformer. As expected, the resulting geometry

(**PDI-BA-1-RO**) did not form an intramolecular hydrogen bond between the amide H and imide O, where the bond length was 4.19 Å. The dihedral angle was almost unchanged (-178.83 °), which enabled the trans-amide structure to be remained. The energy of **PDI-BA-1-RO** was slightly lower than both **PDI-BA-1-DFT** (with cis-amide structure) and **PDI-BA-1-TC** by 0.01 atomic unit (a.u.). As analysed in Figure 2-30c, with **PDI-BA-1-RO** as the monomeric unit, intermolecular hydrogen bonds are expected to be formed along with π-π interactions in the same direction along the molecular array, which caused its polymerization to be favoured.

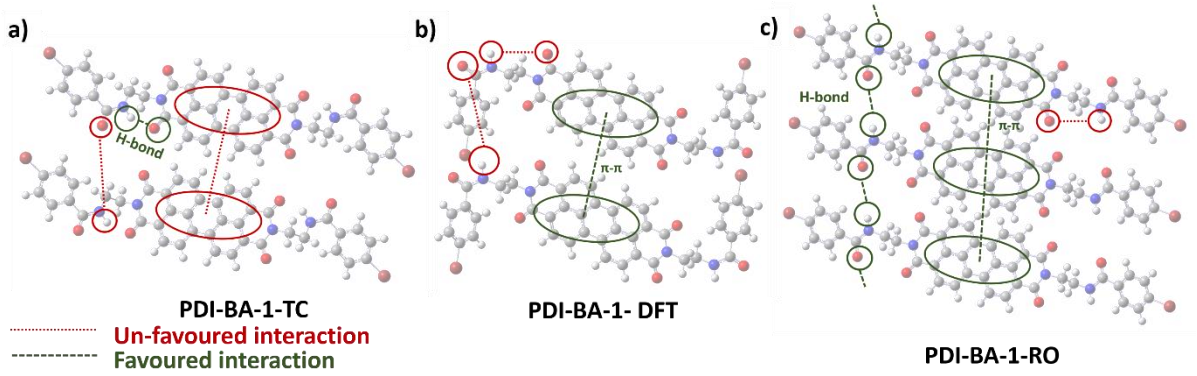

*Figure 2-30 Inter-/intramolecular interaction analysis of **PDI-BA-1** conformers. a) **PDI-BA-1-TC**, b) **PDI-BA-1-DFT** (cis-amide), c) **PDI-BA-1-RO** (trans-amide). Red dot lines denote un-favoured interaction. Green dash lines denote favoured interaction.*

It needs to be clarified that the multi-molecular behaviour shown in Figure 2-30 has not been quantitively calculated due to the time constraints associated with this project. More electrodynamic parameters and periodic boundary conditions are required for multi-layer studies, which would be worth to study in the future.

2.3.2. Excitation analysis of PDI-BA-1

The excitation attributes of **PDI-BA-1-DFT** were studied by single point calculations with time-dependent self-consistent field DFT (TDSCFDFT). Three functionals (B3LYP, CAM-B3LYP and PBEPBE) were compared in single point calculations. The results are listed in Table 2-8.

*Table 2-8 Single point calculations of **PDI-BA-1-DFT** , including method, functional, basis set, solvation and calculated HOMO-LUMO gap, converted to wavelength (all the solvents were chloroform).*

No.	Method	Functional	Basis Sets	Solvation	λ (nm)
SP-2-1-1	TDSCFDFT	B3LYP	6-311g(d)	PCM	546
SP-2-1-2	TDSCFDFT	CAM-B3LYP	6-311g(d)	PCM	486
SP-2-1-3	TDSCFDFT	PBEPBE	6-311g(d)	PCM	785

The HOMO-LUMO energy gaps compared to 530 nm suggested that B3LYP/6-311g(d)/PCM (λ = 546 nm) was still the most suitable method combination for **PDI-BA-1**. CAM-B3LYP (λ = 486 nm) was also acceptable, while PBEPBE (λ = 785 nm) deviated too much from the expected wavelength. In addition to PCM, Self-Consistent Isodensity PCM (SCIPCM) was also attempted.[180] However, for all the three functionals with 6-311g(d), the SCIPCM all raised errors for the surface integrals and thus not successfully converged, which could be explained with the shape-sensitive properties of SCIPCM that was not suitable for **PDI-BA-1**.

The predicted UV-Vis spectra and analysis of key transition pathways of **PDI-BA-1** are shown in Figure 2-31, where orbital **212** and **213** are HOMO and LUMO, which were both located in the perylene core. All the other calculated excited states with non-zero oscillator strength are appended in Table 7-11. The excitation energy of HOMO to LUMO is 2.27 eV, calculated by B3LYP/6-311g(d)/PCM. In addition to HOMO-LUMO transition, excitations are also preferred to take place from the side chains orbitals to the LUMO of perylene core. Some could even reach higher orbitals like LUMO +1, +2, +4 and + 6 in UV region.

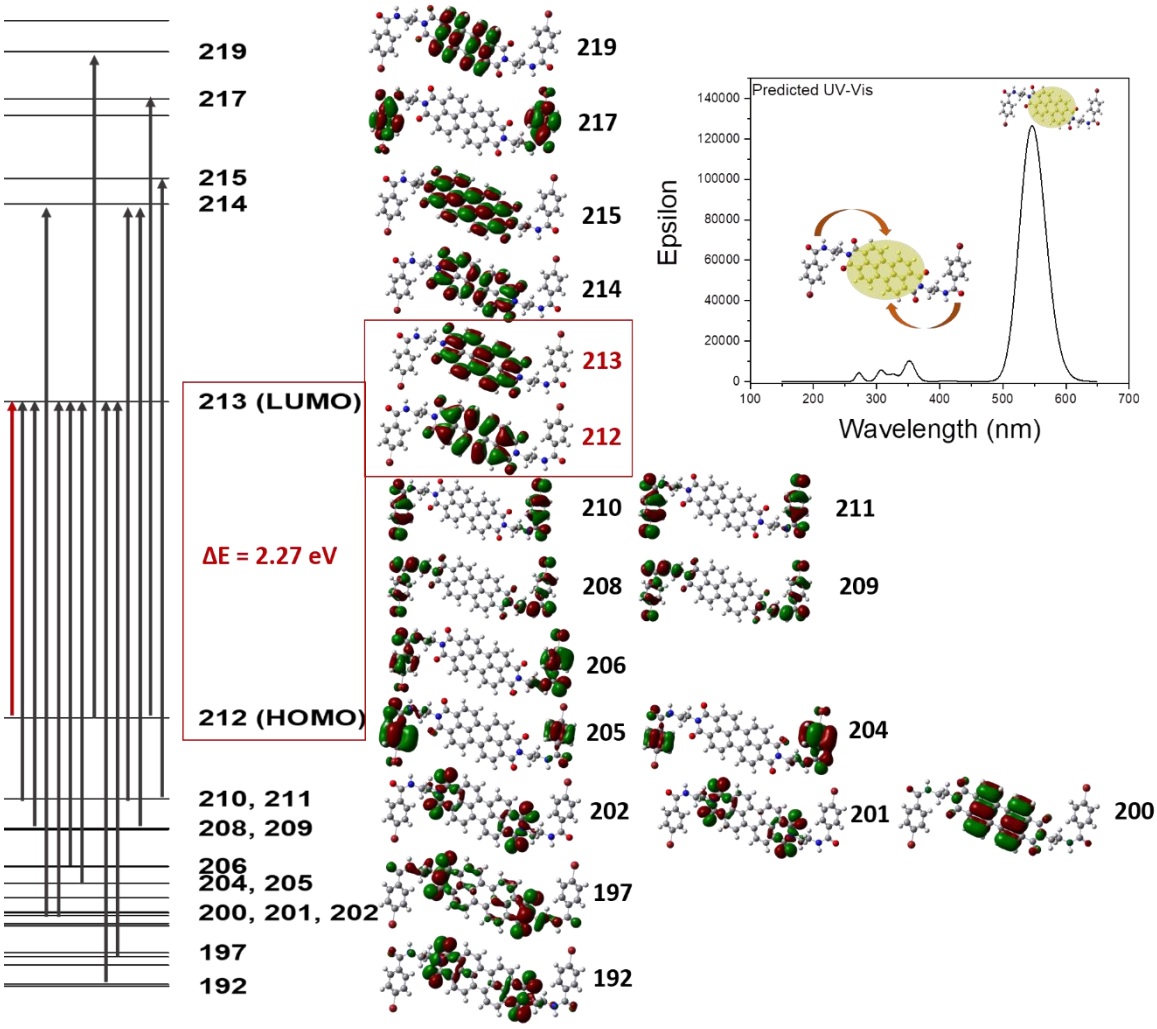

*Figure 2-31 Schematics of key molecular orbitals and excitation pathways and calculated UV-Vis absorbance spectra of **PDI-BA-1** (B3LYP/6-311g(d)/PCM). No. 212 and 213 are HOMO and LUMO, respectively.*

These results confirmed that in the monomeric state of **PDI-BA-1** electrons on the side chains tend to flow to the perylene core. In future work, it would be worth to study the excitation behaviour and corresponding conductivities of multi-molecular state of PDI derivatives.

2.3.3. Geometry optimization of TANI-PDI

Based on the results of **PDI-BA-1**, the geometry of **TANI-PDI** was optimized with a similar method. The default input geometry (**TP-def**) was built in GaussView, followed by optimizing with PM6 in vacuum (Opt-TP1-1), which gave **TP-PM6-VAC**. The atomic coordinates of **TP-def** and **TP-PM6-VAC** are appended in Table 7-12 and Table 7-13. **TP-PM6-VAC** was further optimized with a set of DFT methods (Figure 2-32). The solvent was changed from chloroform to DMSO to simulate the real experimental conditions, where halogen-containing solvents might cause TANI to be doped.

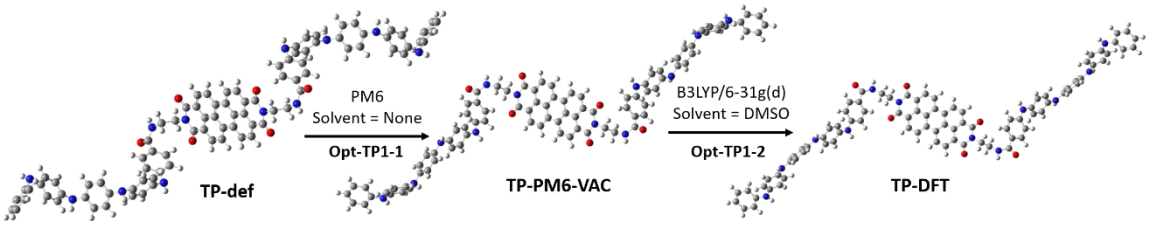

*Figure 2-32 Procedures of **TANI-PDI** optimization. Optimized first by PM6, getting TP-PM6-VAC, followed by B3LYP/6-31g(d) with DMSO, getting TP-DFT.*

As listed in Table 2-9, B3LYP, CAM-B3LYP, 6-31g(d) and 6-31+g(d) were applied as functionals and basis sets for DFT optimization. The energy gaps between HOMO and LUMO were significantly different between B3LYP and CAM-B3LYP, with an 800 nm discrepancy. By comparing the optimized results of **PDI-BA-1** with the same method (B3LYP/6-31g(d)/PCM) in Opt 1-2, the λ of **TANI-PDI** in Opt-TP1-2 was 2.4 times that of **PDI-BA-1**. In the future, the experimental results will be helpful to quantitively evaluate the calculation methods for **TANI-PDI**.

*Table 2-9 Optimization methods, functional, basis sets and solvation of **TANI-PDI** (all the solvents were DMSO). ΔE and λ are calculated energy gap between HOMO and LUMO, and corresponding wavelength.*

No.	Method	Functional	Basis Sets	Solvation	Δ E (eV)	λ (nm)
Opt-TP1-2	DFT	B3LYP	6-31g(d)	PCM	1.04	1190
Opt-TP1-3	DFT	B3LYP	6-31+g(d)	PCM	1.08	1145
Opt-TP1-4	DFT	CAM-B3LYP	6-31g(d)	PCM	3.37	367
Opt-TP1-5	DFT	CAM-B3LYP	6-31+g(d)	PCM	3.51	353

2.3.4. Electron distribution analysis of TANI-PDI

Due to time limitations, the best optimization method for **TANI-PDI** has not been determined yet. Thus, single point calculations could not be operated until a proper method is confirmed. General distribution of frontier orbitals and surface potential of **TP-PM6-VAC** are visualized

in Figure 2-33, where accurate values will be calculated in the future work. As shown in Figure 2-33a, in **TANI-PDI**, the HOMO is no longer located in the perylene core. Instead, it is mainly distributed on the **TANI** chain, whilst the LUMO is still confined to the perylene. This suggests the dominant excitation of **TANI-PDI** will possibly occur from the **TANI** chain to the perylene core. The Mulliken charge distribution and electrostatic surface potential are shown in Figure 2-33c and d, which also suggested a higher potential on the side chains. These results confirmed the donor-linker-acceptor structure of **TANI-PDI**.

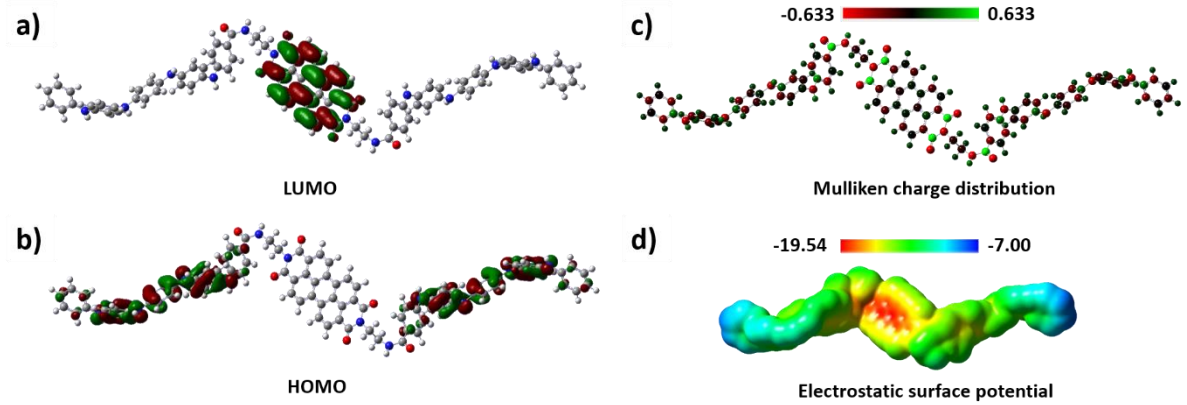

*Figure 2-33 a) LUMO, b) HOMO, c) Mulliken charge distribution and d) electrostatic surface potential of **TP-PM6-VAC**.*

The difference between frontier orbitals of **PDI-BA-1** and **TANI-PDI** suggested that the excitation properties and optical gap of the perylene derivative are also controlled by the electron distribution of side chains. Compared to **PDI-BA-1**, **TANI-PDI** contained a larger conjugated side chain, which is more abundant in electrons and easier to be excited. Further experimental studies will be done to validate the modelling results of **TANI-PDI**.

3. Conclusions

In this project, 4-bromobenzamide di-substituted perylene diimide (**PDI-BA-1**) was synthesized and characterized, where controllable formation of aggregates and crystalline structures were observed, providing a ground of further design of controllable functional supramolecular polymers based on PDI derivatives. The solubility of **PDI-BA-1** was significantly improved compared to **PTCDA**. The self-assembly behaviour, including transition preference, extent of aggregation and morphology of **PDI-BA-1** were proved to be controllable by tuning concentration, temperature and solvent HSP. In suitable concentration and temperature window, higher concentration, lower temperature, and solvents with a small hydrogen-bonding component (δ_H) and dipolar cohesive component (δ_P) of HSP are more suitable for the formation of **PDI-BA-1** aggregates. When tuning the HSP, balance needs to be kept by ensuring the total HSP (δ_T) stays in a reasonable region and does not deviate significantly from the materials HSP, otherwise the spectra resolution will be negatively influenced.

In the modelling study, B3LYP/6-31g(d)/PCM was found to be suitable for geometry optimization of monomeric **PDI-BA-1**. For the monomeric **PDI-BA-1**, the trapped-closed conformer with intramolecular hydrogen bonds was confirmed, whilst the properties of intermolecular hydrogen bonds regarding the reactive-open conformer requires further validation by multi-molecular study. The optical band gap of PDI is possibly tuneable by introducing conjugated side chains (**TANI**), whilst the details of **TANI-PDI** modelling require further validation by experiments. As an extension of this project, based on the polarity and hydrogen-bonding affinity of the studied materials, control over solvent HSPs can potentially be further extended to general supramolecular polymers with hydrogen-bonding interactions as the key polymerization driving force. In addition, the similarity between HSPs of two compounds can also be potentially applied as a guidance for co-polymers design, which will be studied in the future.

Although aggregates and crystalline structures were observed in TEM images of **PDI-BA-1**, fibres, which is an expected form of supramolecular polymers based on PDI, have not yet been obtained. Things can be improved by further tuning the conditions for the formation of supramolecular polymers. The difference between side chains of **PDI-BA-1** and **TANI-PDI** could possibly affect the self-assembly behaviour of corresponding materials. Boc-protected **TANI-PDI**, which has formed fibres according to Wilson-Kovacs work as mentioned in

Section 1.5, contains side chains with larger steric effect compared with **PDI-BA-1**, which potentially aids the formation of well-organized fibres.

To confirm the formation of supramolecular polymers, further characterization will also be carried out to investigate non-covalent interactions involved in the system, where the formation of hydrogen bonds can be confirmed by infrared spectrometry, and π-π interactions can be determined by change of chemical shift of protons on the perylene moiety in NMR spectra. Structural information, including details of crystals, which could also reflect the distance of π-π interactions, can be obtained by XRD. *In-situ* data, i.e., characterizations done in the solution, like dynamic light scattering, will also be collected to minimize the drying effect towards the materials.

The mechanism of polymerization as introduced in Section 1.1.3 can be determined once fibre-like structure is obtained. By measuring the number-averaged (L_N) and weight-averaged length (L_W) of fibres, the dispersity can be calculated by calculating the ratio between L_W/L_N, which can further reflect the mechanism of polymerization, e.g., isodesmic polymerization, living polymerization, etc., which worth to study in the future.

4. Future Work

The author will re-join Prof. Faul's research group as a PhD student, and will this have the opportunity to continue with perylene diimide supramolecular polymers research. There are therefore three areas that can be highlighted for future work: 1) Explore application of HSP in the formation of perylene diimide supramolecular polymers and co-polymers; 2) Explore the modelling of perylene diimide supramolecular polymerization; 3) Formulating and applying design rules obtained from HSP and modelling to new functional supramolecular polymers.

4.1. Exploration of HSPs

HSPs are promising indicators to theoretically guide, understand and tune the conditions for the supramolecular polymerization of PDIs. In future work, HSPs of a series of PDIs with different substituents can be measured and compared, attempting to fully understand the influence and role that the hydrogen bonding component and dipolar cohesive component of HSP (δ_H, δ_P) play.

For each studied PDI, the relationship between solvent HSP and degree of PDI aggregation (at the same concentration) will be evaluated in different solvents with 1) large δ_H and large δ_P, e.g., methanol, 2) large δ_H and small δ_P, e.g., isopropanol, 3) small δ_H and large δ_P, e.g., acetonitrile, 4) small δ_H and small δ_P, e.g., toluene (Figure 4-1).

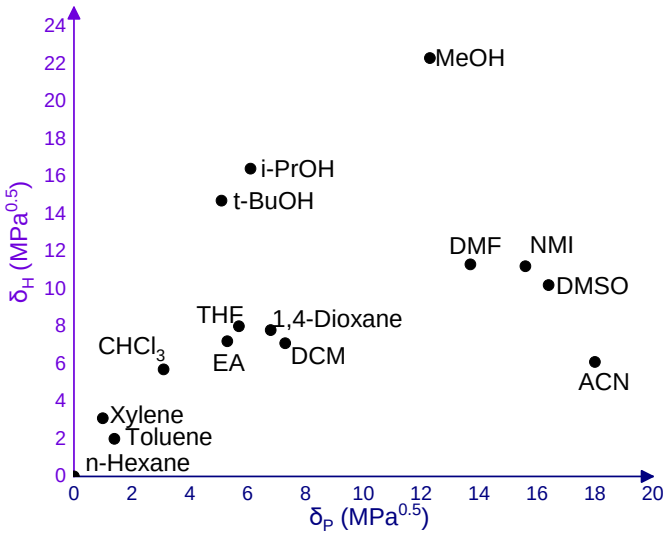

Figure 4-1 HSP of common solvents (δ_P, δ_H).

To reach a wider range of HSP choices, two solvents or even three solvents can be mixed into dual-/tri-solvent system. As shown in Figure 4-2, from the fourteen solvents applied in this project, by mixing two of them at 1:1, 1:3 and 3:1 volume ratios, a wider range of tuneable HSPs will be achievable and accessible. Whilst the miscibility of solvents will also be taken into consideration. This approach will widen the scope of potential application of HSPs to help tune supramolecular homopolymerisations.

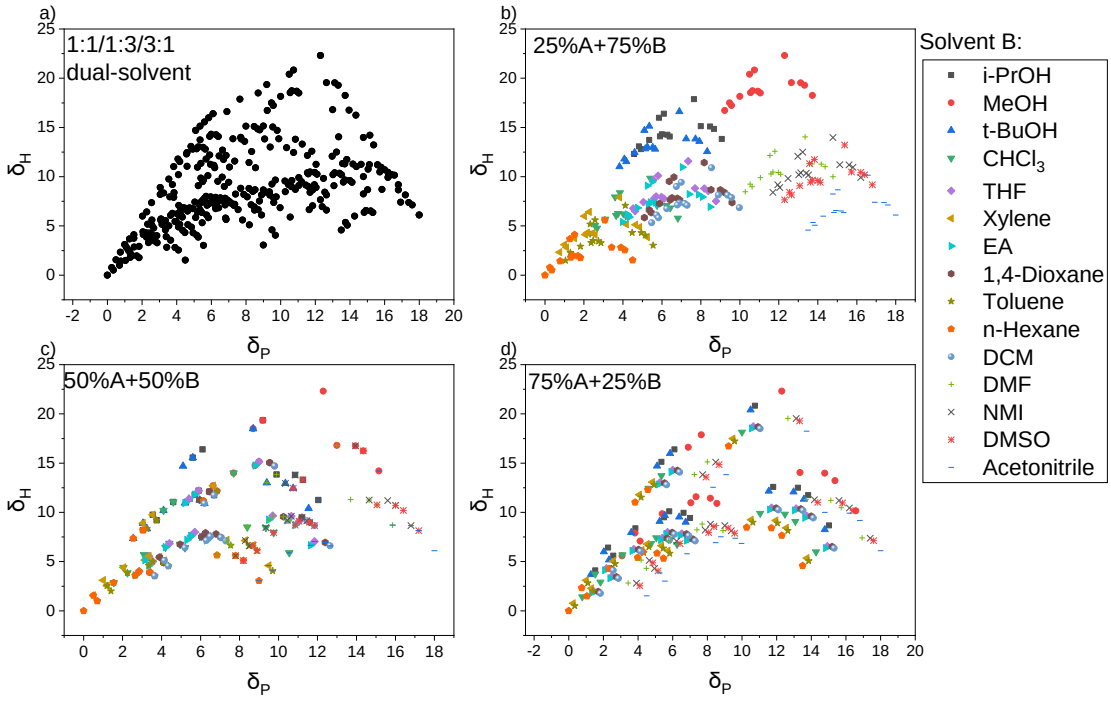

Figure 4-2 δ_P, δ_H of dual-solvent system with 1:1/1:3/3:1 volume ratio. a) All the possible combinations. b) 25%A+75%B. c) 50%A+50%B. b) 75%A+25%B.

After each PDI has been individually studied, they will be compared, in parallel, with each other and be used to generate HSP guide rules for co-polymerization studies.

For co-polymerization investigations, HSPs of each PDI will be individually calculated. The similarity between their HSP will be compared to their co-polymerization performance, and used to optimize and tune conditions to achieve controllable co-polymerization.

4.2. Modelling

The next step for modelling is to first complete the monomeric **TANI-PDI** study. Once the experimental results are obtained, suitable optimization methods for **TANI-PDI** will be determined.

In addition to completing the outstanding computational work, studies into multi-molecular behaviour of PDI derivatives would provide new insights into the formation of supramolecular polymers. Preliminary investigations can be performed with two or three layers of monomers to visualize their molecular orbitals and aggregation mode. Once the appropriate models are developed, a model for predictable self-assembly behaviour of PDI derivatives based on HSPs would be an appropriate goal. Calculations to obtain such a model can be supported with machine learning, whose training set would be built up with HSP-dependent self-assembly behaviour of a series of PDI derivatives.

4.3. Exploration of new functional PDI supramolecular polymers

Once the rules for controlling self-assembly behaviour are found, it is worthwhile to further explore functions of supramolecular polymers and design new functional supramolecular polymers. The immediately desired functions include controllable conductivities, photovoltaics responses and bio-responses. In addition to behaviour in the solution state, the solid-state behaviour can also be investigated to develop potential applications of the resulting materials.

Based on the controllable conductivities of **Ph/NH$_2$-TANI** mentioned in Section 1.3, the next step for designing functional PDI supramolecular polymers can be first focused on the effect of the doped mode of **Ph/NH$_2$-TANI** side chains (ES state), evaluating the controllable conductivities of **TANI-PDI**. During the doping process, various acids can be applied to compare the effect of counterions, and explore the influence of degree of polymerisation of the supramolecular polymeric scaffold on conductivity.

Regarding controllable photovoltaics materials, there are two potential directions for further research, 1) building up the relationship between morphologies of supramolecular polymers and their photovoltaics performance; and 2) combining PDI (n-type semi-conductor) with various p-type semi-conducting materials to construct photovoltaics devices and explore the suitable combinations. As mentioned in Section 1.2.3, modifications can be extended to the *ortho* positions of PDIs to tune the optical band gap whilst maintaining the planar structure of the perylene core, which enables controlling both the self-assembly behaviour and the optical band gap. For 1-D materials, like fibres based on homo-polymer or co-polymer of PDI derivatives, the electronic response can be characterized by AFM.[181] Photo-responsive behaviour can be investigated by testing current-voltage curve under a standard solar light

source (AM 1.5G).[182] Potential photovoltaics device, e.g., tandem solar cell device, can be built up by casting PDI-containing material to substrate coated by conductive layer and hole transport layer, e.g., in Meena et al.'s work, is Indium tin oxide (ITO) /Poly(3,4-ethylenedioxythiophene):poly(styrenesulfonate) (PEDOT: PSS).[182] The performance of photovoltaics device including open circuit voltage, short circuit current, power conversion efficiency, fill factor, etc., which worth to be further investigated to develop the application of PDI derivatives.

The application of PDI derivatives in controllable bio-responsive materials, e.g., as a selective antibacterial coating, is also a promising topic for future study, of which the key mechanism is based on the photothermal behaviour of PDI in its anionic radical state triggered by different reductivity of bacteria.[183] Hereby the reductivity of bacteria can be distinguished by their anaerobicity, i.e., the reductivity of anaerobic bacteria is better than which of aerobic bacteria,[183] whilst the formation of PDI anionic radicals is preferred in more reductive environment,[184] suggesting a potential opportunity to design selective antibacterial materials based on the anaerobicity of various bacteria species. Two requirements that need to be focused on are 1) the formation of stable PDI anionic radicals, which is counteracted by π-π stacking; 2) controllable antibacterial performance, and to realise which PDI (with its end-capped groups exhibiting non-selective bio-toxicity) should be avoided. To meet both ends, Yang et al. previously introduced a bio-compatible guest molecule (cucurbit[7]uril) to the end-capped groups of PDI substituent.[183] Inspired by this strategy, more host–guest complexes based on PDI and biocompatible guest molecules can be further designed in the future work. The efficiency, selectivity, stability and reversibility can specifically be explored.

5. Reference

1 K. Kim and K. D. Jordan, *J. Phys. Chem.*, 1994, **98**, 10089–10094.

2 P. J. Stephens, F. J. Devlin, C. F. Chabalowski and M. J. Frisch, *J. Phys. Chem.*, 1994, **98**, 11623–11627.

3 A. D. Becke, *J. Chem. Phys.*, 1993, **98**, 1372–1377.

4 W. B. Penzes, *Time Line for the Definition of the Meter*, 1889.

5 T. Yanai, D. P. Tew and N. C. Handy, *Chem. Phys. Lett.*, 2004, **393**, 51–57.

6 National Institute of Standards and Technology (NIST), Electron Volt, https://physics.nist.gov/cgi-bin/cuu/Value?evj.

7 National Institute of Standards and Technology (NIST), Planck constant, https://physics.nist.gov/cgi-bin/cuu/Value?h.

8 L. Brunsveld, B. J. B. Folmer, E. W. Meijer and R. P. Sijbesma, *Chem. Rev.*, 2001, **101**, 4071–4097.

9 M. Hartlieb, E. D. H. Mansfield and S. Perrier, *Polym. Chem.*, 2020, **11**, 1083–1110.

10 R. P. Sijbesma, F. H. Beijer, L. Brunsveld, B. J. B. Folmer, J. H. K. K. Hirschberg, R. F. M. Lange, J. K. L. Lowe and E. W. Meijer, *Science (80-.).*, 1997, **278**, 1601–1604.

11 X. Li, Y. Kuang, J. Shi, Y. Gao, H. C. Lin and B. Xu, *J. Am. Chem. Soc.*, 2011, **133**, 17513–17518.

12 L. R. Hart, S. Li, C. Sturgess, R. Wildman, J. R. Jones and W. Hayes, *ACS Appl. Mater. Interfaces*, 2016, **8**, 3115–3122.

13 X. Y. Hu, X. Liu, W. Zhang, S. Qin, C. Yao, Y. Li, D. Cao, L. Peng and L. Wang, *Chem. Mater.*, 2016, **28**, 3778–3788.

14 B. Gole, S. Shanmugaraju, A. K. Bar and P. S. Mukherjee, *Chem. Commun.*, 2011, **47**, 10046–10048.

15 J. Zhang, K. Zhang, X. Huang, W. Cai, C. Zhou, S. Liu, F. Huang and Y. Cao, *J. Mater. Chem.*, 2012, **22**, 12759–12766.

16 G. C. Pimentel and A. L. Mcclellan, *Annu. Rev. Phys. Chem.*

17 F. Lerouge, G. Cerveau and R. J. P. Corriu, *New J. Chem.*, 2006, **30**, 1364–1376.

18 D. W. Oxtoby, H. P. Gills, A. Campion, H. H. Helal and K. P. Gaither, *Principles of Modern Chemistry*, Brooks/Cole Cengage Learning, Belmont, 7th edn., 2012.

19 E. Elacqua, D. S. Lye and M. Weck, *Acc. Chem. Res.*, 2014, **47**, 2405–2416.

20 C. Rest, R. Kandanelli and G. Fernández, *Chem. Soc. Rev.*, 2015, **44**, 2543–2572.

21 G. A. Jeffrey and W. Saenger, *Hydrogen bonding in biological structures*, Springer Science & Business Media, 1994.

22 H. M. Sobell, *J. Mol. Biol.*, 1966, **18**, 1–7.

23 T. Steiner, *Angew. Chemie - Int. Ed.*, 2002, **41**, 48–76.

24 G. R. Desiraju and T. Steiner, *The weak hydrogen bond: in structural chemistry and biology*, International Union of Crystal, 2001.

25 P. Gilli, V. Bertolasi, V. Ferretti and G. Gilli, *J. Am. Chem. Soc.*, 1994, **116**, 909–915.

26 J. C. Ma and D. A. Dougherty, *Chem. Rev.*, 1997, **97**, 1303–1324.

27 M. Levitt and M. F. Perutz, *J. Mol. Biol.*, 1988, **201**, 751–754.

28 H. Road, *Philos. Trans. R. Soc. London. Ser. A Phys. Eng. Sci.*, 1993, **345**, 105–112.

29 D. A. Dougherty, *Science (80-.).*, 1996, **271**, 163–168.

30 S. Ogi, V. Stepanenko, K. Sugiyasu, M. Takeuchi and F. Würthner, *J. Am. Chem. Soc.*, 2015, **137**, 3300–3307.

31 J. L. Wood, *Biochem. J.*, 1974, **143**, 775–777.

32 L. Weng, C. Chen, J. Zuo and W. Li, *J. Phys. Chem. A*, 2011, **115**, 4729–4737.

33 T. F. A. De Greef, M. M. J. Smulders, M. Wolffs, A. P. H. J. Schenning, R. P. Sijbesma, E. W. Meijer and C. Counterpart, *Chem. Rev.*, 2009, **109**, 5687–5754.

34 S. E. Wheeler and K. N. Houk, *J. Am. Chem. Soc.*, 2008, **130**, 10854–10855.

35 A. D. Buckingham, *Q. Rev. Chem. Soc.*

36 M. R. Battaglia, A. D. Buckingham and J. H. Williams, *Chem. Phys. Lett.*, 1981, **78**, 421–423.

37 T. Chemistry, *Proc. R. Soc. London. A. Math. Phys. Sci.*, 1975, **341**, 429–449.

38 M. O. Sinnokrot, E. F. Valeev and C. D. Sherrill, *J. Am. Chem. Soc.*, 2002, **124**, 10887–10893.

39 J. Vrbancich and G. L. D. Ritchie, *J. Chem. Soc. Faraday Trans. 2 Mol. Chem. Phys.*, 1980, **76**, 648–659.

40 M. D. Levenson and A. L. Schawlow, *Opt. Commun.*, 1970, **2**, 192–196.

41 A. K. M. Masood, A. M. North, R. A. Pethrick, M. Towland and F. L. Swinton, *J. Chem.*

Thermodyn., 1977, **9**, 133–137.

42 J. F. Maddaluno, N. Gresh and C. Giessner-Prettre, *J. Org. Chem.*, 1994, **59**, 793–802.

43 R. D. Costa, E. Ortí, H. J. Bolink, S. Graber, C. E. Housecroft and E. C. Constable, *J. Am. Chem. Soc.*, 2010, **132**, 5978–5980.

44 A. Arnaud, J. Belleney, F. Boué, L. Bouteiller, G. Carrot and V. Wintgens, *Angew. Chemie - Int. Ed.*, 2004, **43**, 1718–1721.

45 1913, DE 276357.

46 E. M. García-Frutos and B. Gómez-Lor, *J. Am. Chem. Soc.*, 2008, **130**, 9173–9177.

47 D. J. Cram and J. M. Cram, *Science (80-.).*, 1974, **183**, 803–809.

48 E. Seyrek and G. Decher, in *Polymer Science: A Comprehensive Reference*, eds. K. Matyjaszewski and M. B. T.-P. S. A. C. R. Möller, Elsevier, Amsterdam, 2012, pp. 159–185.

49 Y. W. Yang, Y. L. Sun and N. Song, *Acc. Chem. Res.*, 2014, **47**, 1950–1960.

50 Y. L. Sun, Y. W. Yang, D. X. Chen, G. Wang, Y. Zhou, C. Y. Wang and J. F. Stoddart, *Small*, 2013, **9**, 3224–3229.

51 Y. L. Sun, Y. Zhou, Q. L. Li and Y. W. Yang, *Chem. Commun.*, 2013, **49**, 9033–9035.

52 H. Cai, Y. L. Huang and D. Li, *Coord. Chem. Rev.*, 2019, **378**, 207–221.

53 Y. L. Sun, B. J. Yang, S. X. A. Zhang and Y. W. Yang, *Chem. - A Eur. J.*, 2012, **18**, 9212–9216.

54 A. Jayaraman, V. Balasubramaniam and S. Valiyaveettil, *Cryst. Growth Des.*, 2006, **6**, 636–642.

55 B. Q. Ma, H. L. Sun and S. Gao, *Angew. Chemie - Int. Ed.*, 2004, **43**, 1374–1376.

56 J. W. Steed, *Chem. Commun.*, 2011, **47**, 1379–1383.

57 L. Zang, Y. Che and J. S. Moore, *Acc. Chem. Res.*, 2008, **41**, 1596–1608.

58 A. Shrivastava, in *Plastics Design Library*, ed. A. B. T.-I. to P. E. Shrivastava, William Andrew Publishing, 2018, pp. 17–48.

59 R. B. Martin, *Chem. Rev.*, 1996, **96**, 3043–3063.

60 E. H. Braswell, *J. Phys. Chem.*, 1984, **88**, 3653–3658.

61 J. Gajewska and K. Bolewska, *Biophys. Chem.*

62 J. R. Henderson, *Phys. Rev. E - Stat. Physics, Plasmas, Fluids, Relat. Interdiscip. Top.*, 1997, **55**, 5731–5742.

63 A. J. Kirby, eds. V. Gold and D. B. T.-A. in P. O. C. Bethell, Academic Press, 1980, vol. 17, pp. 183–278.

64 G. Ercolani, L. Mandolini, P. Mencarelli and S. Roelens, *J. Am. Chem. Soc.*, 1993, **115**, 3901–3908.

65 H. Jacobson and W. H. Stockmayer, *J. Chem. Phys.*, 1950, **18**, 1600–1606.

66 M. A. Winnik, *Chem. Rev.*, 1981, **81**, 491–524.

67 A. V. Tobolsky and A. Eisenberg, *J. Colloid Sci.*, 1962, **17**, 49–65.

68 F. S. Dainton and K. J. Ivin, *Q. Rev. Chem. Soc.*, 1958, **12**, 61–92.

69 C. C. Chen and E. E. Dormidontova, *Macromolecules*, 2004, **37**, 3905–3917.

70 E. T. Powers and D. L. Powers, *Biophys. J.*, 2006, **91**, 122–132.

71 F. Ferrone and W. Ronald, *Analysis of protein aggregation kinetics. In Methods of Enzymology*, Academic Press, New York, 1999.

72 C. Frieden, *Protein Sci.*, 2007, **16**, 2334–2344.

73 L. R. De Young, A. L. Fink and K. A. Dill, *Acc. Chem. Res.*, 1993, **26**, 614–620.

74 P. Mukerjee, K. J. Mysels and P. Kapauan, *J. Phys. Chem.*, 1967, **71**, 4166–4175.

75 C. Tanford, *J. Phys. Chem.*, 1974, **78**, 2469–2479.

76 P. Mukerjee, *J. Phys. Chem.*, 1969, **73**, 2054–2056.

77 C. Li and H. Wonneberger, *Adv. Mater.*, 2012, **24**, 613–636.

78 A. Wicklein, A. Lang, M. Muth and M. Thelakkat, *J. Am. Chem. Soc.*, 2009, **131**, 14442–14453.

79 H. Langhals, *Heterocycles*, 1995, **40**, 477–500.

80 M. Yamauchi and S. Masuo, *Chem. - A Eur. J.*, 2019, **25**, 167–172.

81 L. Yang, P. Langer, E. S. Davies, M. Baldoni, K. Wickham, N. A. Besley, E. Besley and N. R. Champness, *Chem. Sci.*, 2019, **10**, 3723–3732.

82 C. Roche, H. J. Sun, P. Leowanawat, F. Araoka, B. E. Partridge, M. Peterca, D. A. Wilson, M. E. Prendergast, P. A. Heiney, R. Graf, H. W. Spiess, X. Zeng, G. Ungar and V. Percec, *Nat. Chem.*, 2016, **8**, 80–89.

83 Z. Wang, K. Liu, X. Chang, Y. Qi, C. Shang, T. Liu, J. Liu, L. Ding and Y. Fang, *ACS Appl. Mater. Interfaces*, 2018, **10**, 35647–35655.

84 D. Wei, L. Ge, Z. Wang, Y. Wang and R. Guo, *Langmuir*, 2019, **35**, 11745–11754.

85 J. Clayden, N. Greeves and S. Warren, *Organic Chemistry*, Oxford, 2nd edn., 2012.

86 S. Chen, P. Slattum, C. Wang and L. Zang, *Chem. Rev.*, 2015, **115**, 11967–11998.

87 C. Huang, S. Barlow and S. R. Marder, *J. Org. Chem.*, 2011, **76**, 2386–2407.

88 W. Herbst and K. Hunger, *Industrial Organic Pigments: Production, Properties, Applications*, Wiley, 3rd edn., 2006.

89 1998.

90 S. Nakazono, Y. Imazaki, H. Yoo, J. Yang, T. Sasamori, N. Tokitoh, T. Cédric, H. Kageyama, D. Kim, H. Shinokubo and A. Osuka, *Chem. - A Eur. J.*, 2009, **15**, 7530–7533.

91 S. Nakazono, S. Easwaramoorthi, D. Kim, H. Shinokubo and A. Osuka, *Org. Lett.*, 2009, **11**, 5426–5429.

92 F. F. So, S. R. Forrest, Y. Q. Shi and W. H. Steier, *Appl. Phys. Lett.*, 1990, **56**, 674–676.

93 V. Bulović, P. E. Burrows, S. R. Forrest, J. A. Cronin and M. E. Thompson, *Chem. Phys.*, 1996, **210**, 1–12.

94 R. Gvishi, R. Reisfeld and Z. Burshtein, *Chem. Phys. Lett.*, 1993, **213**, 338–344.

95 J. R. Ostrick, A. Dodabalapur, L. Torsi, A. J. Lovinger, E. W. Kwock, T. M. Miller, M. Galvin, M. Berggren and H. E. Katz, *J. Appl. Phys.*, 1997, **81**, 6804–6808.

96 X. Zhan, A. Facchetti, S. Barlow, T. J. Marks, M. A. Ratner, M. R. Wasielewski and S. R. Marder, *Adv. Mater.*, 2011, **23**, 268–284.

97 R. J. Chesterfield, J. C. McKeen, C. R. Newman, P. C. Ewbank, D. A. Da Silva Filho, J. L. Brédas, L. L. Miller, K. R. Mann and C. D. Frisbie, *J. Phys. Chem. B*, 2004, **108**, 19281–19292.

98 M. Pandey, G. M. Joshi, K. Deshmukh, N. Nath Ghosh and N. A. Nambi Raj, *J. Phys. Chem. Solids*, 2015, **80**, 52–61.

99 V. Bulović and S. R. Forrest, *Chem. Phys. Lett.*, 1995, **238**, 88–92.

100 S. R. Forrest, *Very High Efficiency Photovoltaic Cells Based on Fully Organic Multiple Quantum Wells Final Report*, 1997.

101 E. Rogel, *Langmuir*, 2002, **18**, 1928–1937.

102 Z. Chen, U. Baumeister, C. Tschierske and F. Würthner, *Chem. - A Eur. J.*, 2007, **13**, 450–465.

103 F. Würthner, V. Stepanenko, Z. Chen, C. R. Saha-Möller, N. Kocher and D. Stalke, *J.*

Org. Chem., 2004, **69**, 7933–7939.

104 M. Sadrai, L. Hadel, R. R. Sauers, S. Husain, K. Krogh-Jespersen, J. D. Westbrook and G. R. Bird, *J. Phys. Chem.*, 1992, **96**, 7988–7996.

105 G. Horowitz, *Adv. Mater.*, 1998, **10**, 365–377.

106 P. E. Hartnett, E. A. Margulies, H. S. S. R. Matte, M. C. Hersam, T. J. Marks and M. R. Wasielewski, *Chem. Mater.*, 2016, **28**, 3928–3936.

107 A. D. McNaught and A. Wilkinson, *IUPAC. Compendium of Chemical Terminology*, Blackwell Scientific Publications, Oxford, 2nd edn., 1997.

108 C. Jarrett-Wilkins, X. He, H. E. Symons, R. L. Harniman, C. F. J. Faul and I. Manners, *Chem. - A Eur. J.*, 2018, **24**, 15556–15565.

109 X. Zhang, Z. Chen and F. Würthner, *J. Am. Chem. Soc.*, 2007, **129**, 4886–4887.

110 R. Liu, M. W. Holman, L. Zhang and D. M. Adams, *J. Phys. Chem. A*, 2003, **107**, 6522–6526.

111 R. M. Metzger, *J. Mater. Chem.*, 2008, **18**, 4364–4396.

112 J. M. Mativetsky, M. Kastler, R. C. Savage, D. Gentilini, M. Palma, W. Pisula, K. Müllen and P. Samorì, *Adv. Funct. Mater.*, 2009, **19**, 2486–2494.

113 L. F. Dössel, V. Kamm, I. A. Howard, F. Laquai, W. Pisula, X. Feng, C. Li, M. Takase, T. Kudernac, S. De Feyter and K. Müllen, *J. Am. Chem. Soc.*, 2012, **134**, 5876–5886.

114 H. C. Hesse, J. Weickert, M. Al-Hussein, L. Dössel, X. Feng, K. Müllen and L. Schmidt-Mende, *Sol. Energy Mater. Sol. Cells*, 2010, **94**, 560–567.

115 Z. Chen, A. Lohr, C. R. Saha-Möller and F. Würthner, *Chem. Soc. Rev.*, 2009, **38**, 564–584.

116 W. Wang, J. J. Han, L. Q. Wang, L. S. Li, W. J. Shaw and A. D. Q. Li, *Nano Lett.*, 2003, **3**, 455–458.

117 S. Ghosh, X. Q. Li, V. Stepanenko and F. Würthner, *Chem. - A Eur. J.*, 2008, **14**, 11343–11357.

118 B. Jancy and S. K. Asha, *Chem. Mater.*, 2008, **20**, 169–181.

119 X. Yang, X. Xu and H. F. Ji, *J. Phys. Chem. B*, 2008, **112**, 7196–7202.

120 M. H. Hennessy, Z. G. Soos, R. A. Pascal and A. Girlando, *Chem. Phys.*, 1999, **245**, 199–212.

121 S. L. Yefimova, G. V. Grygorova, V. K. Klochkov, I. A. Borovoy, A. V. Sorokin and Y.

V. Malyukin, *J. Phys. Chem. C*, 2018, **122**, 20996–21003.

122 E. E. Whiting, A. Schadee, J. B. Tatum, J. T. Hougen and R. W. Nicholls, *J. Mol. Spectrosc.*, 1980, **80**, 249–256.

123 K. Tyagi, Ed., in *Engineering Chemistry*, University Science Press, 2013, p. 89.

124 F. C. Spano and C. Silva, *Annu. Rev. Phys. Chem.*, 2014, **65**, 477–500.

125 T. Canteenwala, V. Anantharaj, S. V. Patil and L. Y. Chiang, *J. Macromol. Sci. Part A Pure Appl. Chem.*, 2002, **39**, 1069–1083.

126 A. G. MacDiarmid, S. K. Manohar, J. G. Masters, Y. Sun, H. Weiss and A. J. Epstein, *Synth. Met.*, 1991, **41**, 621–626.

127 J. Libert, J. Cornil, D. dos Santos and J. Brédas, *Phys. Rev. B - Condens. Matter Mater. Phys.*, 1997, **56**, 8638–8650.

128 A. G. Macdiarmid, J. C. Chiang, A. F. Richter and A. J. Epstein, *Synth. Met.*, 1987, **18**, 285–290.

129 J. L. Bredas and R. Silbey, Eds., *Conjugated polymers: the novel science and technology of highly conducting and nonlinear optically active materials*, Springer Science & Business Media, 2012.

130 J. Y. Shimano and A. G. MacDiarmid, *Synth. Met.*, 2001, **123**, 251–262.

131 V. Egan, R. Bernstein, L. Hohmann, T. Tran and R. B. Kaner, *Chem. Commun.*, 2001, 801–802.

132 A. J. Heeger, *Synth. Met.*, 1993, **57**, 3471–3482.

133 O. Kwon and M. L. McKee, *J. Phys. Chem. B*, 2000, **104**, 1686–1694.

134 Y. Cao, P. Smith and A. J. Heeger, *Synth. Met.*, 1989, **32**, 263–281.

135 R. P. McCall, J. M. Ginder, J. M. Leng, H. J. Ye, S. K. Manohar, J. G. Masters, G. E. Asturias, A. G. MacDiarmid and A. J. Epstein, *Phys. Rev. B*, 1990, **41**, 5202–5213.

136 J. A. Osaheni, S. A. Jenekhe, H. Vanherzeele, J. S. Meth, Y. Sun and A. G. MacDiarmid, *J. Phys. Chem.*, 1992, **96**, 2830–2836.

137 J. Ashkenazi, W. E. Pickett, H. Krakauer, C. S. Wang, B. M. Klein and S. R. Chubb, *Phys. Rev. Lett.*, 1989, **62**, 2016–2019.

138 W. P. Su, J. R. Schrieffer and A. J. Heeger, *Phys. Rev. Lett.*, 1979, **42**, 1698–1701.

139 Y. Cao, *Synth. Met.*, 1990, **35**, 319–332.

140 S. Stafström, J. L. Brédas, A. J. Epstein, H. S. Woo, D. B. Tanner, W. S. Huang and A.

G. MacDiarmid, *Phys. Rev. Lett.*, 1987, **59**, 1464–1467.

141 Z. Wei and C. F. J. Faul, *Macromol. Rapid Commun.*, 2008, **29**, 280–292.

142 K. Lee, S. Cho, H. P. Sung, A. J. Heeger, C. W. Lee and S. H. Lee, *Nature*, 2006, **441**, 65–68.

143 Y. Cao, P. Smith and A. J. Heeger, *Synth. Met.*, 1992, **48**, 91–97.

144 M. Reghu, Y. Cao, D. Moses and A. J. Heeger, *Phys. Rev. B*, 1993, **47**, 1758–1764.

145 Z. H. Wang, C. Li, E. M. Scherr, A. G. MacDiarmid and A. J. Epstein, *Phys. Rev. Lett.*, 1991, **66**, 1745–1748.

146 B. J. S. Miller, *Adv. Mater.*, 1993, 671–676.

147 G. Gustafsson, Y. Cao, G. M. Treacy, F. Klavetter, N. Colaneri and A. J. Heeger, *Nature*, 1992, **357**, 477–479.

148 H. Guo, C. M. Knobler and R. B. Kaner, *Synth. Met.*, 1999, **101**, 44–47.

149 M. R. Anderson, B. R. Mattes, H. Reiss and R. B. Kaner, *Science (80-.).*, 1991, **252**, 1412–1415.

150 P. Humpolicek, V. Kasparkova, P. Saha and J. Stejskal, *Synth. Met.*, 2012, **162**, 722–727.

151 J. Stejskal, M. Hajná, V. Kašpárková, P. Humpolíček, A. Zhigunov and M. Trchová, *Synth. Met.*, 2014, **195**, 286–293.

152 C. M. Hansen, *Hansen solubility parameters: a user's handbook*, CRC press, 2nd edn., 2007.

153 National Institute of Standards and Technology (NIST), Molar gas constant, https://physics.nist.gov/cgi-bin/cuu/Value?r.

154 D. W. Van Krevelen and K. Te Nijenhuis, *Cohesive Properties and Solubility*, 2009, vol. i.

155 S. Abbott, HSP Basics, https://www.stevenabbott.co.uk/practical-solubility/hsp-basics.php.

156 J. Chen, W. Yan, E. J. Townsend, J. Feng, L. Pan, V. Del Angel Hernandez and C. F. J. Faul, *Angew. Chemie - Int. Ed.*, 2019, **58**, 11715–11719.

157 D. S. Surry and S. L. Buchwald, *Chem. Sci.*, 2011, **2**, 27–50.

158 H. Rafii, S. Chalon, J. E. Ombetta, Y. Frangin, L. Garreau, A. M. Dognon, I. Lena, S. Bodard, M. P. Vilar, J. C. Besnard and D. Guilloteau, *Nucl. Med. Biol.*, 1995, **22**, 617–

623.

159 Y. Hu, B. T. Miles, Y. L. D. Ho, M. P. C. Taverne, L. Chen, H. Gersen, J. G. Rarity and C. F. J. Faul, *Adv. Opt. Mater.*, , DOI:10.1002/adom.201600458.

160 J. Wang, Y. L. Liang and J. Qu, *Chem. Commun.*, 2009, 5144–5146.

161 X. Huang, K. W. Anderson, D. Zim, L. Jiang, A. Klapars and S. L. Buchwald, *J. Am. Chem. Soc.*, 2003, **125**, 6653–6655.

162 International Programme on Chemical Safety (IPCS), tert-BUTANOL, http://www.inchem.org/documents/icsc/icsc/eics0114.htm.

163 S. Abbott, *Solubility Science : Principles and Practice*, 1.0.1.3., 2017.

164 P. T. Ruhoff and M. A. Ratner, *Introd. to Phys. Chem.*, 2000, **77**, 383–392.

165 T. a Halgren, *J. Comput. Chem.*, 1996, **17**, 490–519.

166 J. J. P. Stewart, *J. Mol. Model.*, 2007, **13**, 1173–1213.

167 I. Tubert-Brohman, C. R. W. Guimarães, M. P. Repasky and W. L. Jorgensen, *J. Comput. Chem.*, 2004, **25**, 138–150.

168 J. Tirado-Rives and W. L. Jorgensen, *J. Chem. Theory Comput.*, 2008, **4**, 297–306.

169 K. W. Sattelmeyer, J. Tirado-Rives and W. L. Jorgensen, *J. Phys. Chem. A*, 2006, **110**, 13551–13559.

170 A. D. Becke, *J. Chem. Phys.*, 1993, **98**, 5648–5652.

171 M. Ernzerhof and G. E. Scuseria, *J. Chem. Phys.*, 1999, **110**, 5029–5036.

172 R. Ditchfield, W. J. Hehre and J. A. Pople, *J. Chem. Phys.*, 1971, **54**, 720–723.

173 W. J. Hehre, R. Ditchfield and J. A. Pople, *J.Chem. Phys.*, 1972, **56**, 2257–2261.

174 M. M. Francl, W. J. Pietro, W. J. Hehre, J. S. Binkley, M. S. Gordon, D. J. DeFrees and J. A. Pople, *J. Chem. Phys.*, 1982, **77**, 3654–3665.

175 T. Clark, J. Chandrasekhar, G. W. Spitznagel and P. V. R. Schleyer, *J. Comput. Chem.*, 1983, **4**, 294–301.

176 M. J. Frisch, J. A. Pople and J. S. Binkley, *J. Chem. Phys.*, 1984, **80**, 3265–3269.

177 W. Kohn and L. J. Sham, *Phys. Rev.*, 1965, **140**, A1133–A1138.

178 J. A. Pople, P. M. W. Gill and B. G. Johnson, *Chem. Phys. Lett.*, 1992, **199**, 557–560.

179 C. C. J. Roothaan, *Rev. Mod. Phys.*, 1951, **23**, 69–89.

180 J. B. Foresman, T. A. Keith, K. B. Wiberg, J. Snoonian and M. J. Frisch, *J. Phys. Chem.*,

1996, **100**, 16098–16104.

181 C. Hermosa, J. Vicente Álvarez, M. R. Azani, C. J. Gómez-García, M. Fritz, J. M. Soler, J. Gómez-Herrero, C. Gómez-Navarro and F. Zamora, *Nat. Commun.*, 2013, **4**, 1–6.

182 S. Meena, T. Mohammad, V. Dutta and J. Jacob, *RSC Adv.*, 2018, **8**, 30468–30480.

183 Y. Yang, P. He, Y. Wang, H. Bai, S. Wang, J.-F. Xu and X. Zhang, *Angew. Chemie*, 2017, **129**, 16457–16460.

184 R. O. Marcon and S. Brochsztain, *J. Phys. Chem. A*, 2009, **113**, 1747–1752.

185 A. Weißenstein and F. Würthner, *Chem. Commun.*, 2015, **51**, 3415–3418.

6. Experimental

All the details of chemicals, instruments and software applied in this project were appended in Table 7-1, Table 7-2, Table 7-3.

6.1. Synthesis

6.1.1. Synthesis of N-2(aminoethyl)-4-bromobenzoamide (BA-1)

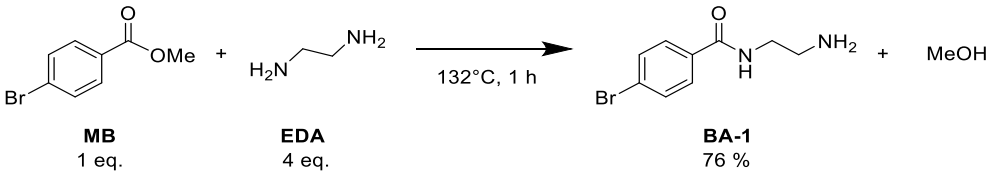

*Scheme 6-1 Synthesis of **BA-1.***

At room temperature, 23.25 mmol (5 g, 1 eq.) methyl-4-bromobenzoate (**MB**, 215.04 g/mol) was added to a dry, 250 mL multi-neck round-bottom flask, followed with 40 mmol (6.6 mL, 4 eq.) ethylenediamine (**EDA**, 60.10 g/mol, 0.899 g/mL at 25 °C) slowly added. The condenser was applied to the flask, with condensing water on. Protected by nitrogen, in the Schlenk line, the mixture was refluxed at 132 °C for 1 hour.[158] The reaction mixture was cooled to room temperature with condenser running. 50 mL toluene (each time) was added to the reaction mixture and sonicated for 1 hour. The solvent was removed by rotary evaporator after pH was tested. The toluene washing step was repeated 3 times until reaching neutral pH. 5 mL 5 M NaOH (50 mmol, each time) was added to the residue and sonicated for 20 minutes at room temperature. **BA-1** was extracted by chloroform and separated by separatory funnel, followed by drying with anhydrous magnesium sulfate ($MgSO_4$). Chloroform was removed through rotary evaporation, getting the yellow solid product **BA-1** (M.W. 243.10 g/mol, yield 76%). The component of **BA-1** was confirmed by ^{1}H NMR (Figure 7-1) and ESI (m/z: calculated, 242.01; found, 242.0).

^{1}H NMR (400 MHz, Deuterium Oxide) δ 7.71 (d, J = 1.6 Hz, 2H), 7.70 (d, J = 0.4 Hz, 2H), 3.50 (t, J = 6.2 Hz, 2H), 2.90 (t, J = 6.2 Hz, 2H).

Previous trails

Before the optimized yield was obtained, the purification procedures were modified and the reaction time was extended from 0.5 hour to 1 hour, as listed in *Table 6-1*.

*Table 6-1 Conditions and yields of **BA-1** synthesis.*

Purification	EDA/MB (mmol/mmol)	Temp. (°C)	Time (h)	Yield %
(a)	4	132	0.5	2
(b)	4	132	0.5	19
(c)	4	132	0.5	71
(c)	4	132	1	76

In general, the key improvement of purification was to avoid contacting water and decrease filtration times as possible. The flowchart of three previous purification procedures were shown in *Scheme 6-2*.

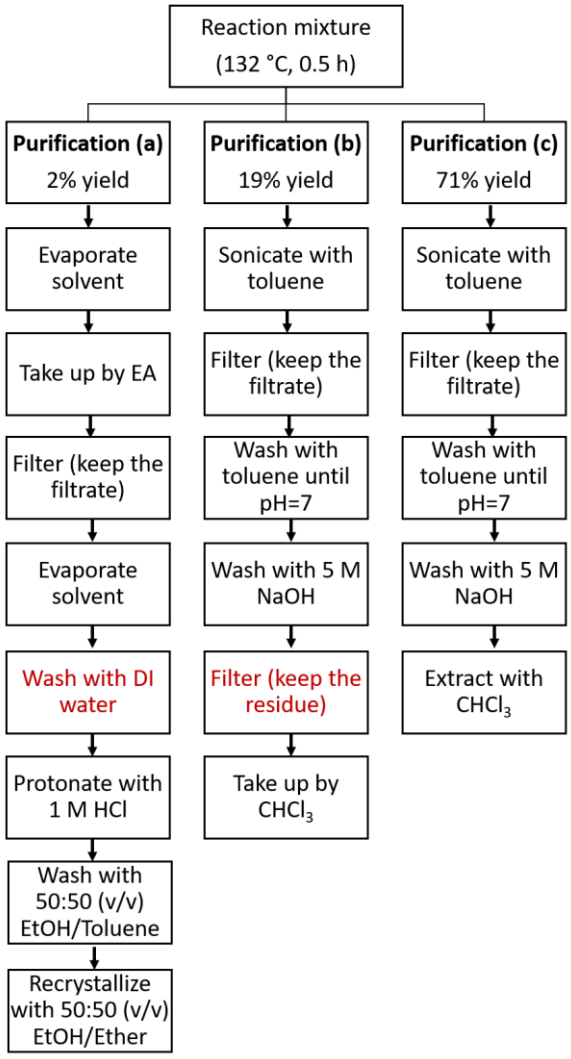

*Scheme 6-2 Purification flowchart applied after **BA-1** synthesis, where the major yield losing procedures are labelled in red.*

In purification (a), the reaction mixture was first taken up with 50 mL ethyl acetate (**EA**) and the filtrate was kept. The solvent was then removed, followed by its residue washed with 6 × 10 mL deionized (**DI**) water to remove the unreacted **EDA**. 10 mL 1 M HCl was added to protonate **BA-1**. The residue was washed with 2 × 100 mL 50:50 (v/v) ethanol/toluene and recrystallized by 50:50 ethanol/diethyl ether. Crude product was washed with 10 mL 1 M NaOH. However, only 2% yield was obtained through this pathway. The low yield was due to the hydrophilic property of **BA-1** caused by its amine end group, which led to great yield losing during the water washing process. Confirmed by solubility tests, **BA-1** dissolved well in DI water. As a result, purification (b) was designed to use as less water in the purification process as possible.

In purification (b), the reaction mixture was first transferred to toluene followed by fully sonication for 1 hour and filtration. After removing the solvent, the residue was washed by 50 mL toluene repeatedly until the pH went to neutral, which suggested the **EDA** had been completely removed. 5 mL 5 M NaOH was then added to remove the unreacted **MB**, which converted the ester to sodium salt. The product was obtained by filtration, whose residue was taken by chloroform sonication, followed by the removal of solvent. This method increased the yield to 19%. However, the filtration process after base washing had caused the residue stuck to the filter paper. The base was attempted to be removed by sparse amount of water, but it caused **BA-1** to be dissolved by water and mixed with the aqueous phase, which met the same problem in purification (a).

In purification (c), the last filtration process in purification (b) was replaced by extraction by chloroform, leading to a 71% yield. This yield was further increased to 76% when the reaction time was increased from 0.5 to 1 hour.

6.1.2. Synthesis of PDI-BA-1

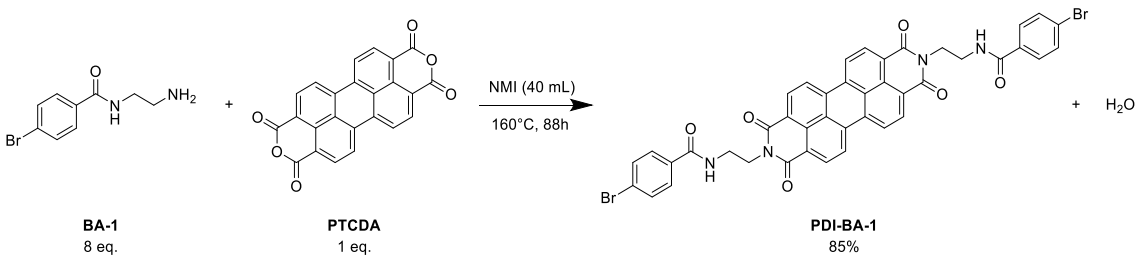

*Scheme 6-3 Synthesis of **PDI-BA-1**.*

At room temperature, 0.148 mmol (0.058 g, 1 eq.) perylene-3,4,9,10-tetracarboxylic dianhydride (**PTCDA**, 392.32 g/mol) and 1.184 mmol (0.288 g, 8 eq.) N-2(aminoethyl)-4-

bromobenzoate (**BA-1**, 243.10 g/mol) were added to a dry, 250 mL multi-neck round-bottom flask. 40 mL 1-Methylimidazole (NMI) (82.1 g/mol, 1.03 g/mL at 25 °C, b.p. 189 °C) was slowly added. Protected by nitrogen, the mixture was stirred at 160 °C for 88 h with condenser running, followed by cooling to the room temperature. After the reaction had completed, the container was placed in cold water bath. 100 mL 1 M hydrochloric acid was slowly added to the reaction mixture and stirred for 0.5 hour to protonate NMI. This step was found to be exothermic, so the addition of hydrochloric acid must be slow enough with fully stirring and protected with cold water bath. The crude product was extracted by chloroform, followed by separation with separatory funnel. The solvent was removed by rotary evaporation. The NMI protonation and separation steps were repeated 4 – 5 times until all the NMI had been removed. The crude product was purified by chromatography 95 : 4.5 : 0.5 (v/v/v) $CHCl_3$: MeOH : Et_3N. The solvent was removed through rotary evaporator, getting dark red solid **PDI-BA-1** (M.W. 842.50 g/mol, Yield 85%). ^1H NMR (400 MHz, DMSO-d_6) was attempted to characterize the product, but due to the poor solubility, the signals were too weak to be processed. MALDI: m/z: $[M+H]^+$ calculated, 841.12; found, 841.523. In the MALDI characterization, trans-2-[3-(4-tert-Butylphenyl)-2-methyl-2-propenylidene]malononitrile (**DCTB**) was applied as the matrix.

Previous trials

Before the optimized yield was obtained, the solvent, reaction conditions and purification processes were modified. In addition to higher temperature, enough reaction time and proper purification process, the yield of **PDI-BA-1** synthesis was also expected to be improved by 1) an excess of **BA-1**, which should be more than 2 eq. to promote the formation of di-substituted products, 2) well dispersion of **PTCDA** in the solvent, which required enough solubility of **PTCDA** in the applied solvent and enough amount of corresponding solvents.

Before NMI was applied as the solvent, N, N'-dimethylformamide (DMF) was also tested as the solvent (Scheme 6-4).[185] However, this route was not further applied due to the purification problem.

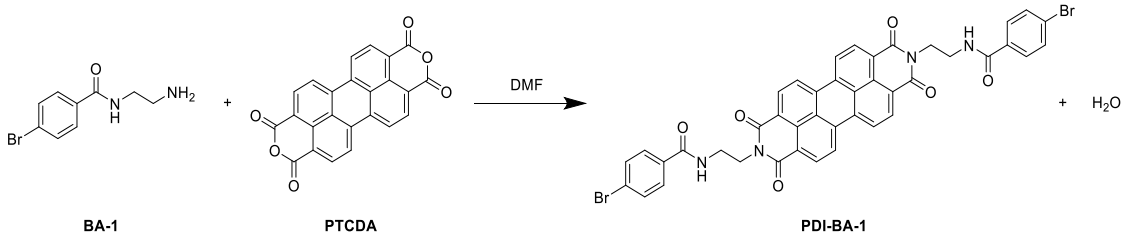

*Scheme 6-4 Synthesis of **PDI-BA-1** (with DMF).*

The reactants of synthesis in DMF were same as which in NMI (**BA-1** and **PTCDA**), whilst the stoichiometry, reaction time and purification process were modified. The detailed reaction conditions and yields were list in Table 6-2. After each reaction had completed, the reaction mixture was poured into DI water. The resulting precipitate was filtered and washed well with methanol, when DMF and **BA-1** were both removed. The crude product was purified by column chromatography with 95 : 4.5 : 0.5 (v/v/v) $CHCl_3$: MeOH : Et_3N.[185]

*Table 6-2 Conditions and yields of **PDI-BA-1** synthesis with DMF as the solvent.*

No.	PTCDA (mmol)	BA-1/PTCDA (mol/mol)	DMF/PTCDA (mL/mmol)	Temp. (°C)	Time (h)	Yield %
D-1	0.393	4	55	110	24	19
D-2	0.296	4	55	155	24	42
D-3	0.296	4	67	155	72	21
D-4	0.296	3	67	155	72	20
D-5	0.296	3	200	155	72	4

In the initial attempt (D-1), 0.393 mmol **PTCDA** (1 eq., 0.154 g) and 1.57 mmol **BA-1** (4 eq., 0.383 g) were reacted in 22 mL DMF (55 mL/mmol **PTCDA**) overnight at 110 °C (yield 19%) under the protection of nitrogen. The temperature was further increased to the boiling point of DMF (155 °C) with a smaller scale of **PTCDA** (0.296 mmol), resulting a 42% yield (D-2). In D-3, DMF was increased to 40 mL (67 mL/mmol **PTCDA)** with the reaction time extended to 3 days. The yield however decreased to 21%. With all the other conditions same as D-3, except stoichiometry of **BA-1/PTCDA** changed from 4 eq. to 3 eq. (D-4). A 20% yield was obtained, which indicated the limiting effect of decreasing the amount of **BA-1** from 4 eq. to 3 eq. When DMF was increased to 60 mL (200 mL/mmol **PTCDA)**, the yield dropped significantly to 4% (D-5), which confirmed that the increase of DMF caused the main yield losing. This phenomenon implicated the negative influence of adding DMF, which was opposite from the expectation, i.e., a system with more solvent will improve the dispersion extent and thus improve the yield.

Solubilities of **PDI-BA-1** in methanol and DMF were studied by UV-Vis to evaluate the purification process, which was suspected to cause the main yield losing. It was found that the solubility of **PDI-BA-1** in both DMF and methanol was good. As a result, the filtration

followed by methanol washing process potentially transferred **PDI-BA-1** from residue into aqueous phase, which caused the yield losing.

To optimize the purification process, the solvent was changed to NMI. The temperature was elevated to the boiling point of NMI (160 °C). Conditions and yields were listed in Table 6-3. After each reaction had completed, 100 mL 1 M HCl was slowly added to the reaction mixture to protonate NMI. The protonated NMI was miscible with aqueous phase, which can be removed by repeatedly extracting with chloroform (4 to 5 times). **PDI-BA-1** was purified through the column chromatography ($CHCl_3$: MeOH : Et_3N 95 : 4.5 : 0.5).

*Table 6-3 Conditions and yields of **PDI-BA-1** synthesis with NMI as solvent.*

Exp. No.	PTCDA (mmol)	BA-1/PTCDA (mol/mol)	NMI/PTCDA (mL/mmol)	Temp. (°C)	Time (h)	Yield %
N-1	0.296	4	67	160	144	23
N-2	0.296	4	135	160	72	39
N-3	0.592	4	135	160	72	36
N-4	0.275	4.3	145	160	72	50
N-5	0.148	8	270	160	88	85

Reaction N-1 started with a same scale as D-3. The yield (23%) did not increased much even if the reaction time was extended from 72 h to 144 h. When the amount of NMI was doubled (N-2), the yield increased to 39%, suggesting a positive effect of adding NMI. The yield almost remained constant but slightly decreased by 3% when the reaction was double-scaled (N-3).

However, the removal of NMI required large amount of 1 M hydrochloric acid and chloroform, which was time-consuming and not environmental-friendly, whilst the amount of dissolved **PTCDA** was significantly limited by the amount of solvent. After the reaction had completed, there was still a part of undissolved **PTCDA** left in the reaction mixture, suggesting the solubility was still a hindrance of yield even if the good solvent was applied. Based on this, the reactant scale was further decreased.

In N-4 and N-5, the absolute amount of **BA-1** (1.184 mmol) and NMI (40 mL) remained unchanged as N-2, whilst the amount of **PTCDA** was decreased, which consequently increased the **BA-1/PTCDA** and **NMI/PTCDA** ratio. The increase of **NMI/PTCDA** ratio improved the dispersion extent of **PTCDA**, whilst the increase of **BA-1/PTCDA** ratio improved the

formation of di-substituted product, both of which were expected to positively affect the yield. When **PTCDA** was decreased to 0.275 mmol (N-4), the yield rose to 50%. When **PTCDA** was further decreased to 0.148 mmol, with the reaction time extended to 88 hours, the yield reached 85% (N-5).

6.1.3. Synthesis of Ph/NH_2-Boc-TANI

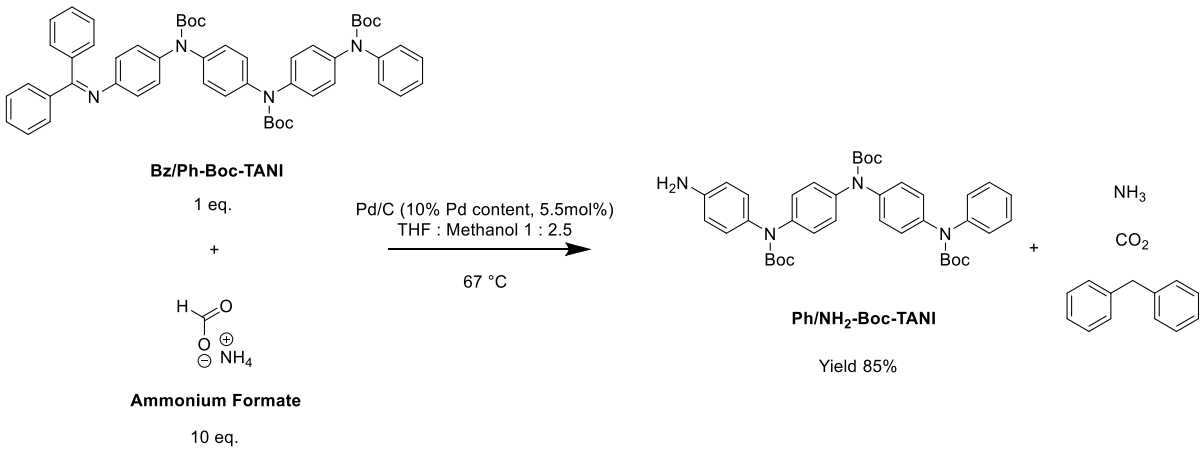

*Scheme 6-5 Synthesis of **Ph/NH_2-Boc-TANI**.*

At room temperature, 5.7 mmol ammonium formate (10 eq., 0.36 g, 63.06 g/mol), 0.60 mmol **Bz/Ph-Boc-TANI** (0.50 g, 1 eq., 831.03 g/mol) and 36 mg Pd/C (10% Pd content, 5.5 mmol%) were successively added to a round-bottom flask. The flask was quickly connected to Schlenk line with nitrogen environment. 30 mL anhydrous THF and 75 mL anhydrous methanol were added to the mixture. The reactants were refluxed at 67 °C until TLC (1:1 (v/v) ethyl acetate : n-hexane) suggested the completion (2 h). The solvent was removed by rotary evaporation. The crude product was taken up with DCM, followed by filtering with celite. The celite were fully rinsed by DCM to ensure all the product was transferred into the filtrate. After removing the solvent, the residue was stirred in n-hexane overnight. The purified product was obtained by filtration, as an off-white powder (85% yield).

^{1}H NMR (400 MHz, DMSO-d_6) δ 7.88 – 6.15 (m, 17H), 5.11 (s, 2H), 1.83 – 0.97 (m, 27H).

Previous trials

This reaction was previously done with different amount of catalyst (Table 6-4). Both reactions started with 0.6 mmol **Bz/Ph-Boc-TANI**. In BT-1, 3 mol% Pd/C was applied. According to the TLC results, it took 6 hours to complete this reaction, resulting a 54% yield. By increasing Pd/C amount to 5.5%, the reaction completed in 2 hours and reached 85% yield (BT-2).

*Table 6-4 Conditions and yields of **Ph/NH$_2$-Boc-TANI** synthesis.*

Exp. No.	Bz/Ph-Boc-TANI (mmol)	Ammonium Formate (eq.)	Pd/C (mol%)	Temp. (°C)	Time (h)	Yield %
BT-1	0.6	10	3	67	6	54
BT-2	0.6	10	5.5	67	2	85

6.1.4. Synthesis of Ph/NH$_2$-Boc-TANI-PDI

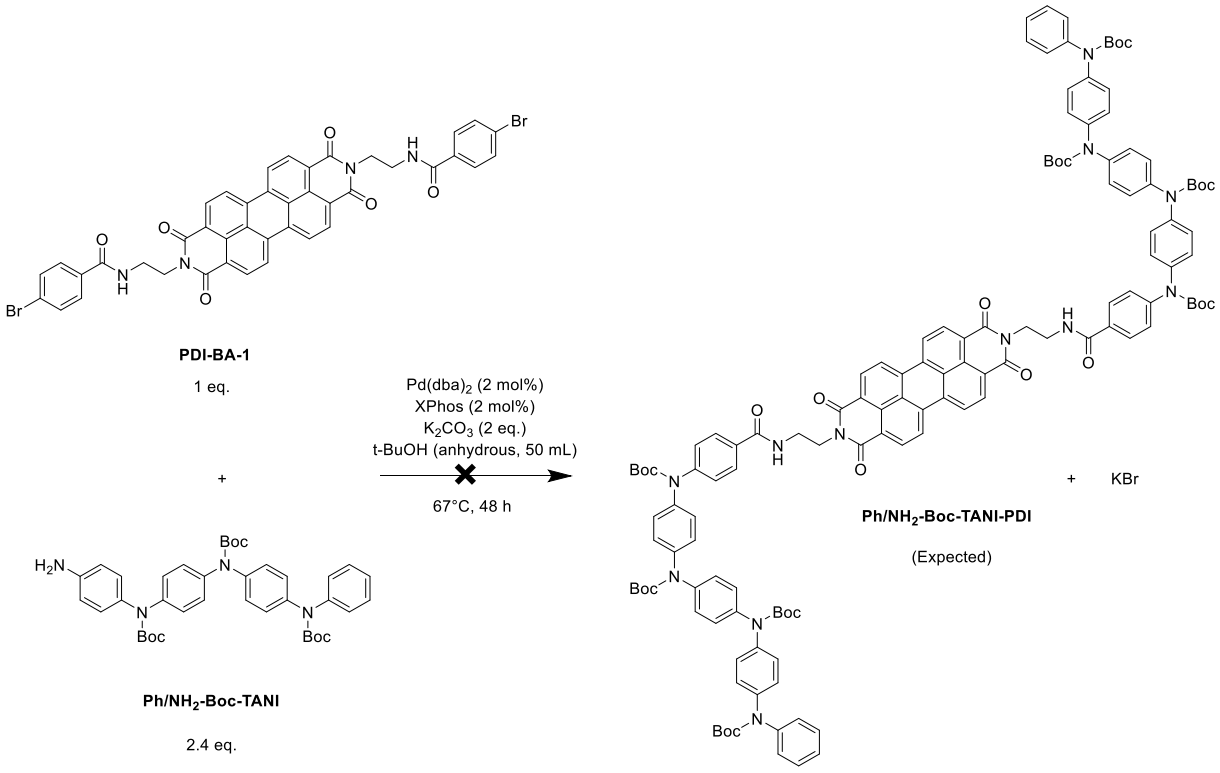

*Scheme 6-6 Synthesis of **Ph/NH$_2$-Boc-TANI-PDI**.*

To a pre-dried round-bottom flask, 0.06 mmol **PDI-BA-1** (1 eq., 0.05 g, 842.50 g/mol), 0.14 mmol **Ph/NH$_2$-Boc-TANI** (2.4 eq., 0.095 g, 666.82 g/mol), **Pd(dba)$_2$** (0.69 mg, 2 mol%, 575 g/mol), **XPhos** (0.57 mg, 2 mol%, 476.72 g/mol) and 0.012 mmol potassium carbonate (**K$_2$CO$_3$**) (2 eq., 16.6 mg, 138.205 g/mol). The reagents were protected under nitrogen, followed by 50 mL tert-butanol (**t-BuOH**) (b.p. 83 °C) was added. The flask was open to Schlenk line and heated at 67 °C for 48 h. After the reaction had completed, the reaction mixture was cooled to room temperature and filtered through celite. The solvent was then removed. The residue was

taken up in dichloromethane and washed with DI water. The organic phase was dried by $MgSO_4$, followed by the removal of solvents. The expected product was **Ph/NH_2-Boc-TANI-PDI** (M.W. 2214.55 g/mol).

This reaction however did not work, as no signal in MALDI or NMR matched the product. The failure could possibly be explained by the low reaction temperature and catalyst load. The 67 °C temperature was initially aimed to protect the boc groups, whilst it was 43 °C lower than the literature suggestion (110 °C). To explore the proper conditions for this reaction, the side chain (**Ph/NH_2-Boc-TANI-BA-1**) was attempted to be synthesized.

6.1.5. Synthesis of Ph/NH_2-Boc-TANI-BA-1

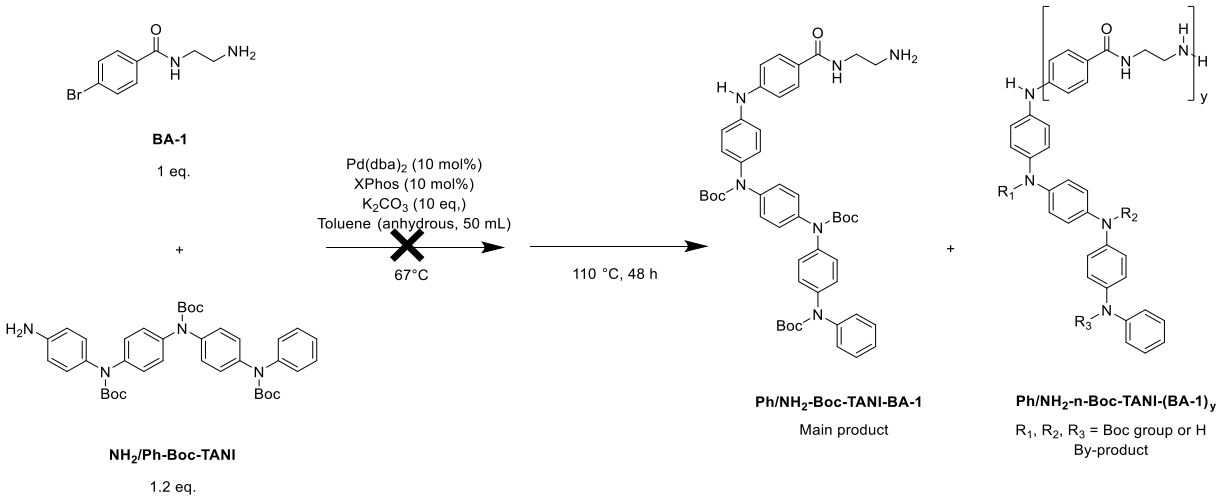

*Scheme 6-7 Synthesis of **Ph/NH_2-Boc-TANI-BA-1**.*

To a pre-dried round bottom flask, 0.118 mmol **BA-1** (1 eq., 0.029 g, 243.10 g/mol), 0.142 mmol **Ph/ NH_2-Boc-TANI** (1.2 eq., 0.095 g, 666.82 g/mol), **Pd(dba)$_2$** (6.9 mg, 10 mol%, 575 g/mol), **XPhos** (5.7 mg, 10 mol%, 476.72 g/mol) and **K_2CO_3** (10 eq., 166 mg, 138.205 g/mol) was added. The flask was kept open to the Schlenk line, with the reagents protected under nitrogen. 50 mL anhydrous toluene (b.p. 110.6 °C) was added. The mixture was first heated to 67 °C and tracked by TLC (1:1 (v/v) ethyl acetate : n-hexane). No formation of new products was observed after three hours. The mixture was then heated to 110 °C for 48 h. After the reaction had completed, it was cooled to room temperature and filtered with Büchner funnel. The solvent in the filtrate was then removed. The crude product was centrifuged three times by 5 mL diethyl ether (each time). Both the supernatant and residue were characterized by ESI.

The expected products and their exact mass were listed in Table 6-5. In the centrifuged residue, 829.4 (m/z) (fully boc-protected **Ph/NH_2-Boc-TANI-BA-1**) was dominate; A peak with low intensity at 991.5 (m/z) (fully boc-protected **Ph/NH_2-Boc-TANI-(BA-1)$_2$**) was also found,

whose height was 5.9% relative to that of 829.4 (m/z). In the centrifuged supernatant, 689.3 (m/z) (fully boc-deprotected **Ph/NH$_2$- TANI-(BA-1)$_2$**) was found. No other by-products were detected.

*Table 6-5 Exact mass of expected compounds in **Ph/NH$_2$-Boc-TANI-BA-1** synthesis.(n is the number of boc groups; y is the number of **BA-1** units; ESI detected signals were **bolded** in font; The desired compounds were underlined.)*

n (Boc) \ y (-BA-1)	0	1	2	3
0	366.18	528.26	**690.34**	852.42
1	466.23	628.31	790.39	952.47
2	566.28	728.36	890.44	1052.52
3	666.33	**828.41**	**990.49**	1152.57
BA-1 (y-oligomers)	-	-	404.09	566.17

The next step will extend the reaction conditions of **Ph/NH$_2$-Boc-TANI-BA-1** to **Ph/NH$_2$-Boc-TANI-PDI** synthesis. As temperature was increased, it was expected to obtain a mixture of **PDI-BA-1** di-substituted or mono-substituted with fully or partially boc-protected **TANI**. All the expected compounds and their exact mass were summarized in Table 6-6. The formation of di-substituted products can be promoted by increasing the equivalence of **Ph/NH$_2$-Boc-TANI**. The partially boc-deprotected products can be further heated at higher temperature to fully deprotected the boc groups. By carefully protected with nitrogen atmosphere, the boc-deprotected **TANI-PDI** can be directly applied for self-assembly study in the future.

*Table 6-6 Exact mass of expected compounds in **Ph/NH$_2$-Boc-TANI-PDI** synthesis.(n is the number of boc groups; x is the number of substituted **TANI**; The desired compounds were underlined.)*

n (boc)\x (TANI)	0	1	2
0	842.02	1128.27	1414.52
1	-	1228.32	1514.57
2	-	1328.37	1614.62
3	-	1428.42	1714.67
4	-	-	1814.72
5	-	-	1914.77
6	-	-	2014.82

6.2. Self-assembly study

6.2.1. Qualitative solubility tests of PTCDA

To 5 mL toluene, chloroform, methanol and DMSO was added 0.01 g **PTCDA**. The suspensions were sonicated well and left overnight. The dispersion extent was determined by how much **PTCDA** was precipitated and how deep the supernatant colour was. The suspensions were observed again after five days without any disturbance.

6.2.2. Characterization of PTCDA

6.2.2.1. Sample preparation

Twelve solvents (1-methylimidazole (NMI), acetonitrile (ACN), N, N'-dimethylformamide (DMF), methanol, DMSO, tetrahydrofuran (THF), tert-butanol, 1,4-dioxane, ethyl acetate, chloroform, toluene and xylenes) were applied in **PTCDA** solubility study.

In an empty vial, 0.5 mg **PTCDA** was dissolved in 22.8 mL studied solvent, resulting 0.05 mM **PTCDA** solution. 0.05 mM **PTCDA** solution was sonicated well. 1 mL 0.05 mM **PTCDA** solution was immediately transferred into a new vial, followed by diluting with another 9.0 mL corresponding solvent, resulting 0.005 mM **PTCDA** solution. The resulting solutions were left overnight with no disturbance before further characterization.

6.2.2.2. UV-Vis characterization

For further solubility (HSP) study, UV-Vis absorbance spectra of each **PTCDA** solution was tested by UV-Vis-NIR spectrometer (UV-2600 Shimadzu), with Mediate scan rate, 1 cm optical path and 5 nm slit width. The baseline (from 1400 to 220 nm) was corrected automatically by scanning the background solvent and cuvette. The absorbance intensities of each sample were recorded from 800 nm to 400 nm.

6.2.2.3. HSP calculations

The 0-0 vibrational transition ($A_{0\text{-}0}$) observed in 0.005 mM **PTCDA** were compared between different solvent systems. Three HSP components (δ_D, δ_P, δ_H) and total HSP (δ_T) of all the solvents were individually sorted with ascending trend. $A_{0\text{-}0}$ of **PTCDA** in each solvent was plotted against the corresponding HSP. The discrete data points were fitted by cubic B-Spline in Origin 2018b. The top of the resulting B-Spline fitting curve was regarded as the corresponding HSP component of **PTCDA**.

After all the four HSP had been fitted, the norm of three HSP components (δ_D, δ_P, δ_H) of **PTCDA** were calculated by Eq. 6-1, giving $\delta_{T\_calculated}$. The calculated δ_T was compared with which from fitting results ($\delta_{T\_fitting}$). The error between fitting results ($\delta_{T\_fitting}$) and calculated results ($\delta_{T\_calculated}$) was given by Eq. 6-2.

$$\delta_{T\_calculated} = \sqrt{\delta_D^2 + \delta_P^2 + \delta_H^2} \cdots\cdots\cdots\cdots\cdots\cdots \textit{Eq. 6-1}$$

$$error\% = \frac{\delta_{T_{fitting}} - \delta_{T_{calculated}}}{\delta_{T_{calculated}}} \times 100\% \cdots\cdots\cdots\cdots\cdots \textit{Eq. 6-2}$$

δ_T of **PTCDA** was then compared with δ_T of each solvent. The difference between them was given by Eq. 6-3. Solvent with smaller $\Delta\delta_T$ are regarded to be better solvent. The thresholds between good solvent/intermediary solvent/poor solvent given by the literature are 1 and 3.[156]

$$\Delta\delta_T = \left|\delta_{T_{PTCDA}} - \delta_{T_{Solvent}}\right| \cdots\cdots\cdots\cdots\cdots\cdots\cdots\cdots \textit{Eq. 6-3}$$

6.2.3. Characterization of PDI-BA-1

The general procedure of PDI characterization is 1) All the samples (in different solvents, with various concentrations) were first tested by UV-Vis absorbance to analyse if any aggregates was formed. 2) The promising samples were characterized by TEM to visualize the morphologies. 3) Samples with well-defined morphologies were further tested with temperature-dependent UV-Vis absorbance to check the response of extent of aggregation towards temperature.

6.2.3.1. Sample preparation

Fourteen solvents (NMI, ACN, DMF, methanol, DMSO, THF, tert-butanol, 1,4-dioxane, ethyl acetate, chloroform, toluene, xylenes, isopropanol and n-hexane) were applied in **PDI-BA-1** solubility study. 1:3, 1:1, 3:1 ethyl acetate/n-hexane were prepared for dual-solvent self-assembly study.

To an empty vial, 0.0278 g **PDI-BA-1** was first dissolved in 30 mL chloroform. After well sonicated, the solution was distributed to 30 aliquots, followed by the removal of chloroform. Each aliquot was dissolved in 11 mL studied solvent to prepare 1.0×10^{-4} M solution. 1.0×10^{-5} M solution was diluted from 1 mL 1.0×10^{-4} M solution by adding another 9 mL solvent. 2.5×10^{-5} M, 5.0×10^{-5} M, 7.5×10^{-5} M solution were diluted from 1 mL, 2 mL, 3 mL 1.0×10^{-4} M solution, respectively, to a total volume of 4 mL. Similarly, 2.5×10^{-6} M, 5.0×10^{-6} M, 7.5×10^{-6} M solution were diluted to 4 mL from 1 mL, 2 mL, 3 mL 1.0×10^{-5} M solution,

respectively. 1.0×10^{-3} M solution in isopropanol was prepared by dissolving an aliquot to 1.1 mL isopropanol.

For concentration-dependent study, all the samples were first heated to 40 °C for 10 minutes before cooling down to the room temperature. Without any disturbance, all the samples were left at room temperature overnight for crystal growth.

6.2.3.2. UV-Vis characterization

For HSP calculations, all the fourteen solvent systems at 1.0×10^{-4} M were characterized. For solvent-/concentration-dependent study, nine solvents (toluene, isopropanol, acetonitrile, chloroform, DMF, DMSO, methanol, THF) from 2.5×10^{-6} M to 1.0×10^{-4} M were characterized. UV-2600 Shimadzu was applied for solvent-/concentration-dependent study. All the instrument settings were same as Section 6.2.2.2..

Absorbance of 0-0, 0-1 vibrational transition and aggregation peaks (A_{agg}) were compared, where $A_{0\text{-}0}$ was around 525 nm, $A_{0\text{-}1}$ was around 480 nm and A_{agg} was around 560 nm. For concentration-dependent study, A_{agg} was normalized by the concentration. For solvent-dependent study, to make the results comparable between each group, extent of aggregation and $A_{0\text{-}0}/A_{0\text{-}1}$ were normalized by 0 and 1.

Temperature-dependent UV-Vis study was done in School of Physics, with Lambda 35 UV-Vis spectrometer (Perkin Elmer Precisely), with 1 nm slit width, 1 cm optical path and 480/min scan rate. The temperature was controlled manually with Pelter temperature programmer (Perkin Elmer Programmer, PTP1). The background of solvent and cuvette was automatically decreased at the beginning of each task.

Three samples (1.0×10^{-3} M in isopropanol, 1.0×10^{-4} M in isopropanol, 1.0×10^{-4} M in toluene) were applied with temperature-dependent study.

Each sample was first cooled to 288 K, followed by heating from 288 K to 323 K with 5 K as an interval. The data from 293 K to 323 K were valid, because 288 K was approximately 10 degree lower than the environmental temperature (23 – 24 °C), which, during the experiment, was observed with water vapour in the air quickly condensed on the cuvette surface that influenced the data quality. When the temperature indicator had been stable, each sample was left for 3 more minutes to ensure the solution was homogeneously heated.

The resulting temperature-dependent UV-Vis spectra were first normalized by their absorbance at 700 nm. To precisely locate the aggregation peaks and compare their intensities, each spectra was further corrected by decreasing the whole spectra of the highest temperature (323 K),

whose extent of aggregation was expected to be the lowest. The relative absorbance enlarged the aggregation signals (around 560 nm) of spectra and made it more accurate for further analysis.

6.2.3.3. HSP calculations

1.0×10^{-4} M **PDI-BA-1** in all the fourteen solvents were applied for HSP calculations. The HSP of **PDI-BA-1** was calculated by the same method as Section 6.2.2.3.

1:3, 1:1, 3:1 ethyl acetate/n-hexane dual solvent system were applied for tuneable HSP study. The HSP of mixing solvents were calculated by Eq. 6-4.

$$\delta_{mix} = \delta_A a\% + \delta_B b\% \quad \cdots\cdots\cdots\cdots\cdots\cdots\cdots\cdots\cdots\cdots \quad Eq.\ 6\text{-}4$$

6.2.3.4. Morphology characterization

1.0×10^{-4} M **PDI-BA-1** in toluene, isopropanol, acetonitrile, chloroform, DMF, DMSO, methanol, THF and 1.0×10^{-3} M **PDI-BA-1** in isopropanol were characterized by TEM (Tecnai 12 - FEI 120kV BioTwin Spirit).

10 μL sample were drop casted from the originated solution to 400 mesh carbon-coated copper grid, followed by characterizing with TEM. The length and widthwere analysed by ImageJ.

6.3. Modelling

The monomeric state of **PDI-BA-1** was studied. Spartan 14.0 and GaussView 5.0.9 were applied for structure building, conformer distribution searching and visualization. Gaussian 09 and Gaussian 16 were applied for calculation. The large calculation tasks were supported by high-performance computing cluster, Grendel. The methods applied in this research were Semi-empirical (SME) method, Density Functional Theory (DFT), Hartree-Fock (HF) and Time dependent-self consistent field (TD-SCF) DFT. The functionals applied were B3LYP, CAM-B3LYP, PBEPBE, PM6. The basis sets included 6-31g(d), 6-31+g(d), 6-311g(d), 6-311+g(d), 6-31+g(d, p).

6.3.1. PDI-BA-1 optimization

6.3.1.1. Conformer searching

PDI-BA-1 monomer molecule was initially built in Spartan. All the conformer searching process were done with Spartan-inbuilt calculation module on local PC. No solvation was applied.

The directly built structure was first applied by 'minimize energy' option to get the rough input structure. The calculation task was set up as conformer distribution at ground state with MMFF. The 'Maximum Conformers Examined' was set as 1000000, with the 'Percent Conformers Kept' set as 100. All the other settings remained default. The 'Global Calculations' was selected before submission. The resulting conformers were further optimized through Spartan-inbuilt PM6 to get equilibrium geometries at ground state. When the task was finished, the calculated conformers were sorted by ascending energy at 298.15K. A number of interested conformers with the lowest energies were kept and exported as *.mol2 file. Spartan output file was then transferred to gaussian input geometry file (*.gjf) via a python script ('spartan2gauss.py'), whose function was to extract conformer geometry information and transfer to a set of gaussian-readable geometry files. The resulting geometries were visualized in GaussView 5.0.9.

6.3.1.2. Optimization method comparison

Optimization that required inbuilt Gaussian methods and solvation models were constructed in GaussView 5.0.9 and calculated with Gaussian 16 on Grendel if not specified. All the multiplicities were set as 1, and charges were 0. All the methods were list in Table 6-7.

*Table 6-7 Optimization methods of **PDI-BA-1**. (Tasks from Opt 1-2 to Opt 1-9 were pre-optimized by Opt 1-1.)*

No.	Method	Functionals	Basis Sets	Solvation
Opt 1-1	PM6	-	-	None
Opt 1-2	DFT	B3LYP	6-31g(d)	PCM
Opt 1-3	DFT	PBEPBE	6-31g(d)	PCM
Opt 1-4	HF	-	6-31g(d)	PCM
Opt 1-5	DFT	CAM-B3LYP	6-31g(d)	PCM
Opt 1-6	DFT	B3LYP	6-31+g(d)	PCM
Opt 1-7	DFT	CAM-B3LYP	6-31+g(d)	PCM
Opt 1-8	DFT	PBEPBE	6-31+g(d)	PCM
Opt 1-9	DFT	B3LYP	6-31+g(d, p)	PCM

The default input geometry (**PDI-BA-1-def**) was built with default bond lengths, bond angles and dihedral angles corresponding to their general hybrid states. Because DFT was sensitive to input geometry, **PDI-BA-1-def** was first pre-optimized by PM6 (Opt 1-1). Opt 1-1 was set in vacuum, with no solvation included. Since PM6 did not cost much time and storage, this step was done with Gaussian 09 on local PC. The resulting geometry was **PDI-BA-1-PM6-G-VAC**.

To choose the best method for **PDI-BA-1** calculation, PM6 pre-optimized geometry (**PDI-BA-1-PM6-G-VAC**) was further optimized with DFT (B3LYP/6-31g(d), 6-31+g(d), 6-31+g(d, p); CAM-B3LYP/6-31g(d), 6-31+g(d)) and HF/6-31g(d). PCM was applied as solvation models. Chloroform was set as the solvent.

The results of HOMO-LUMO energy gap (ΔE) of each calculation task was converted to wavelength (λ) by Eq. 6-5, where h is the planck constant, c is the speed of light.

$$\Delta E = \frac{hc}{\lambda} \cdots\cdots \textit{Eq. 6-5}$$

The calculated λ was rounded up to the nearest integer and compared with experimental $\lambda_{0\text{-}0}$ of **PDI-BA-1** in chloroform (around 530 nm). λ within 530 ± 50 nm were regarded acceptable, whose corresponding methods were B3LYP/6-31g(d)/PCM (Opt 1-2) and B3LYP/6-31+g(d)/PCM (Opt 1-6). The method with lower cost (shorter calculation time and less required storage) was preferred (Opt 1-2).

The effect of PM6 pre-optimization was evaluated by comparing the geometry that directly optimized from **PDI-BA-1-def**. The method/functionals/basis sets/solvation of Opt 2-1 and Opt 2-2 were applied same as Opt 1-2 and Opt 1-6, respectively. However, the resulting energy between HOMO-LUMO showed a limited difference of pre-optimization, as compared in Table 6-8. The main difference was found in the second decimal place, which was ignorable when comparing to the experimental data. Thus, for the further optimization, the geometry resulted from Opt 2-2 (**PDI-BA-1-DFT**) was directly applied and modified.

*Table 6-8 Evaluation of pre-optimization step of **PDI-BA-1** optimization.*

No.	Method	Functionals	Basis Sets	Solvation	λ
Opt 1-2	DFT	B3LYP	6-31g(d)	PCM	495.3072663
Opt 2-1	DFT	B3LYP	6-31g(d)	PCM	495.3611157
Opt 1-6	DFT	B3LYP	6-31+g(d)	PCM	506.3715873
Opt 2-2	DFT	B3LYP	6-31+g(d)	PCM	505.9779614

6.3.1.3. Trapped-closed and reactive-open conformers

To study the geometries of reactive-open (**RO**) and trapped-closed (**TC**) conformers. The input geometry of **TC** conformer (**PDI-BA-1-TC-I**) was modified from **PDI-BA-1-def**, whilst which of **PDI-BA-1-RO-I** was modified from **PDI-BA-1-DFT**. The key interested parameters were atom distances between amide H atom (H52) and two imide O atoms (O32, O30) (Scheme 6-8). Other moieties (4-bromophenyl group, perylene diimide core) were all remained unmodified during the optimization. To rotate the side chains, the dihedral angle between substituent and perylene diimide (N51-C42-C39-N37) were edited by dihedral angle tools in GaussView. The atoms labels were expanded in Scheme 6-8.

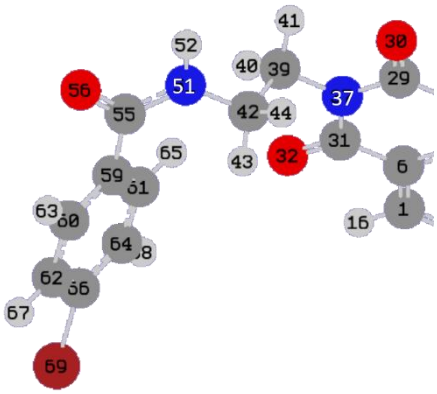

*Scheme 6-8 Atom labels of half side of **PDI-BA-1**.*

The dihedral angle of N51-C42-C39-N37 in both **PDI-BA-1-TC-I** and **PDI-BA-1-RO-I** were 0. **PDI-BA-1-TC** and **PDI-BA-1-RO** were both optimized by B3LYP/6-31g(d)/PCM. The distances between H52 and O30/O32 were recorded. Hydrogen bonds were regarded to be formed if the H-O distance was less than 2.5 Å.

Though there was no evidence of intramolecular hydrogen bonds formed in **PDI-BA-1-DFT**, it was possibly not the exact reactive open conformer. The amide groups in **PDI-BA-1-DFT** were found in their cis- state (Scheme 6-9a), which could possibly not suitable for the formation of intermolecular hydrogen bonds. However, since multi-molecular study was not done in this work, the hypothesis that cis-amide geometry is not preferred in polymerization required to be further confirmed. **PDI-BA-1-RO-I** was thus built as a trans-conformer, whose dihedral angle of C59-C55-N41-C42 was modified to be -180° (Scheme 6-9b).

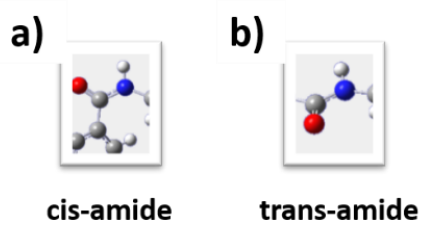

*Scheme 6-9 a) cis-amide and b) trans-amide structure in **PDI-BA-1**.*

6.3.2. Excitation analysis of PDI-BA-1

Single point calculations were operated by TD-SCF-DFT, whose atom coordinates came from the old checkpoint file of the optimization results. The functional for this step ranged from B3LYP, CAM-B3LYP and PBEPBE, with their basis sets 6-311g(d). PCM and SCIPCM were tested as the solvation model, with chloroform as the solvent. The performance of various functionals were compared with the experimental $\lambda_{0\text{-}0}$ in chloroform again.

Before confirming the suitable nstates and root parameter, a set of tests with various nstates (from 10 to 50) and root (from 3 to 50) were applied. Having compared their output quality, nstates and root were set as 30 and 3 for spectra contribution study. Thus, 30 excitation states were allowed in the excitation analysis. The peak half-width at half height when predicting the spectra was set as 0.1 eV. The predicted UV-Vis spectra were visualized in GaussView, while the exact value and transition contribution were extracted through output log files.

6.3.3. TANI-PDI optimization and electron distribution analysis

TANI-PDI was optimized with a similar route as **PDI-BA-1**. All the work regarding **TANI-PDI** were done in GaussView 5.0.9, Gaussian 09 and Gaussian 16.

The default input geometry (**TP-def**) was constructed with default bond lengths, bond angles and dihedral angles. **TP-def** was first pre-optimized with PM6 in vacuum, resulting **TP-PM6-VAC**, which was further optimized with a set of methods in Table 6-9. Once the experimental data is obtained, it will be compared with the calculated results to evaluate the accuracy of each methods. The frontier orbitals, Mulliken charge and surface potential of **TP-PM6-VAC** were obtained by GaussView.

*Table 6-9 Optimization methods tested for **TANI-PDI**.*

No.	Method	Functional	Basis Sets	Solvation
Opt-TP1-2	DFT	B3LYP	6-31g(d)	PCM
Opt-TP1-3	DFT	B3LYP	6-31+g(d)	PCM
Opt-TP1-4	DFT	CAM-B3LYP	6-31g(d)	PCM
Opt-TP1-5	DFT	CAM-B3LYP	6-31+g(d)	PCM

7. Appendices

7.1. Materials and tools

7.1.1. Chemicals

Table 7-1 List of chemicals

CAS NO.	Name	Source
123-91-1	1,4-Dioxane	Fisher Chemical
616-47-7	1-Methylimidazole	Sigma-Aldrich
564483-18-7	2-Dicyclohexylphosphino-2′,4′,6′-triisopropylbiphenyl	Sigma-Aldrich
128-69-8	3,4:9,10-Perylenetetracarboxylic anhydride	Sigma-Aldrich
67-64-1	Acetone	Sigma-Aldrich
75-05-8	Acetonitrile	Fisher Chemical
540-69-2	Ammonium formate	Sigma-Aldrich
32005-36-0	Bis (dibenzylideneacetone) palladium(0)	Sigma-Aldrich
67-66-3	Chloroform	Sigma-Aldrich
865-49-6	Chloroform-d	Sigma-Aldrich
7789-20-0	Deuterium oxide	Sigma-Aldrich
75-09-2	Dichloromethane	Sigma-Aldrich
60-29-7	Diethyl ether	Sigma-Aldrich
67-68-5	Dimethyl sulfoxide	Fisher Chemical
2206-27-1	Dimethyl sulfoxide-d6	Sigma-Aldrich
141-78-6	Ethyl acetate	Sigma-Aldrich

CAS NO.	Name	Source
107-15-3	Ethylene diamine	Acros organics
61790-53-2	Filter aid, celite standard super-cel	Alfa Aesar
7647-01-0	Hydrochloric acid	VWR Chemicals BDH
7487-88-9	Magnesium sulfate - dried	Fisher Chemical
67-56-1	Methanol	Fisher Chemical
619-42-1	Methyl 4-bromobenzoate	Arcos Organics
619-42-1	Methyl 4-bromobenzoate	Alfa Aesar
68-12-2	N,N-dimethylformamide	Fisher Chemical
540-69-2	n-Hexane	Sigma-Aldrich
N/A	Palladium on activated carbon	Acros organics
8032-32-4	Petroleum ether	Sigma-Aldrich
8032-32-4	Petroleum spirit 40-60 °C	VWR Chemicals BDH
584-08-7	Potassium carbonate	Fisher Chemical
67-63-0	Propan-2-ol	Fisher Chemical
14808-60-7	Sand - low iron	Fisher Chemical
7631-86-9	Silica gel 40-63 μm	VWR Chemicals BDH

CAS NO.	Name	Source
1310-73-2	Sodium hydroxide, pellets	Fisher Chemical
1310-73-2	Sodium hydroxide, pellets	VWR Chemicals BDH
865-48-5	Sodium tert-butoxide	Acros organics
75-65-0	tert-Butanol	Alfa Aesar
109-99-9	Tetrahydrofuran	Sigma-Aldrich
108-88-3	Toluene	Fisher Chemical
121-44-8	Triethylamine	Sigma-Aldrich
1330-20-7	Xylenes	Fisher Chemical

7.1.2. Instruments

Table 7-2 List of instruments

Name	Company & Type
400 MHz NMR Spectrometer	JEOL ECS 400
MALDI ionisation	UltrafleXtreme 2 (TOF-TOF) Bruker
Quadrupole Ion Trap mass spectrometer, Electrospray (ESI) ionisation	Esquire 6000 (Ion Trap) Bruker
Rotary evaporator	Heidolph Laborota 4001 efficient
UV-Vis-NIR Spectrometer	UV-2600 Shimadzu
Vacuum heat oven	Fisher bioblock scientific
Vacuum pump trap	Cvc 3000 vacuubrand PC 3001 vario
UV-Vis spectrometer	Lambda 35, Perkin Elmer Precisely
Pelter temperature programmer	Perkin Elmer Programmer, PTP1
Transmission electron microscopy (TEM)	Tecnai 12 - FEI 120kV BioTwin Spirit

7.1.3. Software

Table 7-3 List of software

Software
ChemDraw Professional 16.0
Gaussian 09W
Gaussian 16
GausssView 5.0.9
Spartan 14 v1.1.8
MestRenova x64
Origin 2018b (academic)
Anaconda Navigator (Anaconda 3)
JupyterLab 1.1.4
Spyder 3.3.6
Python 3.7
ImageJ
Visual Studio Code

7.2. NMR spectra

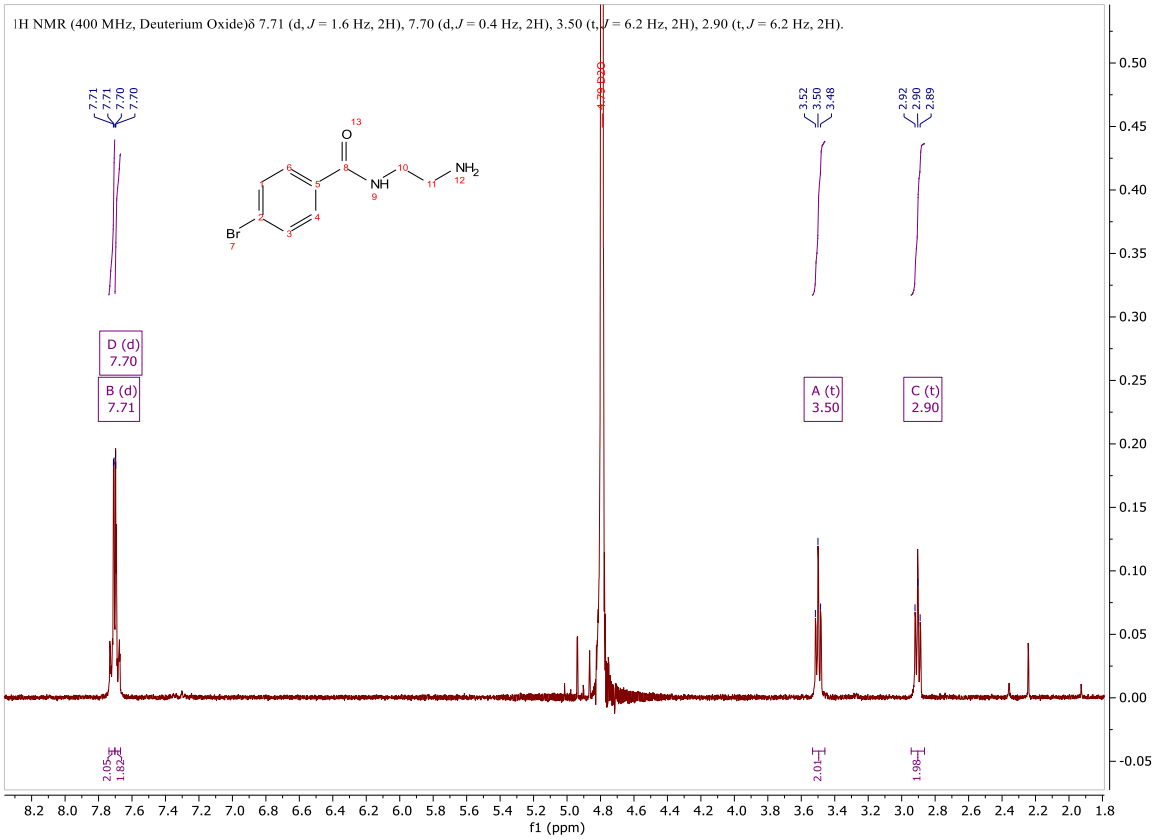

*Figure 7-1 [1]H NMR (400 MHz) spectra of N-2(aminoethyl)-4-bromobenzoamide (**BA-1**) in D_2O.*

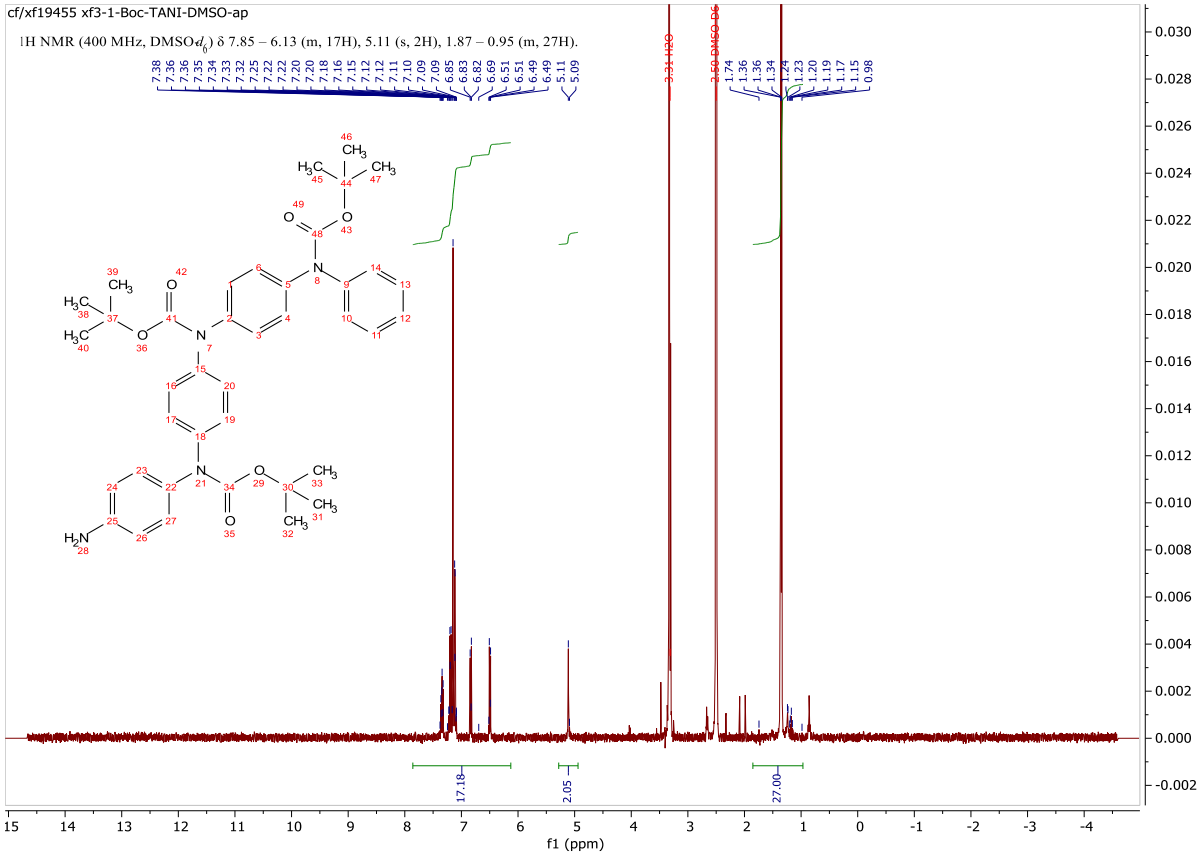

*Figure 7-2 ^{1}H NMR (400 MHz) spectra of **Ph/NH$_2$-Boc-TANI** in DMSO.*

7.3. UV-Vis absorbance spectra

7.3.1. UV-Vis absorbance spectra of PTCDA

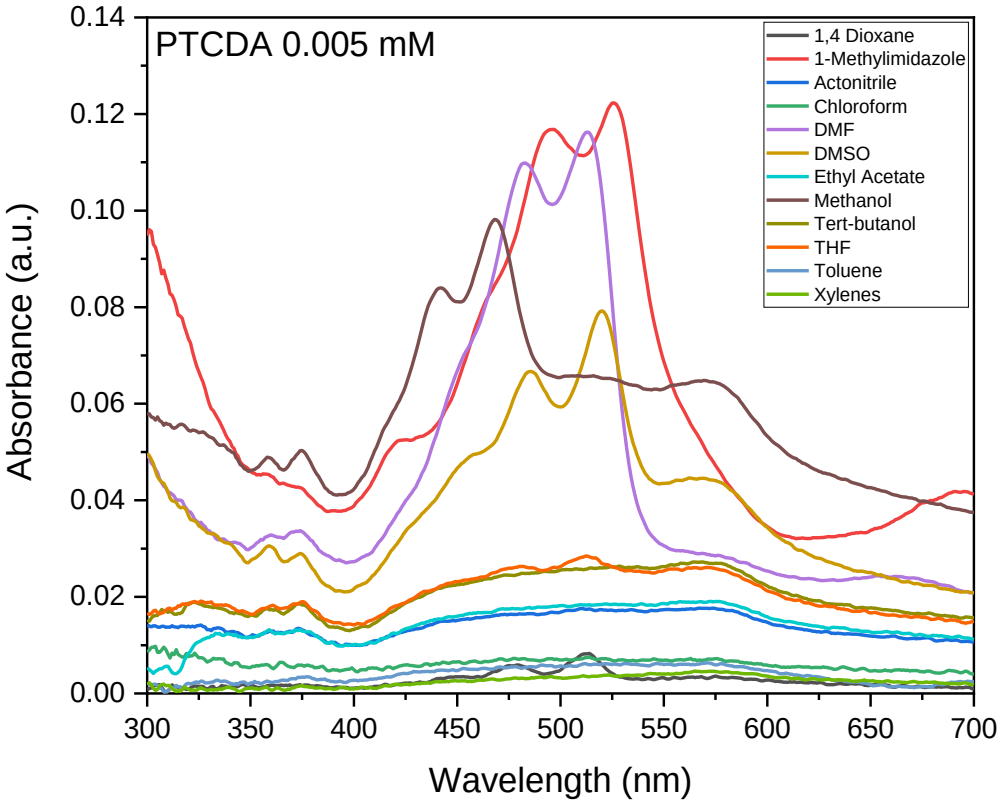

*Figure 7-3 UV-Vis absorbance spectrum of **PTCDA** at 5.0 × 10 $^{-6}$M in different solvents.*

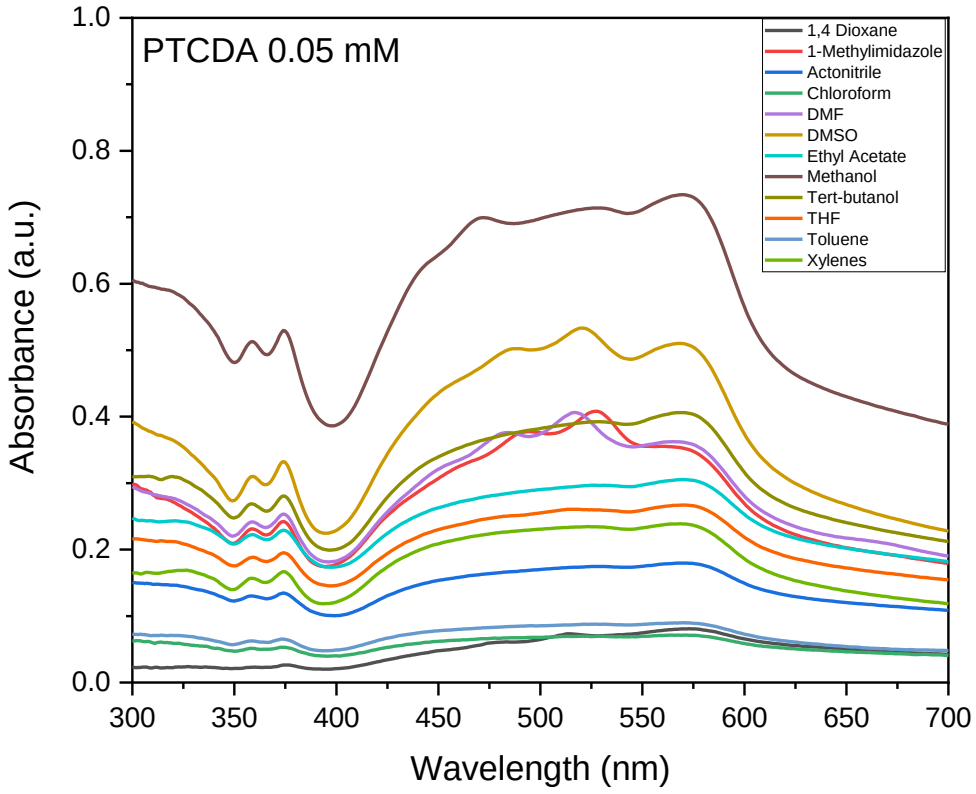

*Figure 7-4 UV-Vis absorbance spectrum of **PTCDA** at 5.0 × 10 $^{-5}$M in different solvents.*

7.3.2. UV-Vis absorbance spectra of PDI-BA-1

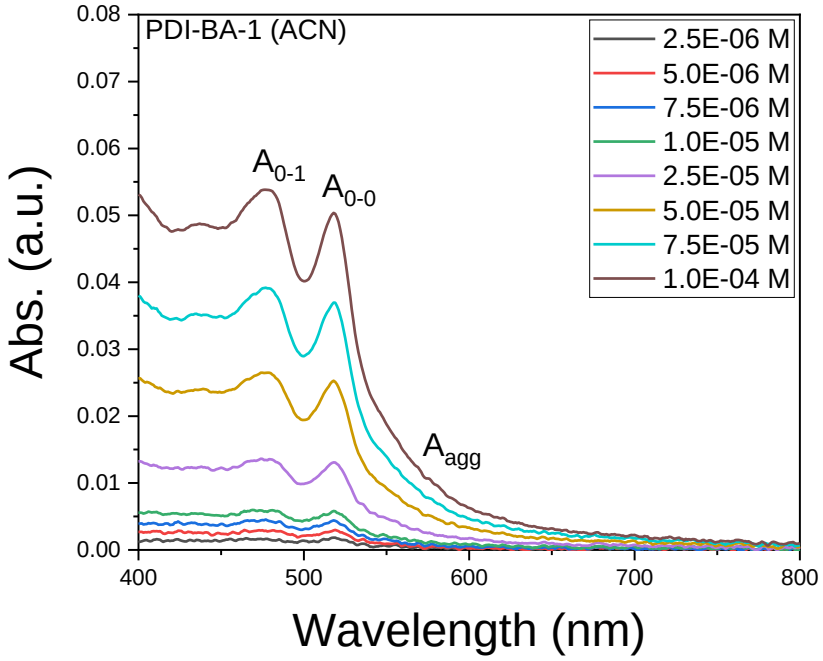

*Figure 7-5 UV-Vis absorbance spectra of **PDI-BA-1** in acetonitrile (from 2.5 × 10^{-6} M to 1.0 × 10^{-4} M, at room temperature).*

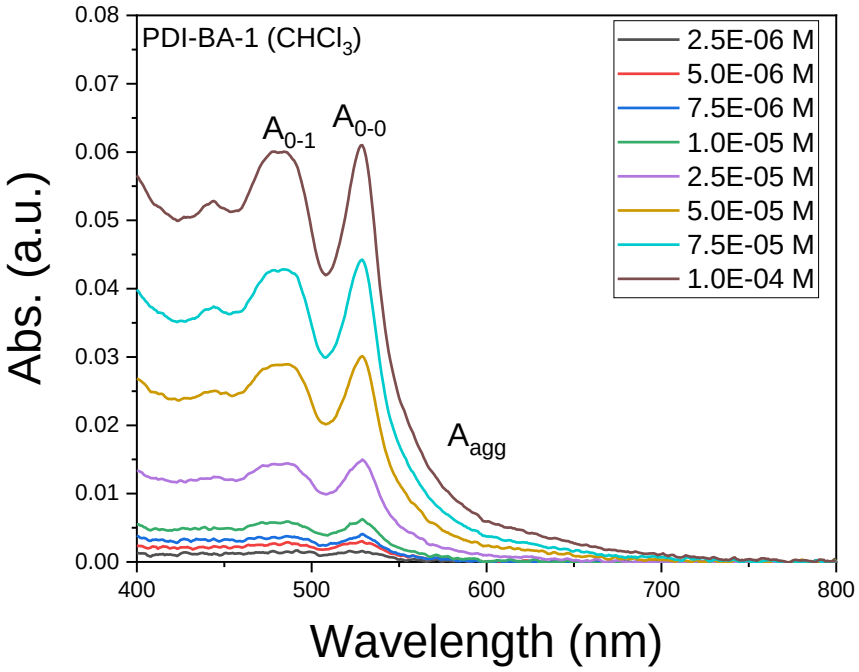

*Figure 7-6 UV-Vis absorbance spectra of **PDI-BA-1** in chloroform (from 2.5 × 10^{-6} M to 1.0 × 10^{-4} M, at room temperature).*

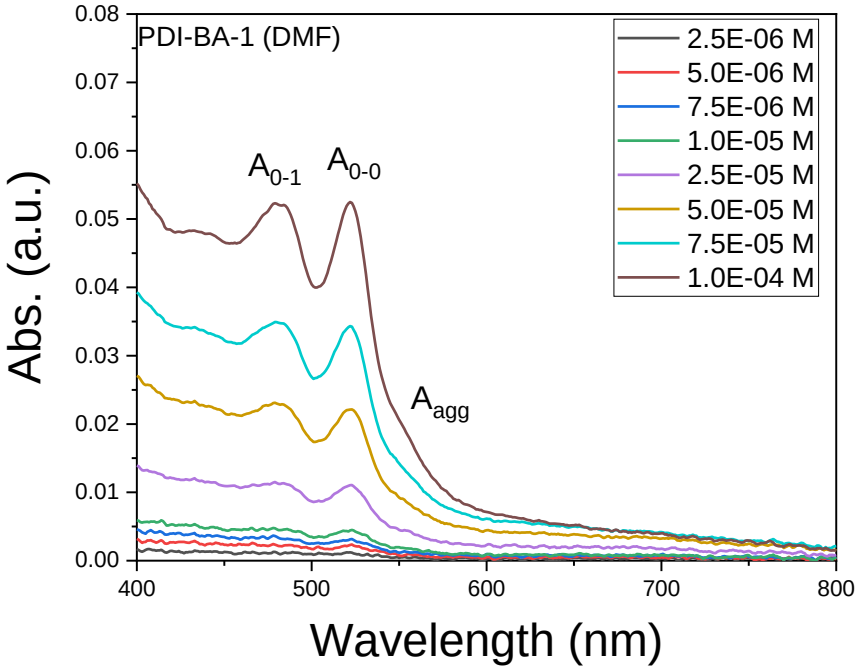

*Figure 7-7 UV-Vis absorbance spectra of **PDI-BA-1** in DMF (from 2.5 × 10^{-6} M to 1.0 × 10^{-4} M, at room temperature).*

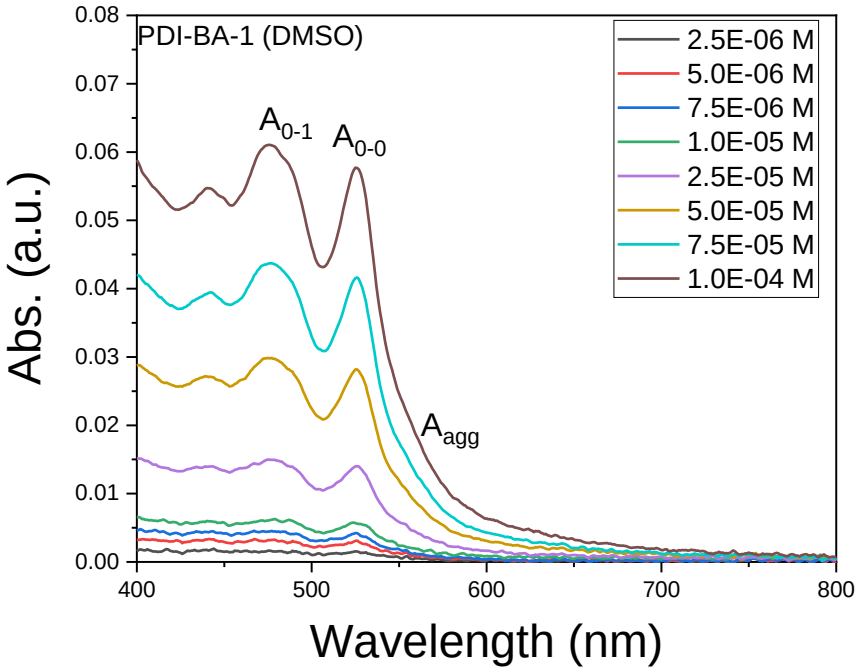

*Figure 7-8 UV-Vis absorbance spectra of **PDI-BA-1** in DMSO (from 2.5 × 10^{-6} M to 1.0 × 10^{-4} M, at room temperature).*

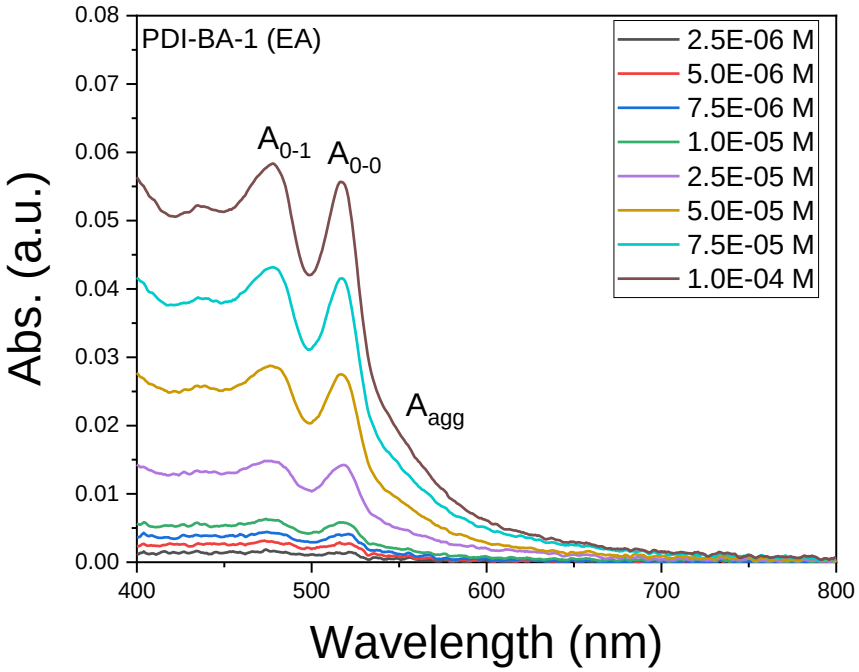

*Figure 7-9 UV-Vis absorbance spectra of **PDI-BA-1** in ethyl acetate (from 2.5 × 10^{-6} M to 1.0 × 10^{-4} M, at room temperature).*

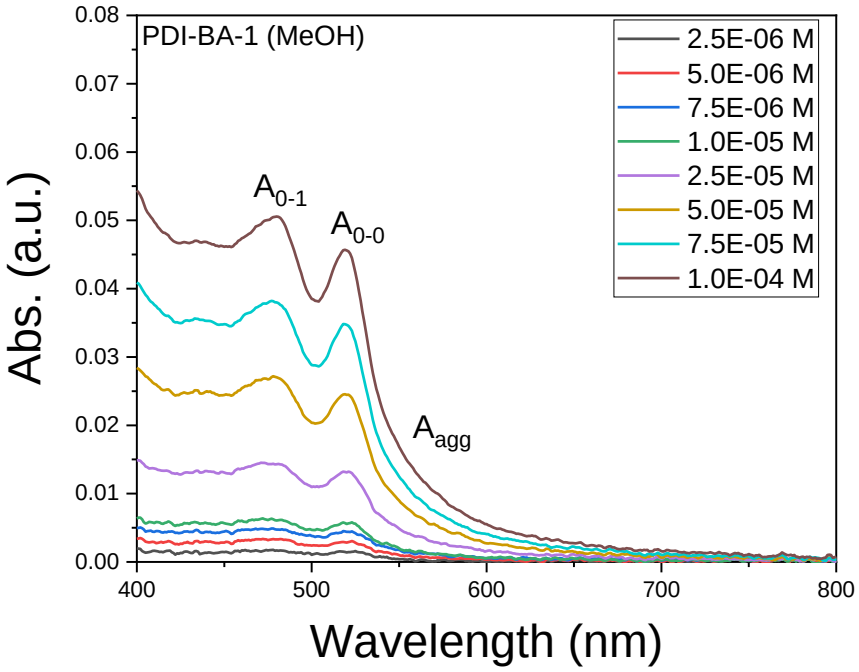

*Figure 7-10 UV-Vis absorbance spectra of **PDI-BA-1** in methanol (from 2.5 × 10^{-6} M to 1.0 × 10^{-4} M, at room temperature).*

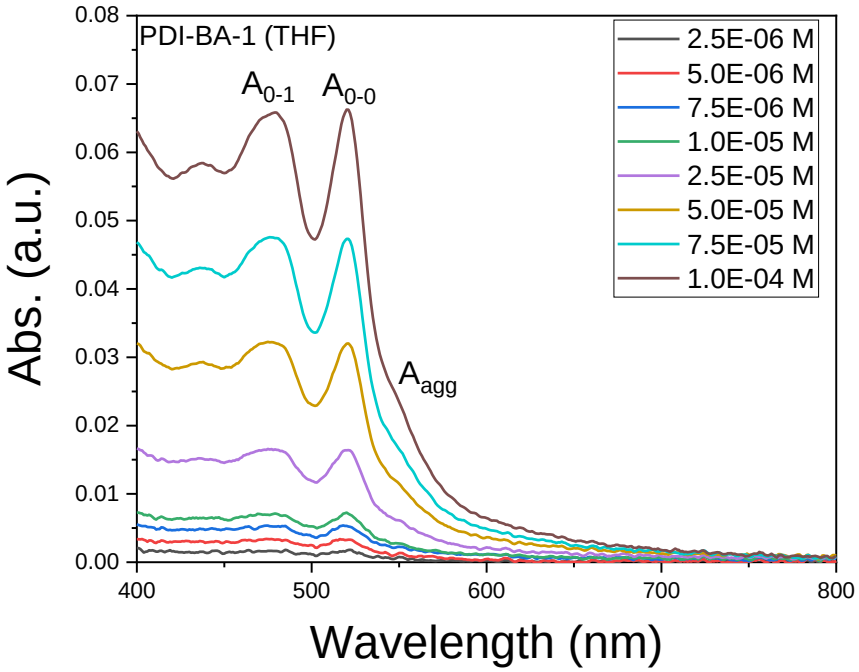

*Figure 7-11 UV-Vis absorbance spectra of **PDI-BA-1** in THF (from 2.5 × 10^{-6} M to 1.0 × 10^{-4} M, at room temperature).*

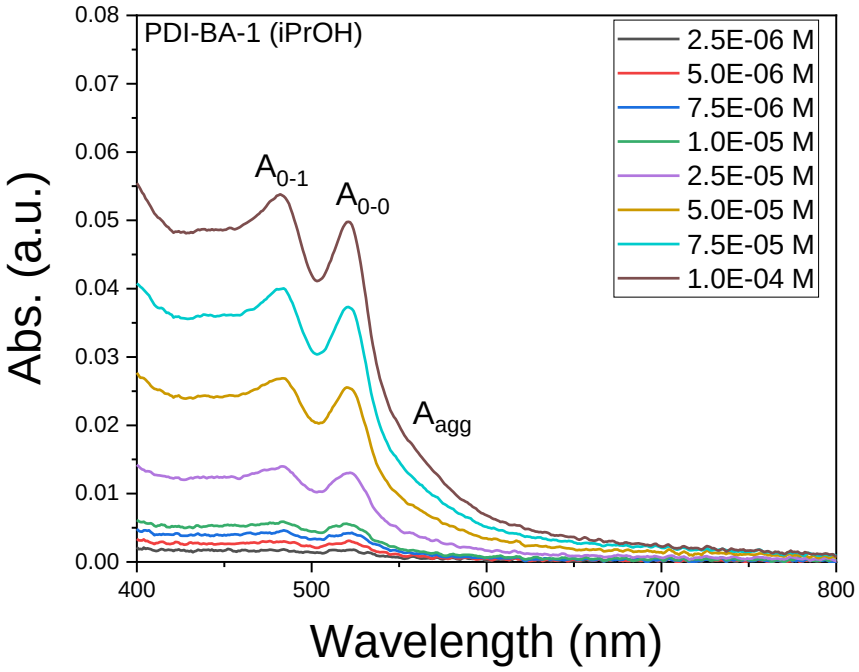

*Figure 7-12 UV-Vis absorbance spectra of **PDI-BA-1** in isopropanol (from 2.5 × 10^{-6} M to 1.0 × 10^{-4} M, at room temperature).*

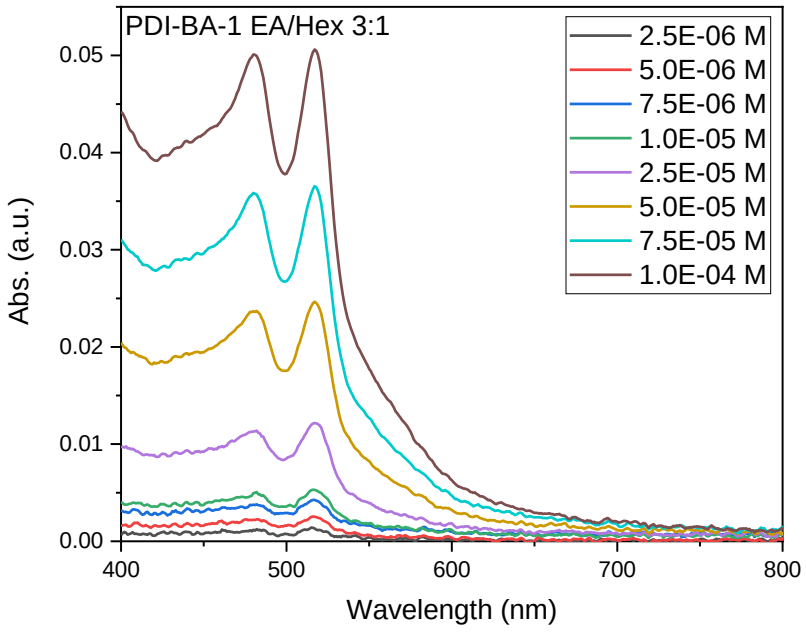

*Figure 7-13 UV-Vis absorbance spectra of **PDI-BA-1** in 3:1 (v/v) ethyl acetate/n-hexane mixing solvent (from 2.5 × 10^{-6} M to 1.0 × 10^{-4} M, at room temperature).*

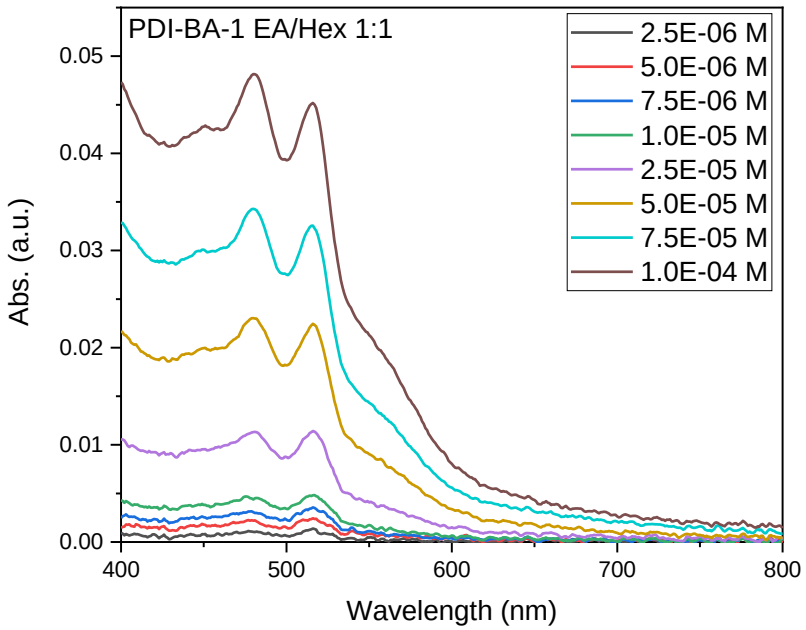

*Figure 7-14 UV-Vis absorbance spectra of **PDI-BA-1** in 1:1 (v/v) ethyl acetate/n-hexane mixing solvent (from 2.5 × 10^{-6} M to 1.0 × 10^{-4} M, at room temperature).*

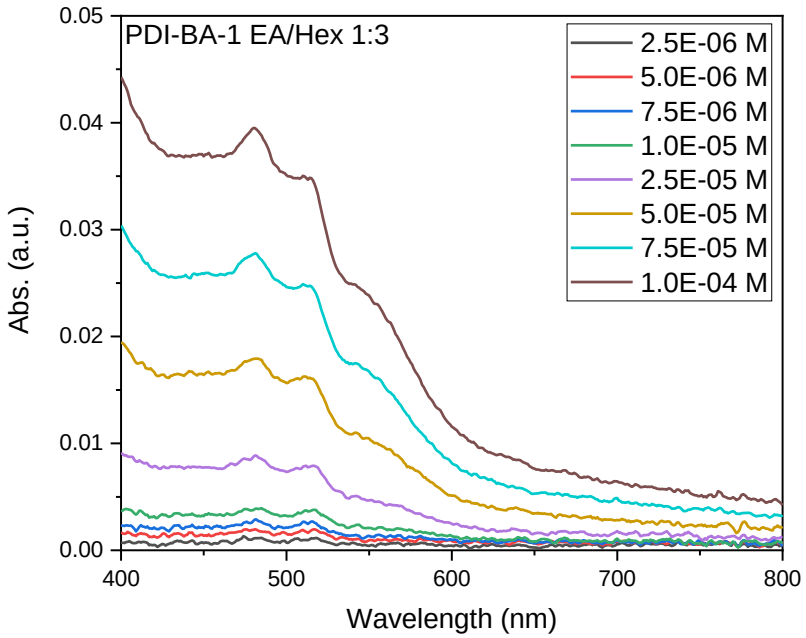

*Figure 7-15 UV-Vis absorbance spectra of **PDI-BA-1** in 1:3 (v/v) ethyl acetate/n-hexane mixing solvent (from 2.5 × 10^{-6} M to 1.0 × 10^{-4} M, at room temperature).*

7.4. TEM images

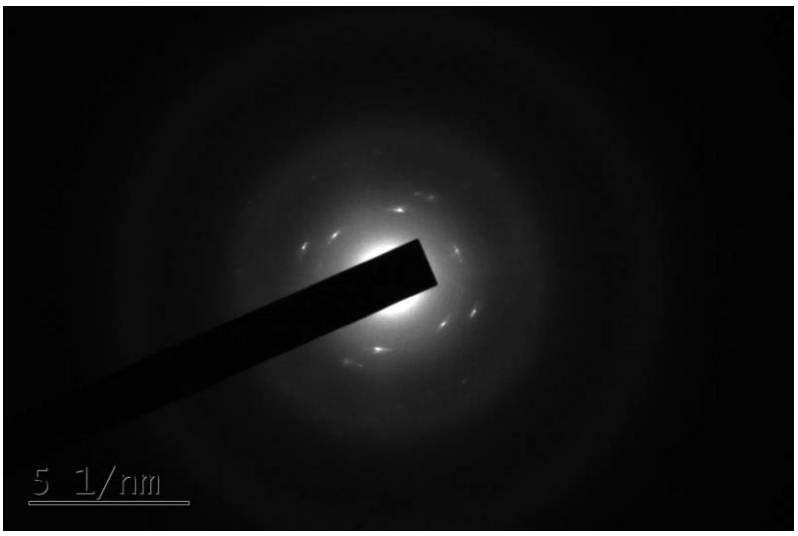

*Figure 7-16 Diffraction pattern of **PDI-BA-1** (from 1.0 × 10^{-3} M isopropanol), by TEM.*

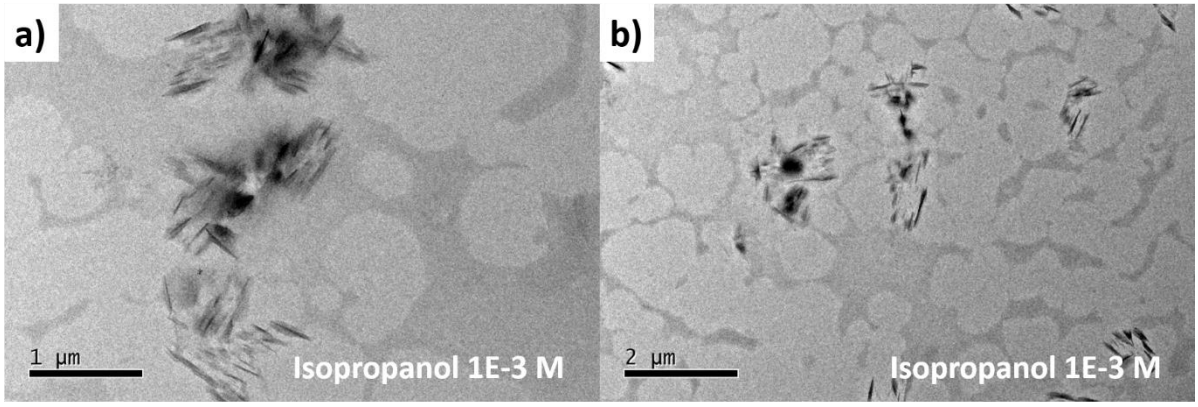

*Figure 7-17 Extra TEM images for **PDI-BA-1** in isopropanol at 1× 10^{-3} M.*

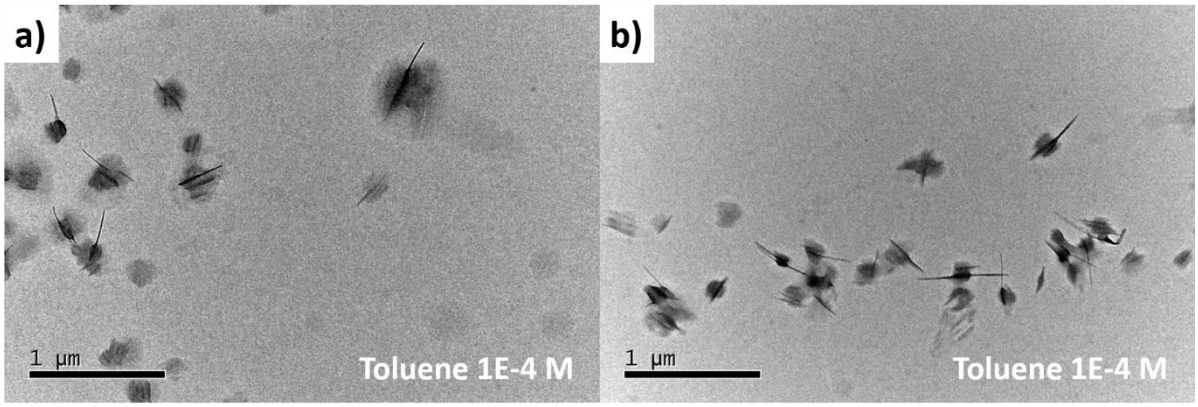

*Figure 7-18 Extra TEM images for **PDI-BA-1** in toluene at 1× 10^{-4} M.*

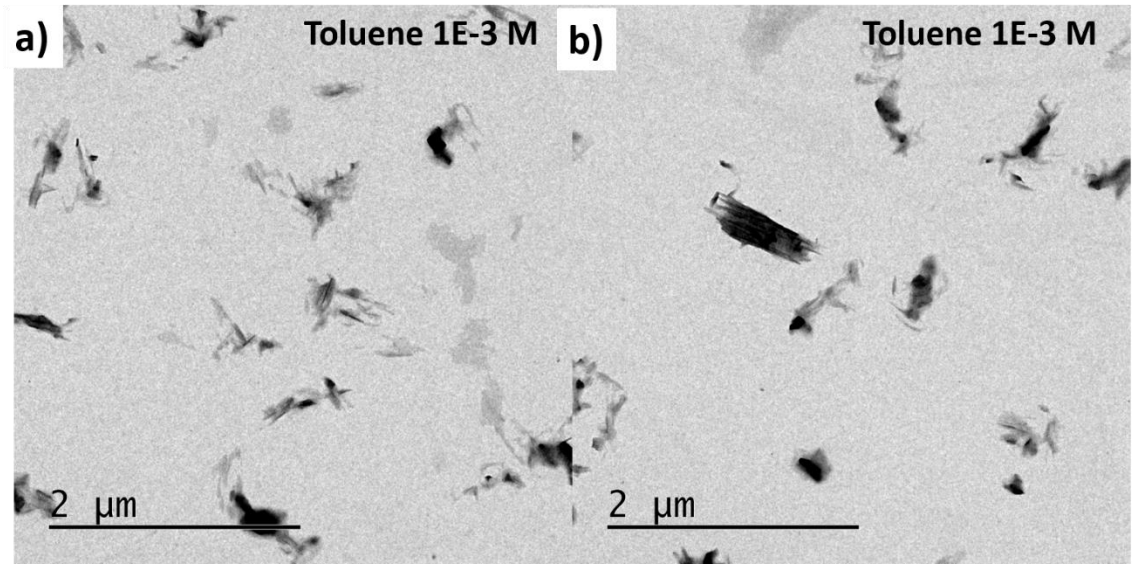

*Figure 7-19 Extra TEM images for **PDI-BA-1** in toluene at 1× 10^{-3} M.*

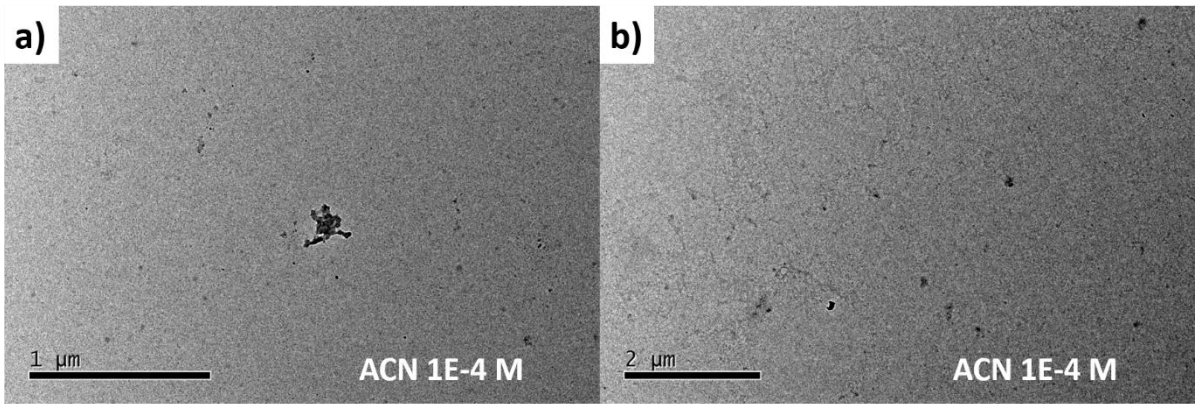

*Figure 7-20 Extra TEM images for **PDI-BA-1** in acetonitrile at 1× 10^{-4} M.*

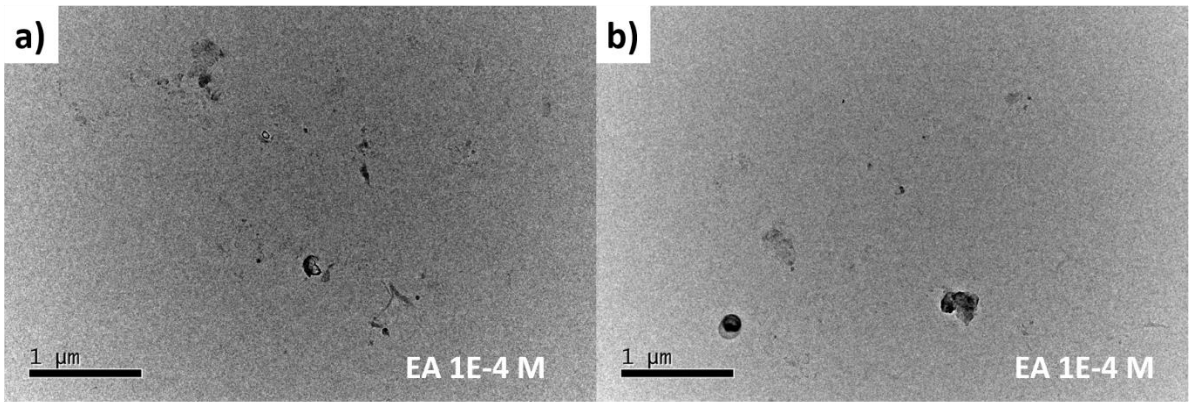

*Figure 7-21 Extra TEM images for **PDI-BA-1** in ethyl acetate at 1× 10^{-4} M.*

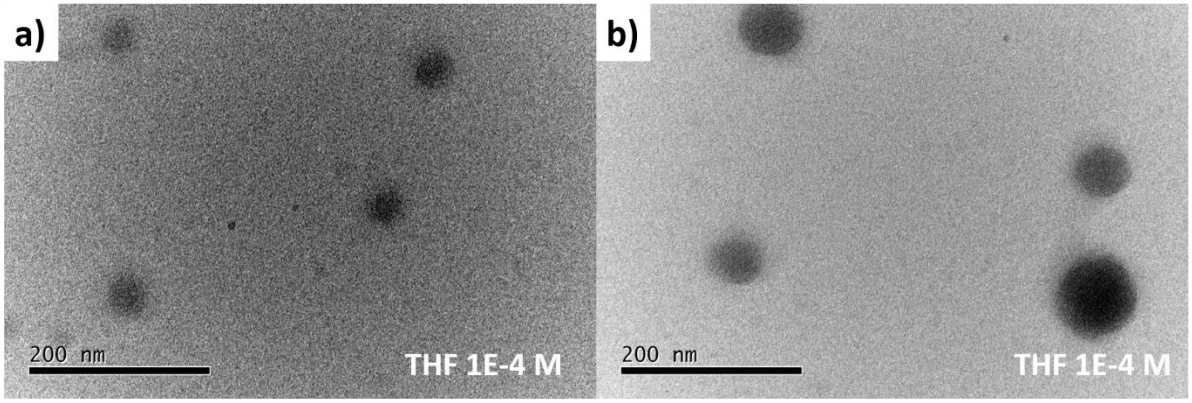

*Figure 7-22 Extra TEM images for **PDI-BA-1** in THF at 1× 10^{-4} M.*

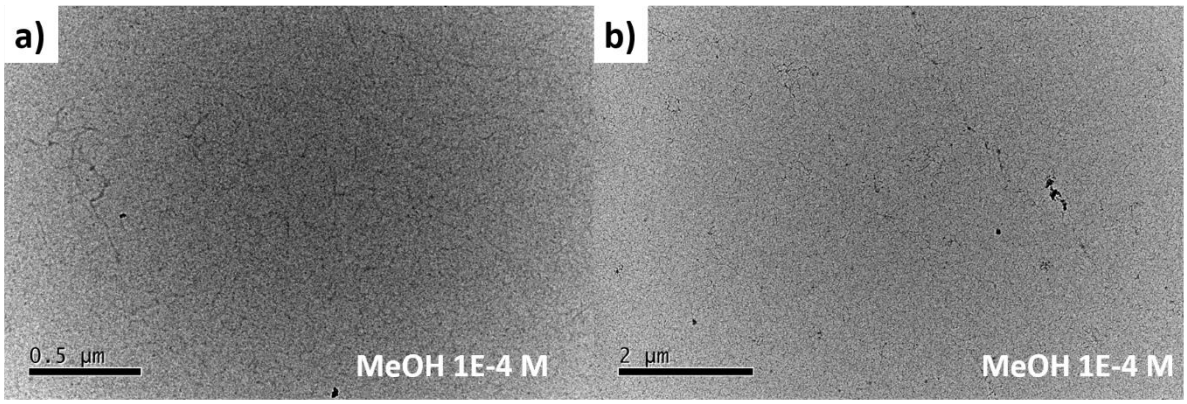

*Figure 7-23 Extra TEM images for **PDI-BA-1** in methanol at 1× 10^{-4} M.*

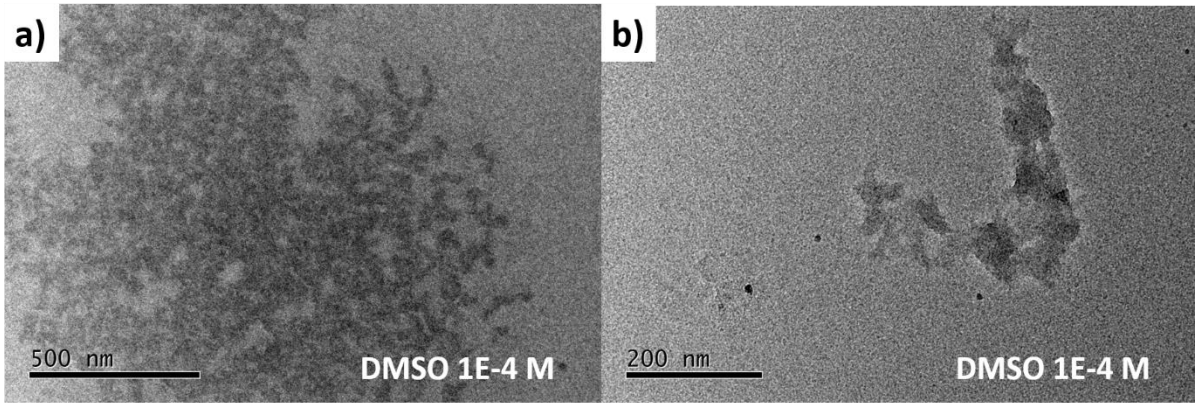

*Figure 7-24 Extra TEM images for **PDI-BA-1** in DMSO at 1× 10^{-4} M.*

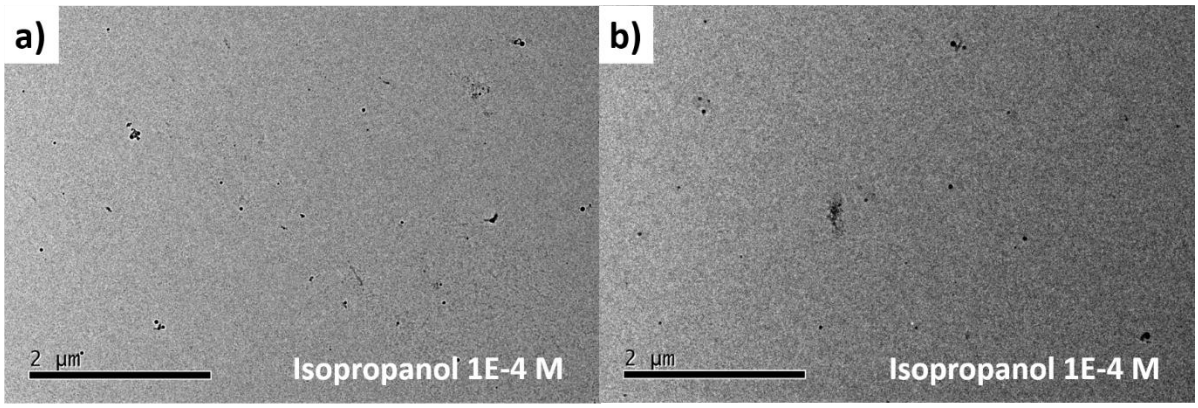

*Figure 7-25 Extra TEM images for **PDI-BA-1** in isopropanol at 1× 10^{-4} M.*

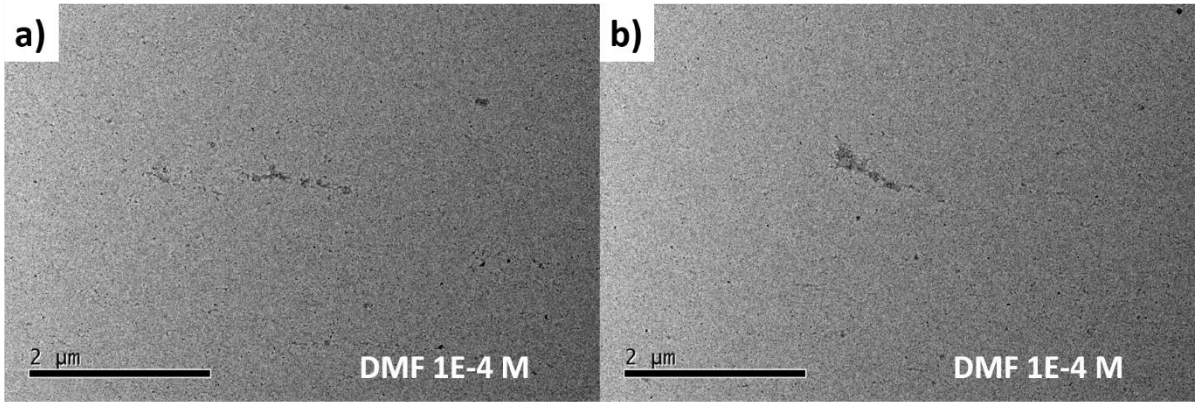

*Figure 7-26 Extra TEM images for **PDI-BA-1** in DMF at 1× 10^{-4} M.*

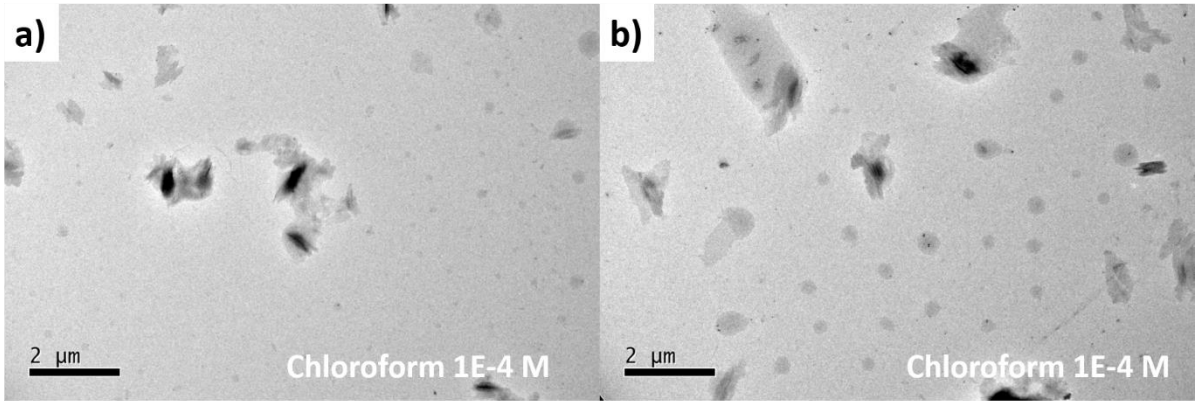

*Figure 7-27 Extra TEM images for **PDI-BA-1** in chloroform at 1× 10^{-4} M.*

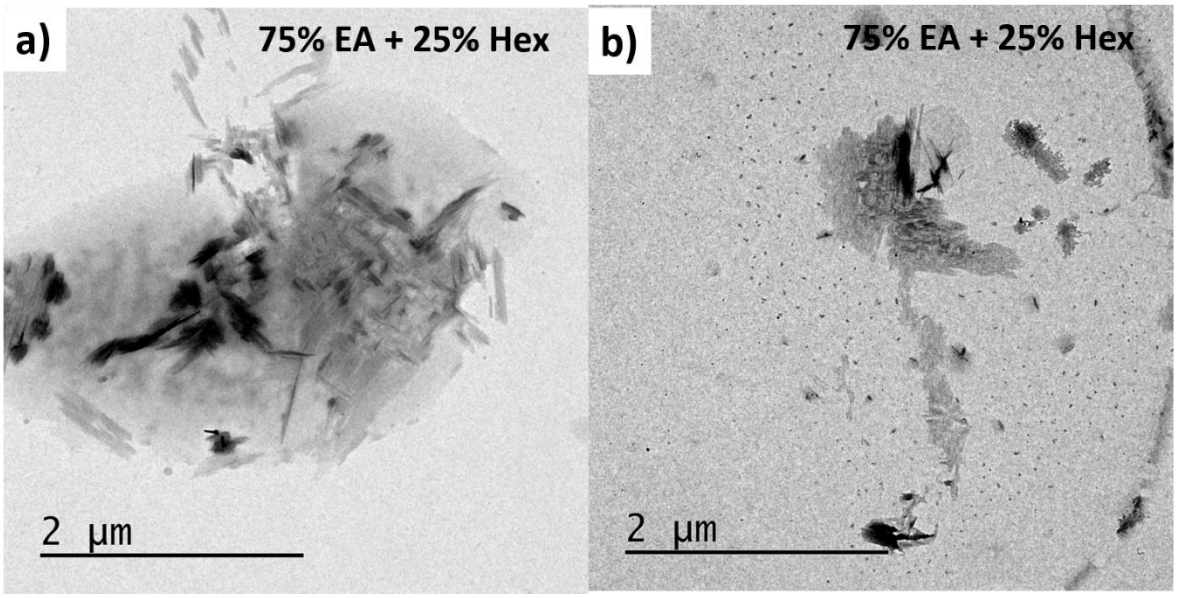

*Figure 7-28 Extra TEM images for **PDI-BA-1** in 3:1(v/v) EA : n-hexane at 1× 10^{-4} M.*

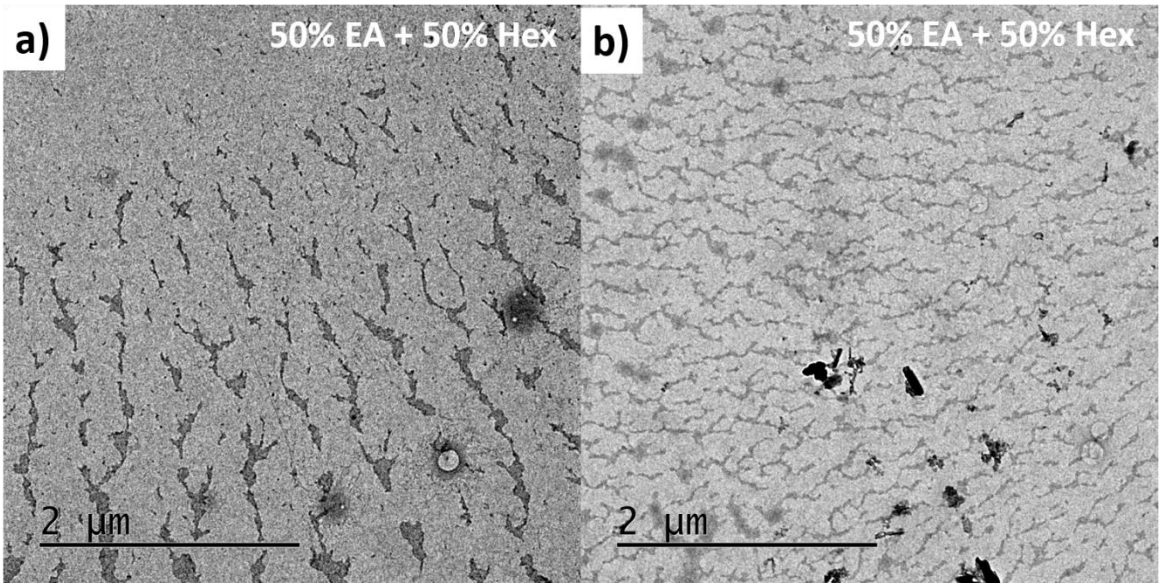

*Figure 7-29 Extra TEM images for **PDI-BA-1** in 1:1(v/v) EA : n-hexane at 1× 10^{-4} M.*

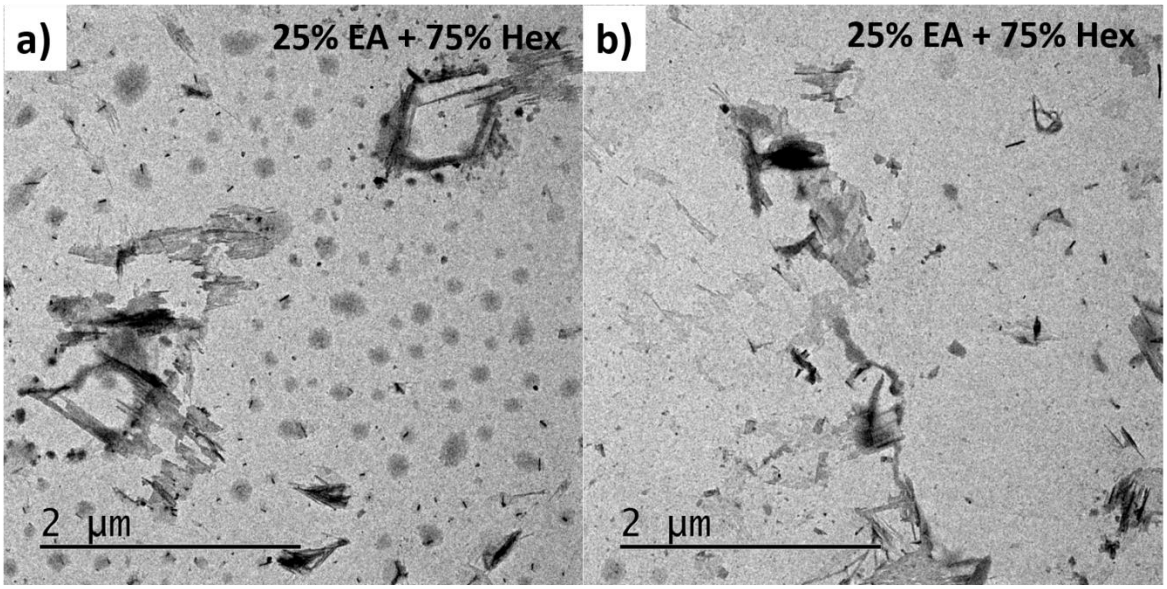

*Figure 7-30 Extra TEM images for **PDI-BA-1** in 1:3(v/v) EA : n-hexane at 1× 10^{-4} M.*

7.5. Modelling

7.5.1. Conformer searching of PDI-BA-1

7.5.1.1. 30 conformers of PDI-BA-1 searched by MMFF-PM6 (Spartan)

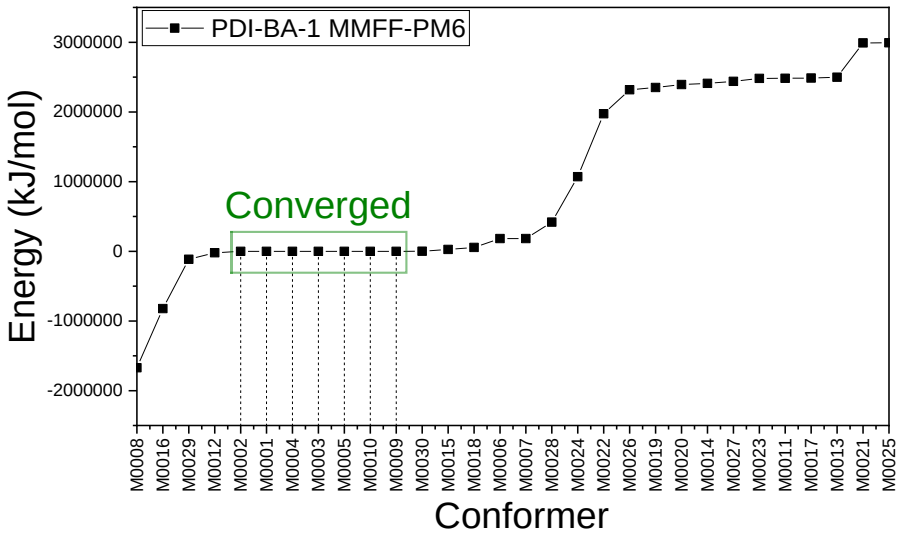

*Figure 7-31 PM6 energies of 30 **PDI-BA-1** conformers with lowest MMFF energies.*

7.5.1.2. PM6 energies of 100 PDI-BA-1 conformers searched by MMFF (Spartan)

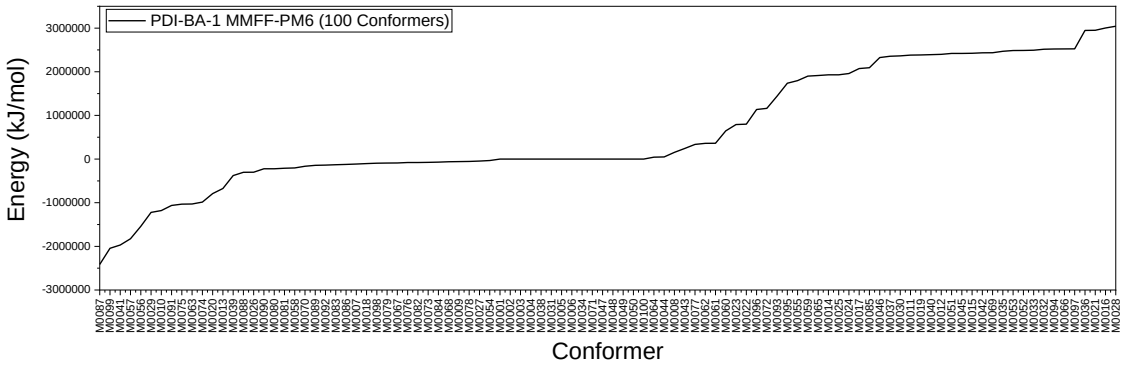

*Figure 7-32 PM6 energies of 100 **PDI-BA-1** conformers searched by MMFF (Spartan).*

7.5.2. Geometries of PDI-BA-1

7.5.2.1. PDI-BA-1-def

*Table 7-4 Default input geometry of **PDI-BA-1** (**PDI-BA-1-def**, X, Y, Z are atomic coordinates).*

Atom	X	Y	Z
C	-3.76072641	2.95580563	-2.06857053
C	-2.75875449	3.93459847	-2.27671441
C	-2.54125727	4.94441037	-1.35456368
C	-3.34446149	5.00419606	-0.16326379
C	-4.34847859	4.02147026	0.04294892
C	-4.54331434	2.99391891	-0.93231439
C	-1.49709334	5.96644354	-1.56903103
C	-3.15839965	6.03225696	0.82485874
C	-2.11425919	7.05430603	0.61037682
C	-1.31106622	6.99453197	-0.58093442
C	-1.89677460	8.06412591	1.53252117
C	-3.95724667	6.04721336	1.95579008
C	-4.95782863	5.06594817	2.15893793
C	-5.15381768	4.07005145	1.22364838
H	-5.57708270	5.10123397	3.06426304
H	-3.91205090	2.16628930	-2.81562550

Atom	X	Y	Z
C	-0.69819758	5.95144817	-2.69992791
C	0.30234579	6.93274359	-2.90310098
C	0.49827015	7.92868878	-1.96785699
C	-0.30708235	7.97728561	-0.78717625
H	0.92161539	6.89744361	-3.80841050
C	-0.89486199	9.04297411	1.32433366
H	-0.74358385	9.83253300	2.07135838
C	-0.11228600	9.00487796	0.18806256
H	-3.83179984	6.82021128	2.71902685
H	-2.49654247	8.12729670	2.44470591
H	-2.15893958	3.87137951	-3.18886340
H	-0.82355674	5.17838051	-3.46310668
C	-6.21033872	3.05174044	1.45986219
O	-6.93995241	3.01294171	2.42907110
C	-5.58831833	1.95528217	-0.73692697
O	-5.82517672	1.04799192	-1.50758602
C	0.93265170	10.04357462	-0.00739963
O	1.16955227	10.95085718	0.76326492
C	1.55477522	8.94700163	-2.20410235
O	2.28432084	8.98582666	-3.17335395
N	-6.35905602	2.05351654	0.45589937
N	1.70341822	9.94530265	-1.20019918
C	-7.39842114	1.03615193	0.66941612
H	-7.77017656	0.70203985	-0.27666370
H	-8.19988886	1.45901314	1.23839582
C	-6.79871529	-0.15739048	1.43584250
H	-6.89409765	-1.04464326	0.84543186
H	-5.76399639	0.02960018	1.63406281
C	2.74273025	10.96272141	-1.41371631
H	3.54376165	10.54018921	-1.98355420
H	3.11517589	11.29612649	-0.46765854

Atom	X	Y	Z
C	2.14260330	12.15686468	-2.17887610
H	2.23561271	13.04310289	-1.58656614
H	1.10851816	11.96872023	-2.37929962
N	-7.51675938	-0.33463813	2.70623455
H	-6.98960036	-0.93672646	3.30589529
N	2.86263478	12.33766480	-3.44764163
H	2.33636655	12.94135095	-4.04647783
C	-8.83360726	-0.93359833	2.44535464
O	-9.33589051	-1.76315068	3.19759228
C	4.17901340	12.93602343	-3.18303955
O	4.68257907	13.76739305	-3.93240808
C	-9.54098447	-0.45101552	1.16538147
C	-9.51451404	-1.23907484	0.01441091
C	-10.20839749	0.77374330	1.15678886
C	-10.15591221	-0.80270570	-1.14464564
H	-8.98890607	-2.20495495	0.02173717
C	-10.84920430	1.21084419	-0.00283148
H	-10.22920829	1.39506510	2.06379225
C	-10.82318494	0.42280914	-1.15342296
H	-10.13562395	-1.42409677	-2.05170574
H	-11.37500231	2.17674641	-0.00943299
Br	-11.70134202	1.02008353	-2.74093782
C	4.88423021	12.45029909	-1.90306255
C	5.56911904	11.23481633	-1.90243884
C	4.83837606	13.22552781	-0.74441422
C	6.20741059	10.79441903	-0.74319087
H	5.60443393	10.62350819	-2.81583743
C	5.47764272	12.78560772	0.41499009
H	4.29877200	14.18362820	-0.74478086
C	6.16198573	11.57020204	0.41582331
H	6.74673680	9.83607505	-0.74244405

Atom	X	Y	Z
H	5.44166692	13.39724816	1.32826767
Br	7.03631642	10.96678692	2.00312795

7.5.2.2. PDI-BA-1-PM6-G-VAC

*Table 7-5 Geometry of **PDI-BA-1** optimized with PM6 (Gaussian) in vacuum (**PDI-BA-1-PM6-G-VAC**, X, Y, Z are atomic coordinates)*

Atom	X	Y	Z
C	-3.59699537	1.21677978	1.89082712
C	-2.29441224	1.73934845	1.76545492
C	-1.24561865	0.95730103	1.30692378
C	-1.49645142	-0.39798384	0.92239504
C	-2.79953402	-0.93057898	1.08812552
C	-3.84873825	-0.10152925	1.56807942
C	0.11324449	1.47895866	1.20892326
C	-0.46893716	-1.23078559	0.37592657
C	0.85321904	-0.65954718	0.14255397
C	1.12322108	0.66993454	0.59810001
C	1.85146281	-1.37208003	-0.50369383
C	-0.75286484	-2.55538793	0.08160880
C	-2.04029435	-3.09132978	0.28532344
C	-3.05455432	-2.29253937	0.77374651
H	-2.23377197	-4.15221628	0.04864758
H	-4.41319542	1.86557506	2.25381681
C	0.44725590	2.73512216	1.69088135
C	1.75587034	3.24270005	1.56638540
C	2.73351169	2.49348292	0.94316590
C	2.42806667	1.20050864	0.43992871
H	1.99355851	4.24399248	1.96628363
C	3.13648272	-0.82527981	-0.69328931
H	3.90912764	-1.41513677	-1.21668726
C	3.42860497	0.43849115	-0.22120997

Atom	X	Y	Z
H	0.01969534	-3.23212486	-0.31757166
H	1.67116206	-2.38741314	-0.89198697
H	-2.14338463	2.79466175	2.04402874
H	-0.29833525	3.37490488	2.18985221
C	-4.40759214	-2.85893742	0.97922265
O	-4.66421306	-4.05618844	0.74511745
C	-5.21670517	-0.64921020	1.71803404
O	-6.17496852	0.06520417	2.07416596
C	4.78440917	1.00345145	-0.41003169
O	5.67778295	0.38718283	-1.02389322
C	4.10491878	3.03748542	0.80896992
O	4.41964725	4.14645461	1.28359159
N	-5.42665035	-2.01516549	1.45728103
N	5.06529877	2.27659495	0.11840981
C	-6.74426519	-2.58001471	1.68255715
H	-7.30884561	-1.89849855	2.38160328
H	-6.61394756	-3.58050798	2.18639974
C	-7.55510200	-2.78477591	0.37427613
H	-7.48932400	-1.86179620	-0.26734770
H	-7.08641776	-3.64029591	-0.19529520
C	6.40214892	2.81415906	-0.05463180
H	6.35202668	3.93606777	0.04562750
H	6.74728748	2.56443924	-1.09893914
C	7.42043957	2.24631100	0.97171768
H	7.50253920	1.13154973	0.83008141
H	7.03282258	2.44133931	2.01410129
N	-8.92738450	-3.10900783	0.62361980
H	-9.09907987	-3.94731030	1.13686059
N	8.70975242	2.85682539	0.86111519
H	8.75608205	3.83115611	1.07337042
C	-9.99698396	-2.26039094	0.44484541

Atom	X	Y	Z
O	-11.12641485	-2.63288354	0.83928713
C	9.84240473	2.28967806	0.32560782
O	10.86770665	3.00555092	0.22696151
C	-9.82696360	-0.96345231	-0.26991002
C	-10.55372081	-0.75632808	-1.44770925
C	-9.00829454	0.05005064	0.23463925
C	-10.44565102	0.45374090	-2.12995539
H	-11.21405814	-1.54947548	-1.83320582
C	-8.90691386	1.26434856	-0.44472787
H	-8.43194108	-0.10046262	1.16471687
C	-9.61685382	1.46419759	-1.63198210
H	-11.01959095	0.60319296	-3.05857829
H	-8.25899305	2.05644686	-0.03601352
Br	-9.44719224	3.07559248	-2.57278057
C	9.88627146	0.85562877	-0.07562591
C	8.99613722	0.31891907	-1.00875318
C	10.91244711	0.05935283	0.44785924
C	9.14211526	-1.00253962	-1.43125530
H	8.17028151	0.92575085	-1.41755452
C	11.05311184	-1.26313397	0.03258702
H	11.61691517	0.48527730	1.18024432
C	10.17438164	-1.79250679	-0.91779356
H	8.43525416	-1.41056149	-2.17176063
H	11.86513073	-1.87839159	0.45238505
Br	10.39924630	-3.54865450	-1.53054755

7.5.2.3. PDI-BA-1-DFT

*Table 7-6 Geometry of **PDI-BA-1** optimized with B3LYP/6-31g(d)/PCM (chloroform) (**PDI-BA-1-DFT**, X, Y, Z are atomic coordinates)*

Atom	X	Y	Z
C	-3.41748200	-0.95415200	-1.24751900

Atom	X	Y	Z
C	-2.14970100	-1.52002500	-1.08078200
C	-1.08162600	-0.79081400	-0.55349000
C	-1.30115700	0.57175400	-0.17474100
C	-2.59947300	1.14265300	-0.35022300
C	-3.65163400	0.36385000	-0.89140300
C	0.25476400	-1.37733200	-0.37503100
C	-0.25417200	1.37712000	0.37605300
C	1.08216600	0.79054000	0.55470400
C	1.30173100	-0.57198700	0.17582800
C	2.15015900	1.51965400	1.08229600
C	-0.53950400	2.69831700	0.72764600
C	-1.81330800	3.24847500	0.55432000
C	-2.84052800	2.48840800	0.01976700
H	-2.01091400	4.27697700	0.83573300
H	-4.23148900	-1.54119600	-1.65821600
C	0.54015600	-2.69845700	-0.72684700
C	1.81397800	-3.24859600	-0.55358200
C	2.84116200	-2.48857100	-0.01890100
C	2.60005600	-1.14287600	0.35127600
H	2.01162900	-4.27704500	-0.83515800
C	3.41793700	0.95377600	1.24904300
H	4.23188800	1.54075100	1.65994700
C	3.65216600	-0.36413500	0.89264400
H	0.23054700	3.33262300	1.14861100
H	2.01707300	2.55327900	1.37647400
H	-2.01668200	-2.55373500	-1.37468800
H	-0.22985200	-3.33270800	-1.14797600
C	-4.17832700	3.09436100	-0.15364900
O	-4.43209900	4.24868200	0.17436900
C	-5.00094000	0.93867500	-1.07909900
O	-5.94048300	0.28764900	-1.52813000
C	5.00149100	-0.93894100	1.08028400
O	5.94093600	-0.28801100	1.52965700
C	4.17898600	-3.09449500	0.15444200
O	4.43265400	-4.24895400	-0.17317300
N	-5.17268700	2.28394500	-0.72370200
N	5.17325400	-2.28418500	0.72479000
C	-6.50071300	2.87818000	-0.93327700

Atom	X	Y	Z
H	-6.94753900	2.39161200	-1.79963900
H	-6.35374200	3.93658900	-1.15062800
C	-7.40429800	2.71187100	0.30052100
H	-7.48474800	1.65937900	0.57176900
H	-6.95562100	3.24067600	1.14938100
C	6.50121100	-2.87850900	0.93460900
H	6.35413600	-3.93687400	1.15211500
H	6.94796700	-2.39181100	1.80092900
C	7.40497800	-2.71230700	-0.29905200
H	7.48522100	-1.65983000	-0.57041200
H	6.95661500	-3.24134000	-1.14793900
N	-8.73561900	3.24779500	0.04671500
H	-8.81581200	4.25922300	0.04989800
N	8.73642200	-3.24779800	-0.04475200
H	8.81684900	-4.25921300	-0.04784100
C	-9.96403500	2.64911200	0.14371600
O	-10.98456200	3.33875400	0.20255000
C	9.96462800	-2.64891400	-0.14372800
O	10.98525300	-3.33831300	-0.20345400
C	-10.07069700	1.14868300	0.16370300
C	-11.10462100	0.60152300	0.93830000
C	-9.27243500	0.29036500	-0.60535800
C	-11.32009100	-0.77302100	0.97960800
H	-11.74270400	1.26826500	1.50846400
C	-9.48754100	-1.08875200	-0.58524500
H	-8.48048100	0.67343300	-1.23887900
C	-10.50418500	-1.60537600	0.21346700
H	-12.11248900	-1.19066400	1.59078800
H	-8.86970000	-1.74643300	-1.18626100
Br	-10.79388800	-3.49794000	0.25544800
C	10.07080700	-1.14847600	-0.16432800
C	9.27312300	-0.29027500	0.60547200
C	11.10358400	-0.60113900	-0.94031000
C	9.48767500	1.08891100	0.58475200
H	8.48208000	-0.67356200	1.24001000
C	11.31848800	0.77348000	-0.98221300
H	11.74121900	-1.26779200	-1.51107900
C	10.50318200	1.60571400	-0.21530400

Atom	X	Y	Z
H	8.87030800	1.74652400	1.18632700
H	12.10999600	1.19127200	-1.59444300
Br	10.79209600	3.49837500	-0.25811700

7.5.2.4. PDI-BA-1-RO-I

*Table 7-7 Input geometry of reactive-open **PDI-BA-1** conformer (X, Y, Z are atomic coordinates)*

Atom	X	Y	Z
C	-3.41748200	-0.95415200	-1.24751900
C	-2.14970100	-1.52002500	-1.08078200
C	-1.08162600	-0.79081400	-0.55349000
C	-1.30115700	0.57175400	-0.17474100
C	-2.59947300	1.14265300	-0.35022300
C	-3.65163400	0.36385000	-0.89140300
C	0.25476400	-1.37733200	-0.37503100
C	-0.25417200	1.37712000	0.37605300
C	1.08216600	0.79054000	0.55470400
C	1.30173100	-0.57198700	0.17582800
C	2.15015900	1.51965400	1.08229600
C	-0.53950400	2.69831700	0.72764600
C	-1.81330800	3.24847500	0.55432000
C	-2.84052800	2.48840800	0.01976700
H	-2.01091400	4.27697700	0.83573300
H	-4.23148900	-1.54119600	-1.65821600
C	0.54015600	-2.69845700	-0.72684700
C	1.81397800	-3.24859600	-0.55358200
C	2.84116200	-2.48857100	-0.01890100
C	2.60005600	-1.14287600	0.35127600
H	2.01162900	-4.27704500	-0.83515800
C	3.41793700	0.95377600	1.24904300
H	4.23188800	1.54075100	1.65994700

Atom	X	Y	Z
C	3.65216600	-0.36413500	0.89264400
H	0.23054700	3.33262300	1.14861100
H	2.01707300	2.55327900	1.37647400
H	-2.01668200	-2.55373500	-1.37468800
H	-0.22985200	-3.33270800	-1.14797600
C	-4.17832700	3.09436100	-0.15364900
O	-4.43209900	4.24868200	0.17436900
C	-5.00094000	0.93867500	-1.07909900
O	-5.94048300	0.28764900	-1.52813000
C	5.00149100	-0.93894100	1.08028400
O	5.94093600	-0.28801100	1.52965700
C	4.17898600	-3.09449500	0.15444200
O	4.43265400	-4.24895400	-0.17317300
N	-5.17268700	2.28394500	-0.72370200
N	5.17325400	-2.28418500	0.72479000
C	-6.50071300	2.87818000	-0.93327700
H	-6.94753900	2.39161200	-1.79963900
H	-6.35374200	3.93658900	-1.15062800
C	-7.40429800	2.71187100	0.30052100
H	-7.48474800	1.65937900	0.57176900
H	-6.95562100	3.24067600	1.14938100
C	6.50121100	-2.87850900	0.93460900
H	6.35413600	-3.93687400	1.15211500
H	6.94796700	-2.39181100	1.80092900
C	7.40497800	-2.71230700	-0.29905200
H	7.48522100	-1.65983000	-0.57041200
H	6.95661500	-3.24134000	-1.14793900
N	-8.73561900	3.24779500	0.04671500
H	-8.81581200	4.25922300	0.04989800
N	8.73642200	-3.24779800	-0.04475200
H	8.81684900	-4.25921300	-0.04784100

Atom	X	Y	Z
C	-9.96403500	2.64911200	0.14371600
O	-10.05168070	1.47386597	0.50656290
C	9.96462800	-2.64891400	-0.14372800
O	10.05179964	-1.47453333	-0.50943925
C	-11.20924162	3.42942276	-0.17821419
C	-12.26808919	2.71405479	-0.75741528
C	-11.40085305	4.77952311	0.14721003
C	-13.48128366	3.33369986	-1.04325446
H	-12.13072016	1.66124521	-0.97990919
C	-12.61769568	5.40931056	-0.11981172
H	-10.61866835	5.36199835	0.62069791
C	-13.64154382	4.68090260	-0.71944750
H	-14.29121690	2.77847990	-1.50325469
H	-12.76085353	6.45240100	0.13895497
Br	-15.30783933	5.54432433	-1.10082774
C	11.21014834	-3.42829955	0.17914935
C	11.40158268	-4.77912968	-0.14335898
C	12.26934498	-2.71156639	0.75599442
C	12.61863643	-5.40825136	0.12422652
H	10.61903608	-5.36265202	-0.61497209
C	13.48277946	-3.33050514	1.04236581
H	12.13206003	-1.65826896	0.97621983
C	13.64287588	-4.67842644	0.72148571
H	12.76167930	-6.45191683	-0.13227001
H	14.29301113	-2.77420972	1.50053683
Br	15.30947074	-5.54091223	1.10365025

7.5.2.5. PDI-BA-1-RO

*Table 7-8 Output geometry of reactive-open **PDI-BA-1** conformer (X, Y, Z are atomic coordinates).*

Atom	X	Y	Z
C	-2.88774600	2.40515800	0.16163100
C	-1.49358700	2.42228900	0.05263500
C	-0.74245200	1.24524900	0.02480400
C	-1.42778100	-0.00812600	0.11245300
C	-2.85246800	-0.01593700	0.22537100
C	-3.57156000	1.20391800	0.24888000
C	0.72333500	1.25340100	-0.09092900
C	-0.72332500	-1.25379400	0.09052800
C	0.74246400	-1.24564100	-0.02520200
C	1.42779200	0.00773400	-0.11285800
C	1.49360200	-2.42268000	-0.05302400
C	-1.45630100	-2.43922300	0.18029200
C	-2.85063400	-2.43763900	0.28778700
C	-3.55267900	-1.24399600	0.31220900
H	-3.39778500	-3.37159400	0.35414700
H	-3.44928500	3.33271500	0.17984100
C	1.45631000	2.43883100	-0.18069100
C	2.85064100	2.43724900	-0.28819400
C	3.55268600	1.24360600	-0.31263800
C	2.85247800	0.01554700	-0.22578400
H	3.39779100	3.37120400	-0.35456500
C	2.88776200	-2.40554700	-0.16201100
H	3.44930300	-3.33310300	-0.18020900
C	3.57157400	-1.20430700	-0.24927800
H	-0.95286600	-3.39793000	0.16811800
H	1.00509900	-3.38709200	0.01016400
H	-1.00508200	3.38670000	-0.01054900
H	0.95287300	3.39753800	-0.16851500
C	-5.02758500	-1.26943400	0.42439800
O	-5.66907900	-2.31481300	0.47753000
C	-5.04729900	1.21509400	0.36375700
O	-5.70126600	2.25163900	0.36980000
C	5.04731400	-1.21548000	-0.36413500
O	5.70129000	-2.25202100	-0.37002800
C	5.02758800	1.26904600	-0.42487200
O	5.66909600	2.31442900	-0.47776800
N	-5.68395300	-0.03181000	0.47158200
N	5.68396900	0.03142500	-0.47194200

Atom	X	Y	Z
C	-7.14896200	-0.04908200	0.60572700
H	-7.44854300	0.88294800	1.08243400
H	-7.40803200	-0.89495500	1.24330000
C	-7.84282900	-0.18334500	-0.76206100
H	-7.65703300	0.71348700	-1.35660100
H	-7.44586300	-1.05149700	-1.29476900
C	7.14899200	0.04870900	-0.60593200
H	7.40810200	0.89455700	-1.24352200
H	7.44864300	-0.88333800	-1.08255900
C	7.84271600	0.18306800	0.76191900
H	7.65696400	-0.71377800	1.35645400
H	7.44559500	1.05118000	1.29457600
N	-9.28186000	-0.34970500	-0.63200900
H	-9.62821000	-1.27544200	-0.42210400
N	9.28173900	0.34961900	0.63200500
H	9.62798300	1.27539800	0.42211300
C	-10.12830500	0.71462700	-0.50789800
O	-9.72875500	1.87991400	-0.52658000
C	10.12834400	-0.71460200	0.50799500
O	9.72896200	-1.87994500	0.52671600
C	-11.58873900	0.39031500	-0.35466800
C	-12.40709400	1.36154900	0.23729100
C	-12.16598400	-0.80775600	-0.79819700
C	-13.77029600	1.13826100	0.41154300
H	-11.95872300	2.29526100	0.55942300
C	-13.53150400	-1.04236100	-0.63841600
H	-11.56707300	-1.55951000	-1.30388200
C	-14.31752800	-0.06706500	-0.02786400
H	-14.39865000	1.88835400	0.87886000
H	-13.97689300	-1.96595800	-0.99083700
Br	-16.19077900	-0.38511000	0.20248800
C	11.58875000	-0.39009700	0.35490400
C	12.16578800	0.80807200	0.79843900
C	12.40729800	-1.36124500	-0.23693000
C	13.53129200	1.04285500	0.63878600
H	11.56672200	1.55976400	1.30403100
C	13.77048800	-1.13778000	-0.41105200
H	11.95908600	-2.29503100	-0.55906800

Atom	X	Y	Z
C	14.31751100	0.06763900	0.02835800
H	13.97652000	1.96652800	0.99121200
H	14.39899100	-1.88780900	-0.87827200
Br	16.19074200	0.38592800	-0.20181500

7.5.2.6. PDI-BA-1-TC-I

*Table 7-9 Input geometry of trapped-close **PDI-BA-1** conformer (X, Y, Z are atomic coordinates)*

Atom	X	Y	Z
C	-3.76072641	2.95580563	-2.06857053
C	-2.75875449	3.93459847	-2.27671441
C	-2.54125727	4.94441037	-1.35456368
C	-3.34446149	5.00419606	-0.16326379
C	-4.34847859	4.02147026	0.04294892
C	-4.54331434	2.99391891	-0.93231439
C	-1.49709334	5.96644354	-1.56903103
C	-3.15839965	6.03225696	0.82485874
C	-2.11425919	7.05430603	0.61037682
C	-1.31106622	6.99453197	-0.58093442
C	-1.89677460	8.06412591	1.53252117
C	-3.95724667	6.04721336	1.95579008
C	-4.95782863	5.06594817	2.15893793
C	-5.15381768	4.07005145	1.22364838
H	-5.57708270	5.10123397	3.06426304
H	-3.91205090	2.16628930	-2.81562550
C	-0.69819758	5.95144817	-2.69992791
C	0.30234579	6.93274359	-2.90310098
C	0.49827015	7.92868878	-1.96785699
C	-0.30708235	7.97728561	-0.78717625
H	0.92161539	6.89744361	-3.80841050
C	-0.89486199	9.04297411	1.32433366

Atom	X	Y	Z
H	-0.74358385	9.83253300	2.07135838
C	-0.11228600	9.00487796	0.18806256
H	-3.83179984	6.82021128	2.71902685
H	-2.49654247	8.12729670	2.44470591
H	-2.15893958	3.87137951	-3.18886340
H	-0.82355674	5.17838051	-3.46310668
C	-6.21033872	3.05174044	1.45986219
O	-6.93995241	3.01294171	2.42907110
C	-5.58831833	1.95528217	-0.73692697
O	-5.82517672	1.04799192	-1.50758602
C	0.93265170	10.04357462	-0.00739963
O	1.16955227	10.95085718	0.76326492
C	1.55477522	8.94700163	-2.20410235
O	2.28432084	8.98582666	-3.17335395
N	-6.35905602	2.05351654	0.45589937
N	1.70341822	9.94530265	-1.20019918
C	-7.39842114	1.03615193	0.66941612
H	-8.35383523	1.51227939	0.74280935
H	-7.19510547	0.50306383	1.57461213
C	-7.74151850	-0.13349703	-0.27175629
H	-7.60204015	-1.05992833	0.24512944
H	-8.76076998	-0.05071356	-0.58667423
C	2.74273025	10.96272141	-1.41371631
H	2.53942244	11.49575424	-2.31894662
H	3.69817730	10.48664997	-1.48704379
C	3.08571288	12.13243539	-0.47258288
H	2.94620080	13.05883399	-0.98951808
H	4.10495522	12.04972944	-0.15761496
N	-7.14980703	-0.51718079	-1.56154864
H	-6.42068967	0.12505950	-1.79801277
N	2.49391939	12.51614275	0.81716481

Atom	X	Y	Z
H	1.76483094	11.87386850	1.05362589
C	-8.18580303	-0.48782354	-2.60402186
O	-7.95398487	-0.10385019	-3.74644553
C	3.52987003	12.48689797	1.85968627
O	3.29792876	12.10333326	3.00222221
C	-9.58136362	-0.97084988	-2.16733409
C	-10.57624354	-0.04233006	-1.85986655
C	-9.85087400	-2.33657147	-2.07948860
C	-11.84052252	-0.47952515	-1.46530246
H	-10.36368106	1.03430614	-1.92996286
C	-11.11519081	-2.77406198	-1.68386890
H	-9.06681593	-3.06852631	-2.32161269
C	-12.11002373	-1.84582441	-1.37691699
H	-12.62493671	0.25228294	-1.22354266
H	-11.32727572	-3.85093447	-1.61429982
Br	-13.84150081	-2.44413228	-0.83644053
C	4.92552186	12.96959636	1.42292746
C	5.20135428	14.33550361	1.35447834
C	5.91388066	12.04129978	1.09587938
C	6.46508149	14.77293425	0.95841052
H	4.42170065	15.06711103	1.61164088
C	7.17834655	12.47868617	0.70062113
H	5.69670680	10.96471188	1.14994465
C	7.45404018	13.84425605	0.63170869
H	6.68237784	15.84954921	0.90383014
H	7.95755273	11.74652966	0.44321330
Br	9.18456482	14.44370992	0.08945460

7.5.2.7. PDI-BA-1-TC

*Table 7-10 Output geometry of trapped-close **PDI-BA-1** conformer (X, Y, Z are atomic coordinates)*

Atom	X	Y	Z
C	2.72727300	-2.56972800	0.33962400
C	1.39438600	-2.48156400	-0.07329100
C	0.69237900	-1.27437100	-0.04290000
C	1.36331400	-0.10104400	0.42762200
C	2.72325500	-0.20125800	0.85394900
C	3.39428200	-1.44743400	0.80366100
C	-0.70763100	-1.17147100	-0.47965500
C	0.70833200	1.17014200	0.48125500
C	-0.69155500	1.27312100	0.04412600
C	-1.36255300	0.09975400	-0.42620700
C	-1.39339400	2.48042300	0.07401900
C	1.42498700	2.27413200	0.94885600
C	2.75610000	2.16700600	1.36316900
C	3.40890200	0.94571500	1.32179600
H	3.29141900	3.03860400	1.72335800
H	3.25300600	-3.51731200	0.30099800
C	-1.42446800	-2.27557400	-0.94671200
C	-2.75562300	-2.16847100	-1.36090100
C	-3.40829000	-0.94709500	-1.31993700
C	-2.72250200	0.19996500	-0.85250800
H	-3.29107700	-3.04015500	-1.72068200
C	-2.72625300	2.56861100	-0.33898300
H	-3.25186800	3.51627500	-0.30071300
C	-3.39340400	1.44622400	-0.80259000
H	0.95811800	3.24972400	1.00097100
H	-0.91425700	3.38558500	0.42551900
H	0.91537500	-3.38665100	-0.42515600
H	-0.95773100	-3.25125000	-0.99843500
C	4.81324600	0.85698800	1.77538200
O	5.44034600	1.82705400	2.18611100
C	4.80459900	-1.56269400	1.22469800
O	5.43239900	-2.61874300	1.14200100
C	-4.80373200	1.56148800	-1.22359200
O	-5.43142000	2.61763200	-1.14126400
C	-4.81265000	-0.85837600	-1.77348000
O	-5.43988000	-1.82851500	-2.18383700
N	5.41952700	-0.41164000	1.72660800
N	-5.41880500	0.41032600	-1.72508000

Atom	X	Y	Z
C	6.78984600	-0.52523600	2.26663000
H	6.88469100	-1.51355900	2.71865100
H	6.87807300	0.23720300	3.03968100
C	7.89256400	-0.29496900	1.22779700
H	7.66073000	0.62313700	0.67464200
H	8.83159100	-0.12331000	1.76366700
C	-6.78914700	0.52388700	-2.26505600
H	-6.87744600	-0.23868500	-3.03796900
H	-6.88397900	1.51214100	-2.71722300
C	-7.89182600	0.29384600	-1.22611400
H	-7.65994600	-0.62410700	-0.67270800
H	-8.83086400	0.12202400	-1.76188800
N	8.03799800	-1.44373200	0.33136800
H	7.28473400	-2.12725700	0.37267700
N	-8.03738000	1.44279700	-0.32996400
H	-7.28360800	2.12579100	-0.37050500
C	9.18062800	-1.94392800	-0.22363500
O	9.21907200	-3.09416300	-0.66936700
C	-9.18015300	1.94373700	0.22406300
O	-9.21822400	3.09399400	0.66976500
C	10.39919600	-1.06521500	-0.30580500
C	11.65039100	-1.68025500	-0.15564400
C	10.34716300	0.30073600	-0.61326900
C	12.82747700	-0.94556500	-0.26966700
H	11.69137300	-2.74486800	0.04936800
C	11.51872900	1.04642300	-0.75093300
H	9.39369100	0.79211600	-0.77605700
C	12.74641000	0.41498300	-0.56671000
H	13.79249700	-1.42230800	-0.13793400
H	11.47465700	2.10056000	-1.00116400
Br	14.35845000	1.43468700	-0.73544900
C	-10.39935400	1.06580100	0.30521800
C	-10.34840400	-0.30019200	0.61268600
C	-11.65004900	1.68162100	0.15410100
C	-11.52053400	-1.04515900	0.74943800
H	-9.39535400	-0.79216700	0.77616000
C	-12.82767500	0.94765100	0.26720800
H	-11.69024000	2.74625900	-0.05094000

Atom	X	Y	Z
C	-12.74768100	-0.41295100	0.56429300
H	-11.47730700	-2.09933100	0.99966900
H	-13.79229900	1.42499200	0.13473600
Br	-14.36048400	-1.43165800	0.73177700

7.5.3. Excitation analysis of PDI-BA-1

7.5.3.1. Excitation contribution of PDI-BA-1 UV-Vis spectra (predicted)

*Table 7-11 Excitation contribution of **PDI-BA-1** UV-Vis spectra (30 allowed excited states were compared, with states having non-zero oscillator strength list here).*

Excited state	Excitation energy (eV)	λ (nm)	Oscillator strength	Excited from	Excited to
1	2.27	546	0.9383	212	213
3	2.84	437	0.0003	210	213
5	3.02	411	0.0012	208	213
7	3.34	371	0.0001	200	214
				201	213
				206	213
10	3.38	366	0.0004	201	213
				206	213
13	3.49	355	0.0015	201	213
				202	213
				204	213
				205	213
15	3.52	352	0.0737	201	213
				202	213
				204	213
				212	219
17	3.80	326	0.0259	192	213
				197	213
21	4.04	307	0.0410	192	213
				197	213

Excited state	Excitation energy (eV)	λ (nm)	Oscillator strength	Excited from	Excited to
				212	219
25	4.39	282	0.0012	211	214
27	4.54	273	0.0002	209	214
				211	215
				212	217
				212	219
28	4.56	272	0.0053	209	214
				212	217
30	4.56	272	0.0259	209	214
				211	215

7.5.4. Geometries of TANI-PDI

7.5.4.1. TP-def

*Table 7-12 Default input geometry of **TANI-PDI (TP-def**, X, Y, Z are atomic coordinates)*

Atom	X	Y	Z
C	-2.18744758	-1.67622729	-2.55733084
C	-1.27454446	-2.01744479	-1.53018148
C	-0.64702711	-1.04046177	-0.77556742
C	-0.92544941	0.34600518	-1.03560878
C	-1.84300333	0.68398195	-2.06501450
C	-2.47012729	-0.35089972	-2.82421601
C	0.30704437	-1.39200345	0.29537275
C	-0.30704437	1.39200345	-0.29537275
C	0.64702711	1.04046177	0.77556742
C	0.92544941	-0.34600518	1.03560878
C	1.27454446	2.01744479	1.53018148
C	-0.60303578	2.71980887	-0.57350005
C	-1.52040666	3.05264375	-1.59945778
C	-2.13293940	2.05649942	-2.33426326
H	-1.74295046	4.10720750	-1.80771275
H	-2.66914010	-2.47096851	-3.14132260
C	0.60303578	-2.71980887	0.57350005

Atom	X	Y	Z
C	1.52040666	-3.05264375	1.59945778
C	2.13293940	-2.05649942	2.33426326
C	1.84300333	-0.68398195	2.06501450
H	1.74295046	-4.10720750	1.80771275
C	2.18744758	1.67622729	2.55733084
H	2.66914010	2.47096851	3.14132260
C	2.47012729	0.35089972	2.82421601
H	-0.13791285	3.53642037	-0.01396104
H	1.08353351	3.08570487	1.36049225
H	-1.08353351	-3.08570487	-1.36049225
H	0.13791285	-3.53642037	0.01396104
C	-3.09499307	2.43545839	-3.40110674
O	-3.40171181	3.58029212	-3.66703490
C	-3.42912086	-0.02204079	-3.90995506
O	-3.98940330	-0.85677504	-4.59520448
C	3.42912086	0.02204079	3.90995506
O	3.98940330	0.85677504	4.59520448
C	3.09499307	-2.43545839	3.40110674
O	3.40171181	-3.58029212	3.66703490
N	-3.68376527	1.36335064	-4.14269033
N	3.68376527	-1.36335064	4.14269033
C	-4.64272946	1.72473991	-5.22996946
H	-4.73970783	0.86168953	-5.93171996
H	-4.22172215	2.57726322	-5.81118344
C	-6.01711504	2.10629744	-4.63101510
H	-6.30303873	1.39836563	-3.81998511
H	-5.95301501	3.11608303	-4.15778505
C	4.64272946	-1.72473991	5.22996946
H	4.22172215	-2.57726322	5.81118344
H	4.73970783	-0.86168953	5.93171996
C	6.01711504	-2.10629744	4.63101510
H	6.30303873	-1.39836563	3.81998511
H	5.95301501	-3.11608303	4.15778505
N	-7.03967445	2.12807819	-5.68934562
H	-7.00653989	2.91407995	-6.34050457
N	7.03967445	-2.12807819	5.68934562
H	7.00653989	-2.91407995	6.34050457
C	-7.97470696	1.11948273	-5.94643164

Atom	X	Y	Z
O	-8.71378387	1.26091847	-6.90732392
C	7.97470696	-1.11948273	5.94643164
O	8.71378387	-1.26091847	6.90732392
C	-8.05384115	-0.04132649	-5.00421656
C	-9.22885191	-0.21037467	-4.25752818
C	-7.01236447	-0.97151825	-4.90909938
C	-9.35658545	-1.30297728	-3.39529985
H	-10.04712344	0.50615839	-4.35693400
C	-7.13544174	-2.07005474	-4.05171907
H	-6.09333427	-0.84961445	-5.49305926
C	-8.30437033	-2.21736217	-3.30346370
H	-10.26905079	-1.43603247	-2.81226575
H	-6.32106666	-2.79324488	-3.98005717
C	8.05384115	0.04132649	5.00421656
C	7.01236447	0.97151825	4.90909938
C	9.22885191	0.21037467	4.25752818
C	7.13544174	2.07005474	4.05171907
H	6.09333427	0.84961445	5.49305926
C	9.35658545	1.30297728	3.39529985
H	10.04712344	-0.50615839	4.35693400
C	8.30437033	2.21736217	3.30346370
H	6.32106666	2.79324488	3.98005717
H	10.26905079	1.43603247	2.81226575
N	-8.43124577	-3.36448611	-2.39301914
H	-8.66390685	-4.18290988	-2.91842502
N	8.43124577	3.36448611	2.39301914
H	8.66390685	4.18290988	2.91842502
C	-9.49093676	-3.09532989	-1.41041549
C	-10.81451434	-3.42445680	-1.70416585
C	-9.17324186	-2.51101620	-0.18436672
C	-11.82019900	-3.16867292	-0.77228886
H	-11.06475845	-3.88440217	-2.67115599
C	-10.17897897	-2.25599251	0.74829917
H	-8.13008336	-2.25171241	0.04738942
C	-11.50232679	-2.58457865	0.45449868
H	-12.86356689	-3.42749119	-1.00400649
H	-9.92813606	-1.79565460	1.71506753
C	9.49093676	3.09532989	1.41041549

Atom	X	Y	Z
C	10.81451434	3.42445680	1.70416585
C	9.17324186	2.51101620	0.18436672
C	11.82019900	3.16867292	0.77228886
H	11.06475845	3.88440217	2.67115599
C	10.17897897	2.25599251	-0.74829917
H	8.13008336	2.25171241	-0.04738942
C	11.50232679	2.58457865	-0.45449868
H	12.86356689	3.42749119	1.00400649
H	9.92813606	1.79565460	-1.71506753
N	-12.56251538	-2.31518531	1.43650041
H	-12.72690098	-3.13619586	1.98323530
N	12.56251538	2.31518531	-1.43650041
H	12.72690098	3.13619586	-1.98323530
C	-13.79755868	-1.93923059	0.73348825
C	-14.65749897	-2.92888505	0.25645768
C	-14.10981134	-0.59315546	0.54341417
C	-15.82906962	-2.57245886	-0.41107832
H	-14.41065709	-3.99002122	0.40579254
C	-15.28219122	-0.23644431	-0.12343848
H	-13.43224518	0.18697744	0.91948037
C	-16.14173678	-1.22581048	-0.60079895
H	-16.50662031	-3.35246440	-0.78765891
H	-15.52833373	0.82496063	-0.27279592
C	13.79755868	1.93923059	-0.73348825
C	14.65749897	2.92888505	-0.25645768
C	14.10981134	0.59315546	-0.54341417
C	15.82906962	2.57245886	0.41107832
H	14.41065709	3.99002122	-0.40579254
C	15.28219122	0.23644431	0.12343848
H	13.43224518	-0.18697744	-0.91948037
C	16.14173678	1.22581048	0.60079895
H	16.50662031	3.35246440	0.78765891
H	15.52833373	-0.82496063	0.27279592
N	-17.37666457	-0.85046643	-1.30434015
H	-17.93079049	-1.66744083	-1.46401885
N	17.37666457	0.85046643	1.30434015
H	17.93079049	1.66744083	1.46401885
C	-18.13651982	0.10452925	-0.48488713

Atom	X	Y	Z
C	-18.80608553	-0.33482007	0.65753371
C	-18.18805978	1.44991204	-0.84935514
C	-19.52756102	0.57095637	1.43487784
H	-18.76589219	-1.39569785	0.94417740
C	-18.90889767	2.35627217	-0.07133590
H	-17.66024899	1.79639090	-1.74963132
C	-19.57871882	1.91701468	1.07056142
H	-20.05586332	0.22461681	2.33501233
H	-18.94901773	3.41706186	-0.35872036
C	18.13651982	-0.10452925	0.48488713
C	18.80608553	0.33482007	-0.65753371
C	18.18805978	-1.44991204	0.84935514
C	19.52756102	-0.57095637	-1.43487784
H	18.76589219	1.39569785	-0.94417740
C	18.90889767	-2.35627217	0.07133590
H	17.66024899	-1.79639090	1.74963132
C	19.57871882	-1.91701468	-1.07056142
H	20.05586332	-0.22461681	-2.33501233
H	18.94901773	-3.41706186	0.35872036
N	-20.33916120	2.87145314	1.89011899
H	-20.88734183	3.45910173	1.29499956
N	20.33916120	-2.87145314	-1.89011899
H	20.88734183	-3.45910173	-1.29499956
C	-21.22546378	2.13575153	2.80341570
C	-22.41807559	1.58927214	2.32853807
C	-20.87413655	1.98389610	4.14470510
C	-23.25943508	0.89169033	3.19497651
H	-22.69514060	1.70982744	1.27120975
C	-21.71516653	1.28528278	5.01131797
H	-19.93412332	2.41438985	4.51911034
C	-22.90773658	0.73931452	4.53673145
H	-24.19978347	0.46146046	2.82088605
H	-21.43770247	1.16535732	6.06872320
H	-23.57124965	0.18920543	5.21968587
C	21.22546378	-2.13575153	-2.80341570
C	22.41807559	-1.58927214	-2.32853807
C	20.87413655	-1.98389610	-4.14470510
C	23.25943508	-0.89169033	-3.19497651

Atom	X	Y	Z
H	22.69514060	-1.70982744	-1.27120975
C	21.71516653	-1.28528278	-5.01131797
H	19.93412332	-2.41438985	-4.51911034
C	22.90773658	-0.73931452	-4.53673145
H	24.19978347	-0.46146046	-2.82088605
H	21.43770247	-1.16535732	-6.06872320
H	23.57124965	-0.18920543	-5.21968587
C	-3.76072641	2.95580563	-2.06857053

7.5.4.2. TP-PM6-VAC

*Table 7-13 Geometry of **TANI-PDI** optimized by PM6 (**TP-PM6-VAC**, X, Y, Z are atomic coordinates)*

Atom	X	Y	Z
C	-3.23677290	-0.28995527	-1.90578173
C	-2.36224629	-1.09694826	-1.13819100
C	-1.20904666	-0.57258069	-0.57887003
C	-0.89093915	0.81537582	-0.77809997
C	-1.77133867	1.62114463	-1.54710290
C	-2.95126997	1.04553023	-2.10977931
C	-0.29353663	-1.41057879	0.22114093
C	0.29353663	1.41057879	-0.22114093
C	1.20904666	0.57258069	0.57887003
C	0.89093915	-0.81537582	0.77809997
C	2.36224629	1.09694826	1.13819100
C	0.55397102	2.75236428	-0.44326538
C	-0.32767736	3.55277723	-1.20967346
C	-1.47126033	3.00218218	-1.75337828
H	-0.09784957	4.61409927	-1.36927585
H	-4.14310176	-0.73146247	-2.33906624
C	-0.55397102	-2.75236428	0.44326538
C	0.32767736	-3.55277723	1.20967346
C	1.47126033	-3.00218218	1.75337828
C	1.77133867	-1.62114463	1.54710290
H	0.09784957	-4.61409927	1.36927585
C	3.23677290	0.28995527	1.90578173
H	4.14310176	0.73146247	2.33906624

Atom	X	Y	Z
C	2.95126997	-1.04553023	2.10977931
H	1.44938714	3.22418963	-0.02935262
H	2.62247832	2.14976523	0.99858234
H	-2.62247832	-2.14976523	-0.99858234
H	-1.44938714	-3.22418963	0.02935262
C	-2.38087164	3.86754014	-2.54977787
O	-2.18837114	5.05064564	-2.74815199
C	-3.88565391	1.86789772	-2.92279277
O	-4.89764468	1.43096125	-3.43653334
C	3.88565391	-1.86789772	2.92279277
O	4.89764468	-1.43096125	3.43653334
C	2.38087164	-3.86754014	2.54977787
O	2.18837114	-5.05064564	2.74815199
N	-3.54183117	3.24216401	-3.10002418
N	3.54183117	-3.24216401	3.10002418
C	-4.46704944	4.09608144	-3.90629308
H	-5.12275252	3.43818669	-4.52693954
H	-3.86328803	4.71783904	-4.60586209
C	-5.31746299	4.99656506	-2.97903742
H	-5.74271517	4.40453987	-2.13634533
H	-4.66819021	5.77972403	-2.51882300
C	4.46704944	-4.09608144	3.90629308
H	3.86328803	-4.71783904	4.60586209
H	5.12275252	-3.43818669	4.52693954
C	5.31746299	-4.99656506	2.97903742
H	5.74271517	-4.40453987	2.13634533
H	4.66819021	-5.77972403	2.51882300
N	-6.38759591	5.64076383	-3.75452298
H	-6.10997799	6.41507296	-4.35814273
N	6.38759591	-5.64076383	3.75452298
H	6.10997799	-6.41507296	4.35814273
C	-7.73833793	5.25931661	-3.77929141
O	-8.47833273	5.91978650	-4.49509943
C	7.73833793	-5.25931661	3.77929141
O	8.47833273	-5.91978650	4.49509943
C	-8.19362828	4.13735148	-2.91900973
C	-9.23865582	4.38190630	-2.01203810
C	-7.67076549	2.84111905	-3.04115754

Atom	X	Y	Z
C	-9.73359392	3.36263992	-1.20665273
H	-9.67016351	5.38420875	-1.94770586
C	-8.15769370	1.80696192	-2.25093763
H	-6.87169742	2.63091803	-3.76124283
C	-9.18937434	2.06276615	-1.31253497
H	-10.55256684	3.56496410	-0.51981165
H	-7.73660445	0.81064818	-2.35635775
C	8.19362828	-4.13735148	2.91900973
C	7.67076549	-2.84111905	3.04115754
C	9.23865582	-4.38190630	2.01203810
C	8.15769370	-1.80696192	2.25093763
H	6.87169742	-2.63091803	3.76124283
C	9.73359392	-3.36263992	1.20665273
H	9.67016351	-5.38420875	1.94770586
C	9.18937434	-2.06276615	1.31253497
H	7.73660445	-0.81064818	2.35635775
H	10.55256684	-3.56496410	0.51981165
N	-9.59684336	0.99900672	-0.48478347
H	-9.39722563	0.05537894	-0.81365512
N	9.59684336	-0.99900672	0.48478347
H	9.39722563	-0.05537894	0.81365512
C	-10.69214432	1.10519074	0.44256400
C	-11.82462962	0.28539501	0.29574962
C	-10.59031670	1.97863296	1.54173255
C	-12.85011512	0.33578201	1.23597451
H	-11.90663029	-0.39376456	-0.55211021
C	-11.61709588	2.04212422	2.47581628
H	-9.70196352	2.60139881	1.65878616
C	-12.76510856	1.22609721	2.32665407
H	-13.71302483	-0.31906619	1.12372392
H	-11.53794652	2.72899371	3.31566339
C	10.69214432	-1.10519074	-0.44256400
C	11.82462962	-0.28539501	-0.29574962
C	10.59031670	-1.97863296	-1.54173255
C	12.85011512	-0.33578201	-1.23597451
H	11.90663029	0.39376456	0.55211021
C	11.61709588	-2.04212422	-2.47581628
H	9.70196352	-2.60139881	-1.65878616

Atom	X	Y	Z
C	12.76510856	-1.22609721	-2.32665407
H	13.71302483	0.31906619	-1.12372392
H	11.53794652	-2.72899371	-3.31566339
N	-13.81348902	1.39232170	3.26672981
H	-13.52900804	1.71662291	4.19183707
N	13.81348902	-1.39232170	-3.26672981
H	13.52900804	-1.71662291	-4.19183707
C	-14.97494752	0.54231381	3.26351904
C	-15.25459430	-0.28772571	4.36484138
C	-15.88006186	0.61449648	2.18905883
C	-16.42168943	-1.04414134	4.38815243
H	-14.56077879	-0.34422267	5.20239454
C	-17.04441273	-0.14707232	2.20383274
H	-15.67210833	1.28105391	1.34974387
C	-17.32194302	-0.99281080	3.29777841
H	-16.62835850	-1.68724685	5.24092296
H	-17.74584030	-0.06689321	1.37413631
C	14.97494752	-0.54231381	-3.26351904
C	15.25459430	0.28772571	-4.36484138
C	15.88006186	-0.61449648	-2.18905883
C	16.42168943	1.04414134	-4.38815243
H	14.56077879	0.34422267	-5.20239454
C	17.04441273	0.14707232	-2.20383274
H	15.67210833	-1.28105391	-1.34974387
C	17.32194302	0.99281080	-3.29777841
H	16.62835850	1.68724685	-5.24092296
H	17.74584030	0.06689321	-1.37413631
N	-18.45321767	-1.85071502	3.34542656
H	-18.80682015	-2.05586703	4.28133816
N	18.45321767	1.85071502	-3.34542656
H	18.80682015	2.05586703	-4.28133816
C	-19.45435429	-1.85226723	2.31530753
C	-20.79907444	-1.58805252	2.63410439
C	-19.10105524	-2.21841148	1.00194018
C	-21.78184051	-1.68088313	1.65194196
H	-21.08230904	-1.31615766	3.65000876
C	-20.07624779	-2.29157149	0.01392359
H	-18.06135361	-2.45052872	0.76517863

Atom	X	Y	Z
C	-21.42650471	-2.01534201	0.33009362
H	-22.82602275	-1.50781089	1.91377176
H	-19.79335958	-2.56152391	-1.00178164
C	19.45435429	1.85226723	-2.31530753
C	20.79907444	1.58805252	-2.63410439
C	19.10105524	2.21841148	-1.00194018
C	21.78184051	1.68088313	-1.65194196
H	21.08230904	1.31615766	-3.65000876
C	20.07624779	2.29157149	-0.01392359
H	18.06135361	2.45052872	-0.76517863
C	21.42650471	2.01534201	-0.33009362
H	22.82602275	1.50781089	-1.91377176
H	19.79335958	2.56152391	1.00178164
N	-22.39344299	-2.14747373	-0.69989901
H	-22.17162364	-2.78539492	-1.46087827
N	22.39344299	2.14747373	0.69989901
H	22.17162364	2.78539492	1.46087827
C	-23.62200963	-1.44434886	-0.78151318
C	-24.64118125	-2.00060356	-1.58856156
C	-23.83028760	-0.21226022	-0.13090769
C	-25.85535633	-1.32879908	-1.71711328
H	-24.48833359	-2.94724425	-2.09870757
C	-25.05705964	0.43735400	-0.27178927
H	-23.03770534	0.24651797	0.45600154
C	-26.07333968	-0.11369383	-1.05803983
H	-26.64351837	-1.75776046	-2.33623951
H	-25.21900878	1.38999916	0.23322401
H	-27.02506374	0.40014972	-1.16078761
C	23.62200963	1.44434886	0.78151318
C	24.64118125	2.00060356	1.58856156
C	23.83028760	0.21226022	0.13090769
C	25.85535633	1.32879908	1.71711328
H	24.48833359	2.94724425	2.09870757
C	25.05705964	-0.43735400	0.27178927
H	23.03770534	-0.24651797	-0.45600154
C	26.07333968	0.11369383	1.05803983
H	26.64351837	1.75776046	2.33623951
H	25.21900878	-1.38999916	-0.23322401

Atom	X	Y	Z
H	27.02506374	-0.40014972	1.16078761